NANOSTRUCTURED MATERIALS

SELECTED SYNTHESIS METHODS, PROPERTIES AND APPLICATIONS

Editors:
Philippe Knauth
Joop Schoonman

NANOSTRUCTURED MATERIALS
Selected Synthesis Methods, Properties and Applications

THE KLUWER INTERNATIONAL SERIES IN:

ELECTRONIC MATERIALS: SCIENCE AND TECHNOLOGY

Series Editor

HARRY L. TULLER
Massachusetts Institute of Technology

<u>**Other Books in Series**</u>

DIAMOND: Electronic Properties and Applications
> Lawrence S. Pan and Don R. Kania, Editors

ION IMPLANTATION: Basics to Device Fabrication
> Emanuel Rimini, Author

SOLID STATE BATTERIES: Materials Design and Optimization
> C. Julien and G. Nazri, Authors

SOL-GEL OPTICS: Processing and Applications
> L.C. Klein, Editor

PHOTOREFRACTIVE EFFECTS AND MATERIALS
> David Nolte, Editor

MATERIALS FOR OPTOELECTRONICS
> Maurice Quillec, Editor

PIEZOELECTRIC ACTUATORS AND ULTRASONIC MOTORS
> Ken Uchino, Author

WIDE-GAP LUMINESCENT MATERIALS: Theory and Applications
> Stanley R. Rotman, Editor

THIN FILM FERROELECTRIC MATERIALS AND DEVICES
> R. Ramesh, Editor

MICRO-ACTUATORS: Electrical, Thermal, Optical, Magnetic, Mechanical and Acoustic
> Massood Tabib-Azar, Author

HIGH-TEMPERATURE SUPERCONDUCTORS: Materials, Properties and Applications
> Rainer Wesche, Author

NANOCRYSTALLINE METALS AND OXIDES: Selected Properties And Applications
> Philippe Knauth, Joop Schoonman

NANOSTRUCTURED MATERIALS
Selected Synthesis Methods, Properties and Applications

edited by

Philippe Knauth
Professor
Université de Provence
Marseille, France

Joop Schoonman
Professor
Delft University of Technology
Delft, The Netherlands

Created in the United States of America

Visit Kluwer Online at: http://kluweronline.com
and Kluwer's eBookstore at: http://ebooks.kluweronline.com

CONTENTS

PREFACE

In the framework of the rapid development of Nanoscience and Nanotechnology, the domain of Nanostructured Materials is attracting more and more researchers, both academic and industrial. Synthesis methods are a major prerequisite for achievement in this rapidly evolving field. This book presents several important recent advances in synthesis methods for nanostructured materials and processing of nanoobjects into macroscopic samples, such as nanocrystalline ceramics. The chapters do not cover the whole spectrum of possible synthesis techniques, which would be limitless, but present highlights especially in the domains of interest of the editors.

M.-P. Pileni presents "chimie douce" approaches for preparation of a large variety of nanostructured materials, including metals, alloys, semiconductors and oxides. Normal micelles, i.e. oil in water droplets, stabilized by a surfactant, and reverse micelles, i.e. water in oil droplets, are used as nanoreactors. Spherical nanoparticles and nanocrystals with a shape anisotropy, such as nanorods, can be obtained.

O. Schäf et al. demonstrate that hydrothermal synthesis with water as solvent and reaction medium can be specifically adapted to nanostructured materials, if crystal growth can be avoided and a high degree of supersaturation is maintained, thereby enhancing the rate of nucleation. Different modes of operation are presented, including rapid expansion of supercritical solutions, rapid thermal decomposition of precursors in solution and static high-pressure hydrothermal synthesis.

T. Ciach et al. present "electrospraying" as a powerful new route for the preparation of nanoparticles, especially of oxides for electroceramics. The principle of the electro-hydro-dynamic atomization technique and bipolar coagulation, i.e. mixing of two electrospray droplets, are explained and examples of nanoparticle production are given.

M. Jak then shows how nanoparticles can be processed into nanostructured ceramics, by using dynamic compaction techniques. This chapter covers the explosive compaction and the room-temperature magnetic-pulse compaction techniques. Examples of ceramic oxides and nanocomposites are presented, which show the broad applicability of these techniques and the advantages in comparison with classical compaction.

The following chapters are devoted to selected properties and applications of nanostructured materials and will be a good complement to those already presented in our previous volume in this series (P. Knauth, J. Schoonman, ed., Nanocrystalline Metals and Oxides : Selected Properties and Applications, Kluwer, Boston, 2002).

J. Molenda et al. discuss the electrical and electrochemical properties of nanostructured manganese spinel, that is potentially important as cathode material in rechargeable lithium-ion batteries.

S. A. Zavyalov et al. use co-condensation of metal nanoparticles in a polymer matrix to prepare nanocomposites. The percolation threshold of metal nanoparticles is important for the electrical, optical, and chemical properties of the nanocomposites.

D. Nesheva et al. study evaporated multilayers with continuous nanocrystalline CdSe layers, or with discontinuous nanocrystals of CdSe, depending on the thickness and morphology of the other layer (SiO_x, GeS_2 or ZnSe). Quantum size effects are attributed to 1D carrier confinement in the continuous CdSe layers and quasi-3D confinement in the discontinuous "composite" films.

J. Pielaszek discusses how X-ray diffraction can be applied to study the structure of nanostructured materials. The determination of an average crystallite size from reflection broadening, especially using Scherrer's equation, and the Rietveld refining, and atomistic modeling of X-ray diffraction patterns from nanostructured materials are described.

H. Zandbergen introduces High Resolution Electron Microscopy as a powerful tool for studying nanostructures. The imaging process of HREM, the relations between the micrography and the material structure are described and examples of HREM studies of grain boundaries are shown. Ways to investigate the chemical composition and electronic effects are outlined.

Given the tremendous importance of this field for the future development of the industrialized world and mankind in general, the final chapter of this book is devoted to « nanoelectronics ». G. Allan et al. present a prospective on further size reduction in microelectronics and on the future of molecular electronics. The first part treats devices built on inorganic materials and quantum effects, such as tunneling junctions. The second part introduces the concepts of molecular diodes, wires, and circuits, experiments on molecules in solution and imaging and fabrication of molecular objects.

Marseille, France, and Delft, The Netherlands, June 2002.

P. Knauth and J. Schoonman

Nanomaterials Production by Soft Chemistry

M.P.Pileni

Laboratoire LM2N, Université P. etM. Curie (Paris VI), B.P. 52, 4 Place Jussieu, F - 752 31 Paris Cedex 05, France.

Abstract. In this paper, various ways to make nanocrystals are presented. It is possible, by using colloidal self-assemblies as nanoreactors, to produce a large variety of nanoparticles, semiconductors, metals, oxides and alloys The limitations in using these colloidal solutions to produce nanomaterials are pointed out.

I. Introduction.

During the last decade, due to the emergence of a new generation of high technology materials, the number of groups involved in nanomaterials has increased exponentially[1,2]. Nanomaterials are implicated in several domains such as chemistry, electronics, high density magnetic recording media, sensors and biotechnology. This is, in part, due to their novel material properties, that differ from both the isolated atoms and the bulk phase. An ultimate challenge in materials research is now the creation of perfect nanometer-scale crystallites (in size and shape) identically replicated in unlimited quantities in a state than can be manipulated and that behave as pure macromolecular substances.

The essential first step in the study of their physical properties and the use of nanomaterials in various technologies is their production. Physical and chemical methods were developed: ball milling[3,4], a flame by vapor phase reaction and condensation[5], chemical reduction[1] and coprecipitation[1,6-10] have been employed to control the particle size (up to 10 nm) and morphology. More recently, new preparation methods have been developed such as sonochemical reactions[11], gel-sol[12], microwave plasma[13] and low energy cluster beam deposition[14]. In 1988, we developed a method based on reverse micelles (water in oil droplets) for preparing nanocrystals[15]. In 1995, we were able to control size and shape of nanocrystals by using colloidal solutions as templates[2]. Using these methods we fabricated various types of nanomaterials : metals $((Ag)_n, (Cu)_n, (Co)_n)$, semiconductors (CdS, CdTe etc...) and alloys (Fe-Cu, CdMnS, CdZnS). Normal micelles make it possible to produce ferrite magnetic fluids[16]. Some of the techniques described above enable preparing amorphous nanoparticles whereas others favor formation of highly crystallized nanoobjects.

One of the challenges is to produce anisotropic nanocrystals. Colloidal solutions can be used as a nano-reactor[17] whose shape partially plays a role in the shape of the nanomaterial produced (see below). In the last two

years, a large number of groups have succeeded in making nanorods. Various nanomaterials such as silver[18,19], gold[19-23], platinium[24,25], copper[26] and semiconductors[27,28] were produced. In most cases, a surfactant, usually cethyltriethylammonium bromide or its derivatives, is added to the preparation solution. However, the colloidal solution is a mixture of several compounds and its structure is unknown. The surfactant is used as a polymer and plays an important role in formation of nanorods. The aspect ratio (length to width ratio) markedly depends on the amount of surfactant, but the key factor in favoring the nanocrystal growth in a given direction is not known.

Self-assembled nanocrystals have attracted increasing interest over the last five years [17,29,30]. The level of research activity is growing seemingly exponentially, fueled in part by the observation of physical properties that are unique to the nanoscale domain. The first two- and three-dimensional superlattices were observed with Ag_2S and CdSe nanocrystals[29,30]. Since then, a large number of groups have succeeded in preparing various self-organized lattices of silver[31-34], gold[35-38], cobalt[39], and cobalt oxide[40]. With the exception of CdSe[30] and cobalt[39] nanocrystals, most superlattice structures have been formed from nanocrystals whose surfaces are passivated with alkanethiols. When nanocrystals are characterized by a low size distribution, they tend to self-organize in compact hexagonal networks. Conversely, if the distribution is too large they are randomly dispersed on a substrate. This is obtained when a drop of solution containing the nanocrystal is deposited on the substrate lying on a paper. Conversely, when the substrate is fixed with anti-capillary tweezers, rings made of nanocrystals, and surrounded by bare substrate, are formed[42]. This is observed with silver, gold, CdS and ferrite nanocrystals. These phenomena were attributed to either wetting[34] or magnetic[43] properties. In fact, they are due to Marangoni instabilities[42]. Under other deposition conditions, large "wires" composed of silver nanoparticles have been observed, in which the degree of self-organization varies with the length of

the alkyl chains coating the particles[44]. Interestingly, it has been recently demonstrated that the physical properties of silver[45,46], cobalt[39,47,48] and ferrites[49,50] nanocrystals organized in 2D and/or 3D superlattices differ from those of isolated nanoparticles. These changes in the physical properties are due to the short distances between the nanocrystals. Such collective properties are attributed to dipole-dipole interactions. Furthermore, the electron transport properties drastically change with the nanocrystal organization[51].

In this paper a colloidal solution with a well-known structure is used as a template to produce nanocrystals. The size and shape of the materials are partially controlled by that of the template.

II. Results and discussions.

Colloidal solutions favor partial control of the size and shape of nanomaterials. In the following, colloid methods developed to make nanocrystals are described.

II. 1. Spherical nanoparticles

Several techniques are used to produce nanomaterials by soft chemistry. Either amorphous or crystalline nanoparticles are obtained. Whatever the procedure is, the major factors involved in controlling the size or shape of nanoparticles are confinement, electrostatic interactions, reactant solubilities and large local amounts of reactant. After or during the production, nanoparticles have to be passivated to prevent coalescence. One of the first approaches to make nanoparticles was based on the variation of the solubility product of reactant with temperature[52]. This controls the particle size. Simultaneously, syntheses of nanoparticles were developed in aqueous solution in presence of a charged polymer that strongly interacts with one of the reactants[53,54]. In the following, data obtained by using colloidal self-assemblies as a nano-reactor to control the nanocrystal sizes are given.

i) Reverse micelles

Reverse micelles are water in oil droplets stabilized by the surfactant[55]. The water to surfactant concentration ratio, $w=[H_2O]/[S]$, linearly controls the size of the droplet[56]. Reverse micelles are subjected to Brownian motion and during these collisions the droplets combine to form a dimer with an exchange of their water contents. The dimer dissociates to again form reverse micelles. These two properties (control of the droplet size[56] and the exchange process[57]) make possible the use of reverse micelles as a nano-reactor. Two micellar solutions are prepared. Each contains one of the reactants. By mixing these solutions, a chemical reaction takes place[58] and nanomaterials are produced[1,2]. The droplet size, which is controlled by w, controls the size of the particle. This procedure has been used to obtain a large variety of materials such as semiconductors[1,59], metals[1,40,60] and oxides[61].

When the two reactants are present as salts, amorphous nanomaterials are formed. Conversely, when one of the reactants is a functionalized surfactant (the reactant is the counter ion of the surfactant) nanocrystals are produced. In the latter case, it is possible to make well defined alloys like $Cd_{1-y}Zn_yS$[62], $Cd_{1-y}Mn_yS$[63] whereas it is not possible with salt ions solubilized in the droplets. All the chemical reactions occurring in aqueous solution cannot be obtained in micelles. This was well demonstrated with telluride derivatives. CdTe is made as described above[64]. But it is not possible to produce $Cd_{1-y}Mn_yTe$[65] whereas $Cd_{1-y}Mn_yS$ nanocrystals are formed. The replacement of sulfur by the telluride derivative induces formation of rods of telluride and CdTe nanocrystals[65]. Similarly, it is possible to produce ZnS and not ZnTe. Again telluride rods are formed. These data clearly show that chemistry in homogeneous solution (aqueous) differs from that of colloids (water in oil droplets).

 In the following, one of the reactants is a functionalized surfactant. On increasing the water content, i.e., the size of the nano-reactor (water in oil droplet), the particle size increases (Fig. 1). However the variation of the nanocrystal diameter depends on the type of produced material. For II-VI

6

semiconductors[59] such as CdS, ZnS, $Cd_{1-y}Mn_yS$, $Cd_{1-y}Zn_yS$, CdTe it is possible to control the particle diameter from 1.8 nm to 4 nm. Conversely for silver sulfide[66] and copper[67] nanocrystals it can be varied from 2 to 10 nm. The major change in the particle size is obtained at low water content: On increasing the water content, the particle size increases to reach a plateau around w=20. If it is
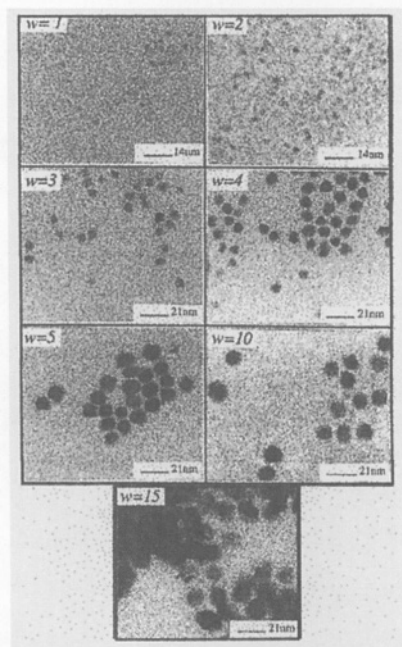

Figure 1. TEM pattern of copper nanocrystals obtained in mixed reverse micelles (Na(AOT)-Cu(AOT)₂) at various water contents
A w=2, B w=5, C w=40

assumed that the largest particle size and that of the water molecule volume is 1, CdS, ZnS, CdZnS, CdMnS, PbS, Co, Ag nanocrystals and the water molecule volume behave similarly as shown in Figure 2. This indicates that the crystal growth is related to the water structure inside the droplet, which is confirmed by the change in the O-H vibration of this water[68] (Fig. 2). This is valid for most of the nanocrystals produced. Discrepancies are observed with silver sulfide and silver nanocrystals. With silver sulfide nanocrystals, a linear increase in the particle size with the water content is seen[66]. With silver nanocrystals, the behavior observed in Figure 2 is obtained when the reducing agent is sodium borohydride. On using hydrazine as the reducing agent, the behavior markedly

changes. At low water content (w=2), the average size of nanocrystals is 5 nm with a low size distribution (12%). On increasing the water content, the size distribution markedly increases (40%) and the average diameter is around 3.5 nm. It does not change with increasing w from 10 to 40. Such changes in the behavior can be related to the fact that with sodium borohydride the chemical reaction is very fast whereas with hydrazine it is rather slow. It also must be noted that it is possible to make larger nanocrystals by using a plastic vessel which again prevents deposition of a silver nanocrystal film on the surface.
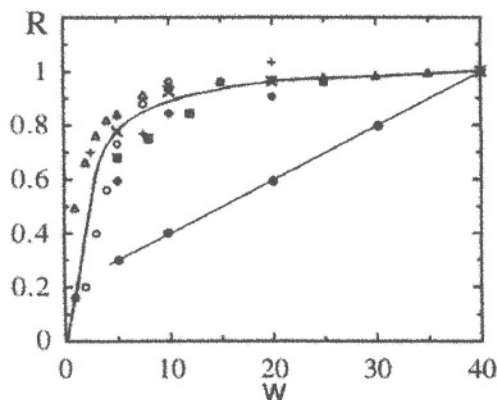

Figure 2. Variation with the water content of the average diameter of nanocrystals and of the volume of water molecules. Nanocrystals CdS (◆), ZnS (x), PbS (⊠), CdZnS (•) CdMnS(+), Ag (O) and Ag_2S (●)

The crystalline structure of nanocrystals usually differs from that of the bulk phase. As an example, the II-VI semiconductors in the nano-scale are characterized by a hexagonal structure (Wurtzite)[69,70] whereas the bulk phase is cubic (Zinc Blende). In some cases, the structure of nanocrystals in the phase obtained in the nanoscale is unstable compared to the bulk phase. In the bulk phase, silver iodide has, at room temperature, two stable phases (β and γ) and an unstable one (α). On the nanoscale range, the α and β phases are stable and the γ phase cannot be detected. These structural changes are observed for a large number of nanocrystals. Of course, this change in the structural behavior is not general. For example, silver sulfide nanocrystals form a monoclinic phase in the nano-scale and in the bulk materials.

By replacing a mixed surfactant by a functionalized surfactant, the phase diagram drastically changes[71,72]. To our knowledge, one of most quantitative studies of the phase diagram obtained using functionalized surfactant was with copper diethyl sulfosuccinate, $Cu(AOT)_2$, water, isooctane. Similar behavior was obtained with many other divalent surfactants such as $Co(AOT)_2$ and $Cd(AOT)_2$. Reverse micelles are formed in two regions for the phase diagram: $0<w<5$ and $30<w<40$. Syntheses in these two regions of the phase diagram induce formation of copper nanocrystals with average particle sizes smaller in the $0<w<5$ region (12-nm) than those at higher water content (7.5-nm) (Fig. 3)[73]. This is explained by the fact that the redox potential changes with the water structure inside the water pool. At low water content, the number of nuclei formed is rather small and large nanocrystals are produced.
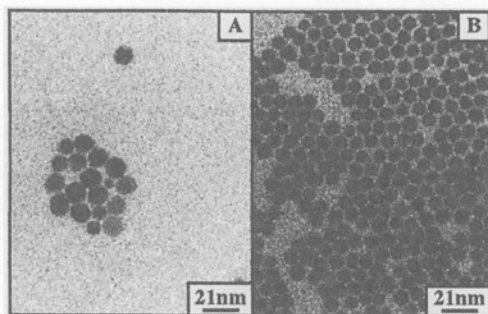
Figure 3. TEM patterns of copper nanocrystals prepared using pure functionalized reverse micelles ($Cu(AOT)_2$) at w=2 and w=40

On increasing the water content, the number of nuclei increases inducing formation of smaller nanocrystals. By replacing $Cu(AOT)_2$ with $Co(AOT)_2$, in the water- rich region ($30<w<40$) cobalt nanocrystals are produced[74]. At the same water content (w=40), the average nanocrystal size. Again this is smaller in mixed micelles (5.6nm)[39] than in pure functionalized surfactant (8 nm)74, this has to be related to the number of nuclei formed during the chemical reduction.

ii) Normal micelles

Normal micelles are oil in water droplets and with these the length of the surfactant alkyl chain controls the size of the droplets. Most of the nanomaterials produced are made with functionalized surfactants. This induces a marked increase in the local amount of reactants and a supersaturation regime is formed. Conversely to reverse micelles, there is no confinement of the reactants. Normal micelles act as a polymer to control the nanoparticles size. It has been possible to make CdS[75] and copper[76] nanocrystals and magnetic fluids[77]. In the latter case, transition metals involved in the ferrofluids form the counter ions of the micelles. This technique makes it possible to produce a large variety of alloys[78,80] with a composition similar to that of the reactant used for the syntheses. The size of the nanocrystals, which can vary from 2 to 8 nm, is controlled by the micellar concentration.

II.2 Nanocrystals having a shape anisotropy.

Colloidal solutions are good candidates for controlling the shape of nanocrystals. For a given surfactant-water-oil system, it is well known that a large variety of self-organizations of the surfactant can be produced[55,81]. This is demonstrated from a careful structural study of the phase diagram. Such joint structural and synthesis studies were done with $Cu(AOT)_2$- water - isooctane solution in the oil-rich region of the phase diagram. Figure 4 shows the various structures of colloidal self-assemblies. At low water content, w<5, reverse micelles are formed. On increasing the water content, the system evolves from spheres to interconnected cylinders (5<w<9). A further increase in the water content results in the appearance of a lamellar phase in equilibrium with interconnected cylinders (9<w<10). At higher water content a pure lamellar phase is formed (10<w<15.5). These changes in the colloidal structure are related to the change in the surfactant head polar group hydration[71]. A further surrounded by interconnected cylinders[72]. Then the system evolves to interconnected cylinders (26<w<31) and spherical reverse micelles (31<w<40). Chemical reduction of the surfactant produces copper nanocrystals[73] and, as
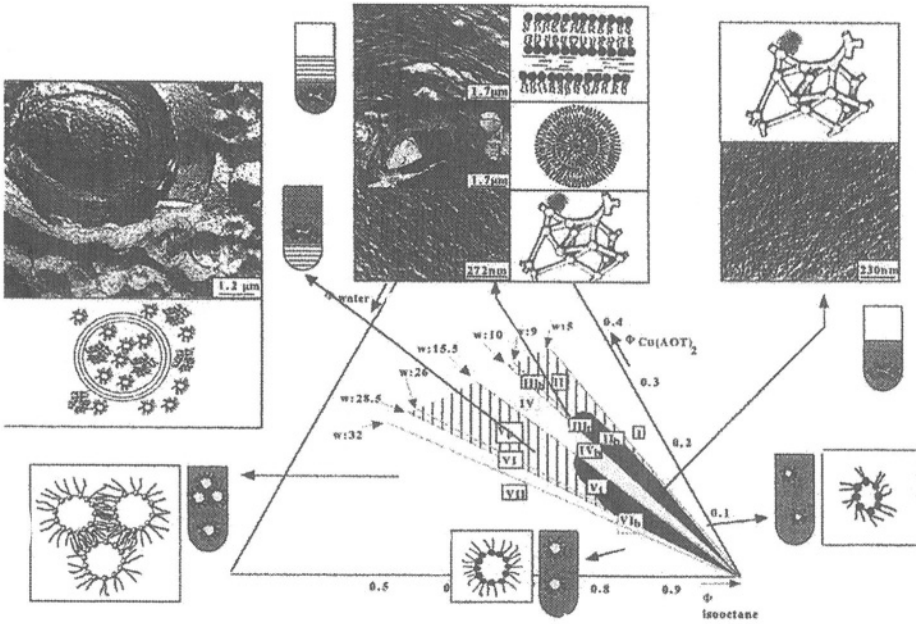
Figure 4. Phase diagram of Cu(AOT)₂-water-isooctane

shown in Figure 5, the shape of the colloid plays an important role in the shape of these nanocrystals. In reverse micellar solution (w<5 and 31<w<40), spherical copper nanocrystals are formed. In the region of interconnected cylinders (5<w<10 and 26<w<31) cylinders and spheres are produced. It can be seen that the average size of these nanocrystals is the same in the various w regions[73,82]. In the stable emulsion region various shapes of nanocrystals are produced (square, triangular, cylindrical). From comparison of Figure 4 and Figure 5, it can be concluded that the shape of the template has to be taken into account to control the particle size and shape. A question arises : Is the template the only parameter which plays a role in controlling the shape of nanocrystals[83]?

Let us consider the region corresponding to 9<w<10, where most of the nanocrystals produced are spheres with a very small number of cylinders (Fig. 6A). Addition of various salts such as NaCl, NaBr, NaNO₃, KCl, KBr
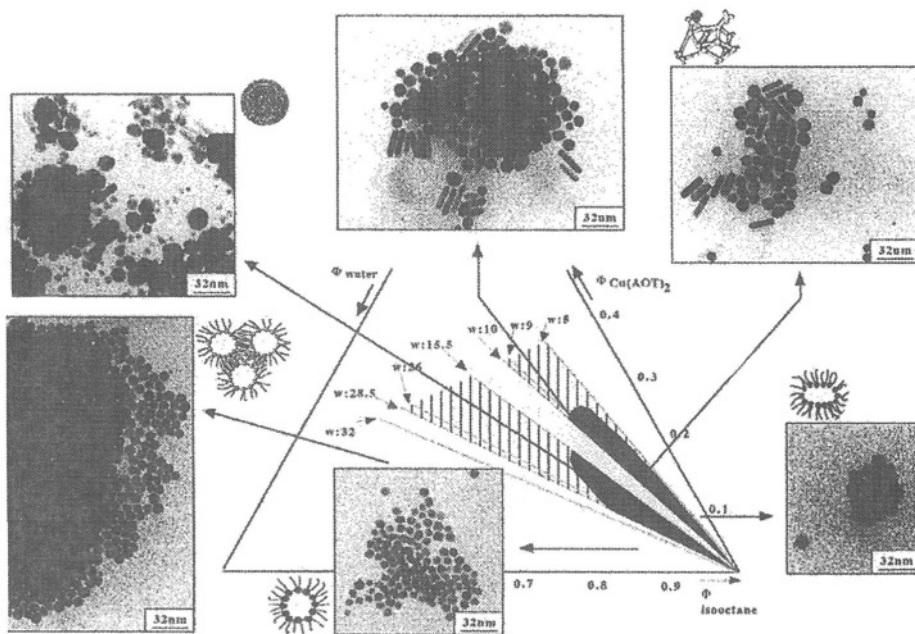
Figure 5. Shape of copper nanocrystals produced in the various parts of the phase diagram described in Figure 4.

and KNO_3 in the mesostructured fluids does not induce, from the macroscopic viewpoint, drastic changes in the phase diagram. With $10^{-3}M$ overall salt concentration, the three phases remain. The relative volume of isooctane remains constant and is rather large compared to the others. Slight changes, close to experimental errors (10%), in the relative volumes of birefringent and isotropic phases are observed. From SAXS measurements of the isotropic phase, it is seen that there is a slight increase in the characteristic diameter and a decrease in the head polar area by salt addition. However no changes in the parameters were observed by changing the salt. The scattering curves obtained with various salts are superimposed and from this it is concluded that the macroscopic structure of the template remains unchanged.
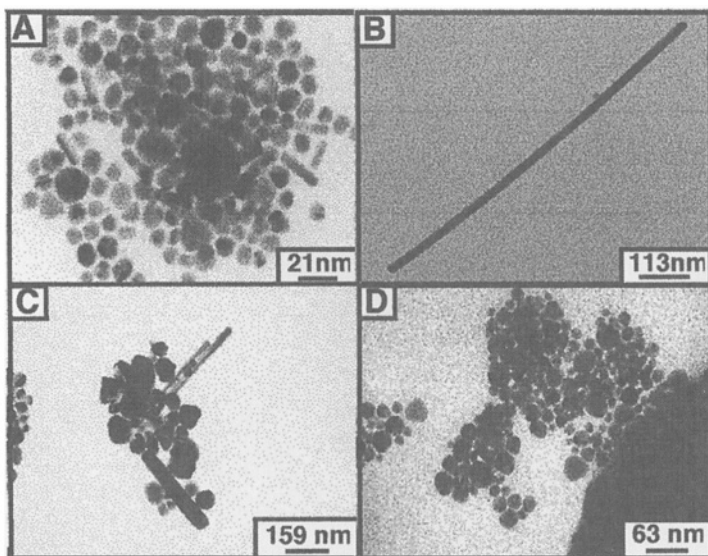
Figure 6. TEM patterns of nanocrystals obtained in presence of various salts (**A**) [salt]=0, (**B**) [NaCl]=10^{-3} M, (**C**) [NaBr]=10^{-3} M, (**D**) [NaNO$_3$]=10^{-3} M.

Synthesis in presence of 10^{-3}M NaCl induces formation of very long rods (Fig. 6B) and along with these, nanocrystals having various shapes (square, triangular, etc...) are produced. The number of rods is too small to be described statistically. However, the shortest length and width of the rods ar 650 nm and 15 nm whereas the maximum values are 1600 nm and 25 nm, respectively. These rods are highly crystalline[84] (Fig. 7A). The HRTEM images of a sample tilted at 0° ±18° and ±36° are in Fig. 7B.

After tilting these cylindrical particles, a periodic sequence can be observed, i.e., every 36° a complete repetition of the high-resolution image, clearly displayed in the power spectrum, is achieved. A second different configuration is obtained by tilting around ±18°. From the real image, it can be seen that for 0° and ±36° tilt angles, the central part of the image shows atomic resolution with strong contrast. However, the particles tilted by ±18° only show lattice planes on the left or the right part of the image. Indeed, the reflections obtained with the different tilt angles correspond to the same lattice parameters and the angles between planes are also in good
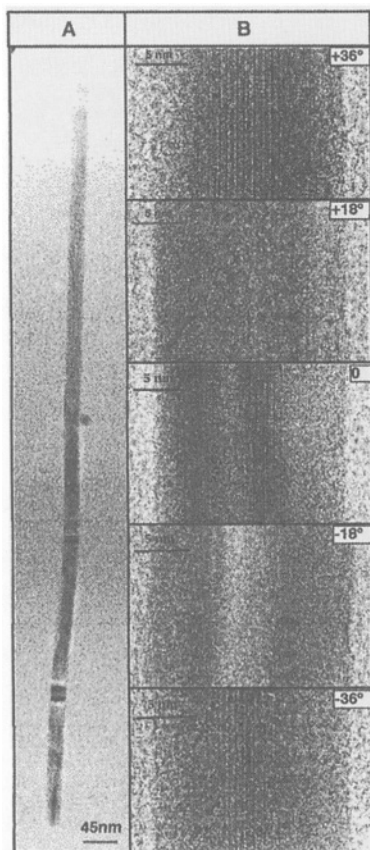
Figure 7. A Overview TEM image of Cu rods with an electron optical magnification
B- Series of tilted samples: From top to bottom: $+36^0$, 0^0, and -36^0.

agreement. The structure of copper rods is a truncated decahedron with 5-fold symmetry. A similar structure with a 5-fold symmetry is observed with cylinders shown in Figure 5 and Figure 6A. Hence, cylinders and rods of copper nanocrystals do not have the same structure as the bulk phase. This is rather surprising because it was established that nanomaterials having a size larger than 10 nm were characterized by a crystalline phase similar to that of the bulk. This claim is probably wrong. In fact, similar 5 fold symmetries were observed recently for silver[85] and gold[86] cylindrical nanocrystals.

By replacing NaCl by KC1, similar behavior is observed with formation of long rods (Fig. 8A). Rods are also obtained with $CuCl_2$ or CTAC (Figs. 8B and 8C). It can be noticed that there are still spherical and other shapes

(square, triangular, etc.). However, no small cylinders are observed in presence of chloride ions which clearly indicates that only the cylinders grow to form rods. This is well demonstrated by following the rod formation kinetics. Figure 9 shows that the length of the cylinders increasespreferentially compared to the width. This indicates that chloride ions inhibit the growth along the [100] direction and favor that along the [110] direction. Of course this phenomenon depends on the amount of chloride ions present in solution. On increasing the chloride ion concentration, the relative length versus width of the rods increases and then decreases as shown in Figure 10. The maximum is reached for $5.10^{-3}M$ chloride ions. The same behavior is observed with $CuCl_2$ and CTAC as additives [87]. The length increases with chloride concentration and then decreases above $10^{-3}M$ whereas the width increases progressively. This
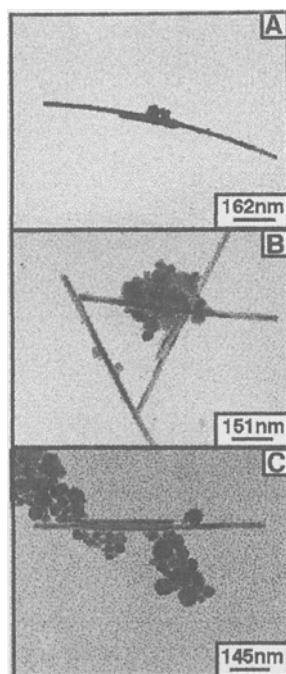

Figure 8. TEM patterns of nanocrystals obtained in presence of various salts **(A)** $[KCl]=10^{-3}$ M, **(B)** $[CuCl_2]=10^{-3}$ M, **(C)** $[CTAC]=10^{-3}$ M.

indicates that above a given chloride concentration, the inhibition efficiency along the [100] direction decreases. On annealing the rods, two behaviors are observed[88,89]:
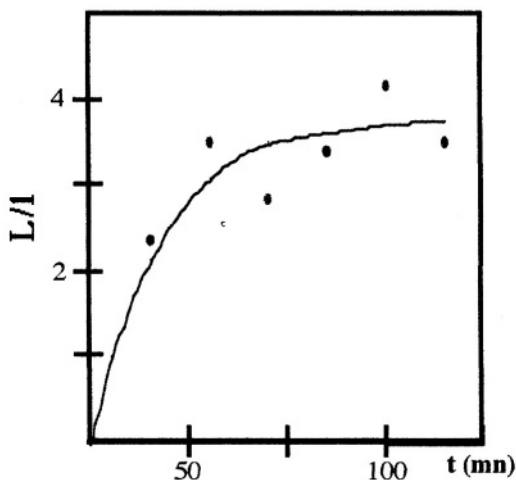
Figure 9. Variation of the length to width ratio of rods with time. [Cu(AOT)$_2$]= 5.10^{-2}M , [NaCl]=10^{-3} M.

i) The rods remain stable at high temperature (925°C). We have to keep in mind that the melting temperature of bulk (phase) copper is 1083°C.
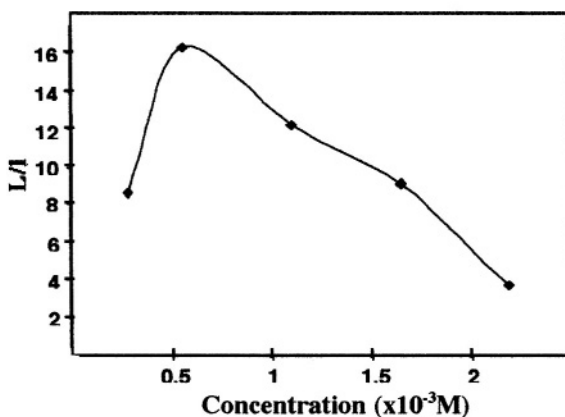
Figure 10. Variation of the length to width ratio of rods with chloride concentration [Cu(AOT)$_2$]= 5.10^{-2}M , reaction time, t= 120min.

ii) The rods form small cylinders having the same structure as the long rods. Hence even after annealing, the rods do not crystallize in the FCC structure of that of copper in the bulk phase.

By replacing NaCl by NaBr at the same salt concentration ($10^{-3}M$), the number of rods markedly decreases (Fig. 6C). The longest length and width are 400 nm and 56 nm whereas the shortest are 230 nm and 24 nm, respectively. It can be seen that that a relatively large amount of square flat nanocrystals appear. The major difference between additions of NaCl and NaBr is the size of the rods and the appearance of this large amount of square nanocrystals. In presence of $NaNO_3$, no rods are formed and spheres are produced (Fig.6D). These data clearly show that the anions added to the microstrucrure play an important role in the nanocrystal shape. Two phenomena take place:

i) The production yield of copper nanocrystals drastically increases by salt addition. This does not seem to change markedly with the salt used and is related to data obtained in presence of CTAC in mixed reverse micelles[87]. This could be attributed to screening of the copper ions interactions with the anionic head polar group of the surfactant. This induces changes in the redox potential of copper ions.

ii) The chloride ions adsorb specifically on a given direction of the lattice plane of the nanocrystals and favor the growth in this direction (110). This adsorption process differs with the salt anion.

References

1- Pileni, M.P.; J. Phys. Chem.; **1993,** 97, 6961

2- Pileni, M.P.; Langmuir; **1997,** 13, 3266

3- Goya, G.F.; Rechenberg, H. R.; J. Mag. Mag. Mat. **1999,** 196-197, 191.

4- Fatemi, D. J.; Harris, V. G.; Browning, V.M.; Kirkland, J. P.; J. Appl. Phys. **1998,** 83, 6867

5- Elmore, W.C.; Phys.Rev. 54, **1938,** 309

6- Sato, T.; lijima, T.; Seki, M.; Inagaki, N.; J. Mag. Mag. Mat. **1987,** 65, 252

7- Ueda, M.; Shimada, S.; Inagaki, M. J.; Eur. Cer. Soc. **1996,** 16, 685

8- Yokoyama, M.; Sato, T.; Ohta, E.; Sato, T.; J. Appl. Phys. **1996,** 80, 1015.

9- Chen, Q.; Zhang, Z. ; J. Appl. Phys. Lett. **1998,** 73, 3156.

10- Vayssières, L.; Chanéac, C.; Tronc, E.; Jolivet, J.P.; J. Coll. Int. Sci. **1998,** 205, 205.

11- Shafi, K.V.P.M.; Koltypin, Y.; Gedanken, A.; Prozorov, R.; Balogh, J.; Lendvai, J.; Felner, I. ; J. Phys. Chem. B **1997,** 101, 6409.

12- Sugimoto, T.; Shimotsuma, Y.; Itoh, H. ; Powder Tech. **1998,** 96, 85.

13- Vollath, D.; Szabo, D.V.; Taylor, R.D.; Willis, J.O.; J. Mat. Res. **1997,** 12,2175.

14- Perez, A.; Melinon, P.; Dupuis, V.; Prevel, B.; Bardotti, L.; Tuallon-Combes, J.; Maselli, B.; Treilleux, M.; Pellarin, M.; Lerme, J. ; Cottancin, E.; Broyer. M. ; Janet, M.; Negrier, M.:; Tournus, F.; Gaudry, M.; Materials Transactions, in press (2001)

15- Petit, C. and Pileni, M.P., J. Phys. Chem., **1988,** 92, 2282,

16- Moumen, N. and Pileni M.P.; J. Phys. Chem.; **1996,** 100, 1867.

17- Pileni, M.P.; J. Phys. Chem.; **2001**, in press

18- Jana, N.R.; Gearhearth, L.; Murphy, C. ; J. Chem. Commun, **2001,** 617

19- Cepak, V.M.; Martin, C.R.; J. Phys. Chem.; **1998,** 102, 9985

20- Wang, Z.L.; Gao, R.P.; Nikoobakht, B.; El Sayed, M.A.; J. Phys. Chem.; 2000, 104, 5417

21- Bianca, M.; Van der Zande, I.; Böhmer, M.R.; Lambertus, G.; Fokkink, J.; Schönenberger, C.; J. Phys. Chem.; **1997,** 101, 852

22- Yu, Y.Y.; Chang. S.S.; Lee, C.L.; Chris Wang, C.R. ; J. Phys. Chem.; **1997,** 101, 6661

23- Jana, N.R.; Gearhearth,L.; Murphy, C.J.; J. Phys. Chem.; **2001,** 105, 4065

24- Kyotani, T.; Tsai.L.F.; Tomita, A.; Chem. Commun.; **1997,** 701

25- Henglein, A.; Giersig. J. Phys. Chem.; **2000,** 104, 6767

26- Toimil Molares, M.E.; Buschmann, V.; Dobrev, D.; Neumann, R.; Scholz, R.; Schuchert, I.U.; Vetter, J.; Adv. Mater.; **2001,** 13,62

27- Wang,S.; Yang, S.; Langmuir; **2000,** 16, 389

28- Chen, C.C.; Chao, C.Y. Lang, Z.H.; Chem. Mater.; **2000,** 12, 1516

29- Motte L., Billoudet F., Pileni M.P.; J Phys Chem.; **1995,** 99, 16425

30- Murray. C.B., Kagan C.R., Bawendi M.G.; Science ; **1995,** 270, 1335

31- Harfenist S.A., Wang Z.L., Alvarez M.M., Vezmar I., Whetten R.L.; J. Phys. Chem.; **1996,** 100, 13904

32- Taleb A., Petit C., Pileni M.P.; Chem. Mater. ; **1997,** 9, 950

33- Harfenist S.A.; Wang Z.L.; Whetten R.L.; , I.; Alvarez, M.M. ; Adv. Mater.; **1997,** 9, 817

34- Ohara, P.C.; Heath, J.R.; Gelbart, W.M.; Angew Chem. Int. Engl.; **1997,** 36, 1078

35- Brust, M.; Bethell, D.; Schiffiin, D.J.; Kiely, C.; Adv. Mater.; **1995,** 9, 797

36- Hostetler, M.J.; Stokes, J.J.; Murray, R.W.; Langmuir; **1996,** 12, 3604

37- Vijaya Sarathy, K.; Raina, G.; Yadav, R.T.; Kullkarni, G.U.; Rao, C.N.R.; J. Phys. Chem. B ; **1997,** 101, 9876

38- Badia, A.; Cuccia, V.; Demers, L.; Morin, F.; Lennox, R.B.; J. Am. Chem. Soc.; **1997,** 119, 2682

39- Petit, C.; Taleb, A.; Pileni, M.P.; J. Phys. Chem.; **1999,**103, 1805

40- Yin, J.S., Wang, Z.L; Phys. Rev. Lett.; **1997,** 79, 2570

41- Vossmeyer, T.; Chung, S.; Gelbart, W.M.; Heath, J.R.; Adv. Mater. ; **1998**, 10,351

42- Maillard, M.; Motte, L.; Ngo, A.T.; Pileni, M.P.; J. Phys. Chem. B; **2000**, 104, 11871

43- Kurrika, V.; Shafi, P.M.; Felner, I.; Mastai, Y.; Gedanken, A.; J. Phys. Chem.; **1999**, 103, 3358

44- Motte L.; Pileni M.P.; J. Phys. Chem. B ; **1998**, 102, 4104

45- Taleb, A.; Petit, C; Pileni, M.P.; J. Phys. Chem. B ; **1998**, 102, 2214

46- Taleb, A.; Russier, V.; Courty, A.; Pileni, M.P.; Phys. Rev. B.; **1999**, 59, 13350

47- Petit, C.; Taleb, A.; Pileni, M.P.; Adv. Mater.; **1998**, 10, 259

48- Russier, V.; Petit, C.; Legrand, J.; Pileni, M.P.; Phys. Rev. B; **2000**, 62, 3910

49- Ngo, T. and Pileni, M.P.; Adv. Mater.; **2000**, 12, 276,

50- Ngo, T. and.Pileni, M.P.; J. Phys. Chem.; **2000**, in press

51- Taleb, A.; Silly, F.; Gusev, O.; Charra, F.; Pileni, M.P.; Adv. Mater.; **2000**, 12, 119

52- Brus, L.E.; J. Chem. Phys.; **1983**, 79, 5566

53- Henglein, A.; Chem. Rev.; **1989**, 89, 1861

54- Fendler, J.H.; Chem. Rev., **1987**, 87, 877

55- "Structure and Reactivity in Reverse micelles" Pileni, M.P.; (ed.) Pub Elsevier ,**1989**, Amsterdam, Oxford, New York, Tokyo

56- Pileni, M.P.; Zemb, T.; Petit, C.; Chem. Phys. Lett.; **1985**, 118, 414

57- Jain, T.K.; Cassin, G.; Badiali, J.P.; Pileni, M.P.; Langmuir; **1996**, 12, 2408

58- Fletcher,P.D.I.; Robinson, B.H; Ber. Bunsenges. Phys. Chem.; **1981**, 85, 863

59- Pileni, M.P.; Catalysis Today; **2000**, 58, 151

60- Pileni, M.P.; Langmuir; **2001**, in press

61- Pileni, M.P.; Adv. Funct. Mater.;**2001**, in press

62- Cizeron, J. and Pileni, M.P.; J. Phys. Chem.; 99, **1995**, 17410

63- Levy, L.; Hochepied, J.F. and Pileni, M.P.; J. Phys. Chem.; **1996,** 100, 18322

64- Ingert, D.; Feltin, N.; Levy, L.; Gouzert, P. and Pileni, M.P.; Adv. Mater.; **1999,** 11,220

65- Ingert, D. and Pileni, M.P., Adv. Funct;. Mater.; **2001,** 11, 136

66- Motte, L. Billoudet, F. and. Pileni, M.P.; J. Phys. Chem.; **1995,** 99, 16425

67- Lisiecki, I. and Pileni, M.P.; J. Amer. Chem. Soc.; **1993,** 115, 3887

68- "Hydrogen bound Networks " Motte, L.; Lisiecki, I. and Pileni M.P.; **1994,** 447, Ed. Dore, J. and Benissan, M.C.; NATO publisher

69- Cizeron, J.; Pileni, M.P.; J. Phys. Chem.; **1995,** 99, 17410

70- Vogel, W.; Urban, J.; Kundu, M; Kulkarni, S.K.; Langmuir, **1997,** 13, 827

71- Lisiecki, I.; André, P.; Filankembo, A.; Petit, C.; Tanori, J.; Gulik-Krywicki, T.; Ninham, B.W. and Pileni, M.P.; J. Phys. Chem.; **1999,** 103, 9168

72- Lisiecki, I.; André, P.; Filankembo, A.; Petit, C.; Tanori, J.; Gulik-Krywicki, T.; Ninham, B.W. and Pileni, M.P.; J. Phys. Chem.; **1999,** 103, 9176

73- Tanori, J. and Pileni, M.P; Langmuir; **1997,** 13, 639

74- Legrand, J.; Petit, C. and Pileni, M.P.; J. Phys. Chem.; **2001,** 105, 5643

75- Petit, C.; Jain, T.K.; Billoudet, F. and Pileni, M.P; Langmuir; **1994,** 10, 4446,

76- Lisiecki, I.; Billoudet, F. and Pileni, M.P; J. Phys. Chem.; **1996,** 100, 4160,

77- Moumen, N. and Pileni, M.P.; J. Phys. Chem.; **1996,** 100, 1867

78- Ngo, A.T.; Bonville, P. and Pileni, M.P.; Eur. Phys. J. B.; **1999,** 583

79- Hochepied, J.F. and Pileni, M.P.; J. Phys. Chem.; **2000,** 104, 905

80- Hochepied, J.F. and Pileni, M.P.; J. Applied Phys.; **2000**, 87, 2472

81- "The language of shape Ed. Hyde,S.; Andersoon, S.; Larsoon, K.; Blum, Z.; Landth, T.; Lidin, S.; Ninham, B.W.; Pub. Elsevier: Amsterdam, New York, Oxford, Shannon, Tokyo, **1997**

82- Pileni, M.P.; Ninham, B.W.; Gulik-Krzywicki, T.; Tanori, J.; . Lisiecki, I. and Filankembo, A.; Adv. Mater. ; **1999,** 11, 1358

83- Filankembo, A. and Pileni, M.P.; J. Phys. Chem.; **2000**, 104, 5867

84- Lisiecki, I.; Filankembo, A.; Sack-Kongehl, H.; Weiss, K.; Pileni, M.P. and Urban, J.; Phys. Rev. B.; **2000**, 87, 1

85- Nepijko, S.A.; Levlev, D.N.; Schulze, W.; Urban, J. and Ertl, G.; Chem. Phys. Chem.; **2000**, 3, 140

86- Wang, Z.L.; Gao. R.P.; Nikoobakht, B. and El Sayed, M.A.; J. Phys. Chem.; **2000**, 104, 5417

87- Lisiecki, I.; Borjling, M.; Motte, L.; Ninham, B.W. and. Pileni., M.P.; Langmuir; **1995**, 11, 2385

88- Lisiecki, I.; Sack-Kongehl, H.; Weiss, K.; Urban and Pileni, M.P.; Langmuir; **2000**, 16, 8802,

89- Lisiecki, I.; Sack-Kongehl, H.; Weiss, K.; Urban, J. and Pileni, M.P.; Langmuir, **2000**, 16, 8807

HYDROTHERMAL SYNTHESIS OF NANO-MATERIALS

O. Schäf, H. Ghobarkar* and P. Knauth
Université de Provence-CNRS, Laboratoire Matériaux Divisés, Revêtements, Electrocéramiques (MADIREL, UMR 6121), Centre St Charles, Case 26, 13331 Marseille Cedex 3, France
* Freie Universität Berlin, Institut für Mineralogie, Takustr. 6, 14195 Berlin, Germany

1. INTRODUCTION

Hydrothermal processing is a non-conventional method to obtain nanocrystalline inorganic materials. A direct precursor-product correlation exists allowing the tailoring of almost any materials synthesis without the presence of further structure directing agents [1,2].

In short, the synthesis method uses the solubility in water of almost all inorganic substances at elevated temperatures and pressures, and subsequent crystallization of the dissolved material from the fluid. As implemented in the name, water at elevated temperatures plays an essential role in the precursor material transformation. If one relies on the phase diagram of water, only the branch between liquid and gaseous water is essential for further considerations (see fig. 1): below 100°C the equilibrium vapor pressure of liquid water is below 1bar; above the boiling point (p_b, ϑ_b) the important hydrothermal pressure range is available. Two different operation modes can be distinguished in general.

In the autogeneous pressure range, the process pressure is due to the existence of a gas phase in equilibrium. Here, the pressure of the closed system is given by temperature, corresponding to the equilibrium line in figure 1. Above 374°C, corresponding to a pressure of 221bar, gas and liquid phase can not be distinguished any more (critical point). However, the autogeneous pressure at a given temperature is often not sufficient for the necessities of hydrothermal processing, although a great number of conventional synthesis experiments are conducted in the region below the critical point.

In the high-pressure mode, water under an external pressure more elevated than the equilibrium water vapor pressure is used. Under these

conditions remarkable synthesis results can be obtained because the solubility of inorganic materials is generally rising with pressure. Temperature, water pressure and the time of reaction are, therefore, the three principal physical parameters in hydrothermal processing.
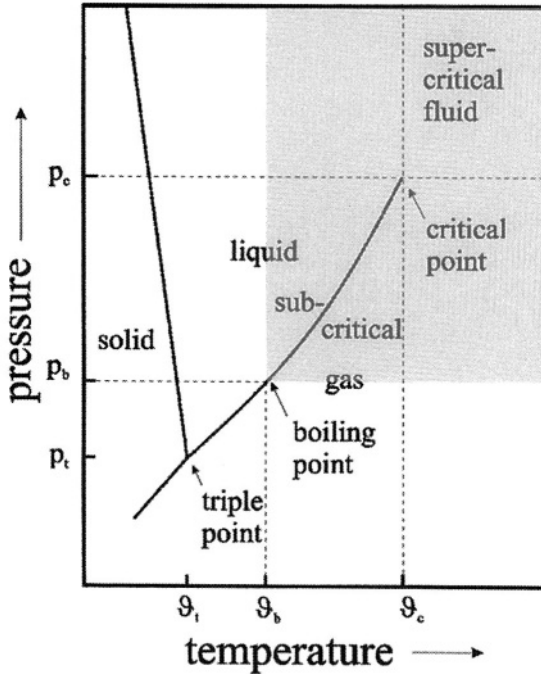

Figure 1. Schematic phase diagram of water showing the important zones for hydrothermal processing. p_t,ϑ_t and p_b,ϑ_b indicate the triple point and boiling point respectively, while p_c,ϑ_c are the pressure and temperature of the critical point (374°C and 221bar). The curve indicates the autogeneous water pressure while high-pressure hydrothermal synthesis (HPHS) is conducted in the whole temperature range of fluid existence above the p_c line.

Generally, the synthesis method is claimed solvothermal[3,4], which means that water, but also other solvents are used, in accordance with the general process principle. It is also possible that additives are employed to modify the initial properties of pure hydrothermal water. Polar solvents (e.g. NH_3, aqueous solutions containing HF, CO_2 or other acids or bases to trim pH) or even non-polar solvents (e.g. pure, supercritical CO_2) can be used for the dissolution–recrystallization process in order to widen the range of applicability of this synthesis method. Although they present some advantages, these solvents also have specific disadvantages concerning mainly their toxicity and corrosion problems for the autoclave materials. In addition, the simplicity and elegance of the original process is getting lost.

2. PRINCIPLES AND OPERATION MODES

Both physical and chemical parameters can be trimmed systematically during the hydrothermal processing in such a way that a direct precursor-product correlation can be established. However, hydrothermal processing is rather complex, because a great number of interacting parameters play essential roles[5,6]. The influence of these parameters can only be sketched as the in-situ observation of the process still rests a problem, which has not yet been solved satisfyingly.

Temperature plays an important role in kinetics of product formation as well as on the thermodynamic stability of the product phase. Pressure is essential for the solubility, the supersaturation range directing the crystallization process as well as for the thermodynamic stability of the product phase (e.g. a too high synthesis pressure leads to the crystallization of denser phases). In order to be independent from the temperature driven autogeneous pressure, the external pressure mode is actually the preferable, as low temperature-high pressure syntheses are only available by this high-pressure hydrothermal synthesis (HPHS) mode. Time is also an important parameter because the synthesis of kinetically stable phases are favored in short term processes while the thermodynamically stable phases are generally formed in long term experiments - corresponding to the chosen temperature-pressure regime. This is caused by re-dissolution and re-crystallization of the already formed phases. However, as will be shown later, further related reaction conditions such as convection within the reaction vessel and the state of aggregation of the precursor materials (e.g. if they are present as macroscopic crystals, nanocrystalline phases or glass) must not be neglected in the effort to control the process parameters.

Based on experimental results, figure 2 shows the principle of the hydrothermal process of dissolution-supersaturation and subsequent crystallization. At a given hydrothermal temperature and pressure convenient for the synthesis (e.g. 1kbar water pressure and temperatures of about 300°C) the precursor material is continuously dissolved in the hydrothermal fluid. The formation of gels is not observed at any time during the process - even if alumosilicate materials are used because bigger molecular units are hydrolysed at elevated temperature and pressure[7,8,9]:

In an aqueous solution under autogeneous pressure conditions far below the critical point, different states of dissolution might be existent and, most important, not only the basic structural building units can be present, but even colloidal states. HPHS synthesis implements, therefore, a first step of crackdown of possibly present "macromolecular" units by chemical reaction, existing e.g. as colloidal solution, as precipitated colloidal solution (crystalline, partially crystalline (e.g. gel), glassy and amorphous) or solid state precursor materials of the same kind, because bigger units exceeding the size present in true solutions are not stable under high

pressure hydrothermal conditions. The formation of a true solution is therefore assumed in which the smallest possible structural building units as well as cations with their respective hydration spheres are transported.

The high pressure hydrothermal conditions do not only increase the solubility in the aqueous medium in comparison to e.g. autogeneous pressure conditions, the region of supersaturated solution, which is essential for continuous crystal growth, is also widened at a given pressure $p_2 > p_1$.
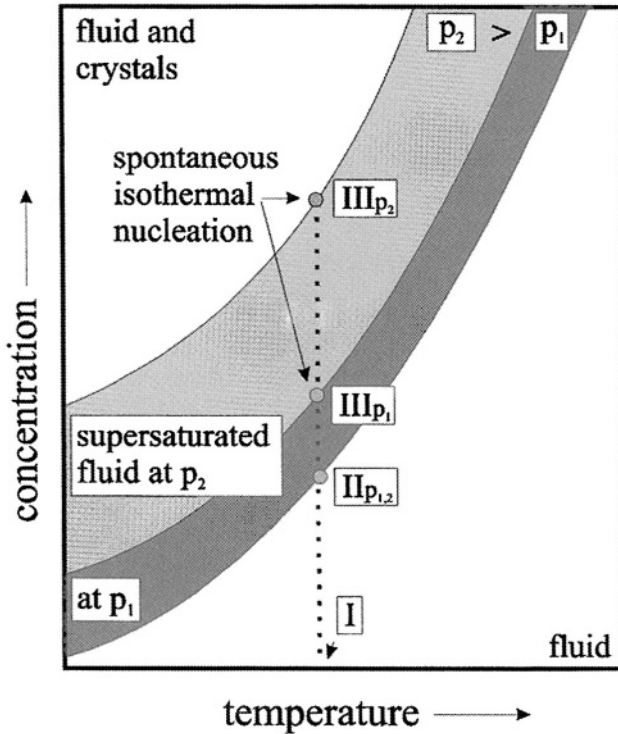

Figure 2: Isothermal-isobar hydrothermal processing: At I) only water and precursor materials are present. Between I) and III): time-dependent precursor material dissolution. Note that the region of supersaturated fluid is often - as in case of alumosilicates - extended at higher pressures. Nucleation occurs spontaneously if point III) is achieved. A subsequent crystal growth process may only take place in the field of supersaturated solution.

Standard hydrothermal experiments are conducted under isothermal and isobar conditions without agitation. At the beginning of the experiment, the hydrothermal fluid consists only of water with solid precursor materials (I –fig. 2); it gets more and more concentrated with time. Even above the solubility limit of the product phase (point II, supersaturation), the precursor materials can still be dissolved. Glassy precursors are faster dissolved than crystalline materials of the same

composition. The zone of supersaturation is wider in case of glassy starting materials than for respective crystalline materials and, in addition, pressure dependent. At a certain level of supersaturation (marked as point III), a spontaneous crystallization will finally occur, leading to a decrease of the concentration in the hydrothermal fluid during the further run of the experiment.

Jung and Perrut[10] give an actual overview on particle design using solvothermal methods. While most of these methods are referred to the treatment of organic materials and pharmaceutical products, the synthesis of inorganic materials has also been successfully performed using solvothermal fluid processes under dynamic flow conditions avoiding the stationary conditions described above. Among them the rapid expansion of supercritical fluid solutions (RESS) and the rapid thermal decomposition of precursors in solutions (RTDS) are the most relevant for the synthesis of nanocrystalline inorganic materials. Studies have been performed using these methods also with water as pressure and reaction medium.

2.1 RAPID EXPANSION OF SUPERCRITICAL FLUID SOLUTIONS (RESS)

If the RESS process is used with water as the solvothermal medium, the precursor material is dissolved under high pressure and high temperature conditions. The dissolution process is stopped before spontaneous nucleation occurs (see fig. 2). For practical purposes, this is achieved under dynamic flow conditions. Nucleation without further growth is performed by an abrupt decrease of the solubility by expansion through a heated nozzle into a medium under ambient temperature and pressure conditions, inducing spontaneous nucleation of the dissolved materials without significant crystal growth[11,12,13]. Pressure, temperature and time of exposure to hydrothermal conditions are important parameters in order to obtain the desired nanocystalline materials. In this way, agglomerates of nanocrystalline GeO_2, SiO_2 and KI were obtained[14], but also nanocrystalline Fe_2O_3[15] and ZrC_2[6]. Either salts of high solubility or oxide materials dissolved under high pressure hydrothermal conditions are used as precursors.

2.2 RAPID THERMAL DECOMPOSITION OF PRECURSORS IN SOLUTIONS (RTDS)

The method of rapid thermal decomposition of precursors in solutions (RTDS) based on high pressure high temperature hydrothermal processing uses water for hydrothermal reactions of precursor materials already dissolved under environmental conditions, leading to a precipitation of a nanocrystalline product. The only brief exposure of a few seconds of the pre-pressurized precursor solution to high temperatures (ca. 300-450°C) initiate a particle nucleation, but prevents a further, subsequent crystal growth of the nucleated product. In contrast to the standard HPHS conditions, the hydrothermal process is used to conduct reactions of the solution, which means that it is performed under dynamic flow and subsequent quenching to ambient pressure and temperature conditions.

The precursor material used depends on the material to be synthesized and it has to be, to a certain extent, soluble in water under ambient conditions. Therefore, inorganic salt precursors with moderate to high solubility under ambient conditions are used. Table 1 shows the grain size of products obtainable by RTDS, adapting precursor salt and the hydrothermal parameters. More detailed descriptions of this technique can be found in references 17,18,19,20,21.

Precursor	Product	Grain Size
$Fe(NO_3)_3$	α- Fe_2O_3 (Hematite)	6-20 nm
$FeSO_4$/urea	Fe_3O_4 (Magnetite)	<12 nm
$Fe(NO_3)_3$/$Ni(NO_3)_2$/urea	$NiFe_2O_4$ (Trevorite)	<10 nm
$Ni(NO_3)_2$	NiO (Bunsenite)	12 nm
$Ni(NO_3)_2$/$ZrO(NO_3)_2$	NiO/ZrO_2	~10 nm
$K_2TiO(C_2O_4)_2$	TiO_2 (Anatase)	3 nm
$Zn(NO_3)_2$/urea	ZnO (Zincite)	34 nm
$ZrO(NO_3)_2$	ZrO_2(Baddeleyite)	6-20nm

Table 1 : Examples of nanocrystalline powders produced by Rapid Thermal Decomposition of Precursors in Solutions (RTDS).

2.3 HIGH PRESSURE HYDROTHERMAL SYNTHESIS (HPHS)

Achieving the limit of supersaturation as shown in figure 2 means that spontaneous nucleation occurs from the solution. The nucleation and a possible crystal growth are, however, dependent on the kinetics of the water-precursor-system under investigation[22]. A growing crystal nucleus is always active because all the material transported to its surface and

compatible with its physical and chemical properties will be built in. This might lead to intercalation or even ion exchange behavior. Growth processes of the nuclei are only possible in the region of supersaturated solution. Only if the isothermal-isobar conditions in the standard synthesis mode outlined in figure 2 are carefully maintained during a long term experiment of hours up to several weeks (60d) and the supersaturation limit is neither exceeded (so that the formation of a second phase can be observed by another spontaneous crystallization and growth) nor the concentration falls below the saturation limit (so that etching of the already formed crystals occurs), microscopic or even bigger single crystals will be observable. Both nucleation and growth take place in the region of supersaturated solution although nucleation is assigned to its upper limit and the rate of nucleation and the crystal growth rate are strongly dependent on the degree of supersaturation (see fig. 3). If synthesis conditions are chosen in such a way that always a high degree of supersaturation can be maintained so that a high rate of nucleation is established, the hydrothermal synthesis of nano-materials is possible.

Of course the synthesis success will strongly depend on the physical and chemical properties of the nano-material to be synthesized as crystal growth might occur in competition. Furthermore the re-dissolution of already formed nuclei to build up microscopic crystals can not always be neglected. However, the synthesis of crystals with a size just above the thermodynamically critical limit for stability (in the nanometer-scale) is in principle a process relatively difficult to maintain.
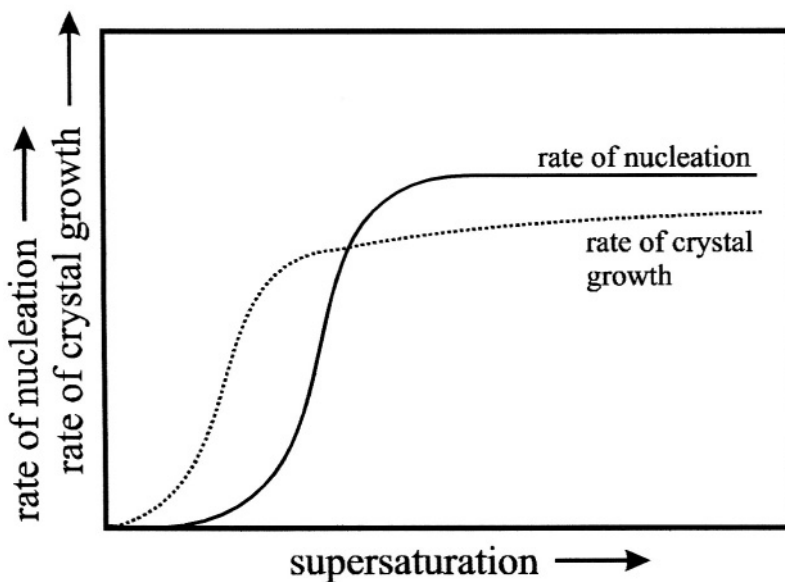

Figure 3: Supersaturation dependence of the isothermal nucleation rate and the rate of isothermal crystal growth.

The experimental set-up for the hydrothermal synthesis is shown in figure 4. The precursor materials are placed in containers with a solid to water proportion of about 1:10. The closed containers are placed into the high pressure vessel, which is then hermetically sealed and put into a furnace. Applying the desired hydrothermal synthesis temperature, an autogeneous pressure is formed. The external pressure is adjusted as soon as the temperature equilibrium is achieved within the autoclave. By installation of the hydrothermal pressure, the reaction process takes place. Temperature gradients within the containers have to be avoided, as they cause convection and therefore a fluid transport which favors in consequence, the crystal growth after nucleation has taken place. Temperature fluctuations of the furnace do have comparable negative consequences because a rise in temperature leads to a higher dissolution rate disturbing the dynamic equilibrium of dissolution-crystallization, while a lowering of temperature leads to a higher supersaturation. Dependent on the rate of crystal growth and, therefore, on the specific material to be synthesized this may lead to an unwanted crystal growth process instead of the desired nucleation only. Additionally a fluctuation of temperature does also imply changes of hydrothermal pressure in the standard experimental set-up, leading to a reinforcement of already present temperature effects.
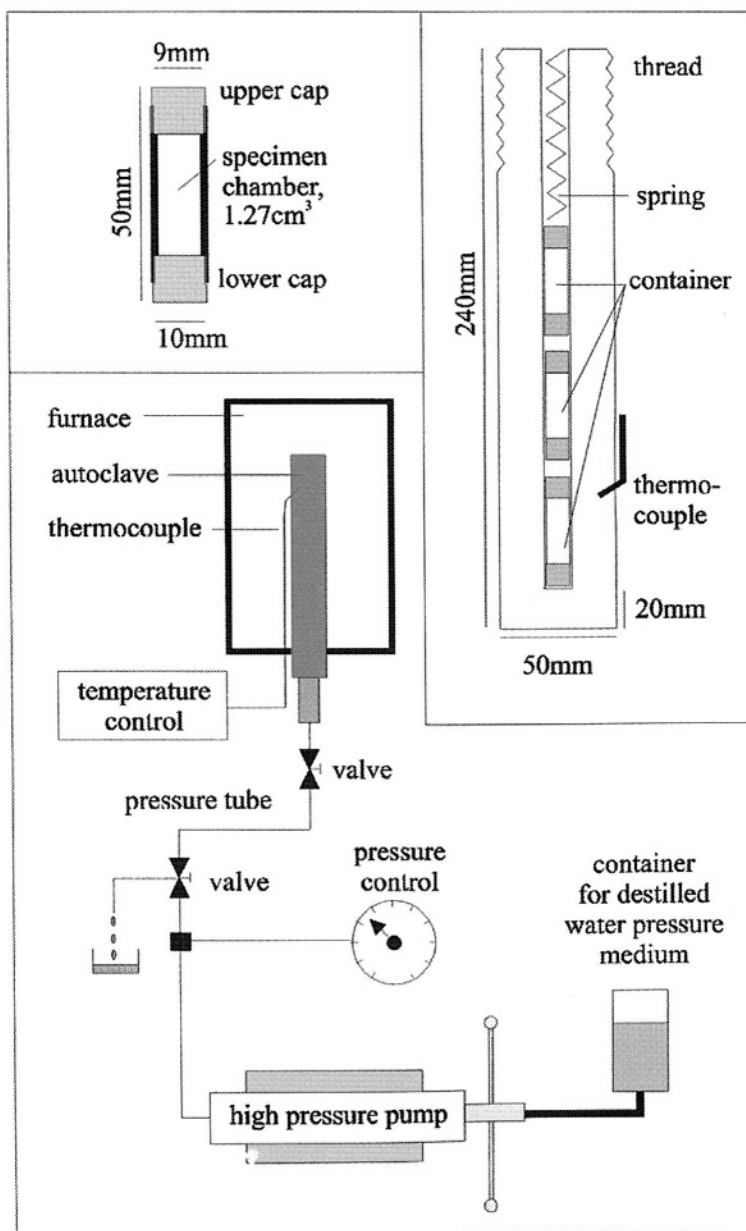
Figure 4: Facilities of standard high pressure hydrothermal synthesis (HPHS): container, made of Teflon, high purity copper or gold; autoclave with container arrangement; experimental set-up (in clockwise order).

3. HIGH PRESSURE HYDROTHERMAL SYNTHESIS (HPHS) OF NANOCRYSTALLINE MATERIALS

High pressure hydrothermal synthesis (HPHS) of nanocrystalline materials has to be controlled by both, the process parameters temperature, pressure and time, as well as the physical and the chemical parameters of the materials system under investigation. The physical parameters in a stationary hydrothermal system as represented in figure 4 have already been outlined. The tailoring of the physical and chemical parameters of the materials under investigation will have to focus on precursor–product correlation using only pure water as pressure and reaction medium. The effect of pH on the dissolution-re-crystallization process can not be taken into account, because the concentration of H_3O^+ is not a solitary parameter but always correlated with the respective counter ion present. The presence of such a counter ion, however, plays a nearly as important role in the process, interacting either during the dissolution process or acting as a sort of ionic template - or even as a constituent during the re-crystallization[23]. Added ionic solutions influence the synthesis process in a similar way. While one sort of ions is directly implemented in the crystallization process, the counter ion acts via the solution. In both cases the concentrations of the present dissolved ions will not be constant during the whole course of the experiment, and the change of this chemical parameter will have effects on the synthesis sequence.

Therefore, the main emphasis is on the transformation of solid precursor materials under the influence of HPHS conditions. In this context, the chemical composition and state of aggregation of the precursors are essential for further considerations.

3.1 GLASSY PRECURSOR TRANSFORMATION TO NANO-MATERIALS

The high pressure hydrothermal transformation of glassy precursor materials has been successfully employed for the systematic synthesis of zeolites almost under the natural formation conditions[24,25,26]. Here, the vitreous state of aggregation is essential for the successful synthesis, because the dissolution of the precursor material of identical composition as the zeolite product is a homogeneous source for the zeolite constitution at any time of the experiment. Under these conditions the formed zeolite phase is thermodynamically more stable than the glassy precursor. As can be seen in figures 2 and 3, nucleation and subsequent growth will only take place in the region of supersaturated solution. Experiments have shown that homogeneous zeolite nucleation from the supersaturated solution at a chosen hydrothermal pressure 1 kbar is possible in a wide temperature

range (at least between 30°C and 400°C)[27]. In contrast to this, further experiments[28] have demonstrated, that using glasses as precursors under standard HPHS conditions, the temperature range of crystal growth is restricted. Long term experiments during 60 days gave the confirmation, that a limited quantity of glass precursor available in the closed container as well as the high stability of the formed zeolite product against re-dissolution enable the synthesis of nanocrystalline materials.

At lower temperatures microscopic crystals were synthesized, because the dissolution rate of the glassy precursor is at a level to establish a low grade of supersaturation where crystal nuclei grow continuously consuming the dissolved material at the same rate. Having carried out this experiment at different temperatures, it can be shown that if the dissolution rate becomes too high for a continuous crystal growth, repeated nucleation can be observed instead (see fig. 5). As can be seen, at 200°C the maximum crystal size observed is about 500nm. Under the same experimental conditions at 220°C only nanocrystalline material can be observed, too small in size to be resolved by scanning electron microscopy.
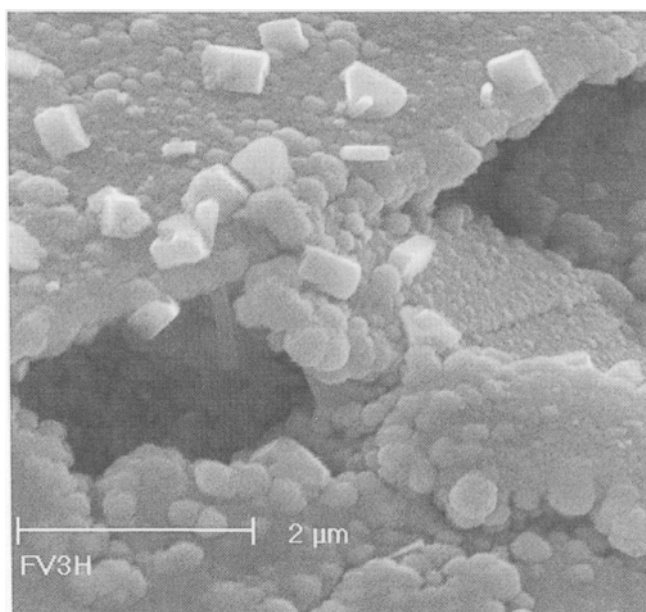

Figure 5: Ideomorphous crystals of zeolite heulandite (about 500nm maximum size) together with ball shaped agglomerates of the same, nanocrystalline zeolite phase - obtained by HPHS (glass precursor, 1kbar water pressure, 200°C, 60d).

The agglomerated crystal nuclei are stable even under long term conditions, which means that once formed by consuming the glassy precursor material, no change occurs. In the experiment no subsequent re-dissolution did take place– as this would have lead to the synthesis of

34

microscopical observable crystals while all nanocrystalline material would have been consumed. In the zeolite system under investigation, re-dissolution of the once formed zeolite phase is only possible above 365°C (same pressure-time conditions). Spherical agglomerates of microcrystals can be formed by re-dissolution and crystal growth of already formed nanocrystalline materials as shown in figure 6.
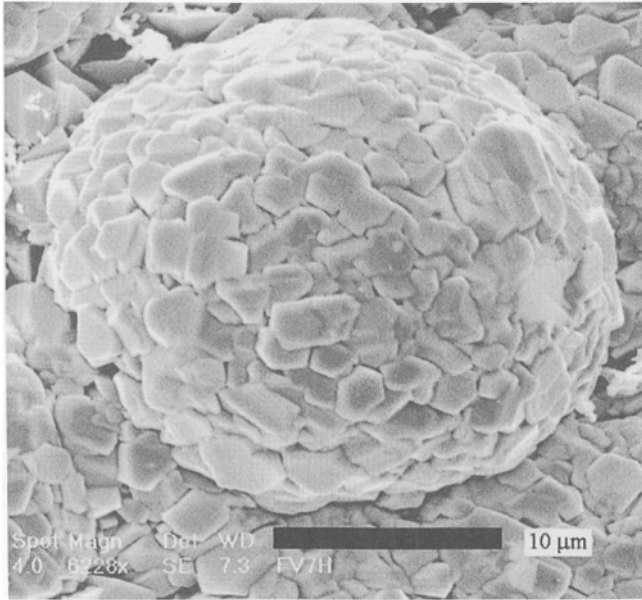

Figure 6: Ball shaped microcrystal aggregates of zeolite heulandite obtained by HPHS by repeated dissolution and growth of already synthesized nanocrystalline zeolites (glass precursor, 1kbar water pressure, 400°C, 60d).

If a glassy precursor is available, certain nanocrystalline materials can be produced by HPHS during long term experiments. However, limitations of the method might be given by the process parameters themselves, because the hydrothermal pressure limits the materials solubility. A too low hydrothermal pressure results in a too slow dissolution kinetics, while a very high water pressure results in a fast solubility kinetics[29], but may favor the crystallization of unwanted high pressure phases[30]. The size of the glassy precursor pieces (e.g. if powdered or pieces in mm size), agitation and temperature gradient induced convection are important process parameters as well. Although zeolites are an extraordinary example in this context, as their stability against re-dissolution is extreme, this synthesis principle can also be applied to other nanocrystalline materials.

Using the standard isothermal-isobar set-up, the experiment is conducted at different discrete temperature levels. In this mode a scan in the ratio of the dissolution to re-crystallization kinetics is a very important experimental process tool in order to obtain nanocrystalline materials during long term high pressure hydrothermal synthesis by controlled elimination of crystal growth. Figure 7 shows a SEM micrograph of nanocrystalline Li-Fe-Silicate obtained by 28d HPHS at 1 kbar, while at lower, but also at higher temperatures, respectively different microcrystalline materials were synthesized.
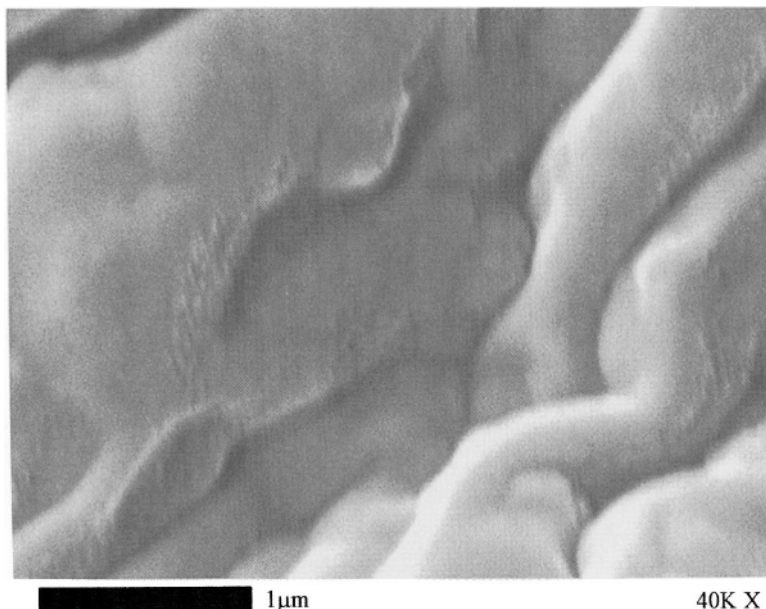

Figure 7: Nanocrystalline Li-Fe-Silicate obtained by HPHS (glass precursor with Li_2O x Fe_2O_3 x $6SiO_2$ composition , 1kbar water pressure, 200°C, 28d).

3.2 CONTROLLED RECRYSTALLIZATION OF NANO-MATERIALS

Nanocrystallinity is present if no or only very minor crystal growth has occured. Some inorganic materials like the class of hexacyano-metallates with transition metal ions as structural elements show only a very reduced solubility in aqueous solutions under ambient pressures[31]. Among them the well known Prussian blue, $KFe^{III}[Fe^{II}CN_6]$ is the most investigated of mixed valence state materials of this type[32]. Its extremely low solubility implements that under wet chemical synthesis conditions instantaneously colloidal agglomerates are formed, which are unable to

grow. Our experiments have shown that Prussian blue submitted to high pressure hydrothermal conditions for up to 52 days at pressures between 500bar and 1kbar and temperatures between 40°C and 100°C is not decomposed but re-crystallized. In figure 8 a SEM-micrograph of a typical result of a re-crystallization experiment is shown.
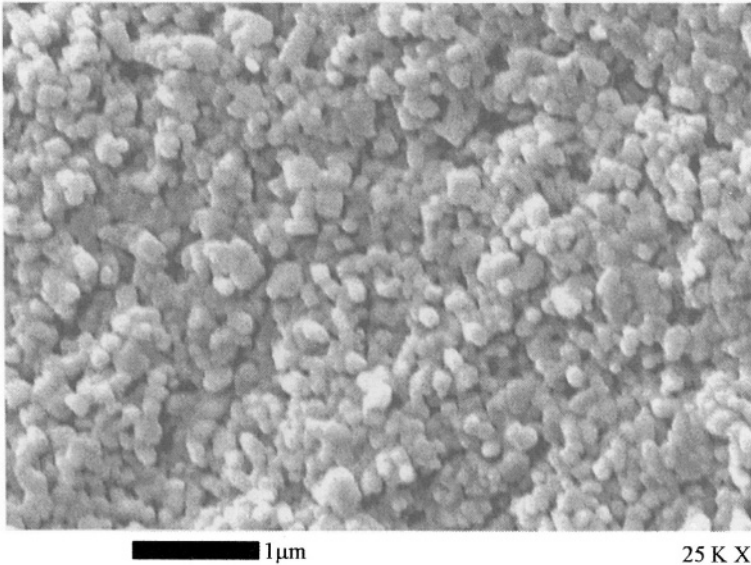

1μm   25 K X

Figure 8: Crystals of re-crystallized nanocrystalline Prussian blue - $KFe^{III}[Fe^{II}(CN)_6]$, obtained by high pressure hydrothermal treatment of a precipitated precursor of the same composition (500bar water pressure, 66°C, 42d).

The experimental results shown in figure 8 are explainable taking into account the processes described in figure 2: even under HPHS conditions the smallest structural building units of Prussian blue are not attacked. However, the solubility is significantly higher than under ambient conditions and, most important, the region of supersaturated fluid is widened. This extension of the region of supersaturated fluid is the reason for a growth of the Prussian blue nuclei, where some of the nuclei grow while most of them are consumed to deliver the material for the growth process. Finally, their size rests in the nanometer range, but it could be shown in principle that the crystal growth of hexacyano-metallate nanomaterials is possible.

3.3 SHORT TERM PRECURSOR TRANSFORMATION TO NANO-MATERIALS

For reasons of the extreme synthesis conditions like the effect that all product materials formed had to pass the dissolution re-crystallization pathway, the hydrothermally prepared materials are formed near equilibrium conditions. To keep the product particle size in the nanometer range, all precursor reaction processes have to occur very rapidly, so that the whole process is finished within several hours in order to avoid a significant growth of the product particles. Different nanocrystalline materials have been obtained in this way. Nanocrystalline zirconia (7-20nm size) and iron oxide powders (55-80nm) already obtained by RTDS and RESS are also obtainable by hydrothermal treatment of nitrate and oxide precursors at 240°C, up to 6h at autogeneous pressure[15]. Different other nanocystalline oxides and oxy-hydroxides can be obtained in the same way by reaction and nucleation of nitrate precursors using water as pressure and reaction medium. Among them are AlOOH with particle sizes of 100-600nm[33], Co_3O_4 of about 50nm particle size[34,], NiO of l00nm particle size[35], Fe_2O_3 with spherical particle size of 50nm[35] and CeO_2 of particle sizes up to 300nm[36]. Nitrate free AlOOH nanocrystals were also obtainable using nitrate precursors under "true" hydrothermal conditions (400°C, 350bar, 30min)[37]. Other simple oxides have been obtained by the same authors[33,34,35] in an analogous way using non-oxide precursors. One can mention TiO_2 of about 20nm size applying $TiSO_4$ and $TiCl_4$ precursors, ZrO_2 of spherical particle size of 10nm from $ZrOCl_2$ precursors and Fe_2O_3 of up to 50nm size employing $FeCl_2$ or $Fe_2(SO_4)_3$ as starting materials. The production of fine powdered oxides in the nanometer scale was also reported by hydrothermal oxidation of the respected coarse grained metals[38]. Nanocrystalline TiO_2 of up to 100nm size was obtained using tetraalkylammonium hydroxide peptized sols as precursors with water as reaction medium for 2 hours under autogeneous pressures at 240°C[39]. Particles of an average diameter between 3 and 4nm could be obtained by hydrothermal reaction between a $Co(OH)_2$ gel and a hydroperoxide (180°C autogenous pressure, 24h)[40]. Our own investigations showed that the short term high pressure hydrothermal treatment of $Cr(OH)_3$ at 500bar lead to a nanocrystalline CrOOH product in a temperature range between 290°C and 450°C (maximum temperature of investigation). The higher the synthesis temperature, the bigger was the average grain size.

Reports were also given that a few nanocrystalline oxides can be obtained in a relatively simple way by treating the coarse grained oxide precursors for a short time. Nanocrystalline Cr_2O_3[41,42] and HfO_2[43,44] have been obtained in this way.
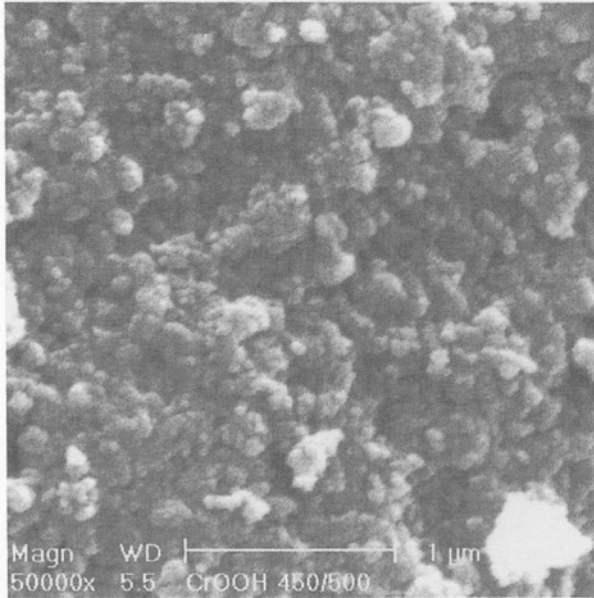
38

Figure 9: Agglomerated nanocrystals (identified as CrOOH by XRD) obtained by high pressure hydrothermal treatment of coarse grained $Cr(OH)_3$ (500bar water pressure, 390°C, 6h).

Different methods to obtain more complex oxides by short term high pressure hydrothermal synthesis using water (as pressure and reaction medium) have been described. Nanocrystalline $LaCrO_3$ could be synthesized using microcrystalline precursors of the respective composition[41,42] and yttria stabilized ZrO_2 of 6-22nm particle size was obtained from a precipitated yttria-zirconia hydroxide-hydrated precursor by a simultaneous dissolution-reaction-crystallization process[45].

Preparation of fine barium-ferrite particle was reported[46] decomposing the just blended precursor materials hydrothermally. Hydrothermal methods could also be applied in order to control the size and shape of lead titanate[47]. Different approaches are known to synthesize $BaTiO_3$ nano-materials by hydrothermal methods. It could be obtained by short term (0.5-2h) autogenous pressure treatment of the mixed precursor solutions using additives in order to obtain a homogenous product of about 100nm size[48]. Using stoichiometric mixtures of hydrated Barium-hydroxide precursors and different Ti-sources, gives almost the same results[49]. Microwave assisted very short term hydrothermal synthesis of nanocrystalline $BaTiO_3$ at 200°C (5-30min) was also reported using barium nitrate, titanium tetrabutoxide and KOH as precursors[50]. The results confirmed that in principle a quantitative synthesis can be achieved within 30min if the appropriate precursor materials are chosen. $SrTiO_3$ with different particle sizes from 50-100nm has been hydrothermally prepared

from different Sr and Ti precursors between 150 and 240°C at autogeneous pressure[51]. An influence of the precursor and additional solutions on the particle size has been found. Even nanocrystalline phases of $Y_2Si_2O_7$ have been synthesized from organic precursors at 170°C and autogeneous pressure (2h)[52]. Differences in homogenity of particle size and phases present have been found between batches using just water and batches with added acid.

These few examples might show the great potential of the process; a more consequent and systematic application of the synthesis principles accompanied with their refinement will lead to a further rapid extension of the method.

4. CONCLUSIONS

As the different examples and principal synthesis strategies might have shown, hydrothermal synthesis is an elegant and straightforward method with a huge potential for the solution of future synthesis tasks. For nano-materials synthesis, one principal problem has to be solved: once obtained, how to prevent nuclei growth. The physical parameters water pressure, temperature and time and the respective precursor-product system have to be tuned in such a way that always a high degree of supersaturation can be maintained so that a high rate of nucleation is established - simultaneously avoiding crystal growth.

Hydrothermal synthesis of inorganic materials is a technique with a relatively simple basic mechanism. Although the physical process parameters are comparably easy to control, less is known about the chemical and physical processes taking place in detail. More information has to be gathered about size and constitution of the smallest structural units transported in the aqueous fluid. The process kinetics associated with the mechanisms of reaction - specific for different kinds of precursor materials during the dissolution-re-crystallization process - play thereby a key role. The aim will be a modeling of the parameters in order to make predictions about the course of the experiment.

5. ACKNOWLEDGMENT

6. REFERENCES

[1] H. Ghobarkar, O. Schäf and U. Guth, Prog. Solid St. Chem. 27(2-4), 29-73 (1999).

[2] M.S. Whittingham, J.D. Guo, R. Chen, T. Chirayil, G. Janauer, P. Zavalij, Solid State Ionics 75, 257-268 (1995).

[3] F. Cansell, B. Chevalier, A. Demourgues, J. Etourneau, C. Even, Y. Garrabos, V. Pessey, S. Petit, A. Tressaud and F. Weill, J. Mater. Chem. **8** (1998).

[4] G. Demazeau, C.R. Acad. Sci. Paris, t. 2, Série IIc, 685-692 (1999).

[5] K. Byrappa, I. Yoshimura, M. Yoshimura (eds.), Handbook of Hydrothermal Technology, William Andrew Publishing (2001).

[6] G. Demazeau, J. Mat. Chem. 9, 15 (1999).

[7] M.M. Hoffmann, J.G. Darab, B.J. Palmer, J.L. Fulton, J. Phys. Chem. A 42, 8471-8482 (1999).

[8] J.L. Fulton, D.M. Pfund, S.L. Wallen, M. Newville, E.A. Stern, Y. Ma, J. Chem. Phys. 105, 2161-2166 (1996).

[9] S.L. Wallen, B.J. Palmer, D.M. Pfund, J.L. Fulton, M. Newville, Y.Ma, E.A. Stern, J. Phys. Chem. A 101, 9632-9640 (1997).

[10] J. Jung, M. Perrut, J. Supercrit. Fluids 20, 179-219 (2001).

[11] D.W. Matson, R.C. Petersen, R.D. Smith, Adv. Ceramic Mat. 1, 242-246 (1986).

[12] R.D. Smith, R. Wash, U.S. Patent #4,582,731 (1986).

[13] D.W. Matson, R.D. Smith, J. Am. Ceram. Soc. 72, 871-881 (1989).

[14] D.W. Matson, J.L. Fulton, R.C. Petersen, R.D. Smith, Indust. Eng. Chem. Res. 26, 2298-2306 (1987).

[15] A.A. Burukhin, B.R. Churagulov, N.N. Oleynikov, Y.V. Kolen'ko, MRS Symposium Proceedings 520, 171.

[16] A.A. Burukhin, B.R. Churagulov, N.N. Oleynikov, High Press. Res. 20, 255-264 (2001).

[17] D.W. Matson, J.C. Linehan, R.M. Bean, Mater. Lett. 14(4), 222-226 (1992).

[18] J.G. Darab, D.W. Matson, J. Electron. Mater. 27(10), 1068-1072 (1998).

[19] B.L. Armstrong, Mater. Manuf. Process 11(6), 999-1012 (1996).

[20] D.W. Matson, J.L. Fulton, J.C. Linehan, R.M. Bean, T.A. Werpy, J.G. Darab, U.S. Patent #5,652,192 (1998).

[21] A.A. Burukhin, B.R. Churagulov, N.N. Oleynikov, High Press. Res. 20, 255-264 (2001).

[22] G. Demazeau, J.M. Mollet, C. Cros, A. Largeteau, J. Alloys and Compounds 262-263, 271-274 (1997).

[23] H.Ghobarkar, O. Schäf, P. Knauth, Angew. Chemie 113(20), 3948-3951 (2001); Int. Ed. 40(20), 3831-3833 (2001).

[24] H. Ghobarkar, O. Schäf and U. Guth, High Pressure Res. 20(1-6), 45-54 (2001).

[25] H. Ghobarkar, O. Schäf and P. Knauth, Ann. Chim., Science des Matériaux 24, 209-215(1999).

[26] H. Ghobarkar, O. Schäf, Verfahren zur Synthese von Zeolithen mit definierter Stöchiometrie und Struktur. German Patent, AZ 198 24 184.4-41, disclosed 2. 12. 1999.

[27] H. Ghobarkar, O. Schäf, Mic. Mes. Mats. 23(106), 55-60 (1998).

[28] H. Ghobarkar, O. Schäf, unpublished results (2001).

[29] K.Th. Wilke, Kristallzüchtung, VEB Deutscher Verlag der Wissenschaften, Berlin (1973).

[30] W. Eitel, Silicate Science Vol. IV: Hydrothermal Silicate Systems, Academic Press (1966).

[31] A.G. Shape, The Chemistry of Cyano Complexes of the Transition Metals, Academic Press, London (1976).

[32] M. Verdaguer, Polyhedron 20, 1115-1128 (2001).

[33] T. Adshiri, K. Kanazawa, K. Arai, J. A. Ceram. Soc. 75(4), 1019-1022 (1992).

[34] T. Adshiri, K. Kanazawa, K. Arai, J. A. Ceram. Soc. 75(9), 2615-2618 (1992).

[35] T. Adshiri, S. Yamane, S. Onai, K. Arai, Proc. 3rd Int. Symp. on Supercritical Fluids, Strasbourg, France, Oct. 17-19, G. Brunner, M. Perrut (eds.), Tome 3, 241-247 (1994).

[36] Y. Hakuta, H. Terayama, S. Onai, T. Adshiri, K. Arai, 4th Int. Symp. on Supercritical Fluids, Sendai, Japan, May 11-14, 255-258 (1997).

[37] G. Li, R.L. Smith, H. Inomata, K. Arai, Materials Letters 53, 175-179 (2002).

[38] M. Yoshimura, S. Somiya, Materials Chemistry and Physics 61, 1-8 (1999).

[39] J. Yang, S. Mei, J.M.F. Ferreira, Mat. Sci. Eng. C 15, 183-185 (2001).

[40] Y. Jiang, Y. Wu, B. Xie, Y. Xie, Y. Qian, Materials Chemistry and Physics 74, 234-237 (2002).

[41] M. Yoshimura, S . Somiya, Am. Ceram. Soc. Bull. 59(2), 246 (1980).

[42] S. Hirano, S. Somiya, J. Am. Ceram. Soc. 59(11-12), 534 (1976).

[43] H. Toraya, M. Yoshimura, S. Somiya, Comm. Am. Ceram. Soc. 65(5), C-72 (1982).

[44] H. Toraya, M. Yoshimura, S. Somiya, Comm. Am. Ceram. Soc. 65(9), C-159-160 (1982).

[45] R.R. Piticescu, C. Monty, D. Taloi, A. Motoc, S. Axinte, J. Europ. Ceram. Soc. 21, 2057-2060 (2001).

[46] K. Arai, T. Ajiri, S. Yuki, I. Ota, U.S. Patent #5,433,878, (1995).

[47] J. Moon, M.L. Carasso, J.H. Adair, H.G. Krarup, J.A. Kerchner, J. Mater. Res. 14(3) 866 (1999).

[48] S.W. Lu , B.I. Lee, Z.L. Wang, W.D. Samuels, J. Crystal Growth, 219, 269-276 (2000).

[49] C.T. Xia, E.W. Shi, W.Z. Zhong, J.K. Guo, J. Crystal Growth 166, 961-966 (1996).

[50] Y.B. Khollam, A.S. Deshpande, A.J. Patil, H.S. Potdar, S.B. Deshpande, S.K. Date, Materials Chemistry and Physics, 71, 304-308 (2001).

[51] C.C. Chen, X. Jiao, D. Chen Y. Zhao, Mat. Res. Bull. 36, 2119-2126 (2001).

[52] I. Maclaren, P.A. Trusty, C.B. Ponton, Acta Mater. 47(3), 779-791 (1999).

EHDA IN PARTICLE PRODUCTION

Application of electrospray in nanoparticle production

T. Ciach, K.B. Geerse and J.C.M. Marijnissen
Particle Technology Group, Delft University of Technology, Delft, The Netherlands

INTRODUCTION

This chapter describes a route to nanoparticle production via Electro-Hydro-Dynamic Atomization (EHDA). This process, also referred to as electrospraying, is a process where a liquid jet breaks up into droplets under the influence of electrical forces. EHDA as a method to produce particles has a number of advantages. There is a great flexibility concerning the particle composition, because precursors can be found for almost any material. In contrast to particle generators applying high temperatures and/or plasma, it is a gentle method in the sense that even easily decomposing compounds remain stable. Even particles of biochemical molecules such as insulin or peptides have been successfully produced. Finally, the method has the potential of producing very narrow size distributions with a simple way of controlling particle size. While this principle has frequently been used for particle production, it has seldom been applied in the nano-particle size range, but it could be seen here as one of the most promising methods.

EHDA has formerly been used for ceramic particle production in the micron range [1]. More recent research has shown that preparation of nano-particles down to a few tens of nanometers is also possible using this method [2,3]. By electrospraying and pyrolysis of a $Zn(NO_3)_2$ and $(NH_2)_2SC$ solution in ethanol, 20 nm ZnS particles were obtained.

ELECTRO HYDRO DYNAMIC ATOMIZATION

The possibility of using electric fields to disperse liquids in order to produce particles has attracted much interest in the scientific world. The phenomenon of an electric effect on menisci is known since the sixteenth century. William Gilbert [4] reported the interaction between a water droplet and a piece of amber, leading to a conical shaped droplet. Zeleny [5] showed in the beginning of this century that liquid meniscus subjected

to a high enough electric field, adapt a conical shape and emit a mist of very small droplets. In the fifties, Vonnegut and Neubauer [6] tried to relate the properties of a liquid to its behaviour in electrospray.

Electrohydrodynamic atomisation refers to a process, where a liquid jet breaks up into droplets under the influence of electrical forces. Depending on the strength of the electric stresses in the liquid surface relative to the surface tension stress and the kinetic energy of the liquid jet leaving the nozzle, different spraying modes will be obtained. The modes are classified into two general categories: those that exhibit a continuous flow of liquid through the meniscus and those that do not. The former consists of the simple-jet, the cone-jet and the ramified-jet, while the latter consists of the dripping, the micro-dripping, the spindle and the intermittent cone-jet modes. The latter are often referred to as pulsating modes. shows the different modes graphically. Most authors have observed both categories although the nomenclature has not been universally accepted.
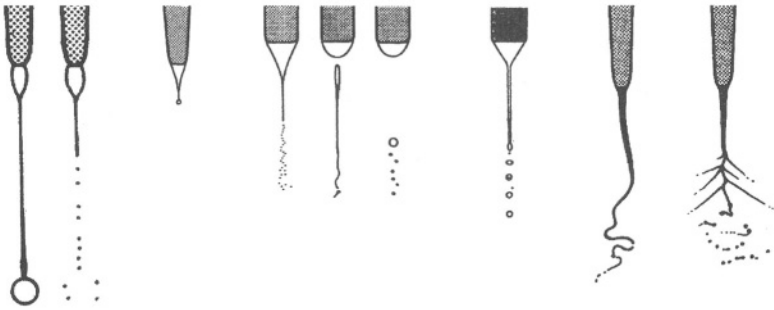
Figure 1. Dripping, microdripping, spindle, cone-,simple- and ramified jet spraying modes (adapted from Cloupeau et al.[7])

For particle production, the cone-jet mode shows the best performance. In this state the process is very stable and small, monodisperse particles are formed. Figure 2 shows a photograph of this cone jet mode.
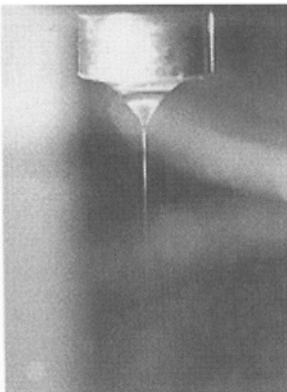

Figure 2. Electrospraying of the liquid in the cone-jet mode.

Taylor made the first mathematical description of the cone by balancing the forces that are present figure 3.
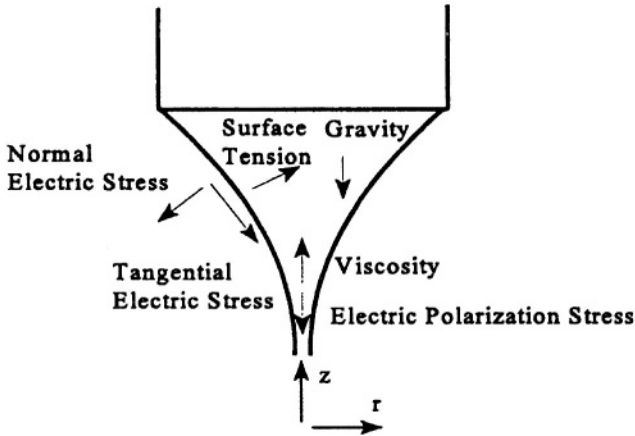

Figure 3. Forces acting on the liquid in the external electric field.

The Particle Technology Section of Delft University of Technology [8] developed a physical numerical model of EHDA in the cone jet mode. The measurement results showed that monodispersity of the droplet produced in the cone depends on the jet break-up mechanism, which was found to depend on the ratio of the electric stress over the surface tension stress. At low stress ratios, the jet breaks up due to varicose perturbations. At higher stress ratios, the jet showed a whipping motion. Figure 4 shows the break up in these two stress regimes.
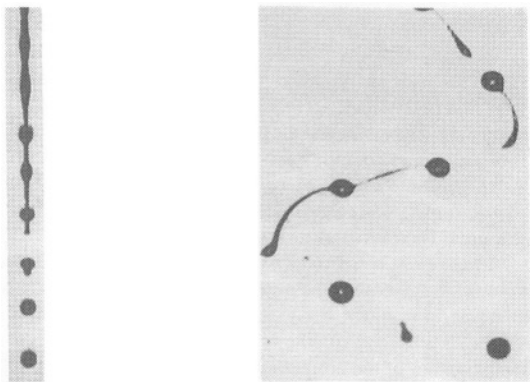
Figure 4. Break up of the jet at low (left) and high (right) stress ratios.

For seven different liquids, the relation between varicose and whipping breaks up and the stress ratio within the jet was investigated. This stress ratio is given by:

$$stress\ ratio = \frac{\sigma^2 / 2\varepsilon_0}{2\gamma / D_{jet}} \qquad (1)$$

where σ is the surface charge on the jet, γ is the surface tension of the liquid considered, D_{jet} is the jet diameter at its breakup and ε_0 is the permittivity of vacuum.

Figure 5 shows the break up mechanisms as function of this stress ratio for seven liquids with different conductivities, varying from 13 to 45 microsiemens per meter. The stress ratio for one liquid was changed by changing the flow rate of the liquid.
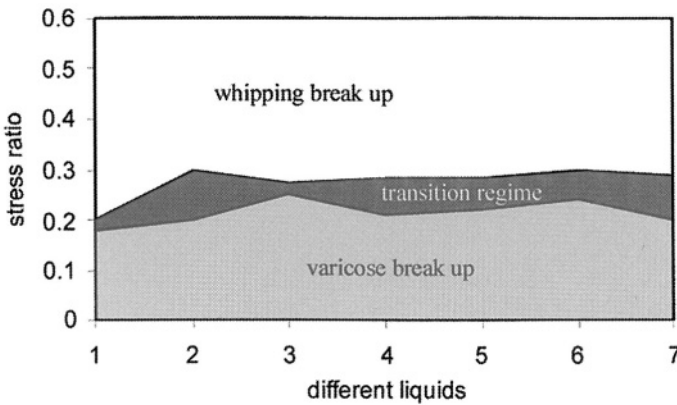
Figure 5. Changing of break up mechanism as the stress ratio in the jet changes.

To be in the varicose break up regime the stress ratio should be below 0.2.

In the physical model of Hartman [8], the influence of spraying parameters on the cone shape, droplet size and droplet charge is investigated. The shape of the liquid cone is calculated by solving the Navier-Stokes equation in one dimension for a steady state situation. To be able to solve these equations, the electric field strenghts, the surface charge and the radial velocity profile inside the liquid have to be known. If a certain cone shape is assumed, then the electric fields in and outside the liquid are numerically calculated using Gauss' law. The surface charge follows then from the current balance at the liquid-air interface and from the estimation of the liquid velocity at the liquid-air interface. The one-dimensional Navier-Stokes equation is then used to calculate a new cone-shape, which is used as input for new electric field, and surface charge calculations. This process is repeated until the input and output cone shapes have converged. The break-up of the jet is calculated numerically by using models of Weber and Melcher [9,10]. The calculations use the previously calcu-

lated jet shape. These models yield the jet diameter before break up, the diameter of the combined main and secondary droplet and the droplet velocity.

In the model of Hartman, the current through a cone jet system was modelled. For the high conductivity case he found for the current:

$$\frac{I}{I_0} = b\left(\frac{Q}{Q_0}\right)^a \tag{2}$$

$$\text{where } I_0 = \left(\frac{\varepsilon_0 \gamma^2}{\rho}\right)^{1/2} \text{ and } Q_0 = \frac{\varepsilon_0 \gamma}{K\rho}.$$

where Q is the flow rate applied, I is the current through the jet, K and ρ are respectively the conductivity and the density of the liquid. The variables a and b are scaling constants.

For a nozzle with a diameter of 8 mm and for n-butanol and ethylene glycol with various conductivities, the scaling law was fitted to current measurements. The result is as follows:

Table 1. Scaling law parameters as function of the dimensionless flow rate.

Q/Q_0	a	b
<50	0.493	2.215
50-250	0.518	1.931
>250	0.427	3.203

It has to be noted that the current also depends on the electrode configuration, and the type of ions used. So, measurements might yield deviations from the scaling laws up to 30%.

For the refining of the droplet size scaling law one of the tools Hartman used was a High Speed Imaging System. Hartman found the following expressions for the droplet size in the varicose break up regime:

$$d_{d,\text{varicose}} = c\left(\frac{\rho \varepsilon_0 Q^4}{I^2}\right)^{1/6} \tag{3}$$

The constant c was fitted to the experiments and was found to be equal to 2.05 for the measurements with the camera.

The process of particle formation by EHDA was extensively studied, both fundamentally and experimentally at TU Delft. In particular, the group has a lot of experience in using EHDA for ceramic and organic microparticles production [1]. Figure 6 shows an example.
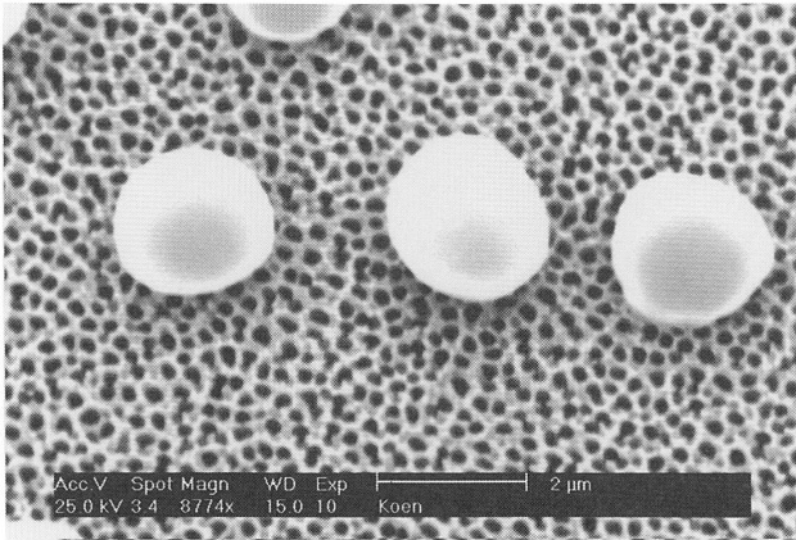

Figure 6. SnO$_2$ particles made via the EHDA route.

The particles shown were made in the setup shown in figure 7. The spraying nozzle operating in the cone-jet mode is fixed in the aerosol reactor. Liquid is supplied via a syringe pump. A ring electrode is placed below the nozzle. The voltage on this electrode is lower then the voltage on the nozzle. This electrode is used to stabilize the EHDA process. On the bottom of the reactor, there is a grounded tip, on which a corona discharge takes place. Ions of a polarity opposite to the droplet charge are produced this way. They neutralize the droplets, to reduce the loss due to the high space charge.

Sprayed particles dry in the air and then pass the heater where thermal decomposition takes place. As a precursor for SnO$_2$ particles Sn(CH$_3$COO)$_4$ solution in absolute ethanol was used. The temperature of the heater was 400 °C. The chemical reaction of thermal decomposition of this precursor is shown below:

$$Sn(CH_3COO)_4 \rightarrow SnO_2 + 2\ CO_2 + 2\ CH_3COCH_3$$
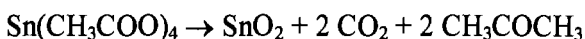
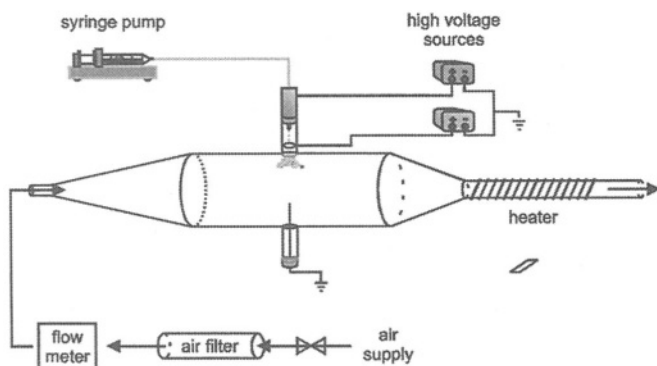The use of chlorine containing precursor always leaves some impurities in the product.

Figure 7. Reactor to produce electrosprayed particles.

BIPOLAR COAGULATION

The bipolar coagulation process consists of the mixing of two electrospray droplets of opposite charges. The principle of this process is shown in the figure 8. These two electrosprays are produced by EHDA of liquids. Because electrical attraction forces will dominate the coagulation and because it is possible to control the size and charge of droplets produced by EHDA, it should be possible to control the coagulation of droplets. The potential of such a process is enormous. It should enable to mix products on a micro-scale and to make chemical reactions in a microenvironment. This process would gives a new degree of freedom to the classical spray processes.
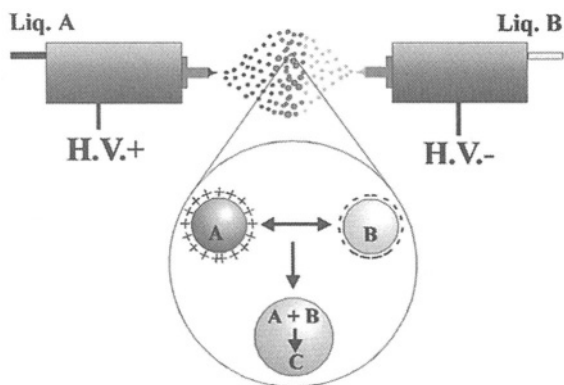

Figure 8. Principle of bipolar coagulation

An example of the bipolar coagulation is the method of production of TiO_2 particles. The powder was produced in the large configuration of the reactor (long residence time), with a titanium solution in anhydrous butanol and a water solution in absolute butanol. The temperature of the tubular furnace was 400°C. The particles were measured online with the aerosizer. The geometric mean diameter of the particles was 5.42 micron and the geometric standard deviation was 1.13. The particles on the photos appear to be smaller than 5.4 micron. They have a size around 2.5 micron. This discrepancy is due to the unknown density of these particles. The geometric mean diameter mentioned above is given by the aerosizer. To obtain this, a density of the particle measured must be entered into the software. The density of the produced particles is unknown so the used density was one. It gave the geometric mean diameter of 5.42 microns.
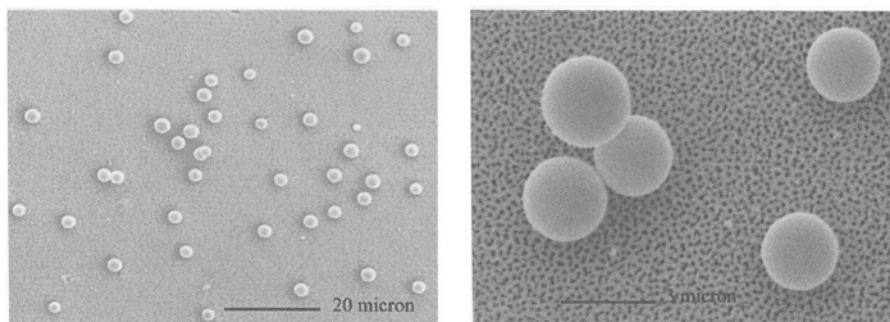

Fig. 9. Monodisperse powder produce with titanium tetrabutylate precursor and furnace temperature of 400 °C.

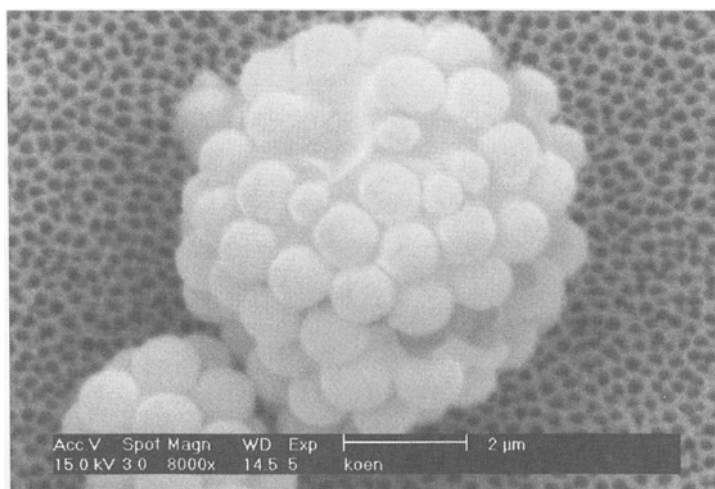Another example of particle that shows intermediate stage of bipolar coagulation is shown in the figure 10.

Figure 10. Intermeidiate stage of particle formation in bipolar coagulation.

APPLICATION IN NANOPARTICLE PRODUCTION

EHDA can be also applied in the production of nanoparticles. In the foregoing we have seen that EHDA is able to yield monosized particles. To apply this for the production of nano-particles the starting conditions must be such that the size of the produced droplets, together with the concentration of the original liquid gives the required particle size. For mono-dispersity the break-up of the jet should take place in the varicose breaking-up regime. To satisfy the size requirements we have to make the flow rate, Q, as small as possible and at the same time the conductivity, K, rather big. In the other parameters there is not much flexibility. Care should be taken to choose a solvent with a relatively low surface tension, e.g. ethanol, since for liquids with a high surface tension like for water the field, required to establish the cone-jet mode is so high that sparking occurs.

To satisfy the second requirement, monodispersity, the stress ratio should be less than about 0.3. As an example we have produced NaCl nanoparticles from a solution (fig. 11.).
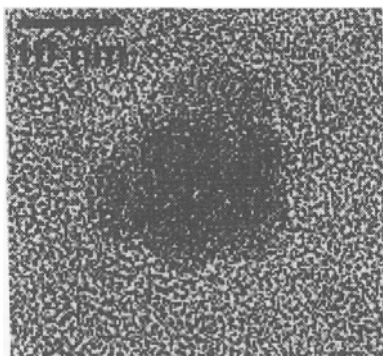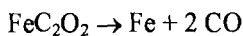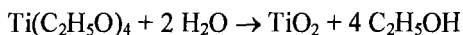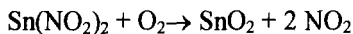

Figure 11. Example of 10 nm NaCl particle made by EHDA route.

It was shown that nanoparticles production by the method is feasible [11]. Particles of sodium chloride of about 5nm diameter were produced using the EHDA principle. These particles were obtained by spraying a mixture of water, ethylene glycol and sodium chloride. For producing these ultra fine particles, the liquid flow had to be kept low and precisely controlled. The conductivity of the solution should be in the proper range.

Organic and inorganic nanoparticles can be produced this way. As a precursor for the particles liquid or dissolvable compounds containing the desired elements can be atomised first in the EHDA reactor. After evaporation of the solvent, nanoparticles are formed. Particles will get their desired chemical composition after oxidation, hydrolysis or thermal

decomposition of the precursors. Examples of the chemical reactions during those processes are:

$$Sn(NO_2)_2 + O_2 \rightarrow SnO_2 + 2\ NO_2$$

$$Ti(C_2H_5O)_4 + 2\ H_2O \rightarrow TiO_2 + 4\ C_2H_5OH$$

$$FeC_2O_2 \rightarrow Fe + 2\ CO$$

For the production of chemically complex nano-particles, a major advantage of EHDA can be used, namely the possibility of producing mixtures of well-defined composition. Mixed oxides, metal-oxide and oxide-coated metal nano-particles can be made.

For the theoretical analysis of production of the nanoparticles currently available semi-empirical models of the EHDA process must be evaluated and eventually modified, since they have been developed for processes forming particles in the micron range. In close interaction with the experimental activity, it is also a goal of current research to find approaches to modeling of nano-particle formation. Theoretical modeling will be also needed to describe particle formation during thermal decomposition. This is especially important in the case of coated particle production. If two precursors decomposing at different temperatures are present, we expect that a solid core be formed. If the second component is liquid at some stage, it may wet the solid core, forming a coated particle. The desired composition is established, after the reactions are completed. The wetting process strongly depends on the surface energies involved. To find the proper conditions, the composition of the chemicals applied and the temperature history has to be carefully controlled.

Spray pyrolysis has already been used in thin film production. In particular, the method provides a high enough purity to produce thin film gas sensors [11]. The technique is liable to open new perspectives in the particulate film domain, because it contains the additional features of producing particles of uniform and variable size down to the regime of a few nanometers. Thin films are used in solar cells, semiconductors, superconductors, supermagnetic cores and as various coating materials, e.g. in smart glasses. Thin particle films of semiconductors change their electrical resistance due to presence of adsorbed gases (SnO_2 / O_2) and are used in gas sensors.

Nano-particles obtained via the EHDA route can find a big variety of other applications in electronics, optics and medicine [12]. They can be used for producing "quantum dots" e.g. for high efficiency tunable LED, low noise semiconductor lasers or high capacity optoelectronic memories. Possible applications also include manufacturing of solar cells. Currently production of this type of energy sources is very polluting and employing it as a way of large-scale energy production will not be environmentally

friendly. New materials as well as production routs are searched for. Titanium dioxide is a very promising compound in this field.

Coated nanoparticles of iron oxide are a promising material for very high frequency magnetic cores due to their superparamagnetic behavior. They can also be used in magnetic refrigeration technology based on the magnetocaloric effect. In both cases magnetic particles need to be coated. Another application of chemically more complicated nanoparticles is in the production of high temperature superconductors. Methods based on spraying have been proven successful in producing chemically complex ceramic nanoparticles as required for superconductor production. EHDA could open new perspectives here, again due to the feature of uniform and variable size down to a few nanometers.

Finally, nanoparticles in medicine already represent a market of many billions of Euros. Nanoparticles extend the range of materials applicable as medicine to compounds that are almost insoluable in water. EHDA could enter here as a flexible method of producing particles of fragile biochemical compounds. Targeted drugs based on special coated particle designs could also be produced by this method.

REFERENCES

1. Vercoulen P.H.W., Camelot D.M.A., Marijnissen J.C.M., Pratsinis S. and Scarlett B. SnO_2 production by an electrostatic spray pyrolysis process. Synthesis and measurement of ultrafine particles. Proceedings of the International Workshop on the Synthesis of Ultrafine Particles; 1993; Delft University Press.
2. Dudout B., Marijnissen J.C.M. and Scarlett B. Use of EHDA for the production of nanoparticles. J. of Aerosol Sci. 1999; 30:687-688
3. Lenggoro W., Okuyama K., De la Mora J.F. Preparation of ZnS nanoparticles by electrospray pyrolysis. *S.* of Aerosol Sci. 2000; 31:121-136
4. Gilbert W. *De magnete, magneticisque corporibus, et de magno magnete tellure; physiologia nova, plurimis argumentis, experimentis demonstrata* London, 1600.
5. Zeleny J. Instability of electrified liquid surfaces. Phys. Rev. 1917; 10:1-16
6. Vonnegut B. and Neubauer R.L. Production of monodisperse liquid particles by electrical atomization. J. Colloid Sci. 1952; 7:616-622
7. Cloupeau M. and Prunet-Foch B. Electrohydrodynamic spraying functioning modes: A crtitical review. J. Aerosol Sci. 1994; 25:1021-1036
8. Hartman R.P.A., Brunner D.J., Camelot D.M.A., Marijnissen J.C.M. and Scarlett B. Electrohydronamic atomization in the cone-jet mode: physical modeling of the liquid cone and jet. J. of Aerosol Sci. 1999; 30:823-849
9. Weber C. Zum Zerfall eines Flüssigkeitsstrahles. Z. für angew. Math, und Mech. 1931; 11:136
10. Melcher J.R. *Field-coupled surface waves.* Cambridge, Mass. M.I.T. 1963.
11. Korotchenkov G., DiBattista M., Schwank J. and Brinzari V. Structural characterization of SnO_2 gas sensing films deposited by spray pyrolysis. Mat. Sci. and Eng. B 2000; 77-1:33-39
12. Kruis F.E., Fissan H. and Peled A. Synthesis of nanoparticles in the gas phase for electronic, optical and magnetic applications – a review. J. of Aerosol Sci. 1998; 29:511-535

DYNAMIC COMPACTION OF NANO-STUCTURED CERAMICS

Michiel J.G. Jak

Delft Institute for Sustainable Energy, Laboratory for Inorganic Chemistry, Julianalaan 136 2628 BL, Delft University of Technology, The Netherlands

1: Introduction

The densification methods of ceramic materials are the same for many years now. Traditionally the densification takes place in a two-step process: shaping of the green body by using static pressing and subsequent sintering. This well-known and widely spread technique results in high densities and large samples with different geometries can be densified. High temperatures and long sintering times are necessary. The sintering time can be reduced by using a high starting density and by applying an external pressure.

However, when high temperatures are used in order to densify nano-structured materials, grain growth will occur and the material can even decompose, react, or melt and lose the optimum properties they were selected for. Therefore, densification of nano-structured ceramics by using high temperatures should be applied with care.

As an alternative for traditional densification using high temperatures, this chapter describes the use of high-pressure techniques. High-pressure techniques can be divided into static and dynamic techniques. With static compaction a constant pressure is applied onto a sample for a certain period of time. Due to the repulsive forces between the nano-sized particles and surface contaminations that hinder intimate contact between the particles, static pressing is not sufficient in many cases. Dynamic compaction uses a pressure pulse with a certain pulse duration, resulting in a pressure wave that travels through the sample. In both cases the pressure can by applied in a uniaxial, biaxial, radial, or isostatic/isodynamic mode. The basic principle of dynamic compaction is the way pressure waves, necessary to densify the sample, are generated. One of the best-known methods is by using explosives, but compaction by magnetic pulses is also used. In the following sections these two methods, i.e., Explosive Compaction (EXC) and Magnetic Pulse Compaction (MPC) are discussed. Both methods can be used for the shaping of green bodies but also final products can be made in a single step process.

2: The difference between dynamic and static compaction

The main difference between dynamic and static compaction is the pressure wave that is generated with dynamic compaction. The difference lies in the distribution and nature of the stresses that cause compaction [1]. Due to the pressure wave velocity, the particles of the powder to be compacted in the pressure wave front obtain a certain velocity. Hence, the impulse of the particles during dynamic compaction is much higher compared with static compaction resulting in higher local pressures that cause more plastic deformation and fracture of the particles. Due to the movement of the particles and the heat generation by friction the surface contaminants are removed and fresh surface areas are available. The high local pressure may result in particle attrition as well leading to new, clean surfaces. These processes, called dynamic cleaning, result in very sinter active powders.

Various methods to dynamically compact powdered materials are classified and reviewed by Clyens and Johnson [2]. A few basic principles hold for all these different methods. The consolidation of powder materials by dynamic compaction can be divided into three stages [2], as shown in Fig. 1.
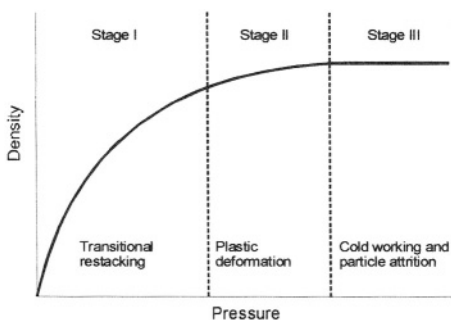

Figure 1: A typical compaction curve of a material comprising three compaction stages.

Stage I: Transitional restacking: powder particles are flowing along one another and repacking. During this stage, the particle surface instantaneously reaches extremely high temperatures due to interparticle friction effects. However, the temperature gradient between the hot surface and the cold center is huge and the cooling rate can be up to one million degrees per second [3]. Due to the very high heating and cooling rate, no diffusion or segregation of material is possible. The interparticle bonding occurs when the interparticle loads become sufficiently high to break up possible present surface contaminants and to bring the particles in intimate contact.

Stage II: Plastic deformation: transitional restacking ceases when the compaction pressure reaches a value such that the particles are locked. Depending on the powder being compacted, transitional restacking is followed by the compaction stage in which particles deform plastically to fill the porosities in the powder.

Stage III: Cold working: in this final stage cold working (fixation of dislocations which increases the hardness of the material) and/or particle attrition takes place.

At very high pressures a fourth stage may occur that comprises phase transformation. The occurrence of this fourth stage depends on the pressure and the stability of the crystal structure [4].

Figs. 2a-d demonstrates the three stages for a Fe powder sample dynamically compacted with different pressures [5]. It must be emphasized that stages II and III not necessarily take place and stage II is of minor importance for ceramic materials.
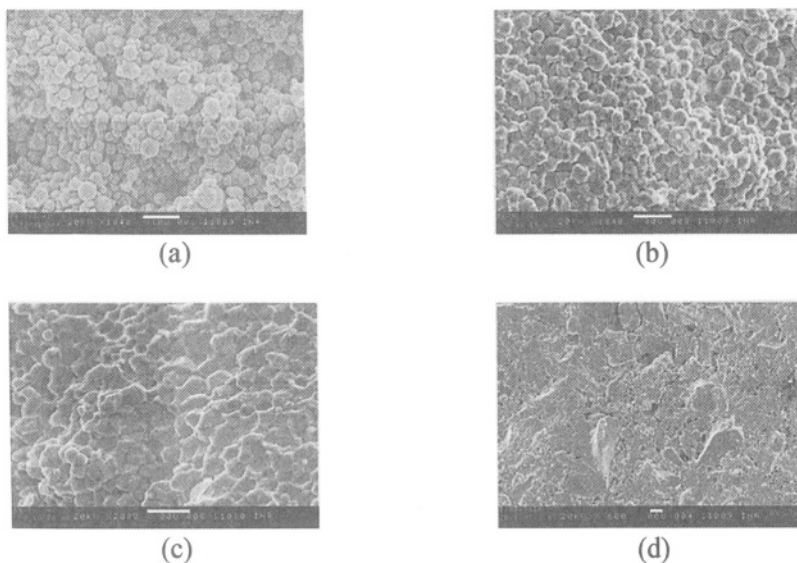

(a)

(b)

(c)

(d)

Figure 2: MPC of Fe powder with an average particle size of 2 □m. a) starting powder, b) Stage I, P=2.2 GPa, c) Stage II, P=2.4 GPa, d) Stage III, P<2 GPa (brittle FePrB), Bar=10µm.

During static compression external stresses are applied which cause particles to move to a denser particle stacking. After this initial compaction (stage I) the density is further increased by fracture and plastic deformation of the particles at contact areas (stages II and III). In the case of dynamic

compaction, the externally applied pressure travels through the powder as an anisotropic pressure wave with very large stress gradients. These anisotropic stresses, however, do not solely result in deformation near the contact areas, but also force other particles, which are not in direct contact, to move toward each other. Furthermore, due to the anisotropic nature of a pressure wave and the large stress gradients in the pressure wave, the amount of plastic deformation during dynamic compaction is very large compared to static pressing [1,6]. The same holds true for explosive compaction, but instead of a pressure wave a shock wave (with a higher velocity) is generated, leading to higher particle velocities and stress gradients. In both cases an additional pressure effect is caused by the impulse of the particles.

It should be stressed that homogeneous and high densities with a minimal crack formation can only be accomplished by compacting samples with a high starting density. Furthermore, the temperature increase of the sample is smaller when using a high starting density due to lower heat generation caused by friction forces.

The general pressure ranges and pressure wave velocities for four different compaction techniques are shown in Fig. 3. Dynamically: Explosive Compaction (EXC) and Magnetic Pulse Compaction (MPC), statically: Cold Uniaxial Pressing (CUP) and Hot Uniaxial Pressing (HUP).
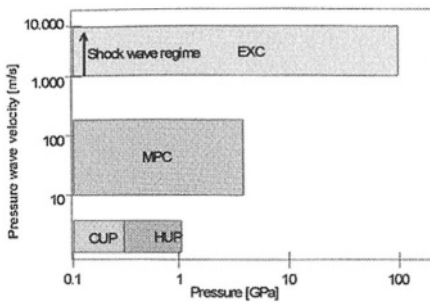

Figure 3: Different compaction techniques with their typical pressure and pressure velocity ranges.

3: Explosive Compaction (EXC)

Explosive compaction [for instance 1-3, 7-9] uses explosives or exploding gases for the generation of a pressure wave with high velocity (shock wave). In this way high pressures can be obtained and large samples can be compacted. The pressure wave is a shock wave with a typical velocity of a few

kilometers per second. The detonation velocity depends on both the chemical structure of the explosive used and the density of the explosives. Higher densities result in higher detonation velocities [10]. Basically, two explosive compaction configurations are possible, i.e., cylindrical and flat (uniaxial). The cylindrical configuration, also referred to as explosive isodynamic compaction, will be described in more detail using Fig. 4.
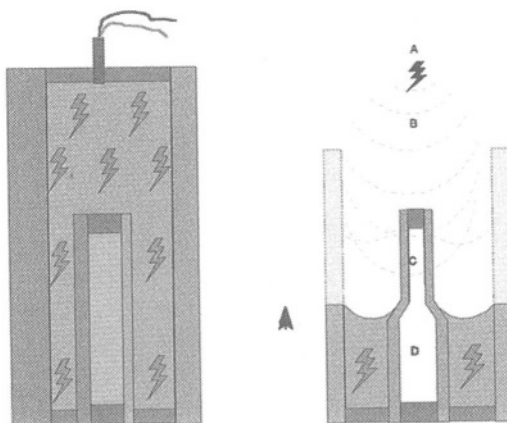

Figure 4: Cylindrical configuration of explosive compaction (see text).

Compaction is achieved due to the pressure caused by the detonation (A) of the explosives along the inner tube (B), and has a radial direction toward the center of the tube. The compacted powder region is marked (C) and the material to be compacted (D). Samples with a diameter up to 15 cm can be compacted and the length of the sample is in principle unlimited, but depends on the capacity of the bunker used.

Typical dimensions of samples compacted using the cylindrical setup are a tube diameter of 0.5 to 5 cm (maximum of 15 cm) and a length of 5 to 25 cm made of aluminum or stainless steel.

After compaction the metal tubes including the compact are normally heat-treated for a few hours at about 200°C. This heat treatment decreases present internal stresses, which are introduced due to the dynamic compaction process.

The second method of compaction is the flat configuration, also referred to as explosive uniaxial compaction [9]. The experimental setup is shown in Fig. 5. Compaction is achieved by placing a metal plate, the so-called target plate, on the powder and the explosives placed on top of the target plate.

A metal tube (⑥) is filled with the powder to be compacted (⑦). The tube is closed using metal plugs (⑤) to avoid loss of powder during the compaction and protection of the powder against the detonation products. This metal tube is centered using disks (①) in another but larger container (③). This container or envelope is only used to hold the explosives (④), and, therefore, can be made of

any material. However, metals are to be preferred as they lead to higher pressures during compaction. The explosives are ignited by a detonator (②) placed on top of the container.
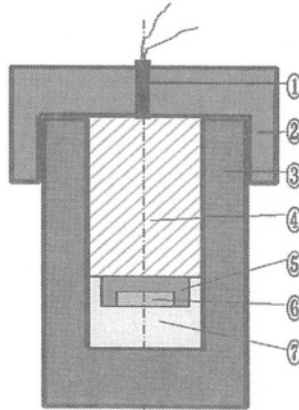

Figure 5: Experimental setup of flat explosive compaction (open configuration). ①=detonator, ②=centering ring, ③=alloyed steel casing, ④=explosives, ⑤=Cu target plate, ⑥=powder sample, ⑦=alloyed steel die.

The advantage of the cylindrical compaction method is that a homogeneous compaction can be obtained, because absorption of the shock wave and enhancement of the pressure takes place at the same time. It should be borne in mind that the shock wave travels from the tube wall to the center of the powder, and that enhancement of the pressure occurs due to a reduction of the surface area on which it acts. This balancing can be more difficult using the flat compaction configuration due to reflection of shock waves from the die.

4: Magnetic Pulse Compaction (MPC)

Another elegant way of generating a pressure wave is by using a magnetic pulse that accelerates a metal target plate or target tube [for instance 5, 8, 11-15]. A mechanical pressure pulse is obtained by conversion of electrical energy into a magnetic field.
The magnetic field is generated by charging a capacitor bank (typical maximum energy storage about 100 kJ) to a preset voltage of typically 1 to 10 kV. The pressure acting on the powder is approximately linearly proportional to the preset voltage. Via a spark gap switch the stored energy is discharged over an induction coil that generates a magnetic field. An electronically conducting material in this magnetic field will pick up this magnetic field and will move in the direction of the Lorentz force. In the case of a spirally wound induction coil the Lorentz force is parallel with the coil's center. As a result, a metal target plate in front of the induction coil is repelled. Consequently, the target plate will

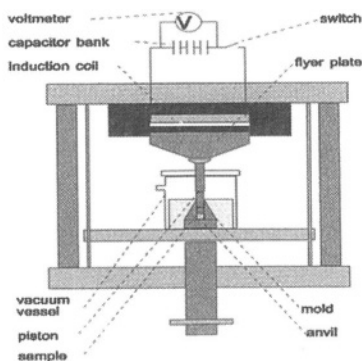interact with a piston which is pushed onto the powder to be compacted (Fig. 6).

Figure 6: Flat configuration magnetic pulse compaction.

The Magnetic Pulse Compaction (MPC) method is easy to control and safe. The powders can be compacted in a controlled atmosphere including vacuum and also (pre)heating is possible. Typical pressure wave velocities are 10-200 m/s and pressures up to 5 GPa, but higher pressures and target plate velocities are possible when proper molds are used.

A cylindrical configuration is possible as well. In this case the to be compacted sample is placed in a metal tube that is placed in the center of a spirally wound induction coil. By discharging the charged capacitors over the spirally wound induction coil a magnetic field is generated. Due to the fast change in magnetic field strength, eddy currents are generated in the metal tube. These eddy currents generate an induced Lorentz force that acts in the opposite direction of its origin (Lenz's law) perpendicular to the tube surface. This induced Lorentz force results in the radial compaction of the metal tube and its contents. For a successful compaction the following should be achieved:

1) homogeneous magnetic field
2) no air gap between the coil and the tube. The magnetic field strength decreases quadratically with increasing distance between the coil and the tube.
3) high electronic conductivity of the tube in order to obtain high eddy currents
4) homogeneity in electronic conductivity of the tube, i.e., no tube wall variation
5) high starting density of the powder
6) short rise time of the magnetic field, i.e., a fast discharge of the capacitor banks

Similar remarks and considerations concerning the cylindrical and flat

configurations, as discussed for EXC, can be made here. Table 1 lists the specifications of the two different dynamic compaction techniques.

Table 1: Comparison of explosive and magnetic pulse compaction [8]

compaction method	pressure [GPa]	pressure wave velocity [m/s]	wave form	production rate [compaction/ hour]	pulse duration [µs]
magnetic pulse (MPC)	< 5	10-200	pressure wave	<3,600	±100
explosive (EXC)	< 100	1,000- 10,000	shock wave	<10	±10

In general the lower pressure wave velocity of the magnetic pulse compaction might cause a less uniform density distribution and a lower mechanical strength of the compacts due to weaker interparticle bonding [16,17]. The effective pressure that acts on the particles of the material to be compacted depends on the nominal pressure as well as on the local pressure gradients. The local pressure gradient depends strongly on the pressure wave velocity.

Some typical experimental aspects for the flat and cylindrical configuration are described below.

Flat configuration: Fig. 6 gives an outline of the MPC set-up used. The diameter of the mold in which the powder is collected varies between 10 and 50 mm and sample thickness varies between 0.1 and 1 cm. Molds made of stainless steel or stainless steel alloyed with tungsten carbide (WC-Co) can be used.

Cylindrical configuration: The cylindrical configuration uses a spirally wound induction coil. The material to be compacted is placed in a metal tube, which is closed at the ends. The inner diameter of the coil (which is the maximum sample diameter) is 25 mm and the effective compaction length about 80 mm. The effective compaction length depends on the thickness and the hardness of the material of the target tube and the starting density of the material to be compacted. A thicker and higher hardness of the target tube results in a more homogeneous compaction length, but higher pressures are necessary. A higher starting density of the material to be compacted also contributes to the homogeneity of the compaction. The generated pressure is in general lower compared to the flat configuration.

To summarize, two different methods for dynamic compaction were described, i.e., explosive and magnetic pulse compaction. Both methods can be used in a uniaxial and a cylindrical mode. With explosive compaction high pressures can be generated resulting in high densities, while densification of large samples is feasible. This very reproducible technique has drawbacks in terms of safety and infrastructure. For application of this compaction technique

bunkers, explosives, and specialized personnel are required, which limit the accessibility to the technique. Furthermore, the compaction rate is quite low due to the long preparation time of the setup. In addition, the setup is not reusable. On the other hand, magnetic pulse compaction has a high production rate of up to one compaction per second without any special safety requirements. The pressure is easy to control and to adjust and compactions at elevated temperatures and in different gas environments or vacuum are possible. As a disadvantage the lower pressure and inherent lower density or smaller sample size should be considered.

It should be stressed that homogeneous and high densities with a minimal crack formation can only be achieved by compacting samples with a high starting density. Furthermore, the temperature increase of the sample is smaller when using a high starting density due to lower friction forces.

5: Examples and applications of dynamic compaction

Dynamic compaction can be applied for the compaction of a variety of materials and is particulary interesting for the compaction of materials which properties negatively change when high temperatures are used. In this respect one can think about amorphous metals, polymers, ceramics, glasses, nano-structured materials, and all their composites. Dynamic compaction is a technique that, in general, does not change the crystal structure of the starting material. Dynamic compaction can also be used for connecting different components, especially layers of different materials [15,18-21], when high temperatures are undesirable or static pressing is inadequate.

In this section the compaction of a selection of nano-structured ceramics and composites will be described.

n-Al_2O_3

Nano-structured Al_2O_3 powder (n-Al_2O_3) has been compacted using uniaxial magnetic pulse compaction [12,22]. The powder has a mean particle size of 20 nm and has been produced by the exploding wire technique [5,13,23] resulting in γ-Al_2O_3 with a specific surface area of 80-100 m^2/g and a theoretical mass density (TMD) of 3.66 g/cm^3. Prior to compaction the powder was heated to about 450°C and evacuated down to 1 Pa in order to remove any absorbed and included gases. The initial density was 0.8 g/cm^3 (i.e., 22%TMD) and the sample diameter was 15 mm and the sample height prior to compaction was 4 mm. After compaction, performed at room temperature, the samples are homogenous and crack-free. Fig.7 shows a scanning electron microscopy micrograph of the MPC n-Al_2O_3 fracture surface.
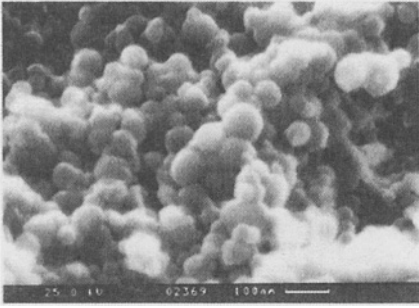
Figure 7: SEM micrograph of MPC n-Al₂O₃ [22] Bar=100 nm.

X-ray diffraction spectra do not reveal any phase change. In Fig. 8 the density after compaction as a function of the applied pressure is plotted and a maximum density of 82% has been obtained at 2 GPa.
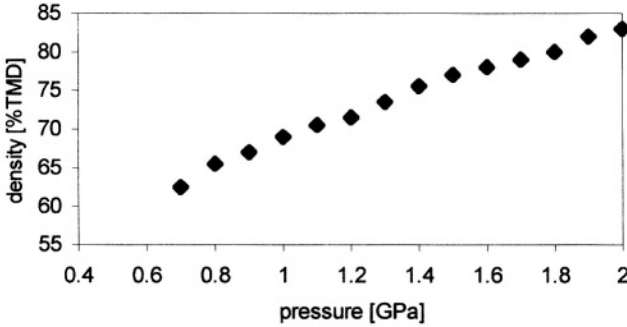

Figure 8: Density as a function of applied pressure of n-Al₂O₃. ◆=MPC [12].

As a comparison the same powder has been compacted using static pressing at room temperature. The density as a function of the applied pressure is shown in Fig. 8.
From the comparison with the MPC samples a significantly lower density (up to 15%) can be observed. The reason for this difference is the so-called dynamic cleaning of the particle surfaces due to the friction forces and heat generation that occurs during dynamic compaction [12].

The MPC samples of **n-Al₂O₃** can be used for further sintering in order to increase the density and the hardness. **γ-Al₂O₃** powders were compacted using MPC using different pressures resulting in different densities. These green samples were sintered using high power millimeter wave radiation from a 30 GHz gyrotron [24-26]. Heating rates of 30 to 50°C/s to a sintering temperature of 1150°C were used in order to prevent excessive grain growth. Fig. 9 shows the final density and the average grain size after sintering as a function of the green density (after MPC). From this figure the importance of a high starting

density for the sintering process is clearly shown. Combined with the densities obtained with MPC and static pressing as presented in Fig. 8 it is obvious that MPC is a very promising technique for the preparation of green bodies that can be used for sintering up to a high density without excessive grain growth [25].
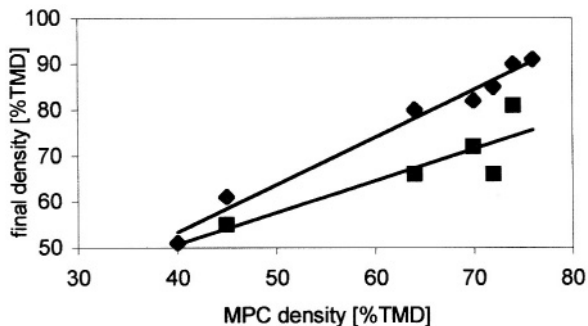

Figure 9: Final density (◆) and average grain size (■) after sintering of n-Al$_2$O$_3$ as a function of the green density (after MPC) [25].

n-TiO$_2$

The n-TiO$_2$ powder used has a mean particle size of 16 nm and has been produced by the exploding wire technique [22]. The theoretical mass density (TMD) is **4.0 g/cm^3** (about 1:1 rutile:anatase). The material was compacted using uniaxial magnetic pulse compaction. Prior to compaction the powder was heated up to about 450°C and evacuated down to 1 Pa in order to remove any absorbed and included gases. The initial density was **0.73 g/cm^3** (i.e., 18%TMD) and the sample diameter was 15 mm and the sample height prior to compaction was 4 mm. After compaction, performed at room temperature, the samples are homogenous and crack-free. Fig. 10 shows a scanning electron microscopy picture of the fracture surface of compacted **n-TiO$_2$**. X-ray diffraction spectra do not reveal any phase change.
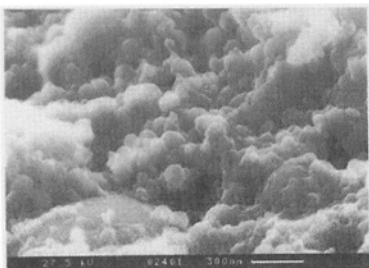

Figure 10: Scanning Electron Microscope (SEM) micrograph of MPC n-TiO$_2$ [22]. Bar=300nm

In Fig. 11 the density after compaction as a function of the pressure is

66

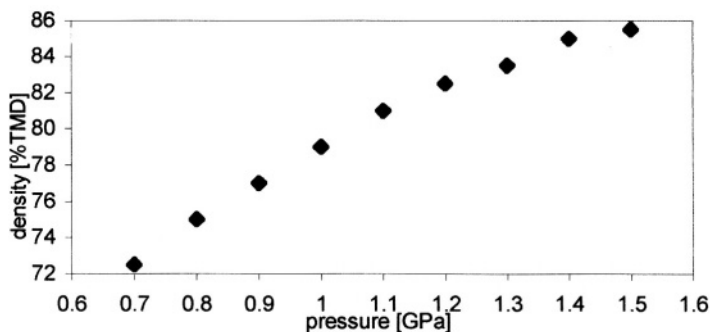plotted and a maximum density of 86% was obtained at 1.5 GPa [12].

Figure 11: Density as a function of compaction pressure (MPC) of n-TiO₂ [12].

Li-BPO₄

Li-doped **BPO₄** is a ceramic Li-ion conducting electrolyte that can be used in all-solid-state Li-ion batteries [27-32]. The crystallite size, determined from the X-ray diffraction line width using the Scherrer equation, is about 30 nm, but the particles are heavily agglomerated to particles of up to 1 μm. Fig. 12 shows a scanning electron microscope picture of the as-synthesized material.
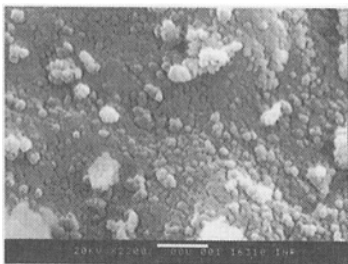
Figure 12: SEM micrograph of 7 mole% Li-doped BPO₄. Bar indicates 1 μm.

The crystallite size can be adjusted by changing the synthesis parameters [31]. Sintering of these nano-structured powders leads to drastic grain growth that results in a huge decrease of the ionic conductivity. The densification of nano-structured 7 mole% Li-doped **BPO₄** has been studied as a function of pressure and different compaction techniques [9,28]. These techniques are: uniaxial magnetic pulse compaction (MPC), uniaxial explosive compaction (EXC), hot uniaxial pressing (HUP), and cold uniaxial pressing (CUP). The HUP experiments were performed at 1500°C for 5 minutes including heating and cooling. Figs. 13 and 14 show the SEM micrographs of the MPC and HUP sample, respectively. The MPC sample shows a rather dense sample with the nano-structured particles still present. The HUP sample however, shows massive grain growth with particles up to 1 μm in diameter.
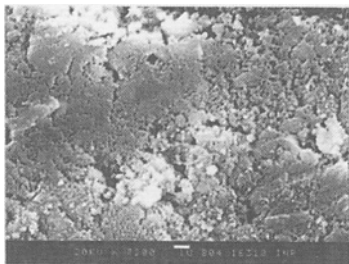
67

Figure 13: SEM micrograph of an MPC Li-doped BPO₄ sample (pressure 1.8 GPa, density 68% TMD).
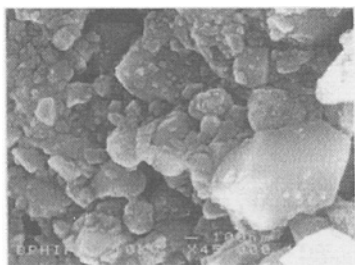

Figure 14: SEM micrograph of a HUP Li-doped BPO₄ sample (pressure 0.5 GPa, T=1500°C, density 90% TMD). Bar=0.1 μm

As a result of the grain coarsening the density of the HUP sample is about 90 %TMD.

Fig. 16 shows the X-ray diffraction spectra of the starting powder and the compacted samples [28]. The spectra show no peak shift and/or additional peaks, proving that no structural changes occurred during compaction. The only effect that the different compaction techniques have on the spectra is a change in peak width and thus on the particle size. The peak width of the starting powder and the dynamically compacted samples are comparable (crystallite size is 26±1 nm calculated from the peak width), while the crystallite size of the HUP and CUP sample is 89 and 43 nm, respectively. These results show that dynamic compaction preserves the nano-structured morphology and does not alter the crystal structure [28].
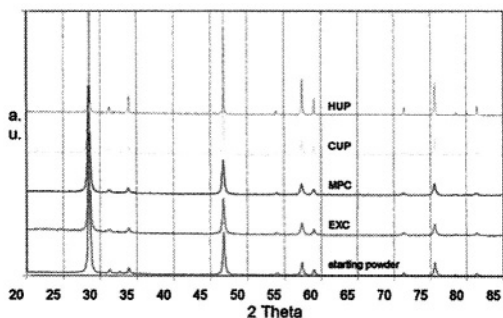
Figure 16: XRD spectra of starting material and compacted samples of Li-doped BPO4 (7 mole% Li).

Table 2 shows the importance of preserving the nano-structured morphology in terms of ionic conductivity. A severe decrease in ionic conductivity is observed with increasing crystallite size. The reason for this decrease in conductivity is that Li-doped BPO_4 is a grain boundary conductor, i.e., the smaller the particles, the more grain boundaries are present, the higher the ionic conductivity will be [28]. Hot pressing of the sample decreases the ionic conductivity with more than 2 orders of magnitude despite the high density of the HUP sample.

Table 2: Li-doped BPO4 compacted with different techniques.

compaction method	pressure [MPa]	density [%TMD]	crystallite size [nm]	ionic conductivity [μS/cm] at R.T.
HUP	500	94	89	0.7-2
CUP	375	56	43	2-20
MPC	1000	65	25	2-50
EXC	3500	70	27	80-200
starting	-		26	-

Nano-nano composites

The advantages of using MPC for compacting composites compared to static pressing will be demonstrated by an example of a zirconia-hematite nano-nano composite [33]. The crystallite size of the hematite phase was 41 nm and 8 nm for the zirconia phase. After compaction with either uniaxial pressing (UP) at 1000 MPa, or isostatical pressing at 400 MPa (IP), or MPC (1500 MPa), the green bodies were pressure-less sintered in air for two hours at different temperatures (heating rate 2°C/min). The relative densities after sintering the different green bodies are shown in Fig. 17 as a function of sintering temperature. It can be clearly seen that the MPC sample shows the highest density of 94 %TMD already at 1000°C.
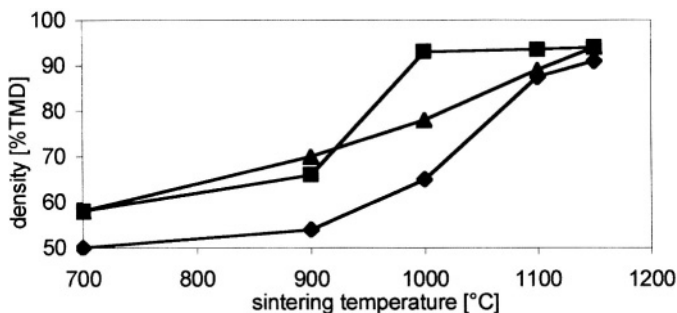
Figure 17: Sintering of green compacts of zirconia-hematite nano-nano composites compacted with different techniques. ◆=CIP at 400 MPa, ▲=CUP at 1000 MPa, ■= MPC at 1500 MPa [33].

6: Conclusion and discussion.

In this chapter several routes of densifying nano-structured ceramics have been briefly described. The advantages of dynamic compaction over static compaction techniques have been shown and explained. The dynamic compaction technique can be used to make final products or half-fabricates due to the relatively high density and mechanical strength. Both properties are related to the intimate particle contact obtained.

It has been demonstrated as well that the dynamically compacted samples can be used as green bodies that can be used for further sintering. Extremely high densities are reached by combining dynamic compaction and a subsequent sintering step while the sintering time and temperature can be much lower than using conventional sintering only. After densification the material can be still nano-structured due to the high starting density.

Nano-structured ceramics are one class of materials that can successfully be densified by dynamic compaction, but the technique is certainly not limited to these materials. Magnetic pulse compaction is a commercially used technique for near-net-shape densifying metal powders into all kinds of shapes with densities close to the theoretical density. The most widespread application is the shaping of gear wheels for the automotive industry, but also connecting different metals (cold welding) and polymer-metal connections are performed commercially using MPC. The advantage of commercial equipment is the ability to compact one sample per second.

Explosive compaction and cladding are commercially applied as well. Artificial diamond is produced on a large scale for abrasive applications using explosive compaction of graphite. Explosive welding

70

and cladding are rapid growing markets for combining cheap or mechanically stable materials with an expensive or weak material with special properties. In addition, explosive compaction generates much higher pressures than magnetic pulse compaction which can be used to achieve higher densities and for the densification of larger compacts. On the other hand is the low production rate and the necessary infrastructure a major drawback for commercial application.

References

[1]   P. Boogerd, *"Dynamic Compaction of Ceramics"*, Ph.D. Thesis, Delft University of Technology, The Netherlands (1995), Ch. 1.

[2]   S. Clyens and W. Johnson, *Mater. Sci. Eng*., **30** (1977), 121.

[3]   R. Prümmer, *"Explosivverdichtung pulvriger Substanzen"* (Springer Verlag, Berlin, 1987), p.56. (in German)

[4]   Ref. [1], Ch. 6

[5]   A. Weisenburger, *"Anwendung der Hochleidtungsimpuls- und Mikrowellentechnik zur Herstellung nanokristalliner Pulver und Festkörper"*, Ph.D. Thesis, University of Karlsruhe, Germany (1999). (in German)

[6]   E.P. Carton, *"Dynamic Compaction of Ceramics and Composites"*, Ph.D. Thesis, Delft University of Technology, The Netherlands (1998), Ch. 2.

[7]   D.K. Dijken, *"Dynamic and Isostatic Densification of Powder Materials"* Ph.D. Thesis, University of Groningen, The Netherlands (1994).

[8]   M.J.G. Jak, *"Dynamic compaction of Li-ion battery components and batteries"*, Ph.D. Thesis, Delft University of Technology, The Netherlands, 1999.

[9]   M.J.G. Jak, E.M. Kelder, J. Schoonman, V.N. Lashkov, A.V. Strikanov, A.A. Selezenev, and A.A. Potanin, *J. Appl. Phys*., **86-10** (1999), 5455.

[10]   Ref. [6], Ch. 3.

[11]   T. Negishi, T. Ogura, T. Masumoto, T. Goto, K. Fukuoka, Y. Syono, and H. Ishii, *J. Mater. Sci.,* **20** (1985), 399.

[12]   V. Ivanov, S. Paranin, A. Vikhrev, R. Böhme, and G. Schumacher, *Proceedings 4th Euro Ceramics,* Riccione, October 2-6, **2** (1995), 169.

[13]   V. Ivanov, Y.A. Kotov, O.H. Samatov, R. Böhme, H.U. Karow, and G. Schumacher, *Proceedings International Conference Nanostructured Materials,* Stuttgart, October 3-7, 1994.

[14]   R. Böhme, M.J.G. Jak, G. Link, and A. Weisenburger, *Abstracts ESF-NSF symposium "Aerosols for Nanostructured Materials and Devices"*, Edinburgh, September 12, 1998, 42.

[15]   M.J.G. Jak, F.G.B. Ooms, E.M. Kelder, W.J. Legerstee, A. Weisenburger, and J. Schoonman, *J. Power Sources,* **80** (1999), 83.

[16]   E.A. Doroshkevich and O.V. Roman, *Rep. 8th Union Powder Met. Conf.,* Minsk (1966), 61.

[17]   J.D. Campbell, *Mater. Sci. Eng.,* **12** (1973), 3.

[18]   Ref. [8], Ch. 3.

[19]   M.J.G. Jak, E.M. Kelder, and J. Schoonman, *"A method for the manufacturing of a lithium battery",* Patent PCT/NL/96/00356, 1996.

[20]   M.J.G. Jak, E.M. Kelder, M. Stuivinga, and J. Schoonman, *Solid State Ionics,* **86-88** (1996), 897.

[21]   M.J.G. Jak, E.M. Kelder, A.A. van Zomeren, and J. Schoonman, *Proceedings of*

the *Electrochem. Soc. "Symposium on Exploratory Research and Development of Batteries and Supercapacitors for Electric and Hybrid Vehicles"*, Eds. W.A. Adams, A. Landgrebe, and B. Scrosati, 1996, p. 58-70,

[22]   Ref. [5], Ch. 6.

[23]   I.V. Beketov, Y.A. Kotov, A.M. Murzakaev, O.M. Samatov, V. Volkov, R. Böhme, and G. Schumacher, *Proceedings 4th Euro Ceramics,* Ed. C. Galassi, Riccione, October 2-6, **1** (1995), 77.

[24]   G. Link, A. Weisenburger, R. Böhme, M. Thumm, in *"Mikrowelleneinsatz in der Materialprozesstechnik, der chemischen Verfahrenstechnik und in der Festkörperchemie",* ed. M. Willert-Porada, Shaker Verlag, Aachen (1998), p. 320 (in German).

[25]   G. Link, A. Weisenburger, R. Böhme, M. Thumm, *Proceedings 9th Int. Conf. on Modern Materials & Processing,* CIMTEC '98, Firence (1998)

[26]   G. Link, V. Ivanov, S. Paranin, V. Khrustov, R. Böhme, G. Müller, G. Schumacher, and M. Thumm, *Materials Research Society Symposium Proceedings,* **430**, *Microwave Processing of Materials,* p. 157, Eds. M.F. Iskander, J.O. Kiggans, and J-Ch. Bolomey (1996).

[27]   Ref. [8], Chs. 4-6.

[28]   M.J.G. Jak, E.M. Kelder, N.M. van der Pers, A. Weisenburger, and J. Schoonman, *J. of Electroceramics,* **2** (1998) 127.

[29]   E.M.Kelder, M.J.G. Jak, F.de Lange, and J.Schoonman, *Solid State Ionics* **85** (1996) 285.

[30]   M.J.G. Jak, E.M. Kelder, and J. Schoonman, *J. of Solid State Chem.,* **142** (1998), 74.

[31]   M.J.G. Jak, E.M. Kelder, S.J. Everstein, and J. Schoonman, *J. of Power Sources,* **81/82** (1998), 808.

[32]   M.J.G. Jak, E.M. Kelder, Z.A. Kaszkur, J. Pielaszek, and J. Schoonman, *Solid State Ionics,* **119** (1998), 159.

[33]   T.P. Raming, *"The synthesis of nano-nano dual phase ceramic composites",* Ph.D. Thesis, Twente University, The Netherlands (2000), Ch. 5.

STRUCTURAL AND ELECTRICAL PROPERTIES OF NANOSTRUCTURED AND COARSE MANGANESE SPINEL

J. Molenda and J. Marzec

Faculty of Materials Science and Ceramics, **Stanisław** *Staszic University of Mining and Metallurgy, Al. Mickiewicza 30, 30-059 Cracow, Poland*

1. INTRODUCTION

$LiMn_2O_4$ manganese spinel is a promising cathode material for 4V lithium accumulators [1-3]. Its reversible capacity of 100 – 130 mAh/g is comparable to the capacity of $LiCoO_2$, but it has higher potential, is cheaper and less environment polluting than $LiCoO_2$. $LiMn_2O_4$ attracts an enormous and still growing interest of the leading laboratories in the world and the number of related papers is increasing recently very fast indicating, that this material will be soon commercialized. The studies of this lithium manganese oxide reported in literature concentrate mainly on the determination of operating parameters of batteries, lithium chemical diffusion coefficient measurements, structural parameters, and attempts to find admixtures that improve battery operating characteristics. The obtained characteristics often concern materials that are not well defined from the point of view of ionic and electronic defects structure. Microscopic mechanism of charge transport that is responsible for the efficiency of the intercalation process is practically not known.

Manganese spinel is synthesized mainly by a traditional high-temperature (~800°C) solid state reaction. Thus obtained stoichiometric manganese spinel $LiMn_2O_4$ undergoes a phase transition from regular (Fd3m) to orthorhombic (Fddd) phase near room temperature (~290K). The transition is connected with the Jahn -Teller distortion of the Mn^{3+} ions surrounding. Basic structural studies performed by Rodriguez-Carvajal and other groups

[4-6] with the use of neutron and electron diffraction methods have shed new light on the nature of this phase transition and have indicated its relation to a specific charge ordering in the manganese sublattice. This ordering, called "electronic crystallization" [4], consists in a columnar (in the c-axis direction) ordering of Mn^{3+} ions surrounded by Mn^{4+} ions and affects transport properties of a cathode material. Unquestionably, the existence of a phase transition in $Li_1Mn_2O_4$ near room temperature, i.e., close to the working temperature of the battery may cause a change of its important operational parameters with temperature. In literature there is a common opinion that the phase transition present at around room temperature worsens the properties of the cathode material, however there is no experimental proof for it. In addition there is still no data on the dependence of the phase transition on the deintercalation degree x in $Li_xMn_2O_4$. There is also lack of data on the dependence of electrical properties of the deintercalated spinel on deintercalation degree x. Only limited data on the properties of stoichiometric $LiMn_2O_4$ at temperatures close to the phase transition are available.

There are particularly poor conditions for electron transport in manganese spinel at room temperature as compared with other widely used cathode materials in Li-ion batteries. Polaron conduction mechanism with activation energy of 0.2-0.3eV cannot explain observed high efficiency of intercalation process.

The issue is what are the physicochemical properties of deintercalated spinel, what is a factual electron transport mechanism in operating spinel cathode and how the phase transition affects the efficiency of intercalation process.

As the conductivity is surely one of the most important features of the cathode material, systematic investigations on electrical transport and related phenomena in $Li_xMn_2O_4$ $(0.4 \leq x \leq 1.006)$ together with structure and DSC characterisation at subsequent stages of deintercalation process were performed.

Literature reports indicate that manganese spinel obtained by low-temperature soft chemistry methods yields better electrochemical characteristics of batteries [7]. Using these methods better homogeneity of materials is obtained as substrate mixing is done in a solution that means on the atomic level. In addition, grains having significantly smaller size are obtained, which has an influence on diffusion processes rate in a cathode material.

Nanostructured manganese spinel $LiMn_2O_4$ was obtained by a sol – gel method and its structural, heat and electrical properties were investigated. Analogous characteristics were determined for the same samples after annealing them at 800°C in air for 24 hours. For comparison a sample of

"δ-spinel" $(Li_{1+\delta}Mn_{2-\delta}O_4)$; $Li_{1.006}Mn_{1.994}O_4$ made from commercial Selectipure SP30 powder (Merck Co.) was also tested. Subsequently all these samples were delithiated and characterised in the same way as the starting materials.

2. STUDIED MATERIALS
2.1. Nanostructured manganese spinel – "series A"

Stoichiometric amounts of $LiNO_3$ (Aldrich, SigmaUltra 99.99%) and $Mn(CH_3COO)_2 \cdot 4H_2O$ (Aldrich 99.99%) were dissolved in a minimal amount of deionized water. Concentrated ammonia (Aldrich, A.C.S. Reagent 28%) at 25°C was added drop by drop to the mixture until **pH=9** was reached, at which a precipitation of colloidal deposit was observed. After **pH=9** had been reached the mixture was left for 1h continuously stired. Thus formed colloid was next dried at 90°C during 48h and subject to calcination in air at 300°C for 24h. The heating and cooling rates were 50°C/min. The whole sol-gel processes were described in details in [8].

2.2. Strictly stoichiometric $Li_1Mn_2O_4$ - "series B"

Series B materials were obtained by annealing series A samples at 800°C in air for 24h and quenched.

2.3. "δ-spinel" with low lithium excess $Li_{1.006}Mn_{1.994}O_4$ – "series C"

$Li_{1.006}Mn_{1.994}O_4$ samples were obtained by annealing for 24h in air at 800 °C pellets of commercial Selectipure SP30 powder (Merck Co.) and then quenched.

2.4. Delithiated materials $Li_xMn_2O_4$

Lithium was extracted by two methods – electrochemical and chemical. Electrochemically deintercalated samples of $Li_xMn_2O_4$ (x = 0.98; 0.94; 0.75 and 0.40) were obtained in a $Li/Li^+/Li_xMn_2O_4$ cell (with $LiPF_6$ in DMC/DME as electrolyte). No additives were doped to the cathode materials. Deintercalation processes were carried out at room temperature with spinel pellets of all A, B and C series as cathodes and the cells were charged at a constant current density $80~\mu A/cm^2$.

Hunter's method [9] of lithium extraction as a partial dissolution of manganese spinel in sulfuric acid was used for chemical deintercalation of the C series. This process is described by reaction:

$$4LiMn_2O_4 + 8H^+ \rightarrow 3(\lambda - Mn_2O_4) + 4Li^+ + 2Mn^{2+} + 4H_2O$$

76
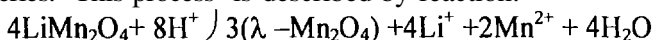
Such Li – extracted materials were already studied by XRD, IR spectroscopy [10] and also characterized by laser diffraction, BET method, scanning electron microscope and electrochemical behaviour [11].

Figs. 1a and 1b present SEM photographs of the surface of the spinel obtained by the sol – gel method and after annealing it at 800°C (series A and B). A comparison of the pictures reveals that annealing of the samples at high temperatures leads to an increase in the grain size. In the case of spinel obtained by the sol – gel method a mean size of the grains is equal to 0.4 μm, while that for the sample annealed at 800°C in air for 24h increases to 1μm. Fig. 2 present SEM pictures (a) and particle size distribution (b) of the C series.

(a)

(b)
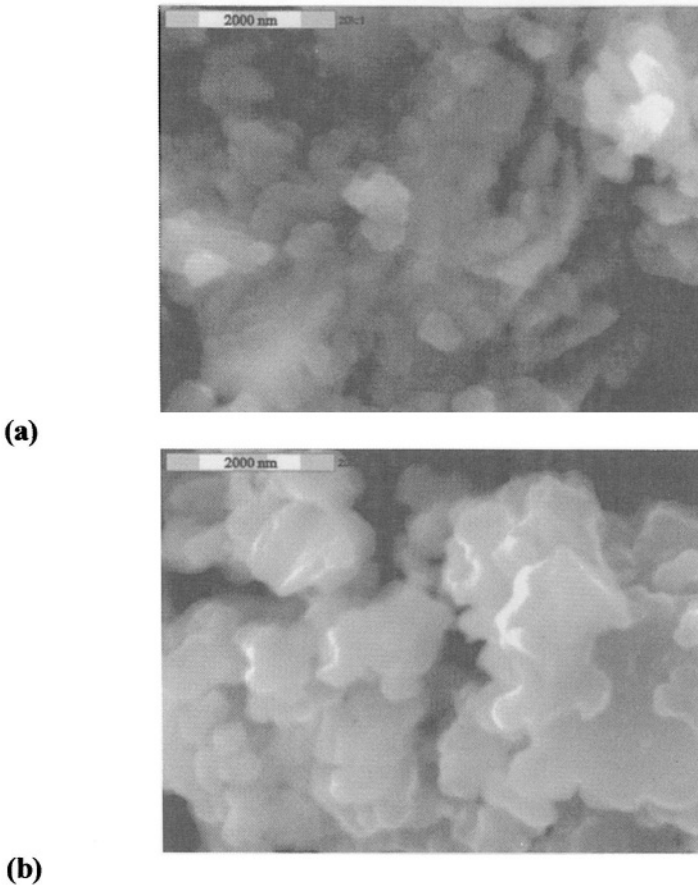
Figure 1. SEM photograph of the surface of manganese spinel sample obtained by a sol-gel method – (a) series A and (b) of the same sample annealed at 800°C in air for 24h - series B; (magnification: 20 000 x).
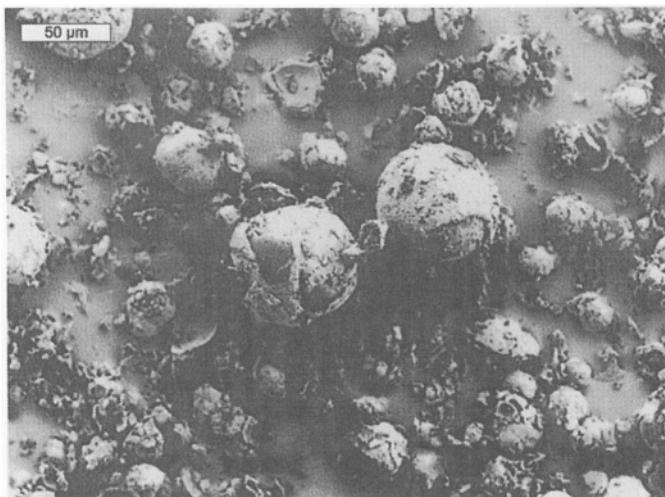
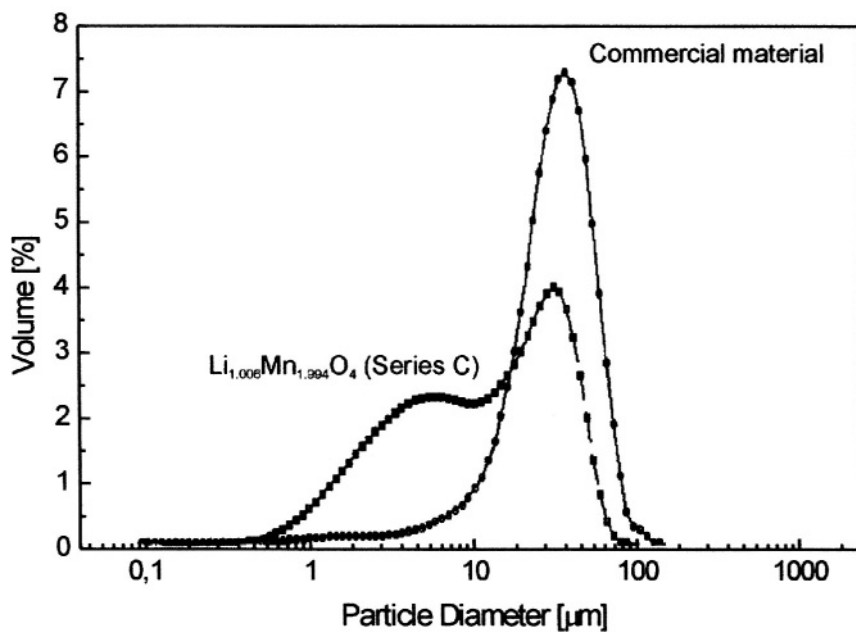*Figure 2a.* SEM pictures of $Li_{1.006}Mn_{1.994}O_4$ (C series)

Figure 2b. Particle size distribution of manganese spinel from C series

3. STRUCTURAL PROPERTIES

The fundamental lattice of the spinel structure can be considered as a face centred cube of O^{2-} ions and the cations are located in the interstitial positions in the anion lattice. In the $LiMn_2O_4$ spinel structure there are two kinds of cation sites. The *8a* sites are occupied by Li^+ ions tetrahedrally coordinated by four O^{2-} anions. The interstices of the coordination tetrahedron are small so the large Li^+ ions enlarge the *8a* position shifting the anions outward. Another cation sites *16d,* each coordinated by six O^{2-}, are occupied by equal number of Mn^{3+} and Mn^{4+} ions and the electric charge is +3.5 on average. These sites can be considered as a diamond type lattice of tetrahedrons formed by *16d* cation sites. These tetrahedrons sharing corners with each other are lined along $\langle 111 \rangle$ direction building Kagomé type lattice.

3.1. XRD analysis
3.1.1. Series A

For the nanostructured manganese spinel sample obtained by the sol – gel method powder X-ray spectra were recorded at 300K and 70K. It was found that at both temperatures the sample remains a single phase one and that its high-temperature cubic structure is maintained also at 70K. Both of the measured X-ray patterns reveal identical and very strong broadening of the lines, which is a sign of small dimensions of the coherently scattering domains and, as a consequence, small grain size or (and) the existence of strong stresses in the sample resulting from heterogeneity of the composition or structure faults. A part of the X-ray pattern recorded at 300K is shown in Fig.3a. Apart from broad lines of $LiMn_2O_4$ the spectrum contains three very narrow lines of pure germanium which was used here as an internal standard (giving in practice apparatus line width). As determined by Rietveld analyses of the XRD pattern, the lattice parameter *a* of the sample at room temperature equals to 8.165(4) Å. The obtained value, unexpectedly low as compared with the anticipated 8.25 Å for exactly stoichiometric material indicates that possibly not all structural sites in the material obtained by the low temperature method are occupied. Thermogravimetric measurements point to irreversible oxygen loss on heating, starting at 400°C (1.6% overall mass loss), in accordance with ASA results yielding high average manganese valency equal 3.83 in the sol-gel material [8]. The series A material exhibiting oxygen excess is not a stoichiometric manganese spinel. The structure of the material can be considered as well formed oxygen framework but with vacancies in cation sublattice leading to the observed low lattice parameter and high manganese valency.

Following annealing at 800°C leads to oxygen loss until the stoichiometric composition $Li_1Mn_2O_4$ is achieved (series B).

3.1.2. Series B

Fig.3b presents a part of the X-ray pattern measured at 300K for the series B sample. One can see a distinct narrowing of the lines as compared with the series A, what indicates significant increase of coherently scattering domains related to the expected growth of the grains and a general improvement of the quality of the sample crystal structure. Lattice parameter a is equal to 8.2479(5) Å at room temperature, characteristic for a stoichiometric $LiMn_2O_4$ phase, what is in accordance with the obtained from ASA experiment 3.53 average manganese valency in the sample.
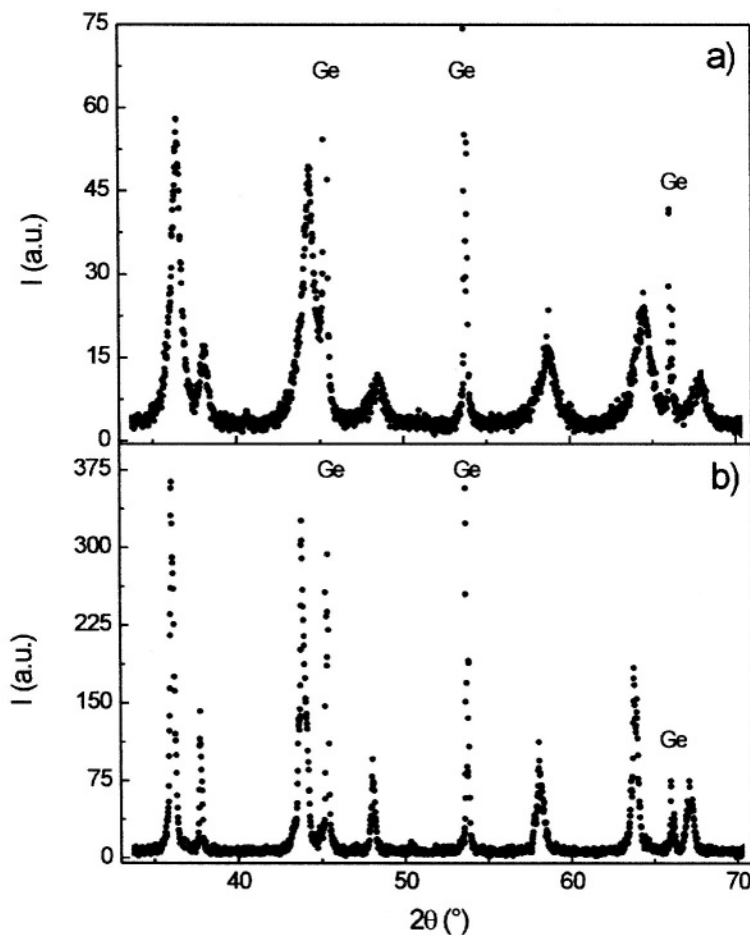
Figure 3. X-ray patterns measured at 300K: (a) for nanostructured manganese spinel obtained by a sol-gel method (series A) and (b) after annealing it at 800°C in air for 24h (B series).

However one can notice differences in relative widths of the lines from Fig.3b resulting from the fact that the sample is a two-phase one. This is due to the phase transition from a high-temperature cubic to a low-temperature orthorhombic structure appearing for a stoichiometric $LiMn_2O_4$ at around 290K. At 300K the sample is in the temperature region of a structure transformation. This means that the true line width for this sample is still smaller and determined by the width of the narrowest lines in the spectrum (excluding germanium lines).

In order to follow the process of crystal structure transformation a series of X-ray spectra were recorded between 320K and 220K both on heating and cooling of the sample. Fig.4 presents a temperature dependence of the (400) line width at half maximum (FWHM). The results show both the sharpness of the structure change and the presence of temperature hysteresis, which indicates that the transition is of the first order type. The results remain in excellent agreement with the literature data [12], where for a stoichiometric $LiMn_2O_4$ sample a first order phase transition from cubic to orthorhombic structure was also observed in this temperature range with a hysteresis of about 20K. At low temperatures the entire sample lattice undergoes the orthorhombic distortion.
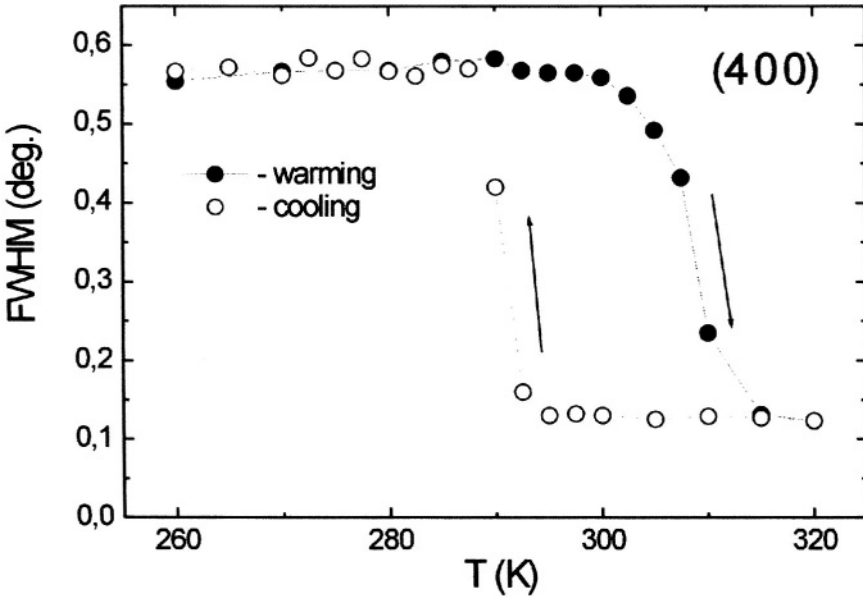

Figure 4. Full width at half maximum (FWHM) for the (400) line of stoichiometric $LiMn_2O_4$ (B series).

3.1.3. Series C

For the $Li_{1.006}Mn_{1.994}O_4$ composition of manganese δ-spinel a broadening of the diffraction lines with lowering temperature was also observed. The broadening was caused by fine splitting of the cubic structure lines resulting from the orthorhombic distortion. In Fig. 5 two selected peaks from XRD pattern fitted with both cubic and orthorhombic components are given. One can notice that the fit nicely follows the experimental peak shape. Fig.6 presents half-maximum width (FWHM) of the (004) line as a function of temperature for $Li_{1.006}Mn_{1.994}O_4$. An analysis using the Rietveld method shows that the best fit to the experimental X-ray patterns is obtained assuming a coexistence of cubic and orthorhombic phases in relative proportions varying with temperature. In Fig.7 is shown the relative content of the cubic phase as a function of temperature. These results indicate a presence of continuous transition (progressing distortion) from cubic to an orthorhombic phase (of lower symmetry) as the temperature is decreased, and contrary, this leads to a decrease of the disordered phase with rising temperature. The temperature value seems only to determine the ratio of both phases, like it takes place in a second order order–disorder transitions. However, observed transition does not lead to a total transformation of the initial cubic structure till below 70K.
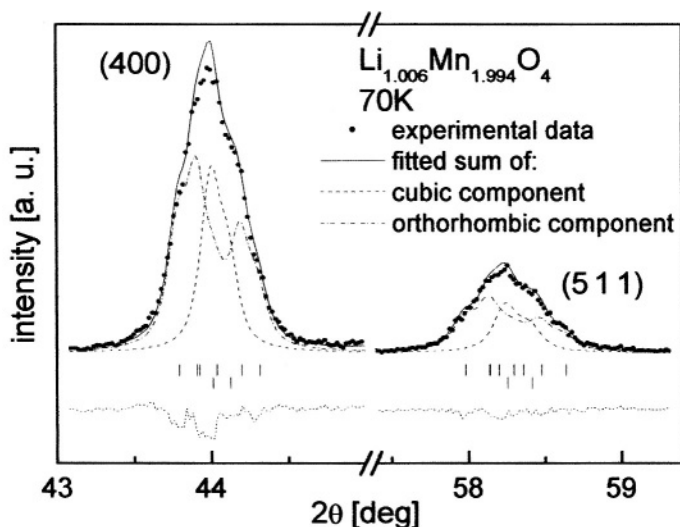

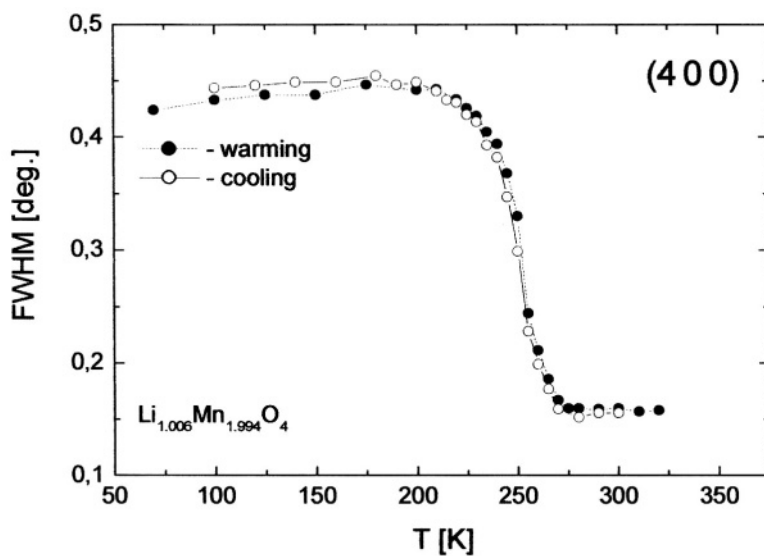*Figure 5*. XRD pattern of $Li_{1.006}Mn_{1.994}O_4$ (series C) at 70 K fitted with orthorhombic and cubic phases.

Figure 6. Temperature dependence of Full Width at Half Maximum (FWHM) parameter of the (400) XRD peak of $Li_{1.006}Mn_{1.994}O_4$ (C series).

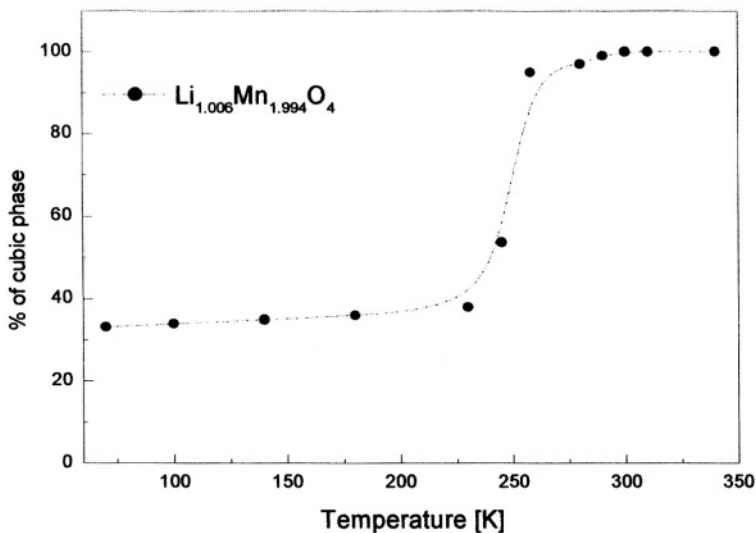*Figure 7.* The cubic phase mass fraction of $Li_{1.006}Mn_{1.994}O_4$ (series C) versus temperature

.

.
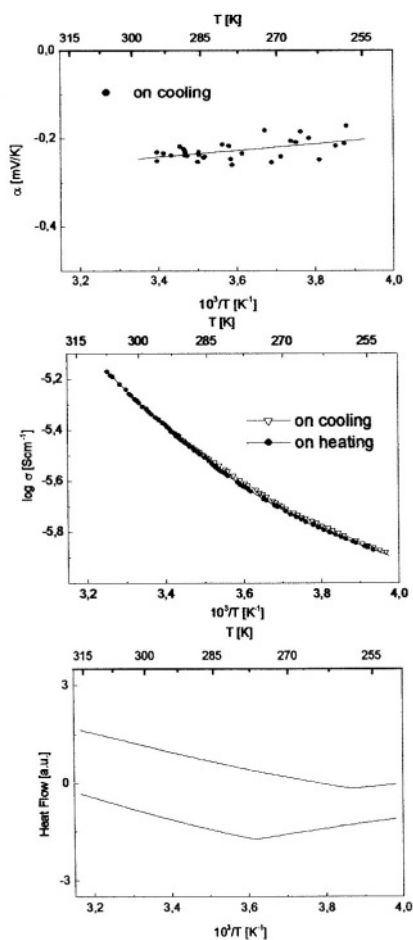
At room temperature the values of electrical conductivity for manganese spinel obtained by a sol – gel method are of the order of 10^{-5} $\mathbf{Scm^{-1}}$ (Fig.8b) which is lower as compared to 10^{-4} $\mathbf{Scm^{-1}}$ for the annealed sample (Fig.9b). The obtained conductivity activation energy (0.1 eV) related to the activation energy for small polaron movement is lower than for the spinel annealed at 800°C (0.2 eV in the temperature range 285 – 310K). This is connected with a significantly smaller value of *a* parameter in the case of low-temperature spinel as compared to the annealed one. Lower absolute values of electrical conductivity in the case of spinel obtained by a sol – gel method are related to lower effective carrier concentration (proportional to the $\mathbf{Mn^{3+} * Mn^{4+}}$ product) as well as scattering of the carriers on intergranular boundaries.

Manganese spinel annealed at 800°C has different electrical conductivity characteristics (Fig.9b). A jump of the conductivity by one order of magnitude is seen at 285K, i.e. at the phase transition temperature (Figs.4, 9c). Comparing the results of Rodriguez-Carvajal [4] who also detected a jump by only ½ order of magnitude, one can conclude that the conductivity decrease by one order of magnitude observed here indicates a high purity of the B series sample and a strictly stoichiometric composition of it.

Figs.8a and 9a present the temperature dependencies of thermoelectric power for A and B series, respectively. The stoichiometric manganese spinel (B series) shows an anomalous characteristics of thermoelectric power (Fig.9a). A sharp peak having magnitude of the order of 500μV/K is observed at the temperature at which the phase transition is detected (compare Figs.4, 9b, 9c). In the case of the nanostructured spinel produced by the sol – gel method (A series) a flat line characteristics is obtained, typical of polaron conduction mechanism (Fig.8a).

4.2. Series C

The phase transition commencing at 280K in the C series sample (figs.5-7) is also visible in conductivity, thermoelectric power and DSC measurements. In figs. 10a,b,c a small peak in thermoelectric power, an obvious change in electrical conductivity and thermal effect can be noticed as associated with phase transition. The observed temperature hysteresis in thermal and conductivity effects can be attributed to different cooling/heating ratios (10 deg/min and 0.3 deg/min rate for DSC and conductivity respectively). For the slowest temperature change as in XRD measurements (0.03 deg/min) no shift was observed (fig.6). However for the same temperature scan ratio for the B series sample a clear hysteresis was observed, indicating a modification of the phase transition nature for the C series material towards a second order type transition.
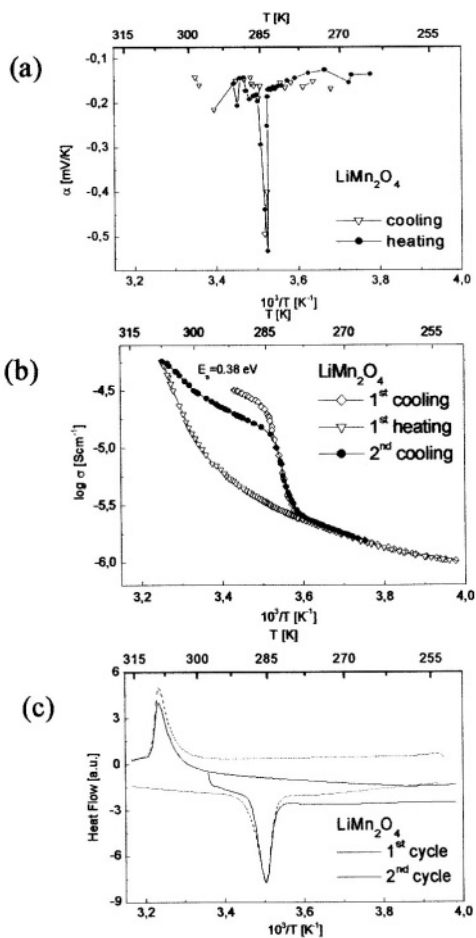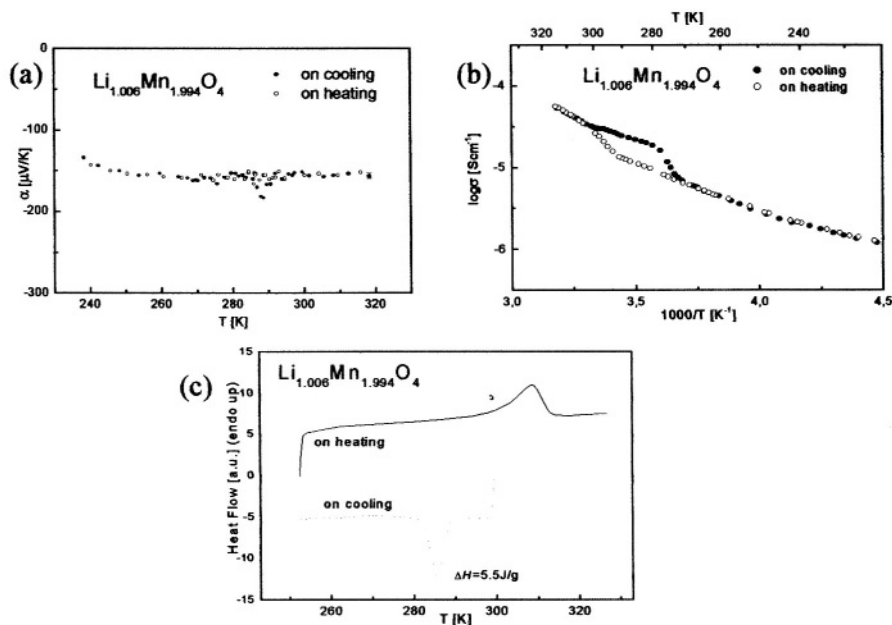
Figure 10. Electrical and thermal properties of $Li_{1.006}Mn_{1.994}O_4$ (C series) as a function of temperature: a) thermoelectric power, b) electrical conductivity, c) DSC

5. EVOLUTION OF THE PHASE TRANSITION IN MANGANESE SPINEL UPON DELITHIATION

The presented results show that in manganese spinel at room temperature conditions for charge transport are rather poor. Its electrical conductivity at 300K (i.e. under the conditions of battery use) is very low, of the order 10^{-4} Scm^{-1}. Under such circumstances the deintercalation/intercalation process should be extremely difficult. Nevertheless it proceeds with a good efficiency. Therefore a question arises: what is the real electron transport mechanism in functioning spinel cathode and is the phase transition still present in a deintercalated cathode material?

Commonly it is known that the phase transition occurs for the critical 50% concentration on Jahn-Teller ions Mn^{3+}. Therefore it should not be visible in deintercalated spinel in which the Mn^{3+} concentration falls. In fig. 11 the dependence of phase transition temperature range on lithium content was shown. For comparison also the results obtained for the strictly stoichiometric, annealed $Li_1Mn_2O_4$ sample (series B) were also presented. From fig. 11 follows that electrochemical deintercalation of $Li_{1.006}Mn_{1.994}O_4$

Cubic phase mass fraction [%]

- ◆ x_u=0.5
- ▼ x_u=0.8
- ● x_u=0.96

- ○ $Li_{1.006}Mn_{1.994}O_4$
- □ $Li_1Mn_2O_4$

Temperature [K]

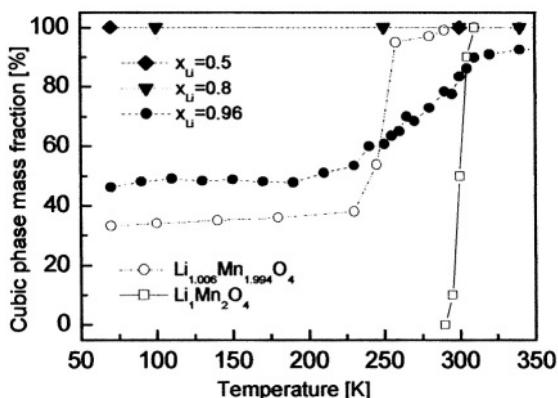*Figure 11.* The cubic phase mass fraction versus temperature. Dependence of the phase transition temperature on the lithium content in $Li_xMn_2O_4$.

series C spinel down to x_{Li}=0.96 shifts the temperature of the beginning of the phase transition to 300K, but it becomes much wider on temperature and leads only to a 50% phase change even down to T=70K. For higher deintercalation degree x_{Li} = 0.8 - 0.5 rather a disordered structure is obtained with various lithium occupancy of the 8a structural sites and in the XRD a line broadening is observed in the whole temperature range (fig. 11). A thermal effect indicating a "glass–like" behaviour (i.e. appearing of local orders) on DSC curves was registered on cooling (fig 14c). Also EPR spectra for those samples are broadened what can be attributed to a local field distributions arising from a disordered structure.

6. TRANSPORT AND THERMAL PROPERTIES OF DELITHIATED MATERIALS

6.1. Series C – electrochemically deintercalated

In figs. 12-15 temperature characteristic of the electrical conductivity and thermoelectric power for the compositions x_{Li}=0.98; 0.94; 0.75 and 0.40 (C series) are shown together with DSC measurements. One can see measured sharp maxima with values as high as 600 – 10 000 µV/K in Seebeck coefficient, stepwise changes in the electrical conductivity and corresponding thermal effects on DSC curves. For x_{Li}=0.98 and 0.94 compositions these anomalies can be associated with the orthorhombic distortion of cubic spinel lattice taking place at around room temperature. The temperature positions of these irregularities do not change with subsequent cycles of heating and cooling. For x_{Li}=0.75; 0.4 compositions the DSC and electrical conductivity results differ (figs. 14, 15). For the $Li_{0.75}Mn_2O_4$ sample on the DSC curve for heating subsequent processes of

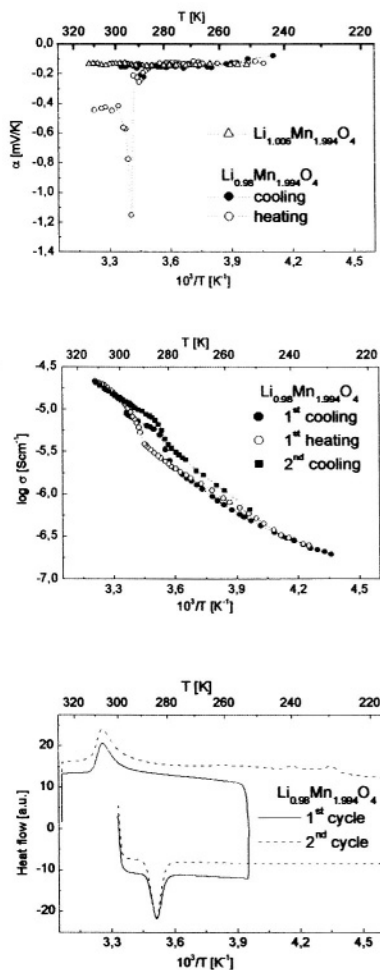Figure 12. Electrical and thermal properties of $Li_{0.98}Mn_2O_4$ (C series) as a function of temperature: a) thermoelectric power, b) electrical conductivity, c) DSC
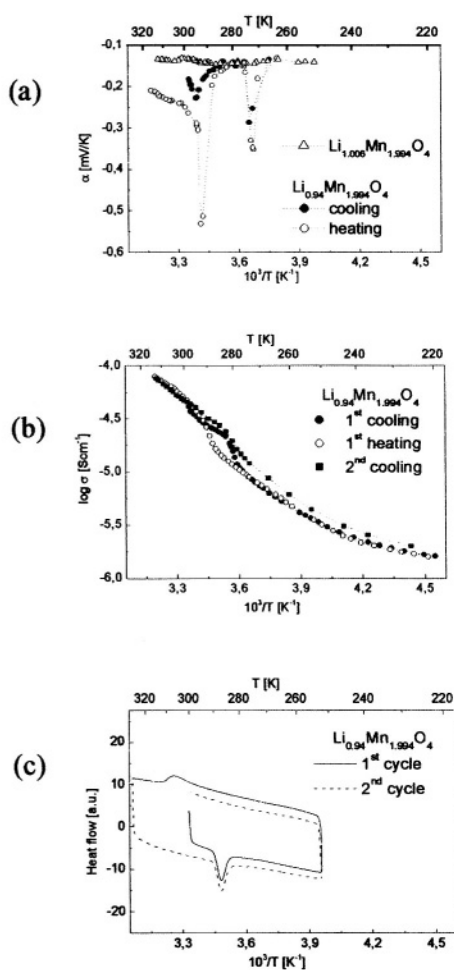
Figure 13. Electrical and thermal properties of $Li_{0.94}Mn_2O_4$ (C series) as a function of temperature: a) thermoelectric power, b) electrical conductivity, c) DSC

"freezing" (exothermic) and "melting" (endothermic) are observed while for $x_{Li}= 0.4$ there is no sharp anomaly (figs 14c and 15c respectively). For both these compositions only a slight change in conductivity is observed (figs. 14b and 15b). In XRD patterns of these samples lines are generally broad in the whole temperature range indicating a presence of a defected structure and no suppositions can be made on appearing of the distorted phase.
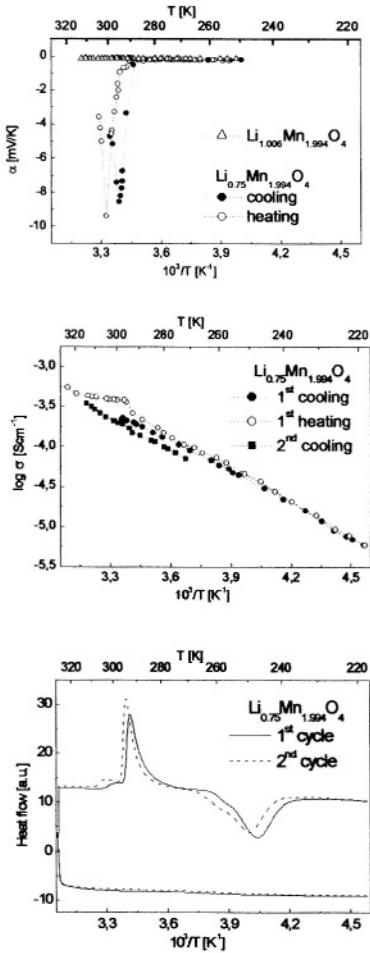
Figure 14. Electrical and thermal properties of $Li_{0.75}Mn_2O_4$ (C series) as a function of temperature: a) thermoelectric power, b) electrical conductivity, c) DSC
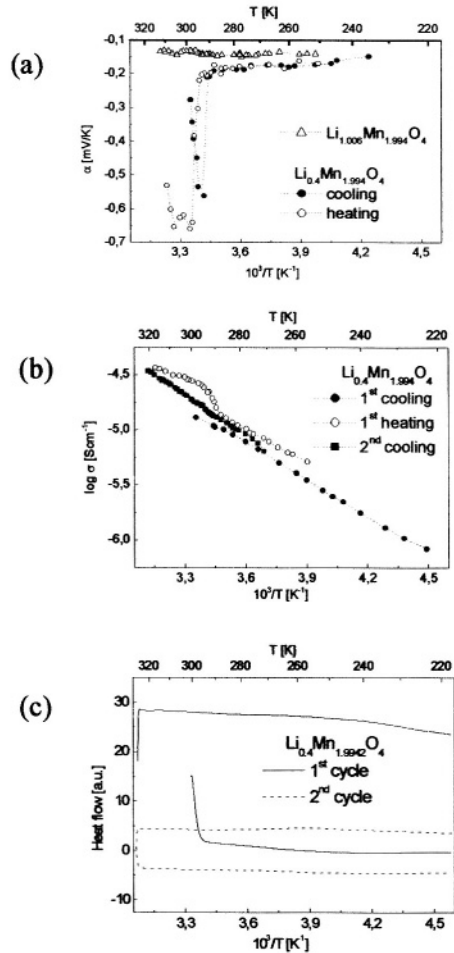
Figure 15. Electrical and thermal properties of $Li_{0.4}Mn_2O_4$ (C series) as a function of temperature: a) thermoelectric power, b) electrical conductivity, c) DSC

The Seebeck coefficient generally reflects the electron energy spectrum weighted by the conductivity. Measured peak values of α of the order of 10mV/K (as well as the peaked dependence on temperature) cannot be ascribed to any conventional electronic mechanism. Relatively narrow and high value peaks in thermoelectric power measurements can originate from two-phase system occurring in the measurement procedure when the whole sample is not at the same temperature. The applied temperature gradient at a certain initial temperature causes the beginning of the order-

disorder phase transition at one end. The instability in phonon spectrum (acoustic mode softening) of the arising phase can lead to the appearance of an additional charge carrier concentration gradient as a result of a process analogous to well-known phonon drag mechanism, leading to such high values of α in narrow temperature range.

The DSC measurements can be interpreted within a framework of order–disorder transition (therefore rather considered as second order type). Especially for $x_{Li} = 0.75$ on cooling curve a glass–like behaviour is clearly visible indicating freezing of a short-range order (fig.14c). When the sample was cooled down to 170K afterwards on heating DSC trace the subsequent "freezing" and "melting" processes were observed.

6.2. Series C – chemically deintercalated

Chemical deintercalation of manganese spinel of the C series leads to a material without the phase transition as it was not seen in XRD patterns and on DSC curves (fig.16c). Consequently no anomalies in electrical properties were observed for those samples (fig.16a,b).
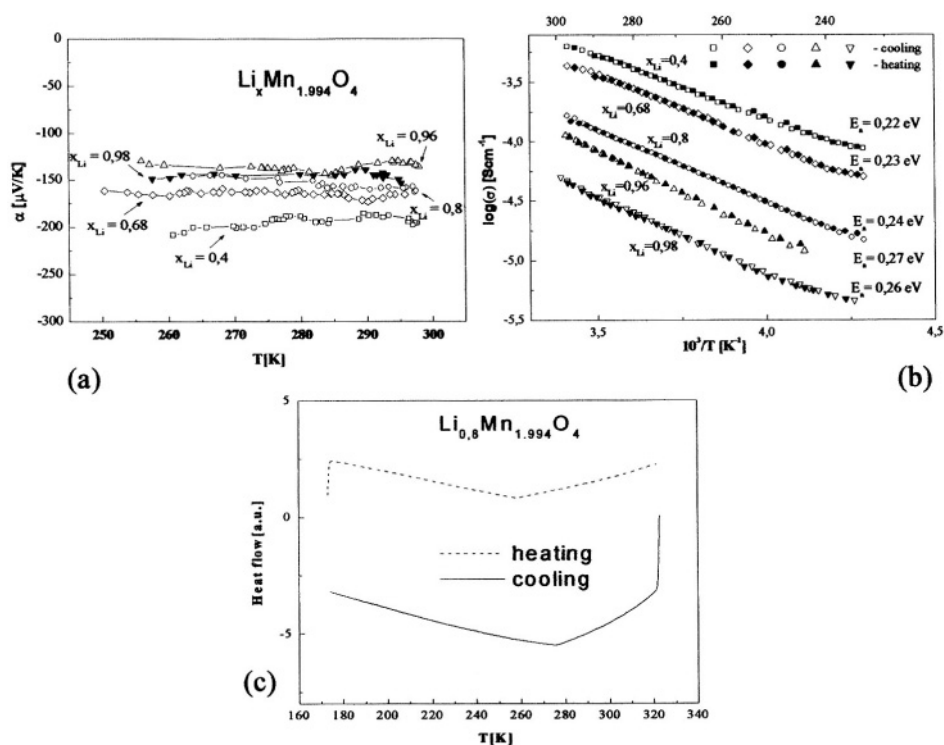

Figure 16. Thermoelectric power (a), electrical conductivity (b) and an exemplary DSC effect (c) for chemically deintercalated $Li_xMn_{1.994}O_4$ samples (C series).

A slight decrease of the activation energy of electrical conductivity with deintercalation degree was only observed as expected in this system with polaron mechanism of electrical conduction where the lattice parameter decreases from starting 8,239C down to 8.039C for the $x_{Li} = 0,4$ (fig. 17).
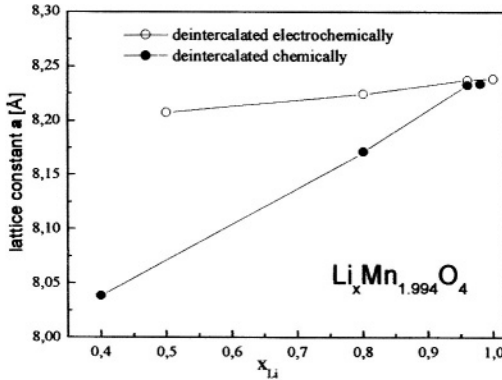

Figure 17. The lattice parameter *a* of chemically and electrochemically deintercalated spinel samples (C series) as a function of lithium content (300K).

The performed studies revealed significant differences in physical properties between chemically and electrochemically deintercalated samples of manganese spinel. That can be attributed to a different microscopic mechanisms of lithium extraction from the spinel structure: a selective one as in the electrochemical process and the relatively rapid, structure destroying when dissolved in the sulfuric acid. The first method leads to a material in which the manganese sublattice remains almost unchanged and that is the reason the material still exhibits the traces of the phase transition, while the samples obtained with the second process possess highly defected the Mn sublattice what disables the occurrence of the structure distortion and all the phenomena related with it.

6.3. Series B – electrochemically deintercalated

In figs. 18 and 19 are shown temperature dependencies of thermoelectric power, electrical conductivity and DSC for deintercalated samples from series B with compositions $Li_{0.98}Mn_2O_4$ and $Li_{0.96}Mn_2O_4$. As can be seen also these samples shows anomalous electrical and thermal properties characteristic of the phase transition, similarly as for stoichiometric samples from B series. Further deintercalation leads to crushed samples what made electrical measurements impossible.
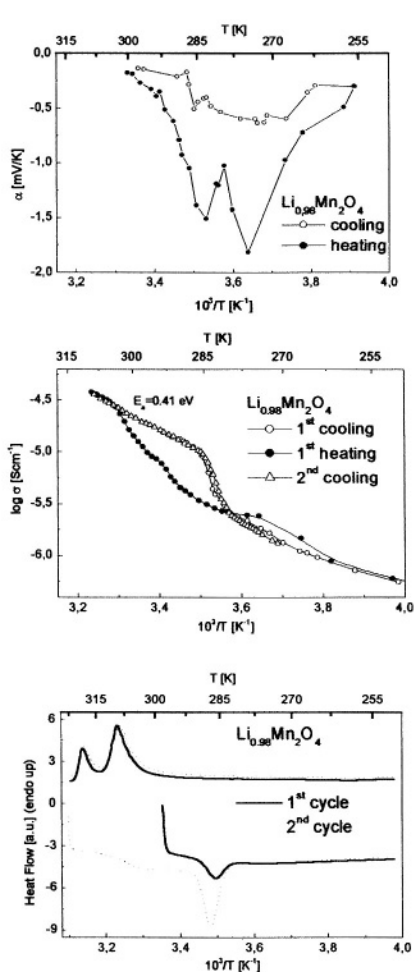
Figure 18. Electrical and thermal properties of $Li_{0.98}Mn_2O_4$ (B series) as a function of temperature: a) thermoelectric power, b) electrical conductivity, c) DSC
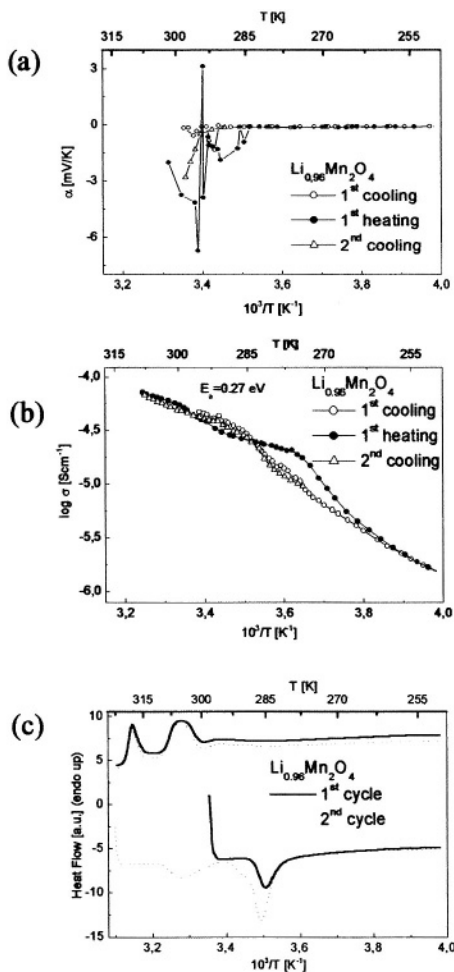
Figure 19. Electrical and thermal properties of $Li_{0.96}Mn_2O_4$ (B series) as a function of temperature: a) thermoelectric power, b) electrical conductivity, c) DSC

6.4. Series A– electrochemically deintercalated

For the nanostructured cathode material, with no additives characterized by low electrical conductivity (fig.8) and high Mn^{4+} content the electrochemical deintercalation route is pretty difficult. In figs. 20 and 21 are shown temperature dependencies of thermoelectric power electrical conductivity and DSC for deintercalated samples from series A with compositions $Li_{0.99}Mn_2O_4$ and $Li_{0.98}Mn_2O_4$. For the first composition no anomalous effects were observed in electrical and thermal properties as for
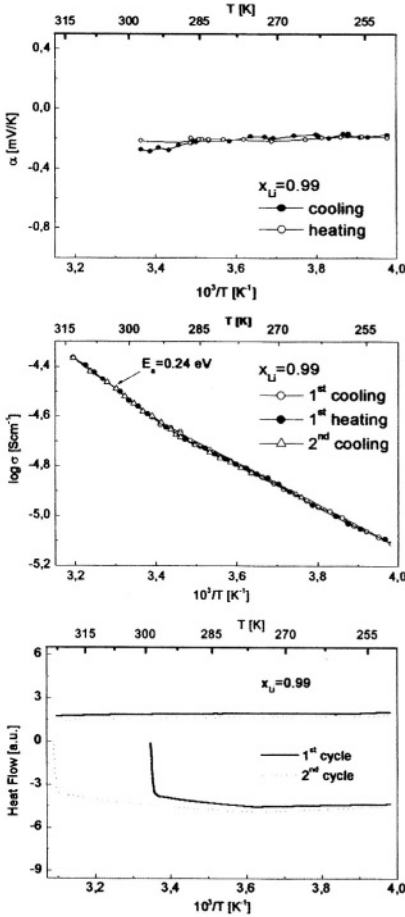
Figure 20. Electrical and thermal properties of $Li_{0.99}Mn_2O_4$ (A series) as a function of temperature: a) thermoelectric power, b) electrical conductivity, c) DSC
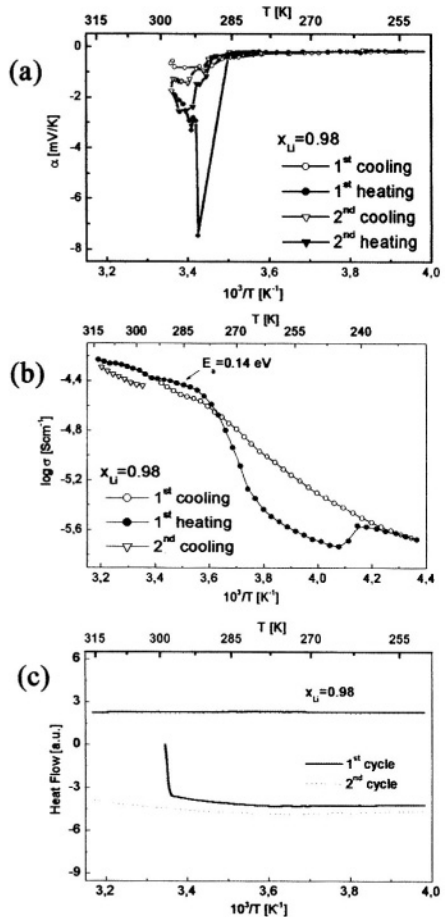
Figure 21. Electrical and thermal properties of $Li_{0.98}Mn_2O_4$ (A series) as a function of temperature: a) thermoelectric power, b) electrical conductivity, c) DSC

the starting material (fig. 8). Further deintercalation degree (x=0.98) leads to irregularities in temperature dependencies of electrical conductivity and thermoelectric power (fig. 21).

6.5. Lithium chemical diffusion coefficient

In fig. 22 results of two independent measurements of the lithium chemical diffusion coefficient are shown as a function of deintercalation

degree of manganese spinel from the C series. This parameter is directly responsible for the speed of intercalation process. In general a quite good intercalation rate is obtained in wide composition range $0.96 \le x_{Li} \le 0.4$. These two different measurements of diffusion coefficient yield values differing of the order of magnitude, anyway from both it is clear that the diffusion coefficient is evidently lower for the starting $Li_1Mn_2O_4$ sample. The high value of $10^{-7}cm^2/s$ is obtained for $x_{Li} \sim 0.75$ composition for which a considerable structure disorder are observed (as assumed from XRD), glass-like behaviour on DSC curve, greatest EPR signal broadening, the lowest (0.l8eV) activation energy in conductivity and the largest peak in thermoelectric power (up to 10mV/K) (fig. 14). It follows from above the disordered structure does not limit the intercalation process. Moreover it seems to be propitious to a conductivity mechanism that seems to take place in working spinel cathode, differing from that present in equilibrium state material [13].
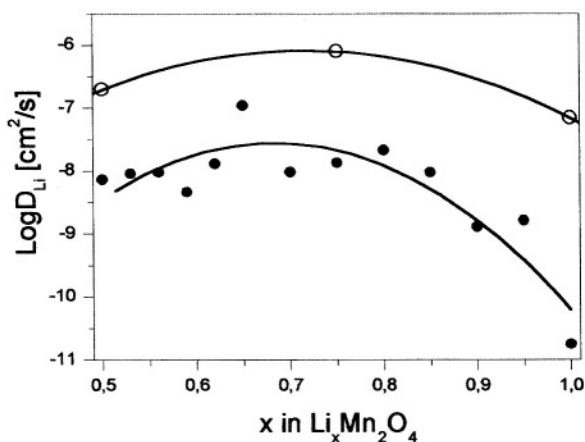
Figure 22. Lithium chemical diffusion coefficient for $Li_xMn_2O_4$ versus composition; o– data taken from [7]

It was noticed a huge difference of the resistivity of working spinel cathode as estimated from the loading circuit and that of the same material picked up from the cell and submitted to standard four probe dc conductivity method. The measured values differ by two orders of magnitude – the electrical conductivity in working cathode is much higher. Similar results can be obtained when Nernst-Einstein relation was used for estimating electrical conductivity of operating spinel cathode basing on determined lithium diffusion coefficient.

7. SUMMARY

The phase transition and related effects can be described in terms of localised polaron condensation being an appearance of a short and a long distance orders of "molecular polarons". A dynamical Jahn-Teller active cluster composed of four *16d* manganese positions as well as four neighbouring oxygens plays role of a self- trapped small polaron, interpreted as "molecular polaron".

Below the "phase transition temperature" the interaction between molecular polarons becomes dominant resulting in observed long distance charge ordering accompanied by small lattice distortions. Within the cluster charge density fluctuations related with lattice distortion are present. This is a vibronic state of molecular polaron in which the motion of the electron and atomic displacements are dynamically coupled.

For strictly stoichiometric sample with good, low in defects initial structure (series B) the ordering process can occur in a narrow temperature range, as was shown. In this case the phase transition is of the first order while for the C series **δ-spinels** it looks like a second order transition with no temperature hysteresis.

In Mn sublattice every *16d* site belongs to two tetrahedrons so the charge at the corners should be divided equally between them. The Coulomb energy between tetrahedrons is lowest when the charge of the each is the same $+7e$ (it means two pairs of $\mathbf{Mn^{3+}}$ and $\mathbf{Mn^{4+}}$ occupy the four corners – then a Coulomb energy within the tetrahedron is also a minimum too). A condition that the charge of the tetrahedron is constant all over the crystal is called Anderson's condition and is a basis for electronic structure of spinel type oxides. It is worth noting there is no charge transport in the crystal if all the tetrahedrons fulfil Anderson's condition. If $\mathbf{Mn^{3+}}$ - $\mathbf{Mn^{4+}}$ pair belongs to the same tetrahedron an electron jump does not change the total charge of it. A finite amount of energy is necessary to violate Anderson's condition and thus to make an electron move from one atom to the other.

Clearly different situation is created when $\mathbf{Li^{+}}$ ion leaves the *8a* position in working cathode. Lithium cation leaves an electron, locally violates the Anderson's condition and the left charge can easily flow within manganese sublattice of a grain as a sequence of $\mathbf{Mn^{3+}}$ - $\mathbf{Mn^{4+}}$ electron jumps. The motion of electrons is mainly governed by the short range order and not by the long range order of Mn ions.

The analysis of electrical conductivity and thermoelectric power characteristics of deintercalated spinel in the vicinity of room temperature (i.e. working temperature of the battery) together with XRD, DSC and

lithium chemical diffusion data, enables to conclude that good operation of the $Li^+/Li_xMn_2O_4$ cathode may be related to the proposed alternative charge transport mechanism involved in working manganese spinel cathode. This mechanism ensures easier electron charge transport and being present in a wide range of compositions x_{Li} ensures a high efficiency of the deintercalation process.

The performed studies indicates that the low temperature, sol-gel preparation method leads to a cathode material with low electrochemical activity in the 4V region due to high content of Mn^{4+} and low electrical conductivity. Annealing at 800°C of the material leads to the strictly stoichiometric $Li_1Mn_2O_4$ manganese spinel with better transport properties and electrochemical activity.

ACKNOWLEDGMENT

REFERENCES

1. M.M. Thackeray, M.F. Mansuetto, D.W. Dees and D.R. Vissers, *Mat. Res. Bull,* 31 No. 2 (1995) 132
2. Yuan Gao and J.R. Dahn, *J. Electrochem. Soc.,* 143 No. 1 (1996)100
3. E.M. Kelder, M.J.G. Jak, J. Schoonman, M.T. Hardgrave, S.Y. de-Andersen, *Journal of Power Sources,* 68 (1997)590
4. J. Rodriguez-Carvajal, G. Rousse, C. Masquelier, M. Hervieu, *Phys. Rev. Letters* 81(1998)4660
5. G. Rousse, C. Masquelier, J. Rodriguez-Carvajal and M. Hervieu, *Electrochem. and Solid-State Lett.,* 2 (1999)6
6. M.R. Palacin, Y. Chabre, L. Dupont, M. Hervieu, P. Strobel, G. Rousse, C. Masquelier, M. Anne, G.G. Amatucci and J.M. Tarascon, *J. Electrochem. Soc.,* 147 (2000) 845
7. L. Chen, X. Huang, E. Kelder, J. Schoonman, *Solid State Ionics,* 76(1995)91
8. R. Dziembaj, *Solid State Ionics* (2002) in press
9. J.C. Hunter, *J. Solid State Chem.* 39(1981)42
10. L.He, S. Tang, Z. Chen, H. Du, *Solar Energy Materials Solar Cells* 62(2000)117
11. L.He, S. Tang, Z. Chen, H. Du, *Solar Energy Materials Solar Cells* 62(2000)125
12. H. Hayakawa, T. Takada, H. Enoki, E. Akiba, *J. Materials Science Letters,* 17(1998)811
13. J. Marzec, **K.Świerczek, J.Przewoźnik,** J.Molenda, D.R. Simon, E.M. Kelder, J.Schoonman, *Solid State Ionics* 146(2002)225

METAL-POLYMER NANOCOMPOSITES: FORMATION AND PROPERTIES NEAR THE PERCOLATION THRESHOLD

S.A.Zavyalov[1], A.A.Timofeev[2], A.N.Pivkina[3], and J.Schoonman[4]

[1]*Karpov Institute of Physical Chemistry, Vorontsovo Pole, 10, 103064 Moscow, Russia;*
[2]*Moscow State Engineering-Physical Institute, Kashirskoe Shosse, 31, 115409 Moscow, Russia;*
[3]*Semenov Institute of Physical Chemistry, Russian Academy of Science, Kosygin st. 4 119991, Moscow, Russia;*
[4]*Delft University of Technology, Delft Institute for Sustainable Energy, P.O. Box 5045, 2600 GA Delft, The Netherlands.*

ABSTRACT

Nanostructured metal (Pd, Sn, Cu, Al)-polymer (poly-para-xylylene) and metal-oxide-polymer composites reveal synergism of properties of the initial components, which gives rise to specific electrical, mechanical, optical and chemical properties related to an ordered distribution of nanoparticles over the matrix volume. Various methods of preparing a metal-polymer nanocomposite exist and from the point of view of homogeneity, methods where polymerization and formation of the nanoparticles are performed simultaneously, are very promising. This chapter reports on the experimental set-up for the production of nanocomposites by vacuum co-condensation of the metal and monomer (paracyclophane) vapours. The morphology, optical, electrical properties and oxidation behavior of the deposited composites have been studied.

The influence of metal concentration on composition, structure, morphology, and particle size of Al/PPX nanocomposites has been studied utilizing transmission electron microscopy (TEM). After air exposure the inorganic particles were identified as aluminium or alumina, depending on metal concentration in vacuum. The size of nanoparticles within the polymeric matrix was measured in the range of 10 to 55nm. The temperature coefficient of resistance and the oxidation behaviour of the synthesized composites were measured.

The collective effects of charge transfer within ensembles of metal nanoparticles in the vicinity of the percolation threshold is proposed to be a reason of observed electro-physical and chemical properties of the synthesized nanocomposites.

INTRODUCTION

To date, nanostructured metal-polymer and metal oxide - polymer composites are the subject of increased attention of researchers in different areas of science and technology. Among the perspectives for using these materials are novel types of solar cells and chemical gas sensors. The electrical, mechanical, and optical properties of the nanocomposites are improved by dispersing a metallic phase in a polymeric matrix.

At a particular concentration of nanoparticles close to the percolation threshold the nanocomposite materials exhibit properties specific to the nanoparticles. These properties differ considerably from those for bulk materials and the composite acquires these during composite formation. As a result such materials reveal synergism of properties of the initial components. Using different polymers adds elements of self-organisation to the formation of the composite, for inorganic particles are located in cells of the polymer between grids and layers [1] which gives rise to specific properties of the composite related to an ordered distribution of nanoparticles over the matrix volume.

Experiments show that unique properties of some thin-film nanocomposites are due to cooperative effects amongst nanoparticles. The improved gas sensitivity and photosensitivity of TiO_2/SnO_2 nanocomposites were measured [1]. The capacity of this material was found to be 40F/g [3]. The maximum of the catalytic selectivity of Pd-containing nanocomposites in the isomerization reaction of 3,4-dichlorobutene-1 to 1,4-dichlorobutene-2 was observed at a Pd concentration close to the percolation threshold [2].

It has been reported that in the vicinity of the percolation threshold thin-film nanocomposites exhibit properties that differ from isolated nanoparticles and from the bulk material [7, 8]. This supports the cooperative, non-equilibrium effects of charge transfer between metal nanoparticles at threshold concentrations [6]. The charge transfer between nanoparticles can be connected with two types of conductivity, i.e. metal-like contact electrical conductivity and tunnel conductivity via a non-conducting polymer layer.

To confirm the realization of the collective effects in metal-polymer nanocomposites, aluminium/poly-para-xylylene nanocomposites have been synthesized via a vacuum co-deposition technique. The properties of the composites are studied by comparing the structure, morphology, electrical properties and the oxidation kinetics.

EXPERIMENTAL PROCEDURE

Figure 1 shows the setup for depositing composite films by co-condensation of metal vapour and an active precursor, which then polymerizes. The set-up consists of four principle units: the zone of treating the polymer precursor, the zone of evaporating metals, the reactor and the deposition zone.
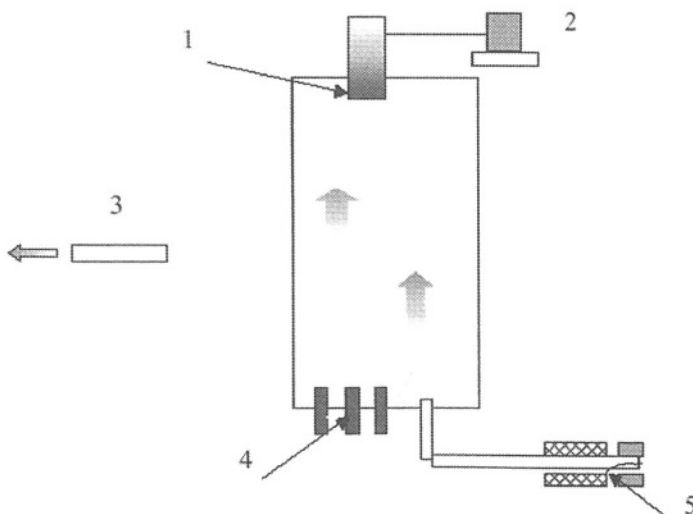

Figure 1. Experimental set-up: 1) cooled substrate; 2) computer data logging; 3) vacuum pump; 4) metal precursor; 5) paracyclophane powder.

The polymeric matrix is synthesised as follows: in the evaporation zone the precursor (paracyclophane [4]) is heated up to 380 - 420K. The paracyclophane pyrolyses at 930K giving rise to biradicals of paraxylylene. These molecules then deposit without polymerisation onto a cooled (down to 77K) substrate. The flux of metal atoms evaporated from a bulk sample condenses onto the substrate together with the monomer. The condensate consists of nanoparticles of the metal and the monomer. Upon heating the substrate to ambient temperature the monomer polymerizes to poly-para-xylylene. The structure thus obtained is a porous matrix with dispersed nanoparticles in it. Below the properties of nanocomposites containing metal or metal-oxide nanoparticles in the polymeric matrix are presented. Manipulating the synthesis conditions, i.e., the distance between the vapour source and the substrate, the tilt angle of the beam, and the deposition time, allowed for optimising the deposition regime. Measuring the electrical resistance of the condensate and composite permitted the control of the film formation.

Three types of substrates have been used in the experiments reported here (Fig. 2), i.e., (1) a polished quartz substrate of size 5x5mm

and 1 mm thick with Pt-contacts for electrical measurements; (2) a polished NaCl single-crystalline substrate of the same size and thickness for TEM analysis; (3) a polished quartz substrate of size 10x20mm and 2mm thick for optical and AFM investigations. To obtain identical samples both types of substrates were fixed close to each other onto a cooled surface of the sample holder (4).
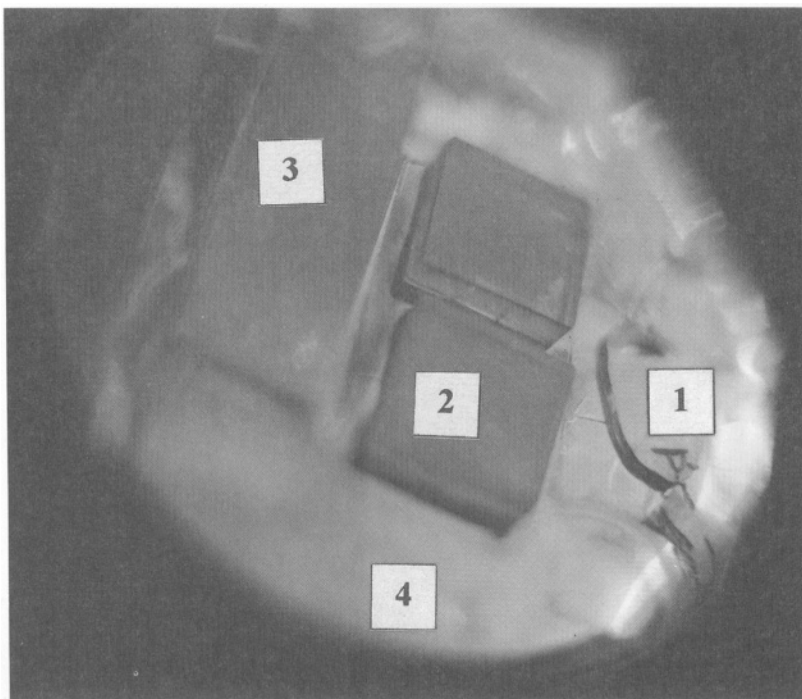

Figure 2. Scheme of the samples after synthesis experiments:
1 - polished quartz substrate with Pt-contacts,
2 - polished NaCl single-crystalline substrate,
3 - polished quartz substrate for optical and AFM investigations,
4 – sample holder.

Oxidation kinetics during the air exposure after vacuum synthesis was measured by means of data acquisition board L-1250, connected to a PC. The temperature coefficient of the electrical resistance in vacuum (the slope of $R_v(T)/R_v(293K)$ *versus* temperature dependency) was measured after re-cooling of the synthesized composite from 293K to 77K.

The morphology of nanocomposites was studied with transmission electron microscopy (JEM-2000 EX-II) at 200kV. Samples for TEM were prepared by standard procedures including separation of the nanocomposite layer from the NaCl substrate in water and the film deposition onto a Cu grid for further investigations. The metal content in the composites was calculated by atomic absorption analysis using a *Perkin-Elmer 503* spectrometer. The surface morphology and composite

structure were studied by atomic force microscopy (*SOLVER-P47)* with an etched silicon cantilever having a tip radius of 10nm and 20° apex angle. Data were taken in ambient air with a contact force of 10^{-10}N. The optical spectra of the films were recorded with a spectrophotometer *Shimadzu UV-3100* in the wavelength range 200 - 2000nm.

RESULTS

Structure and morphology

Freshly synthesised tin-containing samples are normally of grey colour with a metallic lustre. On contacting with the ambient air during 2 minutes the samples became transparent for composites with a Sn concentration below the percolation threshold of 10Vol.%, but the samples with a tin content beyond 10Vol.% do not change their colour during several months (Fig. 3).
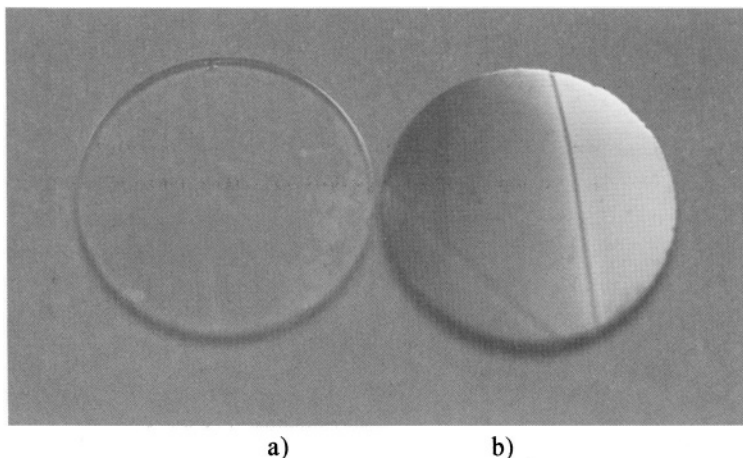

a)   b)

Figure 3. Sn-containing samples of nanocomposites after air exposure:
a)   8Vol.% of Sn; b) 12Vol.% of Sn.

The surface morphology of Sn/PPX nanocomposites with different content of the filler from 8Vol.% to 16Vol.% (Table 1) was investigated.

AFM analysis of model Pd-based composites (Fig. 4) shows that the surface of the nanocomposites is sufficiently uniform. The spherical polymeric globules of a size up to 200nm are well distinguishable. The polymeric spherulites are uniform in size and shape and form a porous rather than a continuous structure. The pore size does not exceed 100nm. In addition, at the spherulite surfaces imperfections are distinguishable deviating their shape from sphere. The phase-contrast regime of the AFM (Fig. 5a) allows for identifying these surface imperfections as the particles of the inorganic phase, establishing location, and evaluating their sizes. According to Fig. 5b, where the cross section of the composition profile is presented, the inorganic particle size is 7 - 10nm.

Table 1. Properties of composites

Sample #	Sn Vol.%	Resistivity in Vacuum	Morphology
1	8	6 MOhm	Isolated particles, localization on the polymer spherulite surface
2	10	880 Ohm	Formation and growth of nanoparticle chains
3	12	45 Ohm	
4	16	13 Ohm	Chains exhibiting percolation

Analysis of the composites reveals that for the metal content in as-prepared samples below or at the percolation threshold (samples 1, 2, Table 1) the inorganic particles are isolated and the interparticle distance varies from 5 to 20nm (Figs. 6, 7). Slightly above the percolation threshold (sample 3) the particles form continuous filaments of varying diameter, but the maximal diameter never exceeds that of the single metal nanoparticle (Fig. 8). Beyond the percolation threshold (sample 4), the nanoparticles form aggregates located on the boundaries between the polymer spherulites (Fig. 9). Hence, the metal-polymer and metal-oxide-polymer nanocomposites are the systems wherein the inorganic particles form structured subsystems with respect to the polymeric matrix. In increasing the metal content the nanoparticles localise along the borders of polymeric spherulites accompanied with the formation of conducting chain structures. Further increase in the metal content gives rise to aggregation of nanoparticles and their coalescence.
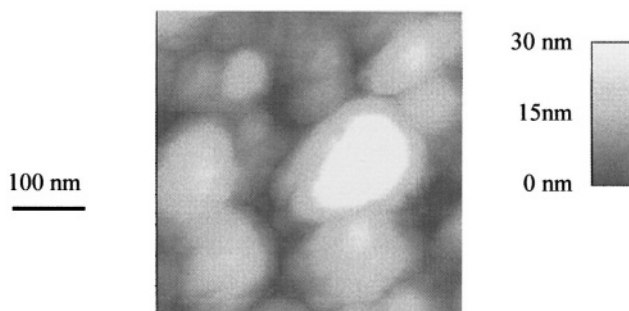
Figure 4. AFM image of a Pd/Polymer composite: 10Vol.%Pd. Scan size 500x500nm.

a) b)
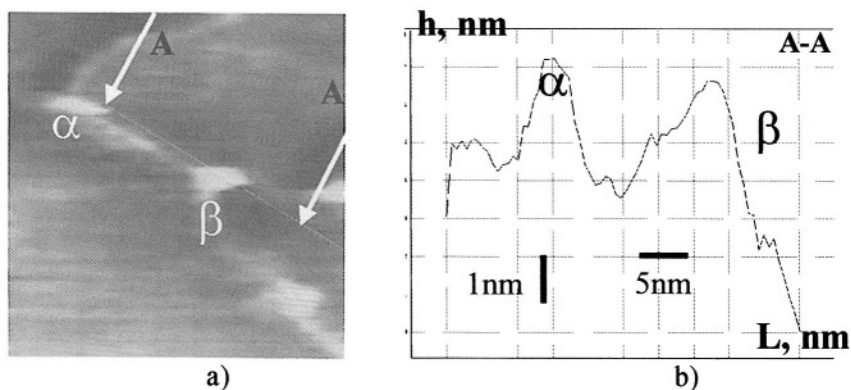
Figure 5 . a) Phase-contrast AFM image of the composite.
Dark regions are polymer spherulites and light spots are Pd nano-particles situated on the boundary between polymer spherulites.
b) Cross-section A-A. Profile maximums correspond to Pd particles embedded into the boundary surface between the polymer spherulites.

a) b)

Figure 6. AFM image of a Sn-Polymer composite (Sample 1, 8Vol.%Sn). Scan size 140*140nm: a) surface morphology; b) the same area in phase contrast with a separated particle.

a) b)
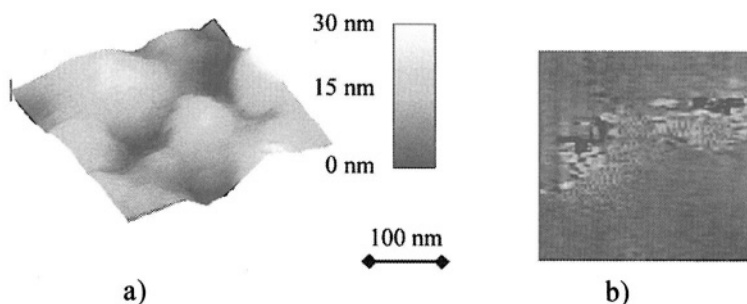
Figure 7. AFM image of a Sn-Polymer composite (Sample 2, 10Vol.%Sn): a) surface morphology, scan size 300*300nm; b) cross-section in phase contrast. Nanoparticles form chains.
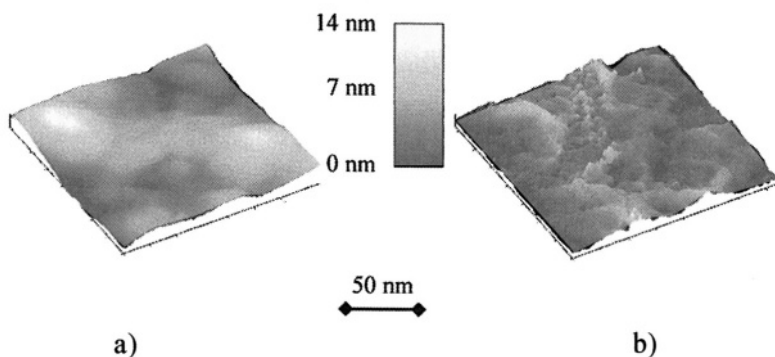
Figure 8. AFM image of a Sn-Polymer composite (Sample 3, 12Vol.%Sn,). Scan size 140*140nm:
a) surface morphology; b) the same area in phase contrast. Nanoparticles aggregate connecting into continuous chains.
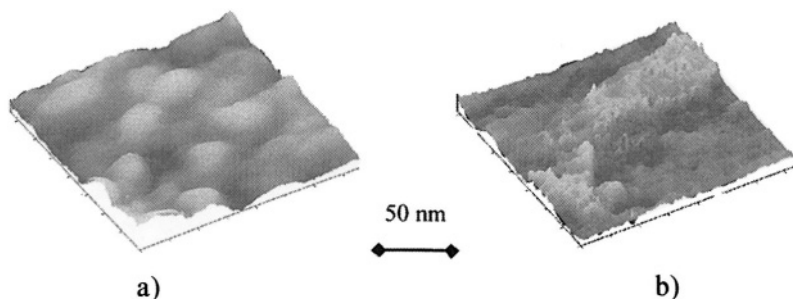
Figure 9. AFM image of a Sn-Polymer composite (Sample 4, 16Vol.%Sn). Scan size 140*140nm:
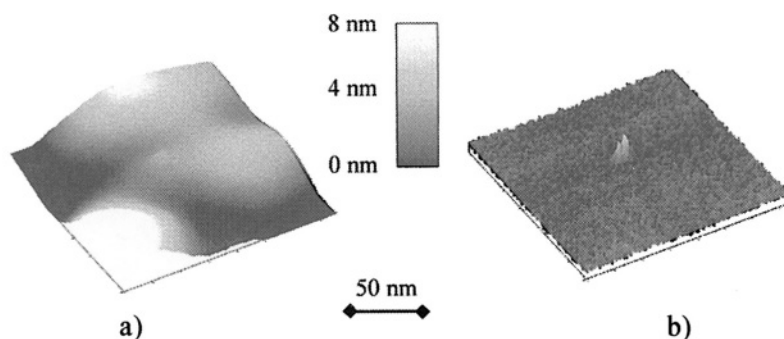a) surface morphology; b) the same area in phase contrast regime. Spreading of connected nanoparticle chains.

Freshly synthesized Al-containing samples (Table 2) exhibit normally a dark colour with a metallic luster in vacuum. On contacting the composite with the ambient air sample 7 became transparent, whereas samples 5 and 6 do not change their colour.

Table 2. Parameters of synthesized $Al(Al_2O_3)/PPX$ nanocomposites

Sample number	Crystal phase	d_m (Al), nm	d_m (Al_2O_3), nm
5	Al	10	-
6	Al + Al_2O_3	6	28
7	Al_2O_3	-	55

Electron diffraction patterns show a high degree of crystallinity of the investigated samples. Figures 10-12 show the TEM micrographs of the synthesized Al-containing nanocomposites and the particle size distribution as observed by TEM. It was found that all the investigated samples comprise rather homogeneously dispersed nanoparticles within poly-para-xylylene globules.
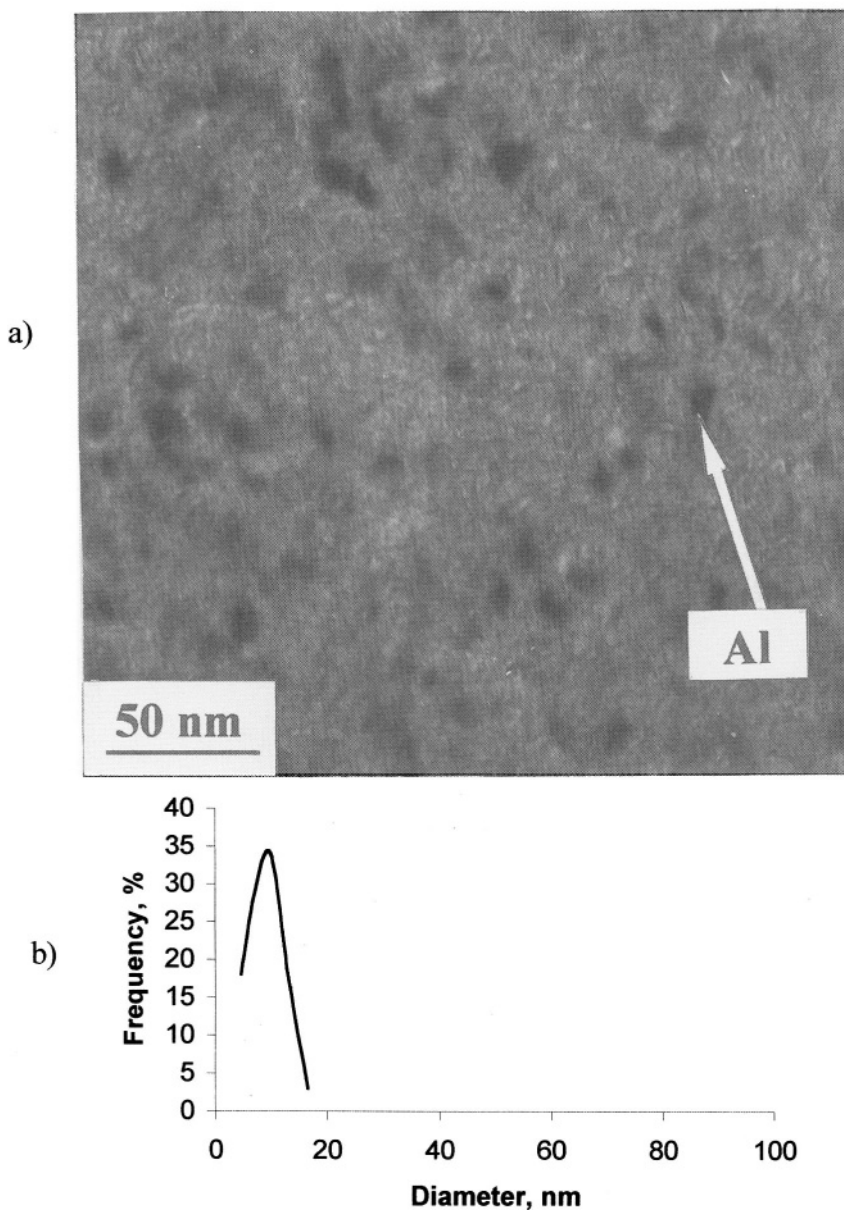
Figure 10. Morphology of Al/Polymer nanocomposite (Sample 5, Table 2):
a)   TEM (light field) of Al nanoparticles within the Al/PPX nanocomposite;
b) Al particle size distribution.

a)

b)

Figure 11. Morphology of Al(Al$_2$O$_3$)/Polymer nanocomposite (Sample 6, Table 2):
a)TEM (light field) of Al and Al$_2$O$_3$ nanoparticles;
b) Al and Al$_2$O$_3$ particle size distribution.

Table 2 shows the crystal phase and the average particle size of Al and Al_2O_3 comprising synthesized nanocomposites. The resulting micrographs for sample 5 (Fig. 10) indicate that a composite containing aluminium nanoparticles with an average size of 10nm and no other crystal phases have been formed. On the contrary sample 7 (Fig. 12) contains rhombohedral Al_2O_3 (corundum) with the crystal parameters a=4,7592Å and c=12,992Å. Sample 6 consists of aluminium and alumina nanoparticles embedded into the polymeric matrix (Fig. 11).
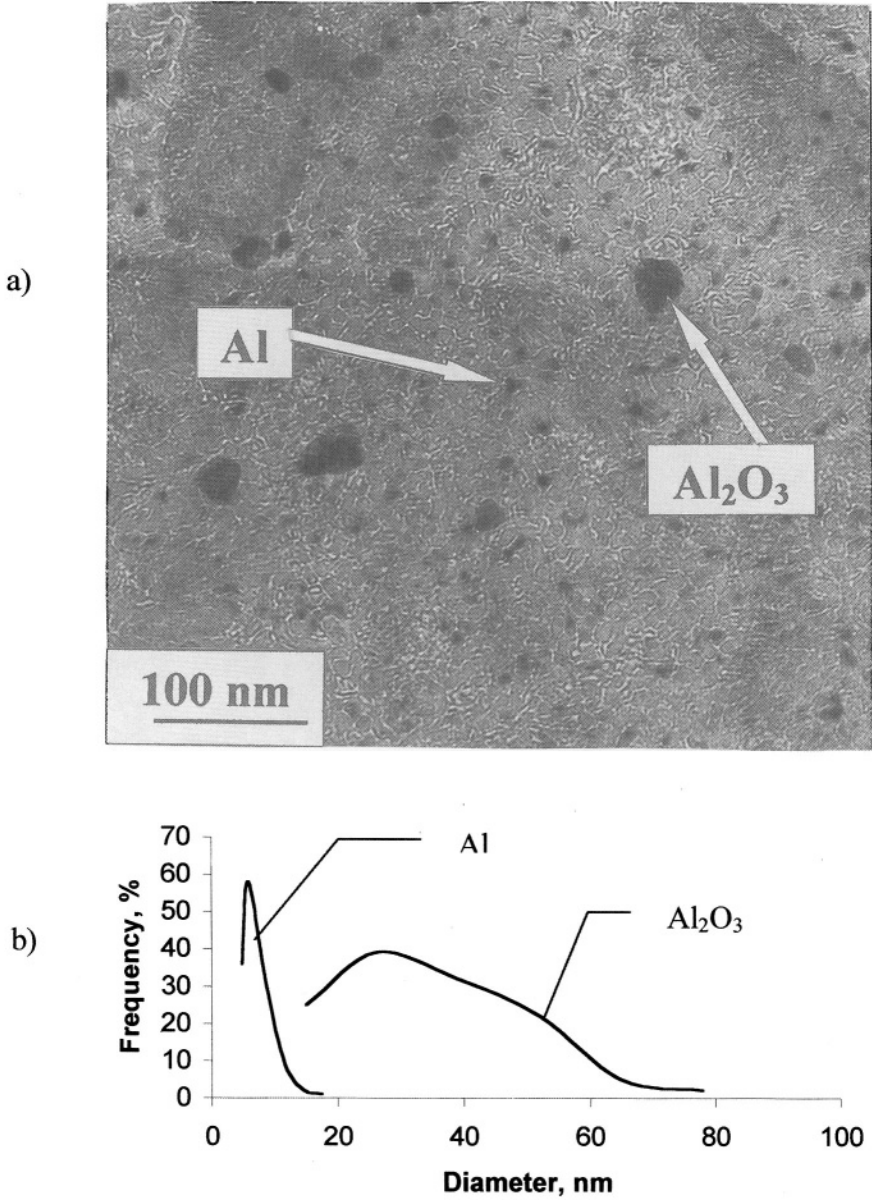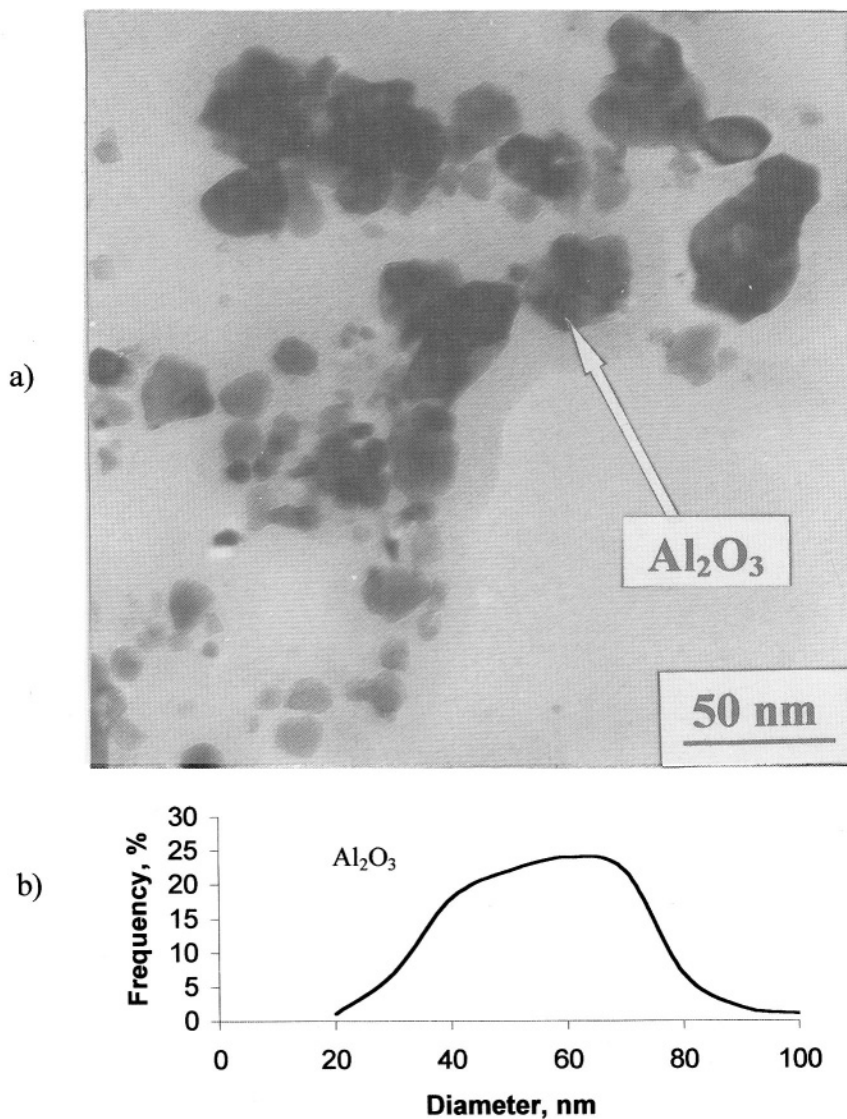

Figure 12. Morphology of Al_2O_3/Polymer nanocomposite (Sample 7, Table 2): a) TEM (light field) of Al_2O_3 nanoparticles; b) Al_2O_3 particle size distribution.

Electrical properties

Fig. 13 shows the temperature coefficient (the slope of R(T)/R(20°C) *versus* Temperature dependency) of the electrical resistance in vacuum of tin, copper and aluminium-containing as-prepared composites for metal contents from 4Vol.% to 12Vol.%. The composites with a metal content of 12Vol.% show a positive temperature-coefficient indicating a conductivity determined by a continuous network with metal-like contacts between the nanoparticles. In contrast, when the metal concentration is 8Vol.%, the temperature-coefficient becomes semiconductor-like. This indicates a loss of metal-like contacts between particles of the metal phase. This is to be expected from percolation behaviour of the composites on the metal filler content. The percolation threshold can be determined by the variation in the temperature dependence of the electrical resistance, which is for the present case 10Vol.% of metal.
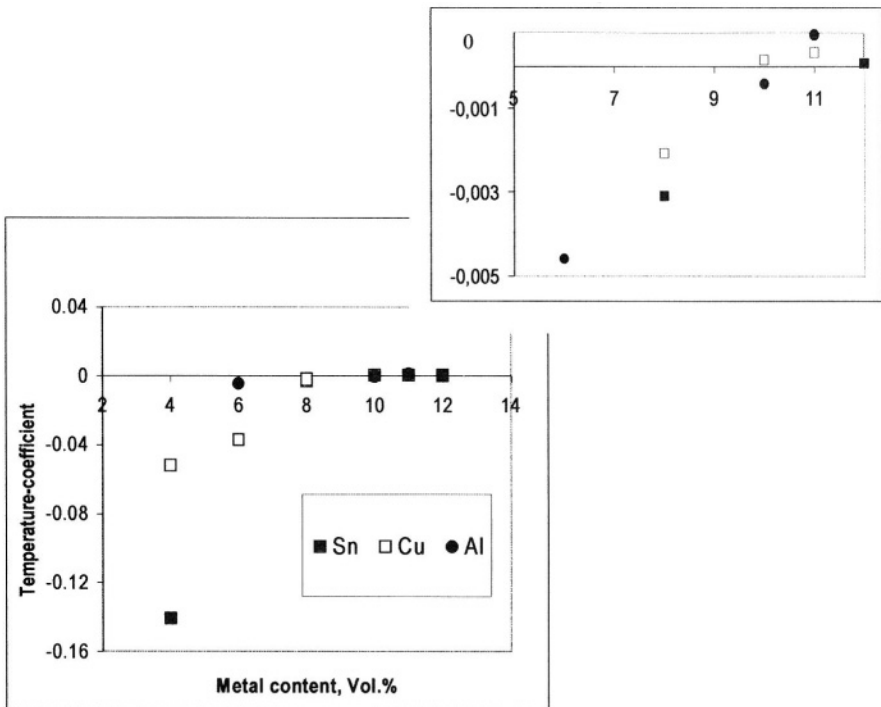
Figure 13. Dependency of the temperature-coefficient of the resistivity in vacuum on the metal content: ■ - Sn/Polymer nanocomposites, □ - Cu/Polymer nanocomposites, ● Al/Polymer nanocomposites

Optical spectra

The reference optical spectrum of the polymeric matrix measured in the absence of a filler (pure PPX, see Fig. 10) practically reproduces the literature data [5]. A strong absorption is observed at $\lambda<240nm$. For $240<\lambda<280nm$ a less intense band corresponding to absorption of PPX is observed. Low-intensity absorption is observed at $300<\lambda<350nm$ decreasing with wavelength.

The inorganic filler entirely changes the absorption spectrum that depends now on the filler concentration. The absorption peaks at 405, 530 and 760nm are observed for 8% metal particles in the polymer matrix (sample 1, Table 1). When the metal concentration reaches 9% the peaks move toward shorter wavelengths and the interpeak distances become smaller. This shift is different for different wavelengths. For the peak at 405nm the shift is 25nm, for the peak at 530nm it is 45nm, and for that centered at 760nm the shift is equal to 80nm. The broadest absorption peak is observed within the wavelength range 1200 to 1800nm. Absorption maxima are located at 1250nm (sample 1) and 1500nm (sample 2). In further increasing the filler content the total absorption increases in the spectral range of 300 to 1000nm. On surpassing the percolation threshold (samples 3, 4) the spectral peaks become less and less intense. At a filler concentration of 16% a mirror metallic film forms at the sample surface. The changes in composite structure on a nanometer scale are crucial for optical absorption. These changes reveal the collective resonance effects in nano-ensembles distributed in a polymeric matrix.
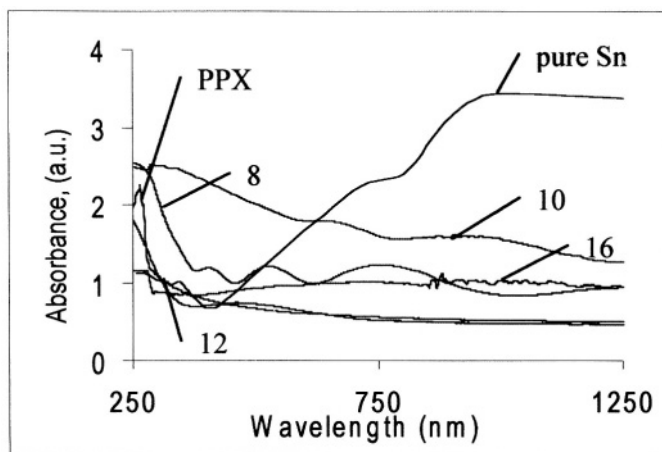
Figure 14. Optical absorption spectra of pure polymer (PPX), Sn-bulk metal (literature data); and samples of Sn-containing metal-polymer nanocomposites with different Sn contents. Numbers correspond to Sn content in Vol.% (Table 1).

Oxidation behaviour

Substantial differences in oxidation behaviour exist between the investigated samples. Figures 15-17 show the resistivity change of freshly synthesized samples 5-7 if exposed to air at 1atm. According to the above TEM results, nanoparticles in sample 5 are aluminium crystallites, which are clearly reflected in the small increase of the electrical resistance (Fig. 15) during air exposure (ΔR_{max}=5.5%). However, the electrical resistivity of sample 7 increases dramatically during several seconds (Fig. 17). In fact, nanoparticles in this sample are pure alumina dielectric material. The high resistivity of the nanocomposite is caused by the high resistivity of the alumina particles and large distance between them. TEM micrographs of sample 6 revealed alumina and aluminium crystallites within the polymeric matrix. The dramatic increase in resistivity is followed by sharp decrease after 84s of air exposure (Fig. 16), which could be attributed to new current path formation to by-pass areas with the high alumina content.

Figure 15 . Kinetics of oxidation during air exposure at room temperature of sample 5.

Figure 16. Kinetics of oxidation during air exposure at room temperature of sample 6.

Figure 17. Kinetics of oxidation during air exposure at room temperature of sample 7.

Discussion

As shown earlier [7, 8], synthesized metal/polymer nanocomposites have an open porosity, and all the nanoparticles are fully accessible to oxygen. However, the experimental data show that the

equivalent oxygen accessibility does not lead to oxidation for some composites.
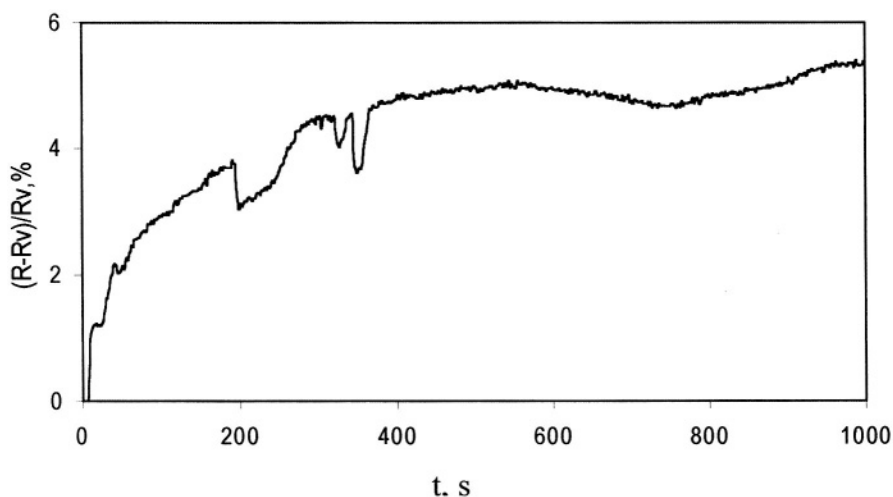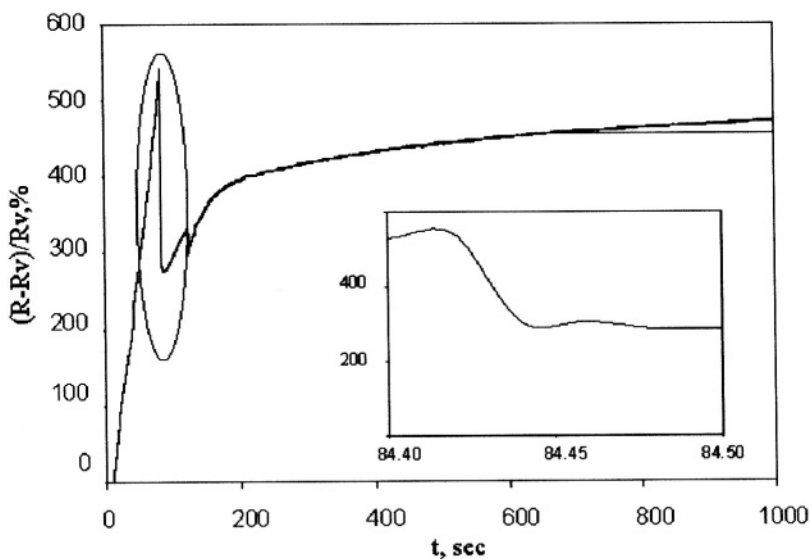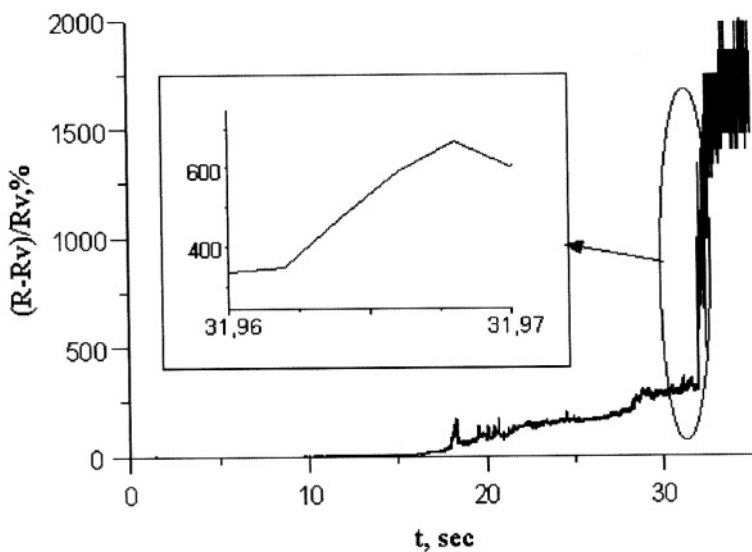
Metal nanoparticles of sample 5 do not form a continuous net of connecting particles; the average distance between nanoparticles is 50nm. The nanocomposite resistance is due to subsequently connected resistances of nanoparticles and polymer layers between them. Because the sign of the temperature coefficient of the resistivity for sample 5 corresponds to the bulk metal, the nanocomposite resistance is a function of particles resistance and polymer layer resistance could be neglected. Thus, the interparticle charging and cooperative effects occur within an ensemble of Al nanoparticles.

For sample 7 all the metal nanoparticles oxidize in air. The Al metal oxidation is a highly exothermic process, so the polymeric matrix needs to be heated. Considering the quite low glass temperature of poly-para-xylylene, i.e., 60°C [9], a high oxide nanoparticle mobility and aggregation is proposed. This fact is reflected in the relatively large particle size of alumina (55nm) within sample 7. The oxidizing process is extremely fast; the resistivity increase is about 600%.

Sample 6 contains nanoparticles of two types, i.e., in type I, particles are interconnected and lead to percolation, whereas nanoparticles of type II form isolated clusters. During oxidation the latter react and oxidize very fast, similar to sample 7. The average number of metal particles to form one alumina particle is estimated to be 100-500. Nanoparticles of type I do not oxidize in air because of the cooperative effects discussed above.

Thus, the observed experimental data show that cooperative effects define the chemical properties of metal/polymer nanocomposites.

SUMMARY

Samples of nanoporous composites of a metal and the polymer PPX have been synthesised in the form of thin films. AFM studies show the metal nanoparticles to have a size of 7 to 10nm. Within the composite the polymer forms more or less spherical globules with a maximum size of about 200nm. The interfacial regions between neighbouring polymeric spherulites contain nanoparticles of inorganic filler. Depending on the metal content in as-prepared samples, three different types of surface morphology are distinguished, i.e., isolated nanoparticles localized on the polymer spherulite surfaces, formation and growth of nanoparticle chains, and spreading of interconnected chains.

TEM analysis of a nanocomposite with Al content above the percolation threshold shows spherical pure metal nanoparticles with a mean diameter of about 10nm, while below the percolation threshold the composite contains agglomerates of rhombohedral Al_2O_3 (corundum) with a mean size of 55nm. A sample with a metal content just at the percolation threshold contains metal nanoparticles of 10nm and alumina aggregates of 28nm in diameter. The inorganic phase is homogeneously dispersed

within the polymeric matrix in all of investigated samples. It has been shown that the nanocomposite structure determines the oxidation behaviour of Al nanoparticles within the polymeric matrix under air exposure.

Measurements of electrical resistance as a function of temperature in vacuum reveal metal-like conductivity of samples above the percolation threshold, whereas samples below the threshold have semiconductor-like conductivity. The percolation threshold of this system is evaluated.

The optical absorption spectra for the sample beyond the percolation threshold differ from that of the sample with a nano-metal content below the threshold.

Results clearly reveal that cooperative effects arising in the metal/polymer nanocomposites in the vicinity of the percolation threshold determine the electro-physical and chemical properties.

ACKNOWLEDGEMENTS

LITERATURE REFERENCES

1. Galyamov B., Zavyalov S., Zavyalova L, Morozova O., Kupriyanov L., Roginskaya Yu. Russian J. Phys. Chem. 1995; 69:971.
2. Vorontsov P., Gerasimov G., Golubeva E., Grogoriev E., Zavyalov S., Zavyalova L., and Trakhtenberg L. Russian J. Phys. Chem. 1998; 72; 1912.
3. Tsirlina G. A., Roginskaya Yu. E., Postovalova G. G., Vasil'ev C. A. (in Russian). Electrochemistry 1999; 35:1380.
4. Nagaev E. L. (in Russian). Advances of Physical Science 1992; 162:49.
5. Takai Y., Calderwood J.H., Allen N.S. Makromol Chem Rapid Comm 1980; B1: 17-21.
6. Pomogailo A.D., Rosenberg A.S., Ufland U.E., *Metal Nanoparticles in Polymers* (in Russian). Moscow, Chemistry, 2000.
7. Zavyalov S., Yablokov M., Pivkina A., Lushnikov A., and J.Schoonman. Nanodispersed Metal Oxide-Polymer Films For Novel Solar Cells: Synthesis and Characterisation. Proceedings of Annual ESF-NANO Meeting; 1999 10-11 December; Duisburg, Germany.
8. S.A. Zavyalov, A.N. Pivkina, and J. Schoonman. Formation and Characterization of Metal-Polymer Nanostructured Composites. Proceedings of Polymer Electrolytes Symposium (PES-2001); 2001 14-16 May; Noordwijkerhout, The Netherlands.
9. Loeb W.E. Soc. Plast. Eng. J. 1971; 27:46.

NANOCRYSTALLINE LAYERS OF CdSe PRODUCED BY MEANS OF A MULTILAYER APPROACH

D. Nesheva[1*], Z. Levi[1], I. Bineva[1] and H. Hofmeister[2]

[1]*Institute of Solid State Physics, Bulgarian Academy of Sciences, 72 Tzarigradsko Chaussee Blvd., 1784 Sofia, Bulgaria*
[2]*Max Planck Institute of Microstructure Physics, Weinberg 2, D-06120 Halle, Germany*

Abstract

Multilayer structures are deposited by sequential physical vapor deposition of CdSe and a second amorphous (SiO_x, GeS_2) or polycrystalline (ZnSe) semiconductor. The layer thickness of CdSe is varied between 1 and 10 nm; the layer thickness of the second material is either equal or twenty times greater then that of CdSe. High-resolution electron microscopy results prove the formation of CdSe nanocrystalline layers, which are continuous in the structures with equal layer thickness of the constituent materials. In the second kind of structures CdSe layers are discontinuous; particles with nearly spherical form are observed, whose spatial distribution followed the surface morphology of the previous film. The mechanism of nonepitaxial semiconductor nanocrystal growth on 'smooth' and 'rough' surfaces is discussed. Quantum-size increase of the optical band gap of CdSe nanocrystals is observed in all multilayer structures prepared. It is ascribed to one-dimensional carrier confinement in the continuous CdSe layers and quasi three-dimensional one in the discontinuous layers.

1. INTRODUCTION

The development of various techniques for growing nanocrystals (NCs) of a great variety of semiconductor materials has allowed intensive studies on their unusual linear, non-linear and electro-optical properties (Klein 1994, Bowen Katari, Cilvin and Alivisatos 1994, Murray, Norris and Bawendi 1993, Ekimov 1996), which result from both quantum confinement of charge carriers and surface effects. Moreover, much attention has been addressed on developing micro- and nanosized structures and devices using such NCs (Grätzel 2000, Alivisatos 1998). Three-dimensional solid-state electronic devices are giving way to new ones including multilayers with two-dimensional layers, nanowires, clusters, and porous nanocrystalline films.

Nanocrystalline elecronic junctions can be constituted by a network of oxide or chalcogenide particles such as TiO_2, ZnO, $CdSe$, $CdTe$ etc., which are interconnected to allow carrier transport. Usually, a paste containing the semiconductor NCs is applied on a glass coated with a transparent conducting oxide; subsequent sintering produces a mesoporous film whose porosity varies between 20% and 80%. Then the pores are filled with electrolyte or a solid charge-transfer material. Important features of such mesoporous films are the extremely large interface area which could be electronically addressable, and appearance of carrier confinement effects for films constituted of quantum dots. The illumination of nanocrystalline electronic junctions can be used to generate electric current from light and, in particular, for solar energy conversion (Grätzel 2000, Alivisatos 1998). It is generally accepted (Grätzel 2000 and references therein) that in mesoporous films charge carrier transport occurs by diffusion, the rate of which is controlled by traps. This distinguishes the nanoparticle conversion devices from the conventional p-n or Schottky junctions, in which the response to photoexcitation is governed by the electric field in the junction.

Electron-hole pair generation in photovoltaic devices occurs from the absorption of photons whose energy exceeds the optical band gap E_g^o of the used semiconductor. This is among the reasons for the relatively low effectiveness of the energy conversion in three-dimensional solar cells. Various solutions of this problem have been suggested such as sets of consecutive photoelements made of semiconductors with different optical band gaps $(E_{g1}^o > E_{g2}^o > E_{g3}^o \ldots)$, application of semiconductors with varying optical band gap etc. In most semiconductor nanocrystals (CdSe, CdS, Si, Ge) the optical band gap can be changed merely by changing their size between 1 and 10 nm. Thus, nanocrystalline photovoltaic devices having photosensitivity in a wide spectral region can be produced if one uses nanocrystals of various sizes in the same device. Furthermore, for generation of electricity from light, it is

necessary that the minority charge carriers can diffuse to the interface before recombination with majority charge carriers has occurred. In a nanocrystalline device, it is possible to apply NCs whose size are smaller than the diffusion length of minority charge carries.

In this chapter a technique for preparation of continuous and discontinuous CdSe nanocrystalline layers in multilayer structures is described. Amorphous SiO_x or GeS_2 as well as polycrystalline ZnSe are used as the second constituent material in these structures. High-resolution electron microscopy measurements are carried out to prove the formation of CdSe nanocrystalline layers. Results on optical absorption of the structures are also presented.

2. SAMPLE PREPARATION

Multilayer structures of SiO_x-CdSe, GeS_2-CdSe, and ZnSe-CdSe were produced in a vacuum chamber at residual pressure of $\sim 1 \times 10^3$ Pa for the first system and $\sim 3 \times 10^{-4}$ Pa for the others. A consecutive evaporation was carried out from two independent tantalum crucibles mounted as far as possible apart from each other. Powered CdSe and ZnSe (Merck, Suprapur) and preliminary synthesized glassy GeS_2 or commercial SiO were used as source materials. Two calibrated quartz microbalance systems were used in order to measure nominal layer thickness and deposition rate of both materials. Their quartz crystal heads were fixed above the respective source. Two kinds of multilayer structures were deposited from each pair of materials: i) structures in which the thickness of layers was approximately equal, now referred to as multilayers, MLs with thicknesses varied between 2.5 and 10 run, and ii) structures in which the nominal thickness of CdSe layers was varied between 1 and 6 nm, while the layers of the second material were 20 times thicker than the CdSe ones, now referred to as composite films, CFs. During the deposition of each layer of MLs Corning 7059 glass and c-Si substrates, respectively, kept at room temperature were rotated at a rate varying between 8 and 30 turns/min. Their residence time over the source is only 1/12 part of the turn time and, hence, ten or more 'layers' with a nominal thickness of ~0.1-0.25 nm in each step form the respective layer in MLs. The substrates were stopped at the greatest possible distance from both sources at the moment the evaporation source was changed. During the preparation of the composite films, CdSe layers were deposited in the same step-by-step manner, while SiO_x, GeS_2 and ZnSe layers (20-120 nm thick) were deposited in a one-step procedure. Some samples of each system were annealed for 60-90 min at 673 K; the SiO_x-CdSe composite films were annealed in air, while the

GeS$_2$-CdSe and ZnSe-CdSe ones were annealed in argon. More details on preparation conditions of MLs and CFs can be found in our previous articles (Nesheva and Levi, 1997, Nesheva, Raptis, and Levi, 1998, Nesheva, and Hofmeister, 2000).

3. EXPERIMENTAL DETAILS

In order to study CdSe nanocrystallite size, structure and spatial distribution, high-resolution electron microscopy (HREM) measurements were performed using a JEM 1010 operating at 100kV and a JEM 4000 EX operating at 400kV. Electron micrographs of SiO$_x$-CdSe-SiO$_x$ and GeS$_2$-CdSe-GeS$_2$ three layer structures were recorded using optimum contrast conditions (near Scherzer defocus).

All samples produced showed good photoconductivity, which allowed us to carry out spectral photocurrent measurements in the 1.45-3.0 eV energy region and thus to obtain useful information of the optical absorption of both kinds of multilayer structures. Planar contacts (~10 mm long and ~1 mm spaced) from In-Ga alloy or sputtered Au were used for the photoelectric measurements on ZnSe-CdSe MLs and CFs. They showed linear current-voltage characteristics at fields of 10^2-10^3 V/cm applied. Samples were illuminated by a chopped (2 Hz) monochromatic light from a diffraction grating monochromator MDR 2 at a spectral resolution of 4 nm. Intensity dependencies of the photocurrent $I_p \sim F^\beta$ were measured in the entire spectral region studied and the relation $\alpha = \alpha_0 (F_0/F)(I/I_{po})^{1/\beta}$ (Moddel, Anderson, and Paul, 1980) was used in order to obtain the spectral dependence of the absorption coefficient α; the subscript "o" refers to a reference energy. The constant photocurrent method (CPM) (Vanecek, Kocka, Stuchlik, Ozisek, Stika, and Triska, 1983) was also employed. Optical transmission of ZnSe single layers and ZnSe-CdSe CFs was measured by a double-beam spectrophotometer, Specord UV VIS.

4. RESULTS AND DISCUSSION

A HREM micrograph of a SiO$_x$ (5.8 nm)/CdSe(4.5 nm)/SiO$_x$ (5.8 nm) three-layer structure annealed for 90 min at 673K is shown in Fig. 1. It is seen from the micrograph that the CdSe layer is continuous; it consists of randomly oriented nanocrystals. The size of CdSe nanocrystals along the ML axis is equal to the layer thickness. The small angle X-ray diffraction measurement
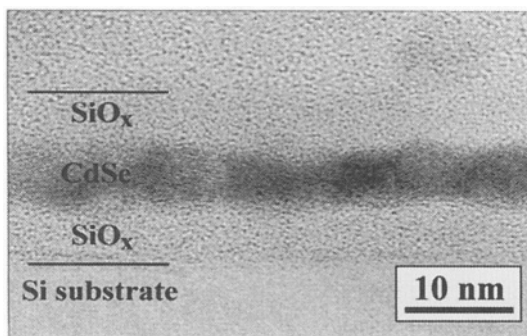
Figure 1. Cross-section view of a SiO$_x$(5.8 nm)/CdSe(4.5 nm)/SiO$_x$(5.8 nm) structure. The micrograph shows a continuous nanocrystalline CdSe layer sandwiched between two amorphous SiO$_x$ layers. The CdSe nanocrystallite size along the ML axes is equal to the CdSe layer thickness.

carried out on an annealed SiO$_x$/CdSe MLs has shown (Popescu, Sava, Lorinczi, Vateva, Nesheva, Tschaushev, Mihailescu, Koch, Obst, and Bradaczeck, 1998) that these MLs exhibit a very good periodicity. Cross-sectional electron micrographs of SiO$_x$-CdSe and GeS$_2$-CdSe three layer structures are shown in Figs.2a and 2b, respectively.'Island' type CdSe layers are seen in both systems. It should be noticed that CdSe nanoparticles are not disposed in a plane; their spatial distribution follows the surface morphology of the SiO$_x$ and GeS$_2$ films, respectively. Most of CdSe nanoparticles are interconnected. The higher magnification has shown (Nesheva and Hofmeister, 2000) that in as-deposited samples the particles have a nearly spherical shape.

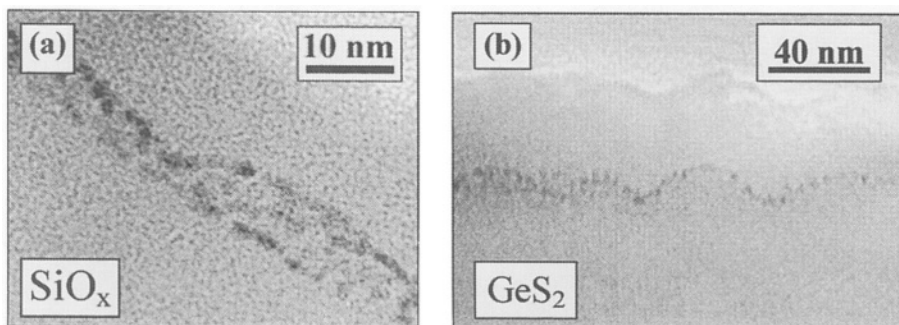*Figure 2.* Cross-section view of as-deposited three-layer structures at low magnification: (a)-SiO$_x$(40 nm)/CdSe(2 nm)/SiO$_x$(20 nm) and (b)-GeS$_2$(40 nm)/CdSe(2 nm)/GeS$_2$(20 nm). CdSe particles, which are not disposed in a plane are revealed in both systems. Their spatial distribution follows the surface morphology of the SiO$_x$ and GeS$_2$ films, respectively.

They are crystalline with their lattice oriented randomly. The annealing improves the spherical appearance and crystallinity of the nanoparticles. It has also been obtained from the HREM results (Nesheva and Hofmeister, 2000) that the average nanoparticle size is more than two times greater than the respective nominal CdSe layer thickness. The annealing slightly increases both average NC diameter d_a and width of size distribution. A relatively narrow nanocrystal size-distribution (σ/d_a = 0.13-0.19; σ-halfwidth at half maximum of the size distribution) has been obtained (Nesheva and Hofmeister, 2000) for CdSe nominal thickness of 1 and 2 nm. Hence, the described deposition technique allows fabrication of 'island' type CdSe nanocrystalline films with various desired average nanocrystallite sizes by varying CdSe nominal thickness.

Sequential vapor deposition of metals and insulating materials having approximately equal thickness of several nanometers, has been applied for non-epitaxial growth of nanosized metallic nanoparticles embedded in insulating matrices. The partial wetting character of the metal with respect to the insulator (Tonova, Patrini, Tognini, Stella, Cheyssac, and Kofman, 1999), the existing valleys on the surface of the insulator (Drüsedau, Panckow, and Klabunde, 1996) and the large difference of surface energies of the two materials (Campbell, 1997) have been considered as responsible for the formation of metal nanoparticles. The cross-sectional electron micrograph of SiO_x/CdSe multilayers shows (Fig.1) that when in the SiO_x/Ga MLs (Tonova, Patrini, Tognini, Stella, Cheyssac, Kofman, 1999) the metal is replaced by a semiconductor film, the latter is continuous rather than 'island' type. However, when the SiO_x surface is 'rough', the CdSe layers deposited are discontinuous (Fig.2a). This implies that, probably, different mechanisms are responsible for the metal and semiconductor nanoparticle formation; neither the assumption for difference of surface energies, nor filling up of the existing valleys could explain our observations. Besides, one could not expect the same partial wetting character of CdSe with respect to SiO_x, GeS_2 and ZnSe.

It has been shown (Chopra 1972, Tersoff, Tu, and Grinstein, 1998) that at the first stage of thin film deposition on a not atomically smooth surface an embryo formation takes place, which is affected by the surface curvature and stress or even disorder of an amorphous surface. They create different environments at different reaction sites and thus strongly affect reaction rates. The HREM and X-ray diffraction results showed that the surface roughness of SiO_x layers in the SiO_x/CdSe MLs is relatively small. Therefore, we assume

that a homogeneous embryo formation could take place at the first stage of CdSe deposition on the 'smooth' SiO_x surface. A gradual increase of the nanoparticle size and coalescence as well as new embryo formation can be expected further; CdSe layers become continuous at a nominal thickness ≥ 2.5 nm. The observed spatial distribution of the CdSe NCs in the composite films (Fig.2) indicates that surface roughness plays an important role in the CdSe nanoparticle formation. It is assumed that at the very beginning of CdSe deposition on a 'rough' oxide or chalcogenide surface, embryos are formed at those surface positions at which the curvature and lattice stress are the greatest. The relatively narrow size distribution indicates that, most likely, further CdSe deposition does not create new embryos but leads mainly to an increase of the nanoparticle size.

Dark and photocurrent measurements have been carried out on all multilayer structures prepared. The obtained results have shown that in both MLs and CFs charge carrier transport involves networks of interconnected CdSe nanocrystals. In the low-conductive CdSe nanocrystalline layers carrier transport is controlled by potential barriers for electrons existing at the CdSe-CdSe interface (with a height <0.25 eV); in high-conductive CdSe layers their effect is marginal (Nesheva, Levi, and Pamukchieva, 2000). Taking advantage of the existence of current paths, optical absorption spectra of all kinds of multilayer structures are obtained with a good accuracy by means of spectral photocurrent and CPM measurements. Different size-induced increase of the optical band gap has been observed in the continuous and discontinuous CdSe layers of the multilayer structures, in which CdSe nanocrystal layers were deposited on amorphous surfaces of SiO_x and GeS_2 (Nesheva and Levi 1997, Nesheva, Levi, Aneva, Nikolova, and Hofmeister, 2000). Thickness dependencies of the optical absorption gap of CdSe nanocrystalline layers in SiO_x-CdSe MLs and CFs are shown in Fig.3. It is seen from the figure that at the same CdSe nominal thickness the E_g^o increase in the discontinuous layer is larger than that in the continuous one. This difference has been explained assuming one-dimensional carrier confinement (along the ML axes) in the MLs (Nesheva, Raptis, and Levi, 1998) and quasi three-dimensional one in
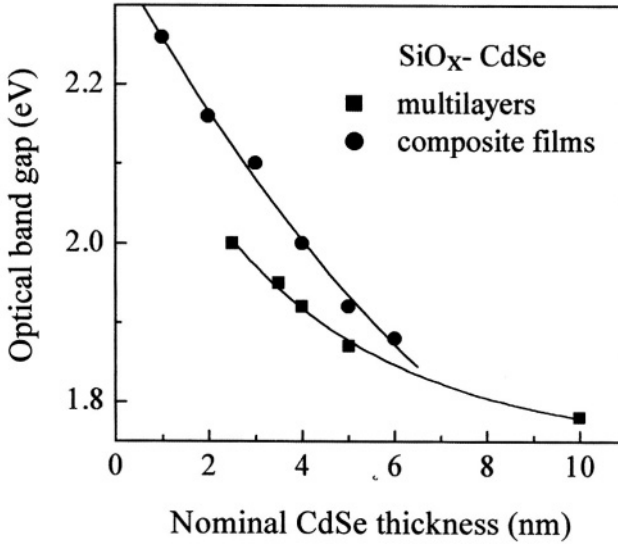
Figure 3. Thickness dependencies of the optical absorption gap E_g^o of CdSe nanocrystalline layers in SiO_x-CdSe multilayer structures. The lines are guides to the eye. The E_g^o values of the composite films correspond to quasi three-dimensional carrier confinement, while the E_g^o values of the multilayers correspond to one-dimensional confinement.

the CFs (Nesheva and Levi, 1997, Nesheva, Raptis, Levi, Popovic, and Hinic, 1999). The assumed difference in the carrier confinement regime appears at a nominal CdSe layer thickness d_{CdSe} <6 nm. Obviously, at d_{CdSe} >6 nm the coalescence of nanoparticle leads to the formation of rather large CdSe 'islands'.

It is known (De, Misra, and Ghosh, 1995) that ZnSe films deposited at room temperature are polycrystalline with small crystallite size. In order to investigate the effect of crystallinity of the second material on the electronic properties of the nanocrystalline CdSe layers, ZnSe-CdSe multilayer structures of both kinds were prepared as well as ZnSe single layers for comparison. Optical transmission measurements were carried out on ZnSe single layers having thickness of ~1 µm and applying Swanepoel's method (Swanepoel, 1983), the spectral dependence of the absorption coefficient α has been obtained. It is known that ZnSe is a direct gap semiconductor and for direct band-to-band electron transitions in crystals the relation $\alpha \sim (E-E_g^o)^{1/2}$ is valid, while for amorphous semiconductors $\alpha \sim (E-E_g^o)^2$ (Tauc dependence). We plotted the $\alpha(E)$ dependence of ZnSe single layers using coordinates $\alpha^2 vsE$ and $(\alpha E)^{1/2} vsE$. A straight line appeared in the first case, which indicated that,

in agreement with the results of other authors, the present ZnSe films are polycrystalline; a value of 2.61 eV has been determined for the optical band gap. Spectral dependencies of the absorption coefficient of ZnSe-CdSe MLs and CFs with different nominal thickness obtained from photocurrent measurements are shown in Fig.4 and Fig.5, respectively. The optical band
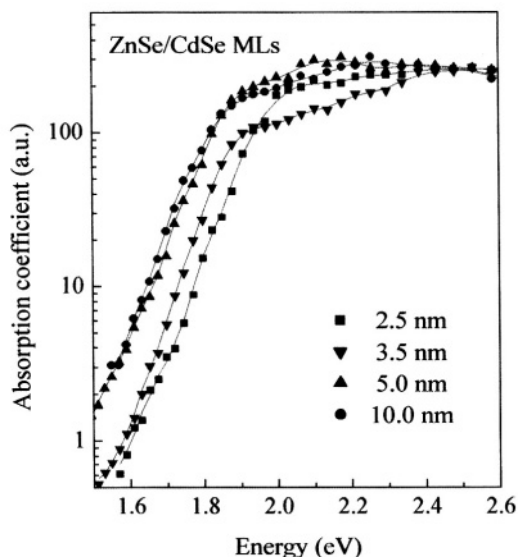

Figure 4. Spectral dependencies of the absorption coefficient of as-deposited ZnSe/CdSe multilayers with different CdSe layer thicknesses given in the figure. The lines are guides to the eye. An overall 'blue' shift of the curves is observed with decreasing layer thickness

gap of ZnSe is significantly higher than that of CdSe and the photoconductivity of CdSe single layers is orders of magnitude higher than that of ZnSe ones. Therefore, it is assumed that the part of absorption spectra at energies <2.5 eV is related to absorption in CdSe layers only. A 'blue' shift of absorption curves is seen in Fig.4 if the CdSe layer thickness decreases from 10 to 2.5 nm; no other features are observed in the ML absorption spectra. The spectra of ZnSe-CdSe composite films look quite different. They show a maximum at the end of the region of steep absorption increase and some other features at higher energies. The first absorption maximum also shows a 'blue' shift with decreasing CdSe nominal thickness. At the same CdSe layer thickness the shift observed in CFs is stronger then in MLs (compare Fig.4 and Fig.5). The optical band gap of semiconductor quantum dots is determined from the energy position of this maximum. It is related to
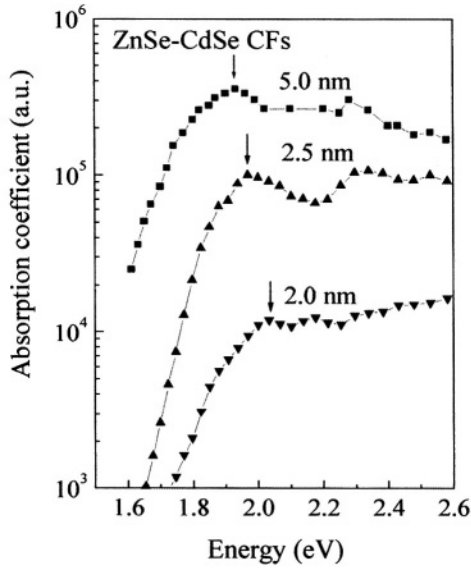
Figure 5. Spectral dependencies of the absorption coefficient of as-deposited ZnSe-CdSe composite films with different CdSe nominal thickness given in the figure. The lines are guides to the eye. A 'blue' shift of the first absorption maximum is observed with decreasing CdSe nanocrystallite size.

electron transitions from the highest occupied energy level in the valence band to the lowest empty level in the conduction band. These results are very similar to those obtained for SiO_x-CdSe multilayer structures, which implies that crystallinity of the second constituent material does not strongly change both CdSe nanoparticle growth process and carrier confinement regime in MLs and CFs.

5. CONCLUSIONS

A technique for preparation of CdSe nanocrystalline layers in multilayer structures has been described. Amorphous SiO_x or GeS_2 as well as polycrystalline ZnSe have been applied as second constituent material. Depending on the thickness ratio of materials, continuous or discontinuous CdSe layers have been produced. It has been shown that neither crystalline structure nor composition of the second constituent material strongly affects CdSe nanoparticle growth; the surface roughness has been considered as the main factor to control the nanoparticle growth process. Quasi three-dimensional carrier confinement has been observed in the discontinuous CdSe

layers; in the continuous CdSe nanocrystalline layers one-dimensional carrier confinement, along the ML axes, takes place. The last observation is different from results obtained in continuous nanocrystalline Ge, Si and GaAs films, in which three-dimensional confinement and tunneling carrier transport mechanism have been observed due to the existence of high potential barriers at interfaces between nanocrystals. The suggested mechanism of non-epitaxial growth of continuous and discontinuous CdSe layers at 'low' and 'high' surface roughness, respectively, implies that it is possible to apply the described multilayer approach for fabrication of nanocrystalline layers from II-VI semiconductors surrounded by a suitable solid charge transfer material. This, along with the low interface potential barriers in CdSe nanocrystalline layers of multilayer structures, opens the door for fabrication of nanocrystalline electronic junctions suitable for various applications.

REFERENCES

Alivisatos A.P., MRS Bulletin, **23** (1998) 18.
Bowen Katari J.E., Cilvin V.L., and Alivisatos A.P., J. Phys. Chem., **98** (1994) 4109.
Campbell C.T., Surf. Sci Rep., **27** (1997) 1.
Chopra K.L., *Electrical phenomena in thin films,* Mir, Moskwa, 1972
De C.K., Misra N.K., and Ghosh T.B., Indian J. Phys., **69A** (1995) 261.
Drüsedau T.P., Panckow A.N., and Klabunde F., J. Non-Cryst.Solids, **198-200** (1996) 829.
Ekimov A., J. Luminescence, **70** (1996) 1.
Grätzel M., in *Handbook on Nanostructured Materials and Nanotechnology,* Ed. Nalwa H.S., Academic Press, 2000, vol.3, 527.
Klein L.C., *Sol-Gel Optics-Processing and Applications,* Kluwer Academic, Boston, 1994 .
Moddel G., Anderson D., and Paul W., Phys. Rev. B, **22** (1980) 1918.
Murray C.B., Norris D.J., and Bawendi M.G., J .Am. Chem. Soc., **115** (1993) 8706.
Nesheva D. and Levi Z., Semicond. Sci. Technol., **12** (1997) 1319.
Nesheva D., Raptis C., and Levi Z., Phys. Rev. B, **58** (1998) 7913.
Nesheva D., Raptis C., Levi Z., Popovic Z., and Hinic I., J. Luminescence, **82** (1999) 233.
Nesheva D. and Hofmeister H., Solid State Commun., **114** (2000) 511.
Nesheva D., Levi Z., Aneva Z., Nikolova V., and Hofmeister H., J.Phys.:Condensed Matt., **12** (2000) 751.
Nesheva D., Levi Z., and Pamukchieva V., J.Phys.:Condensed Matt., **12** (2000) 3967.
Popescu M., Sava F., E.Lorinczi F., Vateva E., Nesheva D., Tschaushev G., Mihailescu I.N., Koch P.J., Obst S., and Bradaczeck H., Proc. SPIE, **3409** (1998) 964.
Swanepoel R. J., Phys. E: Sci. Instrum, **16** (1983) 1214.
Tersoff J., Yu.Tu, and Grinstein G., Appl. Phys. Lett., **73** (1998) 2328.
Tonova D., Patrini M., Tognini P., Stella A., Cheyssac P., and Kofinan R., J.Phys.:Condens. Matter, **11** (1999) 2211.
Vanecek M., Kocka J., Stuchlik J., Ozisek Z., Stika O., and Triska A., Solar Energy Mater., **8** (1983) 411.

X-RAY DIFFRACTION FROM NANOSTRUCTURED MATERIALS

J.Pielaszek

Institute of Physical Chemistry, Polish Academy of Sciences,
01-224 Warszawa, Poland

1. INTRODUCTION

Analysis of X-Ray diffraction (XRD) patterns from polycrystalline materials, very often referred to as powders, is routinely performed. There are many basic and advanced textbooks and review papers dealing with the problem [1-7 and references cited therein]. The development of the methods for the last fifty years is really impressive. Analysis of XRD patterns of nanocrystalline and nanostructure materials may be brought down to the question: are they simply polycrystalline materials but only with sizes of the constituent diffracting structural elements in the nanoscale range and can be studied by XRD using the same procedures?. And what, if any, are the limits of applicability of these standard methods to studies of this kind of materials?. Are they related to the very nature of nanocrystallinity or to the limits of the experimental and computational techniques currently used?. Some information concerning in general the XRD studies of polycrystalline materials with emphasis on problems connected with nanocrystallinity of the samples are presented. The discussed examples illustrate, although rather difficult for the XRD studies, cases of nanocrystalline materials which, as it is shown, can nevertheless be treated.

2. NANOCRYSTALS AND NANOSTRUCTURED MATERIALS

Due to their already found or expected unusual properties, as compared to the bulk, nanosized materials attract attention of many researchers [see e.g. 8-10 and references therein]. There is, however, some confusion in respect to the definition of different terms. Depending on the context, authors attribute somehow different meaning to them. Nevertheless it can be assumed that there is general consensus that nanomaterials are: clusters, nanoparticles and nanocrystals. This is to be distinguished from nanostructured materials. The latter are bulk solids composed of nanoscale (or partly nanoscale) materials.

It is also generally accepted that nanocrystals are entities having linear dimensions (in at least one direction) not exceeding about 100 nm. Thus thin films and nanowires are included, although it is often accepted that the term nanocrystal is reserved to objects having all the three dimensions in the nanoscale range, the others being named either nanocrystals in one or two dimensions or nanoscale materials, although sometimes the nano-thin films are classified as separate kind of nanomaterials.

As used mostly in physical chemistry, the very convenient measure of the size of nanomaterials is dispersion. It is defined as the percentage of the atoms exposed on the surface to the total number of atoms in an average cluster (nanoparticle, nanocrystal). Thus an individual atom has dispersion of 100%, and the cluster of 13 atoms (first coordination sphere in close-packed structure) has dispersion 92%, as presented in Table 1.

Table 1. Relation between number of atoms, dispersion and average diameter for nanocrystals of close packed structure. (The diameters are calculated for the case of palladium nanocrystals).

One atom	Dispersion 100%
First coordination sphere	Dispersion 92%
Second coordination sphere	Dispersion 78%

Aver. diam.~ 4nm	~ 2 900 atoms	Dispersion 26%
~ 7nm	~ 13 000 atoms	18%
~ 9nm	~ 27 000 atoms	13%

When modeling, however, the shape of the nanocrystals are very often approximated by cubooctahedra of "magic" numbers of atoms. They correspond to the number of atoms in consecutive closed shells of a cubooctahedron. Thus the dispersion calculated for both shapes (i.e. closed by coordination spheres and closed shells) slightly differ as the definition is clearly shape dependent and the value calculated for infinite number of atoms in plane is still 100%. The value of dispersion is usually experimentally obtained from chemisorption experiment and can be compared with particle size only assuming specific shape of the particles involved.

3. X-RAY DIFFRACTION PATTERN FROM POLYCRYSTALS

The XRD method is a volume weighted one, i.e. the diffracted intensity from any sample brings about information averaged over the whole irradiated volume which depends on the geometric arrangements (e.g. width and divergence of the X-ray beam) and physical properties of the sample (absorption coefficient). The reader will recall that Transmission Electron

Microscopy (TEM), very often used in studies of nanocrystals, is a surface weighted method.

By common definition polycrystals are highly divided solids composed of coherently diffracting units of sizes down to few hundreds of nanometers. If they are well crystallized their XRD patterns exhibit well resolved reflections even at high diffraction angles. In a classical X-Ray diffraction experiment on polycrystalline samples there are standard procedures of measurements and data treatment. They are supplied nowadays with most of the software when purchasing an XRD diffractometer. First, the data are collected. Then they can be smoothed using any of the algorithms (polynomial smoothing, spline smoothing, Fourier filtering etc.). Very often the $K\alpha_2$ component of the radiation is stripped off (if the data are collected using classical sealed-off X-Ray sources) and the background subtracted. The subsequent treatment of the XRD pattern depends on its quality and aim of the analysis. When the XRD reflections are well defined and in a great part of the pattern well resolved, the phase identification (if necessary) can be done using again, in most cases, a commercial search - match programme equipped with appropriate database. From the intensity distribution of particular reflections and/or their integral intensity, crystallite size distribution and/or average crystallite sizes can be calculated. It is worth mentioning that the XRD supplies information about average crystallite size(s) which are domains of coherently diffracting X-Rays. This should not be confused (but often is) with particle size(s) which may be entities composed of many crystallites separated by different kind of grain boundaries.

4. X-RAY DIFFRACTION PATTERN FROM NANOCRYSTALS

It is well known that with diminishing crystallite size the measured XRD pattern exhibits broadened, and very often overlapping reflections. The broadening of the reflections is inversely proportional to the crystallite size (i.e. size of coherently diffracting domains). This relation is known as Scherrer's [2,11] equation:

$$D= k\bullet\lambda/(\beta\bullet\cos(\theta)) \tag{1}$$

It relates, for the given wavelength λ, the average crystallite size D, diffraction angle θ of a particular reflection and broadening β of this reflection due to crystallite size effect. The β is commonly expressed as a full width at half maximum (FWHM) of the reflection (background subtracted), corrected for instrumental broadening. The constant k, close to 1, depends on the assumption on the crystallite shape and the reflection used [12]. Since the XRD method is a volume weighted, the physical meaning of

the FWHM is not obvious and although in many instances its use gives good results, nevertheless it is recommended to use the integral width of the broadening defined as:

$$\beta_I = (\int I(\theta) \, \partial \, I(\theta) \,) / I_{max}$$

The integral is the integral intensity of the particular reflection (measured above the background) and the I_{max} is the intensity at the maximum of this reflection. The value D calculated both ways is more precisely called "apparent crystallite size". The observed experimentally intensity distribution of a particular reflection is a convolution of instrumental broadening function (which normally is assumed to include spectral distribution function) and crystallite – induced broadening (size, stress, strain). It should be, however, pointed out that introduction of the instrumental correction is much easier in calculation of β then β_I. In the former case as instrumental profile usually the XRD pattern of a standard polycrystalline sample with enough big and strain/stress free crystallites is recorded and FWHMs are measured for particular reflections. Then assuming the same analytical shape (very often gaussian or lorentzian) of the reflections for both standard and measured samples the corrections are introduced [see e.g. 1]. If the FWHMs of measured and standard profiles are B and b respectively, then for the simplest case of the assumed gaussian profiles the β is expressed as $(B^2 - b^2)^{1/2}$. Other assumed analytical shapes of the reflections can also be taken into account [see e.g. 13]. However, to calculate β_I the deconvolution of the observed and instrumental profiles (e.g. using Stokes' method [14] of Fourier analysis) is needed, making procedure more troublesome. It has nevertheless the advantage that the resulting broadening profile can directly be used for particle size and strain determination using Warren and Averbach method [2]. This method, making use of Fourier analysis of the intensity distribution in reflections of different orders from the same set of diffraction planes allows separation of size and strain effects and calculation of "crystallite size" distribution. Under some assumptions the calculation of this distribution is also possible from profile of one reflection [15] and also employing set of reflections from different diffraction planes. At this point it should be remembered that one of the main features of the diffraction pattern from nanocrystalline material, as compared to polycrystalline one, is a quick decrease of the diffracted intensity with diffracting angle, overlapping of the reflections and thus practically making difficult to have well defined distribution of intensity for higher order of reflections. The use of parenthesis above stresses the fact, shown long time ago by Berthaud [16], that the total diffracted intensity for a given Bragg reflection from a crystallite is the sum of independently diffracted intensities by each of the unit-cell columns making-up the crystallite. It means that the calculated size distribution using the Warren-

Averbach method is in fact a distribution of diffraction column lengths in a given crystallographic direction perpendicular to the diffraction planes and not of crystallite (coherently diffracting domains) sizes. Theoretical considerations show that the interference function of a polycrystalline or nanocrystalline solid is identical to that of an arrangement of isolated particles with the same size or size distribution as those of the polycrystalline or nanocrystalline solid [17]. Thus the values of D resulting by using Scherrer's formula are solely an estimate of a volume-weighted average column length. This explains why the term "apparent crystallite size" is often used. The average particle size or crystallite size distribution can be calculated from the average column length or column length distribution provided the shape of the crystallites is known [see e.g. 18]. The definition of the "true size" of the crystallites is not unambiguous. When all crystallites are assumed to have the same size and shape, the cube root of the volume of one crystallite defines the size. Distribution of crystallite sizes will affect this definition. In this case the "true size" can be defined either as a mean value of the cube roots of the individual crystallites volumes or as a cube root of the mean value of volumes of the individual crystallites. Expressions for effective Scherrer's constants when there is a distribution of crystallite sizes for two definitions of "true crystallite size", are given in [12]. The general considerations on different definitions can be found elsewhere [e.g. 18]. The problem of the influence of crystallite shape on the intensity distribution of reflections was considered by many authors.
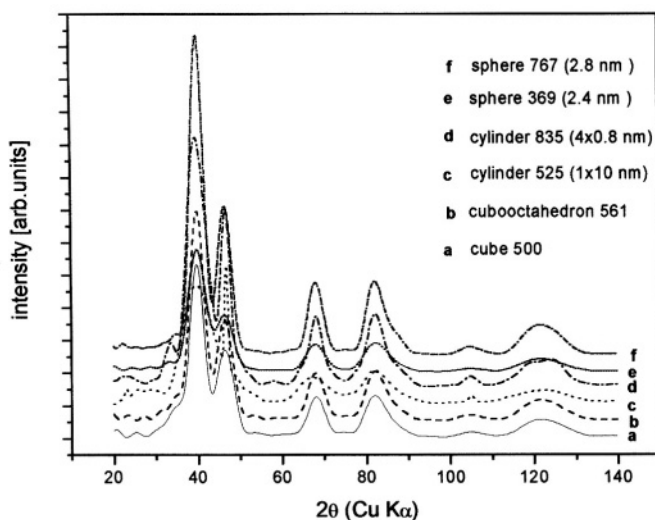

Figure 1. Interference function calculated for different number of atoms and different shapes for Pd nanocrystals of F.C.C. lattice.

Both the shape and size of nanocrystal affect the interference function. It represents only the pure diffraction effects. Only when convoluted with instrumental and spectral functions, it is what we are recording as an XRD pattern. In Fig. 1 interference function is presented for different shapes of randomly oriented nanocrystals of ideal FCC lattice (palladium) of about 400 to 800 atoms.

Whereas for regular shapes (cube, sphere) the interference functions are very similar, they are significantly different for crystallites with flat or elongated cylindrical shapes of approximately the same number of atoms. There were many calculations of the intensity distribution in the reflections and value of constant k in Scherrer's equation depending on the crystallites shape. The detailed analysis of the intensity distribution from nanocrystals in form of cylindrical prism and hexagonal prism [19] shows that it is possible to distinguish between the broadening from both kinds of shapes. In principle it is only necessary to record two lines to determine the average dimensions of the average cylinder (prism) provided that their orientation with respect to the crystallographic axis is known or can be assumed. This can very often be the case of materials which belong to hexagonal system. Analysis of an annealed ZnO powder revealed that the crystallites are hexagonal prism with an average height of 21.3 nm and edge length 8.7 nm and z axis parallel to the axis of the prism and x or y parallel to an edge and to differentiate them with high degree of probability from cylindrical ones. The measurements performed on nanocrystalline Pd samples obtained by gas condensation and compacted showed that average crystallite size in [h00] direction was about 8 nm whereas a larger average crystallite size of about 16 nm was obtained from measurements of (hhh) reflections [20].

5. XRD PATTERN FROM NANO-STRUCTURED MATERIALS

XRD pattern from nanostructured materials is, in principle, similar to that from nanocrystalline materials. If the lattice orientations of particular entities forming a solid, nanostructured material are distributed at random, the interference functions are identical and they sum up. There are, however, additional factors which should be considered. First these materials can be multiphase. The phases can all be nanocrystalline or a nanocrystalline phase can be embedded inside a polycrystalline and/or amorphous matrix. Thus besides the influence of nanocrystal size, also the grain boundaries, defects and microstrains (being the result of local plastic deformation) are to be considered. Simple modeling of XRD pattern from material with different density and arrangement of dislocations in the grain boundaries show that the different methods of its analysis (Scherrer's equation, Williamson - Hall method [21], Warren-Averbach [2]), based on different assumptions can

bring about significantly different results [22]. In many instances the method of material preparation and its history can suggest which factors can mostly influence the observed diffraction pattern. The measurements of XRD profiles on nanocrystalline palladium [17], depending on the history of the preparation of the sample shows that there is a different structure of grain boundaries and the number of atoms at the grain boundaries being not on crystal lattice side, i.e. in disordered state. A particular example of nanostructured materials can be *supported metal catalysts* in which the prevailing part of a mass is a support, and interest is mostly in the structure of a small fraction of the highly dispersed (nanocrystalline) metal. Due to the high specific surface of the support and usually low loading of the metal, the nanocrystals of the metal phase are distanced each from other. The XRD pattern of the catalyst is usually a superposition of two: from the metal phase and, usually predominant, from the support. The contribution to the pattern originating from the distances between the support and the metal in most cases can be neglected. The simplest case can be when the background is from amorphous (or quasi-amorphous) phase which can be e.g. for silica. In such a case the background can easily be modeled with smooth analytical function and subtracted from the measured pattern and the resulting profile fitted to an analytical function [23]. This way it was possible to follow for Pd-Au nanocrystalline palladium catalyst (on silica support) changes in the
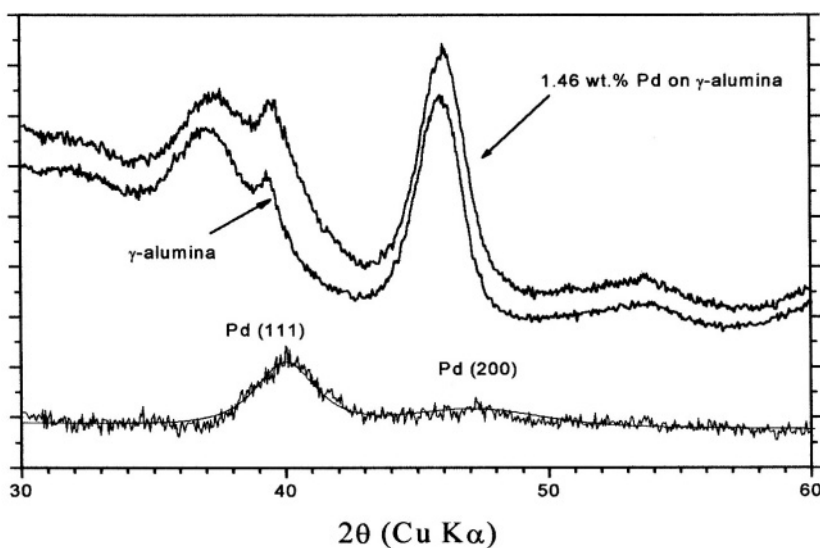

Figure 2. XRD pattern of 1.46 wt.% Pd on γ-alumina and XRD pattern of γ-alumina. The lower part of the figure shows the pattern from palladium nanocrystals after subtracting alumina background. The solid line is analytical function fitted to the pattern.

positions of XRD reflections caused by series of reduction-oxidation cycles [24]. It was shown that for nanocrystallites of about 10 nm in diameters and nominal composition of 70 at.% Pd – 30 at.% Au there is a shift in the position of reflections which could be interpreted via Vegard's law as the apparent average increase of the concentration of palladium in the alloy by about 3 at.% due to the reduction of the sample in hydrogen. It means that in air the surface layer of these bimetallic nanocrystals is enriched in palladium. In addition to immediate application of these results in the interpretation of catalyst behavior it is worth to indicate the more general aspect; the XRD being, as mentioned before, the volume weighted method can be, for the case of nanocrystalline materials, also the surface sensitive method. This aspect of XRD is especially interesting when combined with atomistic modeling (see below).

Another example of using fitting of analytical functions to the bi-phase system XRD pattern is shown in Fig. 2. This is one of the XRD patterns measured for a series of palladium on *γ*-alumina samples with concentration of palladium varying from 0.3 wt.% to about 2.7 wt.%. For the presented case of 1.46 wt.% of palladium the palladium phase is hardly visible on the XRD pattern of this sample as compared with XRD pattern from the *γ*-alumina. However the proper scaling of both patterns and subtraction of support [23] gives the XRD pattern originating from the metal alone. Analytical function fitting (Pearson VII in this case) allowed calculation of the average crystallite size using Scherrer's equation employing integral breadth and resulted in the estimated size of 3 nm.

6. MODELLING OF XRD PATTERN

There are, in general, several methods of modeling XRD pattern. The very first step is to fit an analytical function to distribution of intensity of a particular reflection and subsequently extract from the fitted values (position, intensity, widths) the required physical information. As it was said before there are different analytical functions which approximate well, depending on the case, the experimentally observed intensity distribution of a reflection. This method can be used even when there is overlapping of individual reflections. In principle, this is a method of decomposition of a measured XRD pattern into constituent individual reflections, fitted with analytical function(s). Therefore it is often referred to as the decomposition method. One of the important drawbacks of this method is that there are arbitrarily defined truncation limits for given reflection(s). These are usually chosen as points on both sides of the reflection position being apart by a multiplicity of the FWHM value of the reflection on both sides of the ordinate of the reflection position. In the case of overlapping and low-

intensity reflections (particularly at high diffraction angles) this can pose a serious problem. Due to the different shape of the tails of different analytical functions it can be shown [25] that to include 99% of the integral intensity it is sufficient to have for Gaussian function the truncation at the distance of 3xFWHM on each side of the maximum, whereas for Lorentzian function this should be 63xFWHM. Therefore acceptable (especially from the point of view of overlapping reflections), intermediate, although arbitrary, values are usually chosen. An example of the decomposition procedure is presented in Fig. 3.

The nanocrystalline palladium (10 wt.%) on silica was subjected to reduction in hydrogen at 873 K and it was concluded [26] that Pd_3Si phase is formed. Closer examination of the XRD profile as presented in Fig. 3 by open circles (data after subtraction of silica background) showed that there are probably more phases. So the pattern was decomposed into minimum number of Pearson VII function to obtain the best fit and the result is presented in the middle part of the figure. The lower part of the figure presents histograms of possible Pd-Si phases. The solid line superimposed on XRD profile is a sum of the decomposed profiles. As it can be seen the fitting is quite good, supporting conclusion that in fact there is a mixture of different Pd-Si phases. The estimated crystallite sizes resulting from the fitted parameters are less than 10 nm.

6.1 Total pattern fitting

Fitting of superimposed individual analytical profile functions (as described above) together with suitable background function model to the observed data is one of the methods of the total profile fitting. The resulting set of profile parameters can be used for calculation of physical parameters. There are, however, substantial difficulties with application of this method to nanocrystalline materials. In general the XRD pattern from these materials becomes increasingly difficult to fit with increasing diffraction angle (decreasing values of d spacing). This is due, besides the intrinsic crystallite size effect, to the influence of thermal atomic vibrations and decreasing values of atomic scattering factor. As a result the reflections become more and more difficult to be distinguished from the statistical noise of the background. The procedures of XRD pattern treatment and our understanding of their shapes are all the time being developed. One of the problems still to be solved is to obtain the real crystallite size distribution from XRD. It is now commonly accepted that the particle size distribution of materials obtained by vacuum deposition or gel techniques is close to lognormal. Assuming this and the shape of the crystallites, it was shown [29] that even for very low crystallite sizes (ceria samples with average apparent crystallite sizes of 3-4 nm) it is possible to model the observed XRD profiles.
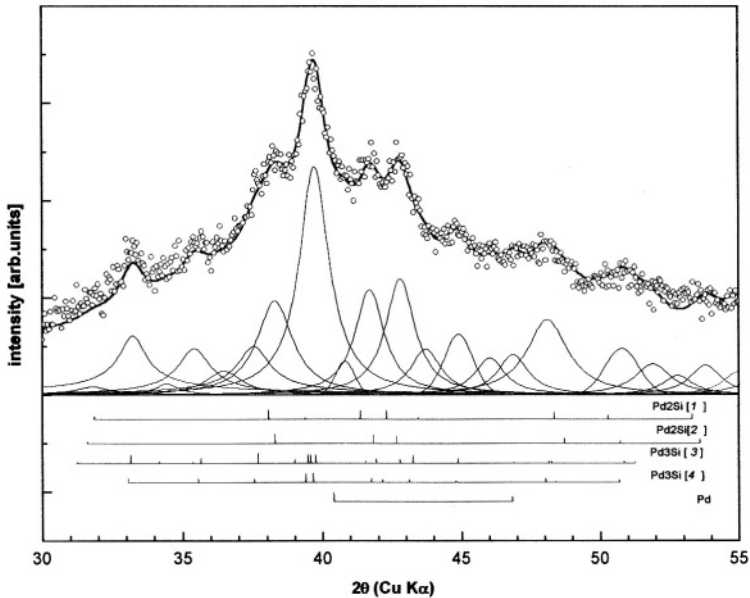
Figure 3. XRD pattern after background subtraction for 10 wt.% Pd on silica subjected to hydrogen reduction (open circles), decomposed into a number of analytical profiles of Pearson VII type (solid lines). The solid line superposed on points is a sum of the decomposed profiles. In the lower part of the fig. positions and relative intensities of different Pd-Si phases are indicated. The numbers1 and.3 refer to JCPDS files 19-893 and 17-369 resp. and numbers 2 and 4 to data from ref.[27] and [28] resp.

6.2. Rietveld refinement

The method which in the last decade underwent a vivid development and increasing applicability in solving different structural problems is the Rietveld method. This is a total pattern fitting method introduced by Rietveld for fitting structural parameters obtained from neutron diffraction data [30], but soon applied to XRD data and now very popular and effective in XRD data analysis [31,32]. The experimentally observed XRD pattern is fitted to the calculated one. To calculate the XRD profile two models have to be known (or assumed): the model of approximate positions of atoms in the structure and the model describing the Bragg reflections (their shape) in terms of analytical functions. Then the calculated XRD profile is compared with the measured one. The total intensities of reflections and their (starting) position are defined by structural models. Parameters describing the form of

the Bragg reflections depend on the instrumental functions and on the microstructure of the sample (e.g. crystallite size).
The quantity to be minimized is:

$$S = \sum [y_{obs}(x_i) - y_{cal}(x_i)]^2 \qquad (2)$$

Where the $y_{obs}(x_i)$ and $y_{cal}(x_i)$ are the calculated from the model and measured intensities at the i-th point of the pattern, respectively, the sum being over all data points in the diffraction pattern. The $y_{cal}(x_i)$ is expressed by:

$$y_{cal}(x_i) = s\sum_j I_j G_j \Phi (x_i-x_j) + b(x_i)$$

where I_j is the integrated intensity of the j-th reflection, expressed as:

$$I_j = s \, m_j \, (LP)_j \, |F_j|^2$$

With s being the scale factor, m_j – the multiplicity, $(LP)_j$ – Lorentz-polarization factor and G_j is a preferred-orientation function. $b(x_i)$ is background at the point x_i.
F_j is the structure factor given by:

$$F_j = \sum_I N_i \, f_i \, exp[2\pi i \, (hx_i + kx_i + lz_i)] \, exp(-B_i)$$

Where x_i, y_i, z_i are the coordinates of the I-th atom in the cell, expressed as the fraction of the edges; h, k, 1, are the Miller indices; N_i is the fractional occupancy for the i-th atomic site; f_i is the X-ray scattering factor and B_i is the temperature (Debye – Waller) factor. Function Φ describes the shape of reflections (its parameters being also angle and, in general, lattice direction dependent). The summation is over all reflections which contribute to the intensity at x_i. It means that the minimization of (2) involves directly the assumed (starting) structure of the phase to be considered. The parameters are fitted by a non-linear gradient minimization till the minimum values of the function S (2) are obtained. The final results of the goodness of fit are estimated on statistical ground (see e.g. Table 1 in [33]). Interpreting the data only on the basis of these parameters can sometimes be misleading. As an example, examination of a series of Li-Mn-O spinels [34] can be presented. Some of the spinels, prepared by low-temperature sol-gel synthesis were nanocrystalline with average crystallite sizes, as estimated from FWHM of the (111) and (311) reflections, equal to about 17.0 nm. The quality of the Rietveld fit of the δ-spinel (non-stoichiometric composition $Li_{1.005}Mn_{1.995}O_4$) was good when fitted to the structure of Fd3m symmetry and lattice constant corresponding to the $Li_4Mn_5O_{12}$ phase. Closer examination of the shape of the resulting fitted profile at higher angles of
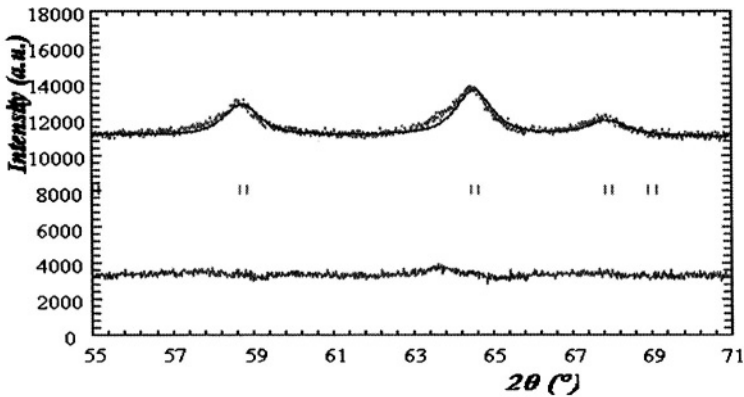
Figure 4. Part of the fitted XRD pattern from δ-Li-Mn-O spinel (see text). The measured (points) and fitted (solid line) patterns are in the upper part of the figure, the difference of both(residuals) in the lower part of the figure. Bars indicate the positions of reflections of the fitted structure.
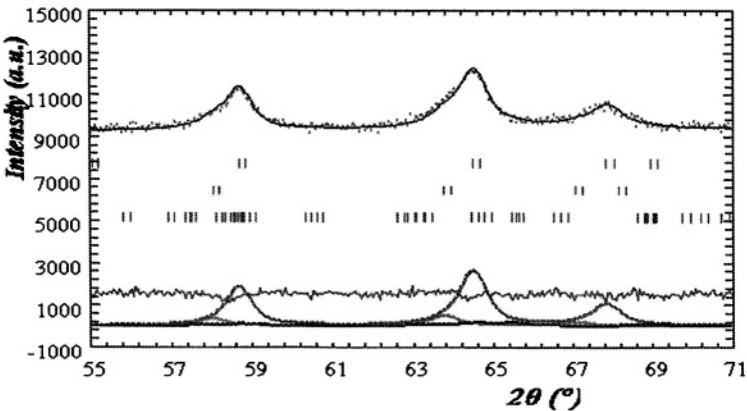

Figure 5. The same part of the pattern as in Fig.4 but fitted to the mixture of three phases (positions of reflections indicated by bars). The residuals of the fitting and reflections of the fitted phases are in the lower part of the figure.

diffraction (see Fig. 4) showed however that there is noticeable discrepancy between the observed and fitted profiles, especially for some reflections. These were the low intensity reflections due to the intrinsic nature of the XRD pattern from nanocrystalline substances (see above), but nevertheless the discrepancies were noticeable indicating the possible presence of

additional weak reflections. Thus the fitting was repeated taking into account this possibility of multiphase composition. The best agreement between the shapes of measured and fitted profiles (see Fig.5) was obtained for three phase system. The dominant phase was the one identified before (about 76%), but two others were also tentatively identified: stoichiometric, high temperature spinel (about 17%) and Mn-O oxides. It should be pointed out that the parameters describing goodness of fit were very similar for both fittings (e.g. the R-Bragg factor was for one and multiphase fitting 4.6 and 4.82 respectively).

6.3. Atomistic modeling.

The interference function which reflects solely the effect of the positive and negative interference of the incident and diffused X-Ray beams on individual diffracting centers (atoms) is calculated using Debye formula [see e.g. 5]. As it was shown in Fig. 1 the interference function from nanocrystals of few nm in size exhibits well defined reflections of widths depending on the linear dimension of the nanocrystal in a given direction. With increasing crystallite size the XRD pattern more and more resembles that from conventional coarse grain polycrystalline material. In most cases the material under study is not a monoatomic one. In the case of metals very common are bi- or multimetallic systems. For the simplest case of a solid solution of two elements it is usually assumed that the change of lattice parameter (and thus position of reflections) of the matrix element depends linearly on concentration of the solute element randomly distributed in the matrix. This relationship known as Vegard's law is often observed and exploited in practice for studying polycrystalline materials. It is however known that for many multielement systems there is a preferential surface segregation of one of the elements, often observed in surface studies of single crystals and in gas adsorption probing of different systems. For large crystals this surface enrichment does not influence noticeably the average bulk concentration. For nanocrystalline materials the situation can be, however, different. Due to a significant proportion of the surface atoms in respect to the bulk, the surface segregation of one element can substantially disturb the average concentration inside the nanocrystal. The calculations [35] of the XRD interference function were performed for a nanocrystal of f.c.c. structure and shape close to sphere, having about 2000 atoms (i.e. about 3 nm in diameter) and consisting of 25 at.% Pd – 75 at.% Co. Different concentration profiles in the clusters were considered. In the simplest case of an ideal Pd lattice imbedded in an ideal Co lattice the resulting XRD pattern was a simple superposition of the two, the interphase intensity contribution being not noticeable. When, however, it was assumed that the outer layers of Co atoms are arranged in such a way as to gradually accommodate their distances to those of the underneath layer (the model of complete segregation or epitaxial

growth with distortions in Co-Co distances), the positions of reflections in the resulting XRD pattern were almost identical with these of pure Pd (without any presence of reflection from Co phase). Changing Co profile concentration inside the crystallites resulted in changes in the shape and position of the calculated reflections but nevertheless their positions were very distant from what can be expected from Vegard's law and indicated much lower than actual concentration of the Co atoms. This example show that for multi-element
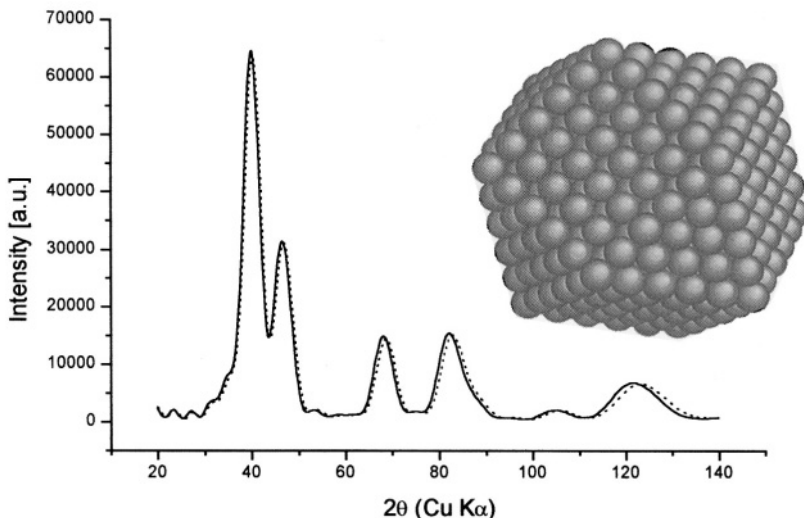
Figure 6. Structural model of a 561 atom palladium cubooctahedral cluster and calculated XRD patterns for energy- minimized (dashed line) and non-relaxed (solid line) structure

(but also multi-phase) nanocrystalline materials, the positions and intensities of the XRD reflections do not necessarily reflect the nominal composition but strongly depend on other factors (e.g. surface segregation which in turn can depend on the environment). Even in the case of one element nanocrystalline materials XRD patterns, exhibiting distinct reflections, their interpretation can be ambiguous. For the nanocrystals of sizes down to 2 – 3 nm we observe that the lattice parameters calculated from different reflections (and corrected for errors) give different values. Thus the indexing of the reflections makes a limited sense. As was pointed out by Kaszkur [36] "we depart from the Bragg interpretation zone". When modeling nanocrystal (cluster) with minimum energy configuration, one can get more "realistic" structure because the presence of the free surface (or interphase boundary) can induce the displacement of atoms from their lattice sites. In energy minimization procedure, of crucial importance is a choice of the interaction potentials. It was shown [37] that modified Sutton-Chen [38] potentials work

well for some transition metals (palladium, cobalt). Thus the structure of the energetically minimized clusters can be modeled and the resulting XRD pattern calculated. To make however the simulated XRD pattern more close to the real (experimental) one, which is measured over a definite period of time, the Molecular Dynamics (MD) run on energy minimized nanocrystal should be done and then the resulting XRD pattern (averaged over the runs) presented. This way it was shown [36] that for Pd nanocrystals the overall, average lattice constant decreases with decreasing crystallite size. Fig. 6 presents the 561 atom cubooctahedral cluster and calculated XRD pattern (solid line) together with the XRD pattern calculated for the energy minimized cluster (dashed line). The shifts in the position of the reflection, increasing with the diffraction angle, are visible. It means that if the influence of the environment on the positions of surface atoms is significant, this should be reflected in the average position of the XRD reflection. It was in fact shown [39] that there is a shift of Pd(111) reflection when palladium nanocrystals (palladium catalyst on support) is subjected to change of the atmosphere from air to argon. Moreover, the atomistic modeling of the XRD pattern of palladium nanocrystals showed that to explain the change in position and shape of the pattern when transforming palladium into its hydride it should be assumed that part of the nanocrystals has the icosahedral symmetry and these nanocrystal do not undergo transformation into hydride. Thus the atomistic modeling when compared with experiments can bring about the information otherwise not possible to retrieve.

7.   CONCLUDING REMARKS

The presented above considerations and results show that for studying nanocrystalline materials the methods usually used in XRD studies of polycrystalline materials are applied. This include also the modeling of the XRD profiles and whole pattern fitting. Nanocrystallinity of the materials needs however some special attention in experimental procedures and data treatment. In the former case it is especially important when high dispersion and properties of the material make them sensitive to the environment. This make the handling of the samples more difficult, but in return very minute changes in the surface structure of nanocrystalls can be followed up, especially when aided by atomistic modeling. It can be speculated that this opens the way for studying by XRD the surface reactions on nanocrystalline materials. It should be finally mentioned that the combination of the XRD method with other physical methods of studying nanocrystalline systems, especially EXAFS should push forward our understanding of their structure and perhaps predict some of their properties.

ACKNOWLEDGMENTS

REFERENCES

1. Klug H.P. and Alexander L.E., *X-Ray Diffraction Procedures for Polycrystalline and Amorphous materials.* New York: Wiley, 1974.
2. Warren B.E., *X-Ray Diffraction.* New York: Dover Publ. 1990.
3. Louër D., *Advances in X-Ray Analysis,* **37** (1994) 27.
4. Louër D., *J. de Phys. IV,* (Suppl. J. de Phys. III), C4 **6** (1996) 57.
5. Klug H.F., Alexander L.E , *X-Ray Diffraction Procedures.* John Wiley , 1974
6. Jenkins R., Snyder R.L., *Introduction to X-Ray Powder Diffractometry.* John Wiley, 1996
7. Delhez R., deKeijser Th.H., Mittemeijer E.J., *Fresenius Z.Anal.Chem.* **312** (1982) 1
8. Morris D.G, *Mechanical behavior of nanostructure materials.* Ueticon-Zuerich, Trans TechPub., 1998
9. *Nanomaterials: synthesis, properties and applications.* Ed. by Edelstein A.S and Cammarata R.C, Bristol, Philadelphia: Institute of Phys. Pub., 1998
10. *Metal clusters in chemistry. Volume 3, Nanomaterials and solid-state chemistry.* Ed. by Shihe Yang and Ping Sheng, London, New York: Taylor & Francis, 2000.
11. Scherrer P., *Nachr.Ges.Wiss. Goetingen, Math.-Phys. Kl.* **2** (1918) 96.
12. Langford J.I. and Wilson A.J.C., *J. Appl. Cryst.* **11** (1987) 102.
13. de Keijser Th.H., Langford J.B., Mittemeijer E.T., Vogels A.P.B., *J.Appl.Cryst.* 15 (1992) 308.
14. Stokes A.R., *Proc. Philos. Soc. London, Ser A,* **61** 382 (1948)
15. Nandi R.K., Kuo J., Schlosberg W., Wissler G., Cohen J.B., Crist B. Jr, *J.Appl. Cryst.* 17, 22(1984)
16. Berthaud E.F., *Acta Cryst.,* **3** (1950) 14
17. Löffler J. and Weissmüller J., *Phys.Rev B.* **52** (1995) 7076.
18. Matyi R.L., Schwarc L.J., Butt J.B., *Catal.Rev.Sci.Engn.* **29** 41 (1987)
19. Langford J.I., Louër D., *J.Appl.Cryst.* **15** (1982) 20.
20. Fitzsimmons M.R., Eastman J.A., Müller-Stach M., Wallner G., *Phys. Rev. B* **44** (1991) 2452.
21. Williamson D.K. and Hall W.H., Acta Metall. **1** (1953) 22.
22. Alexandrov I.V., *Materials Sci. and Engn. A* **286** (2000) 110
23. J.Pielaszek, *X-Ray Diffractometry in Supported Catalyst Studies,* Institute of Physical Chemistry Monogr. Series, Warszawa 1995.
24. J.Pielaszek, in *Applied Crystallography, Proceedings of the XVI Conf. On Appl. Cryst, Cieszyn, Poland, 1995,* H.Morawies, D.Stroz (Eds), World Scientific 1995, p.21
25. Toraya H., *J.Appl.Cryst.* **18** (1985) 351.
26. Juszczyk W., Pielaszek J., Karpinski Z., Sobczak J.W., *New J. Chem.* **17** (1993) 573.
27. Anderko K., Schubert K., *Z.Metallkd.* **44** (1953) 307.
28. Wysocki J.A., Duwez P.E., *Metall. Trans.* **A12** (1981) 1455.
29. Langford J.I., Louër D., Scardi P., *J.Appl.Cryst.* **33** (2000) 964.
30. Rietveld H.M., *Acta Cryst.,* **20** (1966) 508, **21** (1966) A228
31. *The Rietveld Method,* Ed. By Young R.A., International Union of Cryst. Book Series, Oxford Univ. Press, 1993.
32. McCusker L.B., Von Drelle R.B., Cox D., Louër D., Scardi, P., *J.Appl. Cryst.* **32** (1999) 36.
33. Langford J.I., Louër D., *Rep. Progr. Phys.* **59**, 131 (1996).

34. Lisovytskiy D., Kaszkur Z., Baumer V.N., Pielaszek J., Marzec J., Molenda J., Dygas J., Kopec M., Krok F., *Proceedings of the European Powder Diffraction Conference, Uppsala 23-26 may 2002, Sweden ,* to be published in *Materials Sci. Forum.*
35. Pielaszek J., Barczynska J., *Mat.Sci Forum,* **79-82** (1991) 139
36. Kaszkur Z., *J.Appl.Cryst.* **33** (1999) 87.
37. Kaszkur Z., Mierzwa B., *Phil.Mag.* **77** (1998) 781.
38. Sutton A.P., Chen J., *Phil. Mag.* **61** (1990) 139
39. Kaszkur Z., *J.Appl.Cryst.* **33** (2000) 1262.

HIGH RESOLUTION ELECTRON MICROSCOPY OF SURFACES AND INTERFACES

H. W. Zandbergen
National Centre for HREM, Laboratory of Materials Science, Delft University of Technology, Rotterdamseweg 137, 2628 AL Delft, The Netherlands

Introduction

Compared to other techniques used to obtain structural information of materials, high resolution electron microscopy (HREM) has the great advantage that it yields local information about the atomic arrangements, projected along the direction of electron incidence at a resolution comparable to the interatomic distances. This enables the study of complicated structures, crystal defects, precipitates, etc. down to the atomic level. Furthermore the electronic structure can be probed by electron energy loss spectroscopy (EELS), yielding information on the local environment of the atoms in the illuminated area.

Knowledge of the atomic arrangements of surfaces and interfaces is of vital importance for the understanding of the properties. With the increasing need of the accurate determination of the atomic arrangements at non-periodic structures in materials design and control of microstructures and nanostructures, techniques that provide quantitative structural information at the sub-angstrom level will be indispensable. High-resolution electron microscopy (HREM) is by far the best technique to obtain sub-surface structural information on a local scale. X-ray and neutron diffraction can only give structural information that is averaged over a large area. This is in part because the interaction between electrons and matter is much higher than for X-rays and neutrons (about 10^5 to 10^7 times respectively) and in part because electrons can be focussed very easily by magnetic lenses. The local 3-D information is essential for understanding the properties of all types of materials, since the local structure plays a paramount role in this respect. In particular for further improvements of these materials based on materials design, accurate atom positions are required, with a precision of the order of 0.01 nm. Scanning tip microscopy can provide the resolution but only 2-D information is obtained in this way. Although the resolution of HREM is about 0.1 nm, the scattering potential of atoms is known which allows a position accuracy of 0.003 nm provided the atom columns in the viewing direction are sufficiently separated. HREM gives 2-D information about

the atom positions, but by combination of HREM information from different directions a 3-D reconstruction can be made. Thus HREM can provide the required accuracy. However, at the moment this accuracy cannot be obtained because of the aberrations imposed by the optics of the electron microscope. In this respect, important steps towards quantitative HREM are the developments of through focus exit wave reconstruction and off-axis electron holography. Both methods provide the complex image wave in the image plane allowing proper aberration correction.

A major advantage of the reconstructed exit wave (corrected for the aberrations) is that it allows a more straightforward quantitative interpretation than HREM images, in particular for non-period features like grain boundaries. Whereas grain boundaries play a large role in most materials, their role is even larger in nanophase materials, which consist of mostly synthetic materials with an average grain size below 100 nm [Siegel, 1993]. The various grains can be of different phases or structures, but the basic idea behind nanophase materials is the generation of materials with new atomic structural arrangements by introducing of a very high density of defects such as grain boundaries, interphase boundaries and dislocations resulting in new macroscopic properties. As divers as the compounds and the applications, are also the actual reasons for using electron microscopy techniques. Evidently, size and shape can be easily determined by TEM, whereas small angle X-ray and neutron diffraction allow determination of the size distribution. Still, in dense nanophase material the grain boundary structure (Merkle (1995), Möbus (1998), King (1998) and Kienzle (1998)) is the most important part. Determination of the grain boundary structures is, however, a difficult task because it requires a 3D determination of the whole grain boundary to be done by making 2D images, which are in a first approximation projections. Because of that, the 2D imaging requires that the grain boundary is (almost) parallel to the electron beam, without steps in that direction and being continuous throughout the specimen. Also the grains on both sides of the boundary should be in such an orientation that the structures of both grains are imaged. Finally the specimen should not be covered with an amorphous layer. Since the boundary core structure depends on the interatomic bonding forces and the boundary crystallography and since many different grain orientations and grain boundary orientations occur, a large variety of grain boundary core structures will occur in a given specimen. Therefore a HREM study can only provide fragmented information, describing only a part of the grain boundary structures. Obviously, the higher the resolution the more grain boundaries can be characterised and the higher the precision will be.

The imaging process

Due to the aberrations of the electron microscope, the information coming from one point in the object is delocalised in the image. The amount of delocalisation depends on the spatial frequency (and on the microscope). One can reduce this delocalisation by defocusing of the microscope, but only up to a certain spatial frequency. When we only consider the phase contrast of perfect-periodic specimen, the image reveals at Scherzer focus directly the projected potential, i.e. the structure of the object, provided the object is very thin and the atom columns are so far separated that they are not masking each other by the blurring. The resolution which can be obtained in this way (point-point resolution) is about 0.17 nm for the best microscopes at intermediate acceleration voltage (100 to 200 kV). For non-periodic specimen like defects and grain boundaries, the delocalisation (see Figure 1) due to aberrations prevents a direct interpretation of images of these structures. The information beyond the point resolution is transferred with a non-constant larger phase shift and, as a consequence, is dispersed over a larger image area.
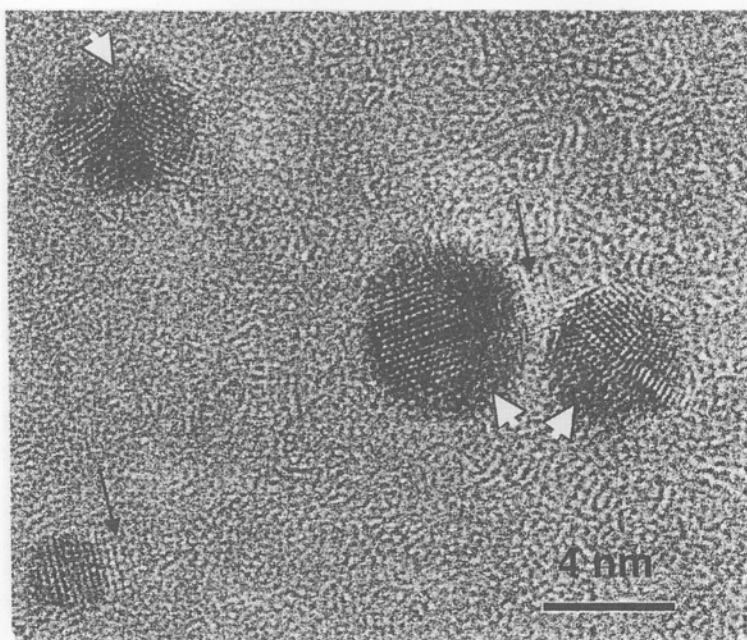
Figure 1. HREM image of several Au particles on an amorphous C film. The black arrows point to fringes that are present outside the actual particles, which is due to delocalisation. The white arrowheads point to areas inside the particles, that show no or only weak fringes, due because of the local misorientation of the lattice. Note that the average grey level in these areas is rather weak, hampering a straightforward 3D reconstruction in case of overlapping particles.

The information limit corresponds to the maximal diffraction angle that is still transmitted with appreciable intensity, i.e. the transfer function of the microscope is a spatial band filter such that all information beyond the information limit adds to the background. For a thin specimen, the damping envelope of chromatic aberration (temporal incoherence) mainly determines this limit. A typical value of the information limit for the best microscopes operating at 300 keV (with field emission gun) is slightly better than 0.1 nm.

Since the information limit is mostly better than the point resolution, a logical way (Kirkland (1984), Kirkland et al (1985), Van Dyck (1990)) of increasing the resolution consists in restoring the information that is present between the point to point resolution and the information limit. For this purpose, electron holographic methods (through focus holography and off-axis electron holography) have been developed. It should be stressed that the improvement of the resolution from 0.17 nm (point resolution) to 0.1 nm (information limit) is not just a simple reduction, because this improvement crosses the boundary beyond which atom columns separated by 'normal' interatomic distances can be discriminated. Especially for non-periodic structures, the aberration correction, which is included in the holographic reconstruction algorithms, makes a direct imaging of atom columns within grain boundaries and defects feasible.

The retrieval of the maximum amount of information from HREM images

The information of the electron wave that has passed through the specimen is scrambled in the image due to the aberrations of the microscope. The unscrambling (deblurring) can be done in two steps. First, one has to reconstruct the wavefunction in the image plane. Since by recording the image only the amplitude information is collected, one has to find a way to determine also the missing phase information. By definition this can only be done using holographic methods. After determining the image wave one has to reconstruct the exit wave of the object. For the latter the microscope parameters have to be known very precisely. This forces the microscopist to perform the experiments with care and to decide beforehand which information he wants to achieve, such that the experiments are optimised to obtain this information.

Two holographic methods exist to determine the phase in HREM images: off-axis electron holography [Lichte (1986, 1992)] and focus variation [Van Dyck (1996a)].

In the focus variation method, the focus is used as a controllable parameter so as to yield a through focus series from which both amplitude and phase information can be extracted [Schiske (1973), Saxton (1986)] [Van Dyck (1990), Coene et al, (1992), Op de Beeck (1995)]. Images are

captured at very close focus values so as to collect all information in the three-dimensional image space. Each image contains linear information and non-linear information. By Fourier transforming the whole 3D-image space, the linear information of all images is located on a parabola. By selecting only the information on this paraboloid [Van Dyck (1990)] the contribution to non-linear interference is strongly reduced. This reconstruction also allows the retrieval of the phase and amplitude of the wave function at the image plane. The aberrated electron wave can still be refined by iteration comparing calculated images from the aberrated electron wave with all HREM images of the focus series. The best matching criterion for this purpose is the maximum likelihood criterion (for details see Coene et al (1992)). In this way all information, both linear and non-linear, that is present in the images is fully exploited, so that the highest precision is achieved. In practice a maximum likelihood fitting can suffer from a low convergence rate. Therefore the procedure can be best started with the paraboloid method of Van Dyck after which the maximum likelihood fitting can be performed straightforwardly. An important limitation of the reconstruction method is that the non-linear interaction is underestimated due to a smaller contrast in the experimental images compared to that in the calculated one.

For off-axis electron holography, the electron optical set-up of an electron microscope has to be changed only slightly. The object plane is illuminated by a plane electron wave where the object covers only half of the plane while the other half serves as a reference area. Behind the object, one finds the exit wave and the unscattered reference wave. Both waves are imaged by the objective lens. A Möllenstedt biprism [Möllenstedt (1956)], which is located (behind the specimen) in the selected area aperture holder, deflects both waves towards each other when a positive voltage is applied to the biprism filament. Therefore, the aberrated electron wave and reference wave interfere in the overlapping region of the image plane, resulting in an interference pattern which is highly magnified by projective lenses and recorded by means of a slow-scan CCD camera. The intensity distribution of this "off-axis electron hologram" can be written as

$$I_{hol}(\vec{r}) = 1 + A^2(\vec{r}) + 2\mu A(\vec{r})\cos(2\pi\vec{q}_c\vec{r} + \Phi(\vec{r}))$$

where $\vec{q}_c$ denotes the carrier frequency and μ the contrast of the interference fringes. This intensity distribution consists of two parts: The first part, $1 + A^2(\vec{r})$, represents the intensity of the corresponding conventional electron micrograph, whereas the second part shows both amplitude $A(\vec{r})$ and phase $\Phi(\vec{r})$ of the aberrated electron wave encoded as contrast modulation and bending of interference fringes, respectively. The reconstruction of the aberrated electron wave is performed by means of a computer programmed with the applicable laws of wave optics [Franke et al. (1988), Rau et al. (1991)]. The first step is a Fourier transformation yielding a complex spectrum. The central band represents the

diffractogram of a conventional electron micrograph, whereas each of the two side-bands corresponds to the complex diffraction pattern found in the back focal plane of the objective lens. In the second step, one of them is numerically centred and isolated in order to exclude information from the auto-correlation. Finally, an inverse Fourier transformation yields the aberrated electron wave in amplitude $A(\vec{r})$ and phase $\Phi(\vec{r})$.
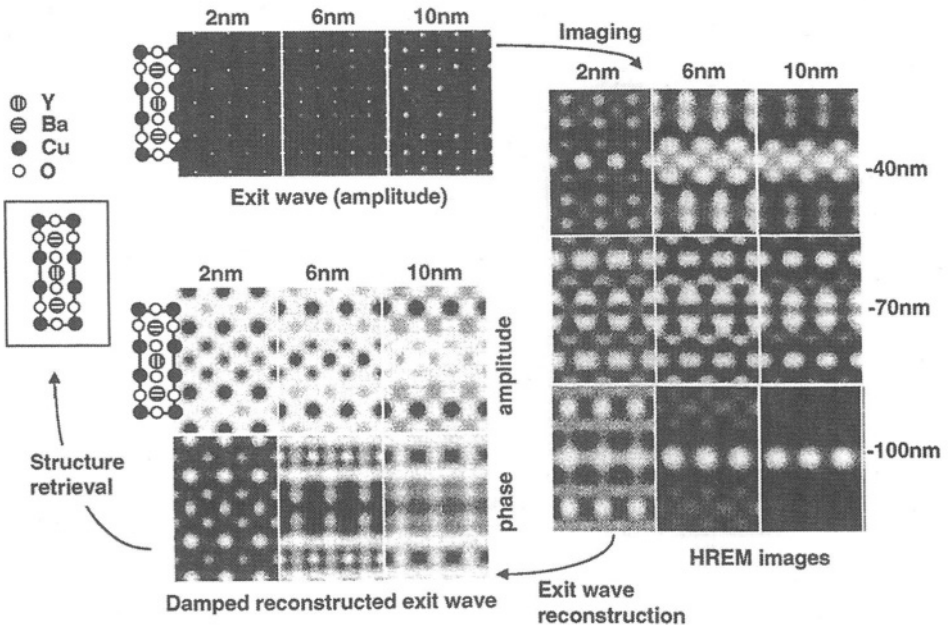

Figure 2. Schematic representation of the through focus exit wave reconstruction. One records a series of HREM images with precisely known focus steps. The images are corrected for specimen drift by cross correlation. With these HREM images and the microscope parameters a computer program estimates a first exit wave, which is subjected to the transfer of the microscope allowing a comparison of the experimental HREM images and the calculated ones, which in turn allows a further refinement of the exit wave. On the parabola, in the 3D transform of the series of HREM images, the linear information is located. In the first step of the exit wave reconstruction the information on this parabola is taken to reconstruct the exit wave. In a subsequent step images calculated from the exit wave are compared with individual HREM images of the series, thus including the non-linear interactions.
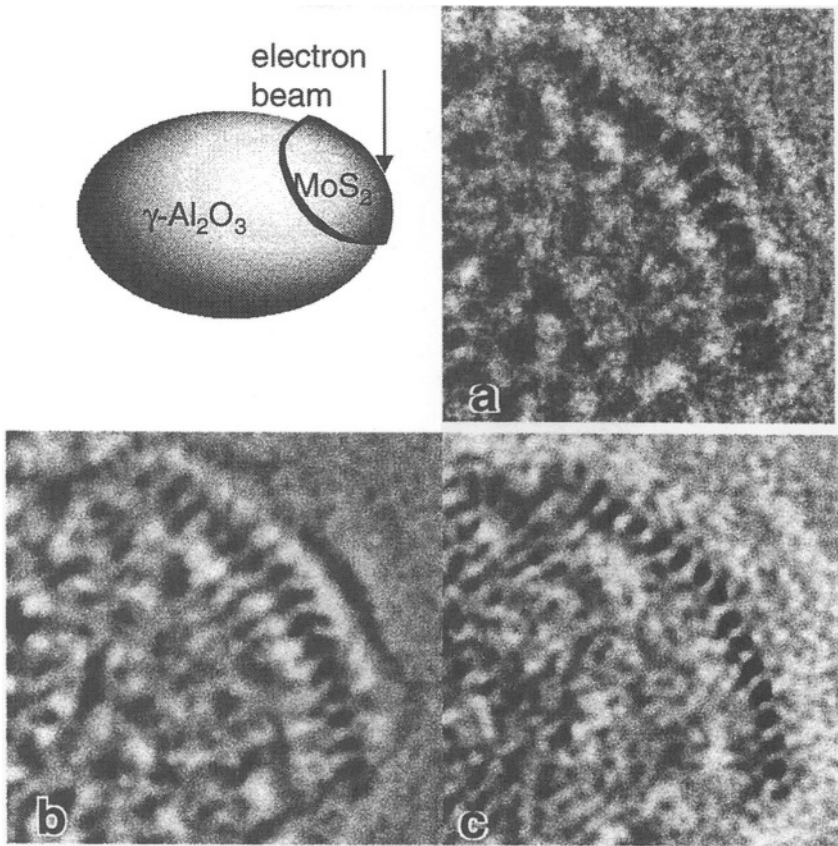
Figure 3. Schematic representation of the location of a MoS$_2$ particle location on the γ-Al$_2$O$_3$ substrate. The covering of the γ-Al$_2$O$_3$ particle by the MoS$_2$ particle like a blanket. (a), (b) and (c) show HREM image of a MoS$_2$ particle on γ-Al$_2$O$_3$ and the phase and the amplitude of the reconstructed exit wave respectively. The amplitude shows predominantly the Mo and Co atoms whereas the phase shows the S atoms as well leading to a v-shaped image feature. Note also that only the part of the slab that is parallel to the electron beam is highlighted.

The wavefunction at the exit face of the object can be calculated from the wavefunction in the image plane by applying the inverse phase transfer function of the microscope. This procedure is in principle straightforward. However, the retrieval of information up to the information limit requires that the transfer function must be known with highest accuracy. Hence, this requires an accuracy of better than 1% for C_s and 1 nm for the absolute focus. The accuracy and hence the knowledge of the aberration coefficients is most crucial for all high-resolution methods.
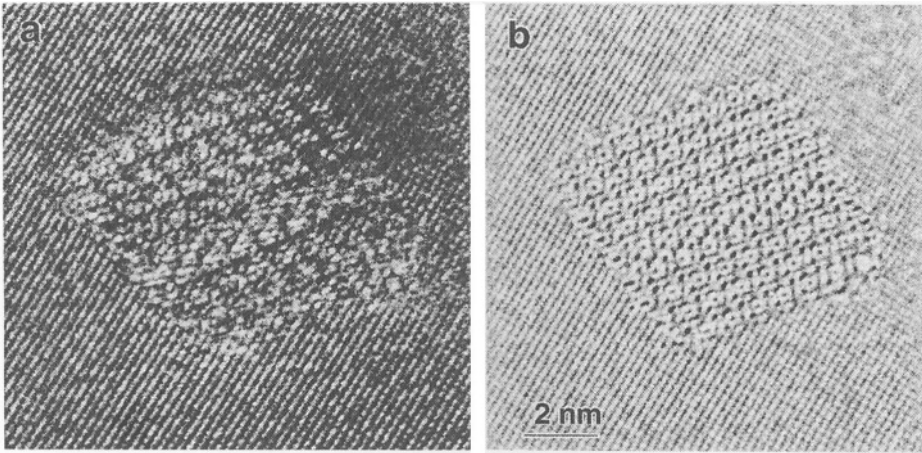
Figure 4. (a) Experimental HREM image, being the first (defocus is about -70 nm) of the series of 20 images used for the reconstruction of the exit wave given in (b), which shows the phase of the exit wave; the amplitude of the exit wave is quite similar and is therefore not shown.

The exit wave can only be correctly interpreted if this is done at the exact focus and with a proper correction of all the lens aberrations, because otherwise phase and amplitude information are mixed. A robust method for determining the exact focus is to exploit the entropy of the exit wave as a function of focus [Tang et al (1996), Van Dyck et al (1996c)]. An efficient determination for all microscope parameters is possible with the optical fingerprint method reported by Thust et al (1996). This method, however, requires a round illumination (not the elliptical illumination used for acquisition of off-axis electron holograms) and a thin amorphous part of the specimen which should not be present at clean specimen. In off-axis electron holography, an algorithm for determination and correction of the coherent wave aberration has been developed which is based on a combination of Genetic Algorithm and Downhill-Simplex-Algorithm [Lehmann (2000)]. The basic criterion is the minimisation of the amplitude contrast, which is a well-established correction guideline for weak phase objects.

Two examples of the strength of the reconstruction are given in Figures 3 and 4. Figure 3 illustrate the use of through-focus exit wave reconstructions for the imaging of MoS_2 slabs to improve the interpretability of the data. MoS_2 to which cobalt sulphide or nickel sulphide has been added on an atomic scale (CoMoS and NiMoS catalysts respectively) is employed on a large scale as catalyst in the hydrotreating of oil. Figure 4 shows the use of exit wave reconstructions in the analysis of the structure of small precipitates in commercial Al-Mg-Si alloys, which

play a crucial role in increasing their mechanical strength. The composition and structure of the β'' phase, occurring as precipitates of typically $4x4x50$ nm^3, which are associated with a particularly strong increase in mechanical strength, has been determined. Element analysis using a small electron beam probe indicates the composition to be Mg_5Si_6 [Zandbergen et al (1997a)]. Fig 4b shows a reconstructed exit wave of a β'' precipitate embedded in aluminium, whereas one of the HREM images of the through focus series is shown in Figure 4a. A comparison of Figures 4a and 4b shows that a major advantage of the exit wave is that the information, which is delocalized in the HREM images resulting in a blurred image (Fig. 4a), is restored to its origin (Fig. 4b).

From HREM images to the structure

Once the exit wave has been accurately determined a major final step remains: the retrieval of the projected structure of the object from the exit wave. This is only straightforward if the object is thin enough to act as a phase object: in that case the phase is proportional to the electrostatic potential of the structure, projected along the beam direction. However, if the object is thicker as is mostly the case, the problem is much more complicated. In principle one can retrieve the projected structure of the object by an iterative refinement based on fitting the calculated and the experimental exit wave. This is basically a search procedure in a giant parameter space whereby it is possible to get stuck in a local maximum [Thust and Urban (1992)]. It is possible, however, to obtain an approximate structure model in a more direct way. If the object is a crystal viewed along a zone axis, the incident beam is parallel to the atom columns. It can be shown [Van Dyck (1996b)] that in such a case, the electrons are trapped in the positive electrostatic potential of the atom columns, which then act as channels.

If the distance between the columns is not too small, a one-to-one correspondence between the wavefunction at the exit face and the column structure of the crystal is maintained. Within the columns, the electrons oscillate as a function of depth without however leaving the column. It is important to note that channelling is not a property of a crystal, but occurs even in an isolated column and is not much affected by the neighbouring columns, provided the columns do not overlap. Hence the one-to-one relationship is still present in case of defects such as translation interfaces or dislocations provided they are oriented with the atom columns parallel to the incident beam. One can explicitly specify the thickness dependency of the wavefunction at the exit face of a column as [Van Dyck, 1996b, 1997]:

$$\psi(\mathbf{R},z) = 1 + \left[e^{-i\pi\frac{E}{E_o}kz} - 1 \right]\phi(\mathbf{R})$$
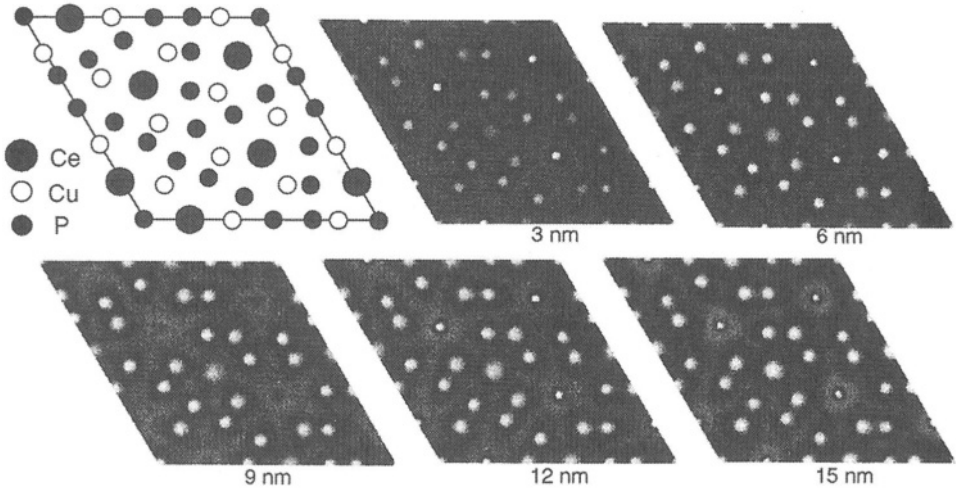
Figure 5. A structure model of $Ce_5Cu_{12}P_9$ and 5 calculated exit waves (amplitude) for 5 different thicknesses and indicated below the images. The images are one unit cell large and correspond to the structure mode. Note that the Ce atoms (the strongest scattering atoms) are most dominant in the very thin exit wave but for instance almost absent in the exit wave of 9 nm thickness.

where z is the thickness, E_o a constant expressing the electron matter interaction and E the energy of the column. This result holds for each isolated column. In a sense, the whole wavefunction is uniquely determined by the eigenstate $\phi(\mathbf{R})$ of the Hamiltonian of the projected columns and its energy E which are both functions of the "density" of the column and the crystal thickness. It is clear from the formula above that the exit wave is peaked at the centre of the column and varies periodically with depth. The periodicity is inversely related to the "density" of the column. In this way the exit wave still retains a strong correspondence with the projected structure, whereby the positions are still (almost) the same but the contrast (in phase or amplitude) cannot be used to determine the scattering potential in the projected structure unless the thickness is accurately known. We used this to determine the structure of $Ce_5Cu_{12}P_9$ [Zandbergen (1998a)]. From the exit wave we were able to determine the positions of the columns. This model was the basis of a structure refinement using electron diffraction data for several thicknesses, whereby first the position of the columns was refined assuming all columns to be equal Cu columns. Next the occupancies were refined, allowing one to decide which atom columns contained, Ce, Cu or P. The final refinement gave very accurate atomic positions.
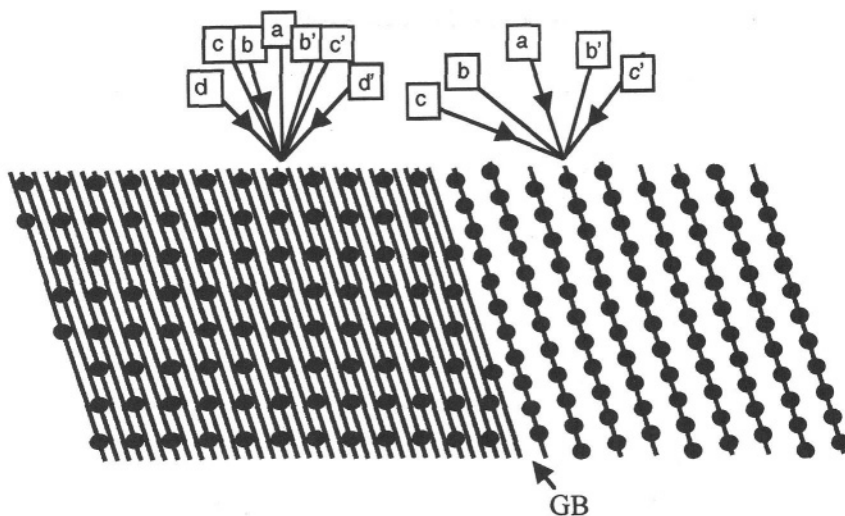
Figure 6. (a) Schematic representation of an atomic arrangement around a grain boundary. It is supposed that lattice imaging is only possible along the directions a, b, c and d. The crystallographic arrangement of the grains is such that the direction b in the left grain is parallel to the direction a of the right grain, and the grain boundary is parallel to the a direction of the grain on the right. Because of that favourable orientation relation structure images of both grains are obtainable and the image of the grain boundary is as sharp as possible. For this orientation columns can replace the rows of atoms, each with its own scattering potential depending of the weight of its atoms and their spacing. The further the orientation deviates from the directions a, b, c and d, the poorer the contrast of the HREM images, which trend is faster for thicker specimens. Thus a very thin specimen will still allow an appreciable misorientation (several degrees).

HREM investigation of grain boundaries

In the HREM investigation of grain boundaries and surfaces three aspects are very important restrictions: the shape and orientation of the grain boundary, the crystal lattices of the adjacent crystals and the resolution of the electron microscope. The shape and orientation of the grain boundary is important, because HREM provides in first approximation only projections of the structure, such that only lateral information and no depth information is available. This implies that the information of a grain boundary that is not parallel to the electron beam

will be smeared out. Concerning the determination of rough shapes, a lot of development has been done in the last few years on the determination of the shape of biological particles by means of electron tomography [Waltz (1997), Bakker (1996)]. The present state of the art is that a 3-D resolution of about 1 nm can be obtained. For this a tilt series from –70° to +70° with increments of 2° are typically used. The 3D reconstruction of these biological specimens is based on contrast changes due to the overlap of scattering material in projection. In the study of inorganic solid state materials a 1 nm resolution is insufficient and also more difficult to obtain. The 1 nm resolution is insufficient because one will be interested in the atomic arrangements at the grain boundary (e.g. even an amorphous grain boundary layer of 0.5 nm can strongly influence the properties). The 3D reconstruction of grain boundaries is more difficult when these materials consist of (small) crystals. Crystallinity results in extra contrast as can be seen in Figure 1, which depends very strongly on the orientation. In orientations where the crystal is in a low-index orientation (a low index orientation is an orientation [hk1] that has a low sum h+k+1.), it scatters the electrons much stronger than in a high-index orientation. This cancels the one-to-one correspondence between contrast and the projected average scattering potential. This problem can be partly overcome by using a conical illumination or by using a high angular dark field detector in combination with scanning transmission electron microscopy [Thomas, 2001].

A crystalline specimen allows one to obtain a structure image. In this case one has to orient the crystal such that the projection of the structure along the electron beam results in image features that can be resolved given the resolution of the electron microscope. This implies that the imaging can only be done with the electron beam along a small selection of crystal directions (see Figure 6), whereby the better the resolution of the electron microscope the more directions can be used.

If the crystal is perfectly aligned, the atoms can be considered as aligned in columns. In this case a column scattering potential [Van Dyck, 1996b, 1997] can replace the scattering potential of the atoms. The column scattering potential depends on the weight of the atoms and their distance along the column. If the crystal is tilted such that the column is not exactly along the electron beam (mistilt less than 1°) this column approach is still valid.

Summing up the requirements for obtaining HREM images of grain boundaries that can be interpreted in a straightforward way: i) the grain boundary is straight, ii) the grain boundary is parallel to the electron beam, iii) one of the grains and preferable both are in such an orientation, that lattice imaging is possible. Obviously most of these requirements become the more stringent the thicker the specimen. On the other side, a too thin specimen might not reflect the initial structure of the grain boundary due to changes induced by the thinning of the specimen or lattice relaxation due to the very limited thickness of the specimen. The interaction between

electrons and matter is very large (about 10^5 times larger than for X-rays), such that very small specimen thicknesses can be investigated. The specimen thickness required for a good image contrast ranges from 1 to 10 nm depending on the scattering potential. This implies that the requirements that the electron beam is parallel to the grain boundary and parallel to atom columns are not very stringent.
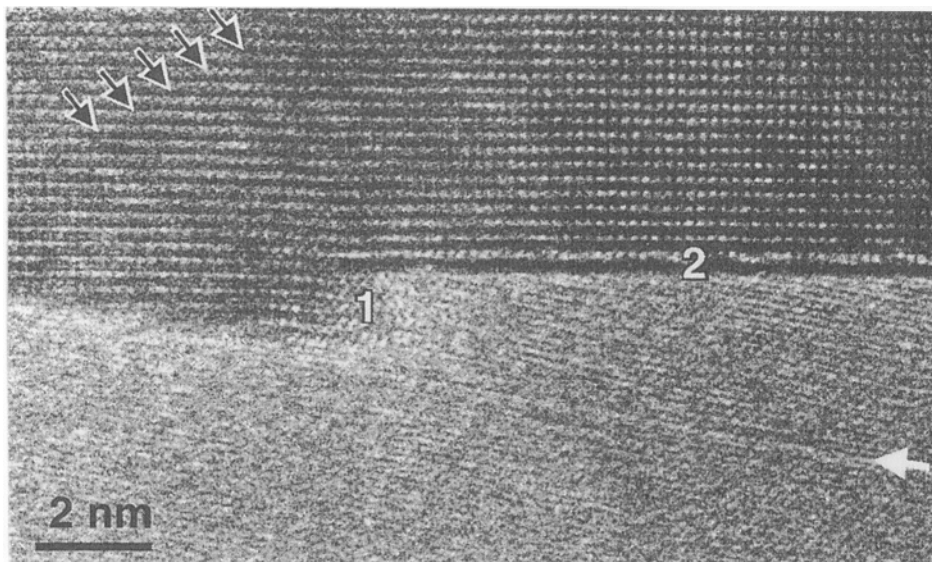

Figure 7. HREM image of grain boundaries in MgB$_2$ polycrystalline material. The top grain is in [100] orientation such that the crystal lattice can be seen in two directions. The lower part consists of two grains that are both in an orientation that allows only the imaging of the (001) fringes. These two grains are twisted about the c axis; the twist boundary is visible as a somewhat whiter line (indicated by the white arrow). The twist angle cannot be deduced from this single HREM image but can be obtained easily by a specimen tilt and monitoring the diffraction patterns of both grains. The atomic positions at this grain boundary cannot be determined from this viewing direction. Also the structure in the well oriented crystal is not obvious in areas such as 1 and 2, because of overlap of two crystals along the viewing direction as in 1 or because of delocalisation as in 2. The line of bright dots in the top grain nearest to the grain boundary shows a different contrast compared to the other lines of bright dots. This could be due to some lattice relaxation near the boundary or due to delocalisation effects. The black arrows indicate weak Moire fringes due to the overlap of yet another crystal with the one in the top.

Obviously, the better the resolution of the microscope, the more directions one can get structural images from. In particular for the study of grain boundaries this increase in suitable directions is important. Assuming that a HREM allows a double tilt of ±30°, one out of three grain boundary can be aligned along the electron beam. Assume next that by rotation of the specimen about the interface normal with a range of 40°, one orientation can be reached allowing structure imaging for the first or the second adjacent grain. Then the chance of being able to have a grain boundary being parallel to the electron beam with the first grain only (the situation for a surface) is still one out of three. Assuming random orientation of the grains and that the maximum misorientation is 2°, the chance that an orientation can be found in which both grains are in a both grains in an orientation allowing structure imaging is 1 over 30. A doubling of the number of orientations allowing structure imaging increases this chance to 2 over 15. Figure 2 illustrates the interpretation problems one can encounter. Here an example of the study of grain boundaries in the superconducting MgB_2 is shown.

Adding information of the compositional and electronic structure

In fact one aims at a complete picture of the *Atomic* arrangement, the *Chemical* composition and the *Electronic* structure on an atomic scale. The atomic arrangement with a resolution of about 1.7 Å can be obtained through HREM experiments as discussed above. The chemical composition can be obtained through Energy Dispersive X-ray analysis (EDX-analysis) combined with analysis of the energy loss of the electrons that are transmitted through the specimen (Electron Energy Loss Spectroscopy (EELS)). In both cases the minimum area that can be analysed depends on the probe size, which can be as small as 2Å (see for instance Yan (1998)). The electronic structure can in principle be determined from EELS data, since the loss of energy of the inelastically scattered electrons will be determined by the electron-specimen interactions, which are not only atom dependent (coarse structure of EELS spectrum), but depend also on the environment of the atom (fine structure of the EELS spectrum). EELS is presently possible with a resolution of approximately 0.1 eV. This will create new and exciting possibilities in the investigation of the physics and chemistry of materials.

References
Bakker T.S. and R.H. Cheng, J. Struct.Biol., **116** (1996) 120.

Bokel R.M.J., Jansen J.,Zandbergen H.W. and van Dyck D. (2001), Ultramicroscopy 87 89-96
Bokel R M J, J Jansen, D van Dyck, H W Zandbergen; Ultramicroscopy, 1999, p. 255-269.
Coene W., Janssen G., Op De Beeck M. and Van Dyck D. (1992a), Phys. Rev. Lett., **69**, 3743
Franke F.J., Herrmann K.-H., Lichte H. (1988), Scanning Microscopy Supplement **2**, 59 - 67

Fu Q., Lichte H., Völkl E. (1991), Physical Review Letters **67**, 2319

Hÿtch M.J. and W.M. Stobbs (1994), Ultramicroscopy **53**, 191.

Ishizuka K., Tanji T., Tonomura A., Ohno T., Murayama Y. (1994), Ultramicroscopy **53**, 361

Jansen J., Tang D., Zandbergen H.W. and Schenk H. (1998), Acta Cryst A. Acta Cryst. A **54**, 91

Kienzle O., F. Ernst and G. Möbus, Journal of Microscopy, **190** (1998) 144-158 144-158

King W.E., G.H. Cambell, S.M. Foiles, D. Cohen K. Hanson, J. Micr., **190** (1998) 131-143.

Kirkland E.J (1984), Ultramicroscopy **15**, 151-172

Kirkland E.J., Siegel B.M., Uyeda N. and Fujiyoshi Y. (1985), Ultramicroscopy **17**, 87-104

Kirkland E.J. (1982),. Ultramicroscopy **17**, 87-104

Lehmann M., Lichte H. (1994) , 13ᵗʰ Intern Congr on Electron Microsc, ICEM13, Paris, 293

Lehmann M. (2000), Ultramicroscopy **85**, 165 - 182

Lichte H. (1986), Ultramicroscopy **20** 293

Lichte H. (1992), Ultramicroscopy **47**, 223

Malamidis D., Lichte H. (1998), Proceedings of the 14ᵗʰ International Congress on Electron Microscopy ICEM14, Cancun, Vol I, 561

Merkle K.L., Interface Science **2**, (1995) Kluwer Academic Publishers, Boston, 311-345.

Meyer R.R. (2001), submitted to Ultramicroscopy

Möbus G., R. Schweinfest, T. Gemming, T. Wagner M. Rühle J. Micr., **190** (1998) 109-130.

Möllenstedt G., Düker H. (1956), Vol. 145, 377 - 397

Op de Beeck M., Van Dyck D., Coene W. (1995), (Ed. A. Tonomura et al.), North Holland-Elsevier, ISBN 0-444-82051-5, p. 307-316.

Orchowski A., Rau W.D., Lichte H. (1995), Physical Review Letters **74**, 399

Rau W.-D., Lichte H., Völkl E., Weierstall U. (1991), Journal of Computer-Assisted Microscopy **3**, 51

Saxton W.O. (1986), in: Proc. XIth International Congress on Electron Microscopy, Kyoto, post deadline contributions page 1.

Schiske P. (1973), in: Image Processing of Computer-aided Design in Electron Optics (Ed. P. Hawkes).

Siegel R.W., Mater. Sc. Eng, A168 (1993) 189

Stadelman P.A. (1987), Ultramicroscopy **21**, 131-146

Steinecker A. and W. Mader (1998), Journal of Microscopy 190 281.

Tang D., Zandbergen H.W., Jansen J., Op de Beeck M. and van Dyck D. (1996), Ultramicroscopy **64**, 265-276

Thomas P.J., Midgley P.A. (2001), J. Phys. Chem. B, 105, 7882.

Thust A. and Urban K. (1992), Ultramicroscopy **45**, 23-42

Thust A., Overwijk M.F.H., Coene W.M.J., and Lentzen M. (1996), Ultramicroscopy **64**, 249.

Van Dyck D., M. Op de Beeck(1990), in: *Proc. XIIth International Congress for Electron Microscopy (Seattle),* San Francisco Press Inc., p. 26-27

Van Dyck D. and De Jong A.F. (1992), Ultramicroscopy **47**, 266

Van Dyck D., Lichte H. and K.D. van der Mast (1996a), Ultramicroscopy **64**,1

Van Dyck D. and Op De Beeck M. (1996b), Ultramicroscopy **64**, 99

Van Dyck D., op de Beeck M., Tang D., Jansen J. and Zandbergen H.W. (1996c), IEEE Intern. Conf on image processing 1996 Los Alamitos 737-170

Van Dyck D., Handbook of Microscopy 1997.

J. Walz, et al, J. Struct.Biol., **120** (1997) 387-395.

Yan Y., M.F. Chisholm, G. Duscher, A. Matti, S.J. Pennycook and S.T. Pantelides, Phys. Rev. Lett. **81** (1998) 3675-3678

Zandbergen H.W., Andersen S.L. and Jansen J. (1997), Science **227**, 1221

Zandbergen H.W. and Jansen J. (1998), J. Microscopy **190**, 222

Zandbergen H W, R M J Bokel, E Connolly and J Jansen 1999; Micron, 30, p. 395 - 416

NANOELECTRONICS

G. Allan, C. Delerue, C. Krzeminski, M. Lannoo*

Institut d'Electronique et de Microélectronique du Nord, Département Institut Supérieur d'Electronique du Nord, 41 boulevard Vauban, 59046 Lille Cédex, France
* Laboratoire Matériaux et Microélectronique de Provence, ISEM, Place G. Pompidou, 8300 Toulon, France

1. INTRODUCTION

In this chapter we intend to discuss the major trends in the evolution of microelectronics and its eventual transition to nanoelectronics. As it is well known, there is a continuous exponential tendency of microelectronics towards miniaturization summarized in G. Moore's empirical law. There is consensus that the corresponding decrease in size must end in 10 to 15 years due to physical as well as economical limits. It is thus necessary to prepare new solutions if one wants to pursue this trend further. One approach is to start from the ultimate limit, i.e. the atomic level, and design new materials and components which will replace the present day MOS (metal-oxide-semiconductor) based technology. This is exactly the essence of nanotechnology, i.e. the ability to work at the molecular level, atom by atom or molecule by molecule, to create larger structures with fundamentally new molecular organization. This should lead to novel materials with improved physical, chemical and biological properties. These properties can be exploited in new devices. Such a goal would have been thought out of reach 15 years ago but the advent of new tools and new fabrication methods have boosted the field.

We want to give here an overview of two different subfields of nanoelectronics. The first part is centered on inorganic materials and describes two aspects: i) the physical and economical limits of the tendency to miniaturization; ii) some attempts which have already been made to realize devices with nanometric size. The second part deals with molecular electronics, where the basic quantities are now molecules, which might offer new and quite interesting possibilities for the future of nanoelectronics.

2. DEVICES BUILT FROM INORGANIC MATERIALS

These are mainly silicon based microelectronic devices which have invaded our life. Integrated circuits are now found everywhere not only in Personal Computers but also in a lot of equipment we use each minute as cars, telephones, etc. We always need more memory as well as faster and cheaper processors.

The race for miniaturization began just after Kahng and Atalla [1] demonstrated in 1960 the first metal-oxide semiconductor field effect transistor (MOSFET) (Fig. 1). It turned out to be a success because a large number of transistors and their interconnections could be easily built on the surface of a single silicon chip. Ten years later, the first 1 kilobyte memory chip was on the market and this trend has been followed until now (a 64 megabit one contains more than one hundred millions electronic components). In 1965, Gordon Moore predicted what is known as the Moore's law: for each new generation of memory chip on the market, the number of components on a chip would quadruple every three years. Miniaturization not only decreases the average current cost per function (historically, ~25%/year) but also improves the cost-performance ratio. In the same time, the market growth was close to 15%/year.

Most of the improvement trends are exponential and are resumed in the scaling theory [2]. It shows that a MOSFET operates at a higher speed without any degradation of reliability if the device size is scaled by a factor 1/k and at the same time the operating voltage is scaled by the same factor. The speed of the circuits has increased up to one Gigahertz in today's personal
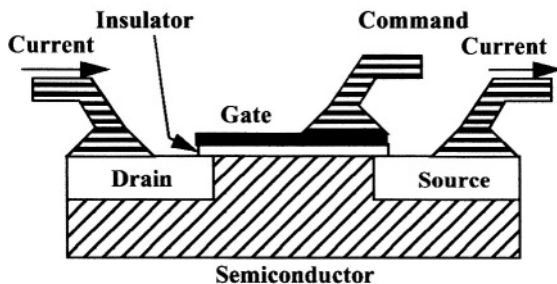
Figure 1: A metal oxide semiconductor field-effect transistor (MOSFET). When the voltage of the gate is positive, electrons accumulate near the semiconductor surface making the channel between source and drain conducting.

computers. Continued improvements in lithography and processing have made possible the industry's ability to decrease the minimum feature sizes used to fabricate integrated circuits. For four decades, the semiconductor technology has distinguished itself by the rapid pace of improvement in its products and many predicted technological limitations have been overcome. In the same time it is difficult for any single company to support the progressively increasing R&D investments necessary to evolve the technology. Many forms of cooperation have been established, as the «International Technology Roadmap for Semiconductors" [3] which is the result of a large world consensus among leading semiconductor manufacturers. It looks at the 10-15 years in the future showing that most of the known technological capabilities will be approaching or have reached their limits. Continued gains in making VLSI (Very Large Scale Integration) seem to be first severely limited by technological considerations [4].

The first one which is known as a «power crisis» is an heat dissipation problem. While the size of the components is reduced by a factor k, the scaling theory shows that the power density increases like $k^{0.7}$ [2]. A today's single chip processor in production requires 100 W and this value will rise to 150 W during the next decade. Low-power design of VLSIs is also necessary because they are more and more used in mobile electronic systems which need long-lasting batteries. The reduction of the supply voltage (~0.37 V in 2014) will be accompanied by an increase of the current needed to operate VLSIs to huge values (500 A). This contributes to the second limitation: the «interconnect crisis».

A large operating current gives rise to voltage drop problems due to the resistance of the interconnections and to reliability degradation due to electro-migration of defects in the conducting wires. On the other hand, to be attractive, a scaling of the components must be accompanied by a scaling of the interconnect line thickness, width and separation. Then signal integrity is also becoming a major design issue. A high crosstalk noise is due to larger capacitive couplings between interconnects. A smaller geometry also increases the RC (resistance-capacitance) delay (it increases as $k^{1.7}$ [2]). If this delay increases, the signal cannot propagate anywhere within the chip within a clock cycle.

According to T. Sakurai [2], a «complexity crisis» will appear. Design complexity is increasing superexponentially. The first obvious reason is the increased density and number of transistors. The complexity is also growing due to designs with a diversity of design styles, integrated passive components and the need to increase incorporate embedded software. The integrated circuit is built on several interconnected levels which interact. Verification

complexity grows with the need to test and validate the designs. Finally the tests must be done at higher speed, higher levels of integration and greater design heterogeneity.

There are potential solutions to solve some of these problems during the 15 next years [3]. In some other cases the solution is still unknown and this will have a price that people could not continue to afford. Moreover until now, we have considered more technological limitations but new fundamental quantum phenomena will also appear. The first one which has already been investigated is the tunnel effect through the gate insulator which is made of the silicon native oxide SiO_2 [4]. One important factor of the MOSFET is the gate capacitance of the parallel plate capacitor made by the gate and the conducting channel in the semiconductor (Fig. 1). This capacitor is filled by an insulator which is at present silicon dioxide. The charge of this capacitor controls the current between the drain and the source. When the gate (which is one of the capacitor plates) is scaled by 1/k, the gate thickness scales as 1/k to maintain the same capacitance. It will be reduced to 0.7 nm in 2014. at the same time the gate voltage should be reduced to maintain the electric field across the oxide below an undesirable value. This is equivalent to 3 layers of oxygen and 2 of silicon in the oxide. When the insulator thickness is reduced, the overlap of the electronic wavefunctions on both barrier sides increases exponentially and this gives rise to a non-zero probability for the electrons to tunnel across the barrier. An other formidable challenge is to replace the silicon oxide by a dielectric material with a higher dielectric constant. A review of current work and literature in the area of alternate gate dielectrics is given in reference [5].

Doping the semiconductors with impurities, donors (n type) or acceptors (p type), is an essential feature to get free carriers and thus get a substantial conductivity. With current impurity concentration one can show that below a 0.1 * 0.05 mm gate, there are about 100 free carriers only. This means that a fluctuation of plus or minus one charged impurity in the channel gives a 1% error, which represents another type of limitation.

Some other new quantum effects appear due to the size reduction:

- as in a molecule or an atom, the electron energy can only take discrete value as opposed to the classical value or to the existence of bands of allowed energies for bulk materials.

- when the wave function associated with an electron takes several distinct channels, interference effects occur which give rise to conductance fluctuations with a root mean square deviation equal to e^2/h. Such effects are only observed when the phase is not destroyed by inelastic collisions, i.e. when the distance covered is lower than the inelastic mean free path. This is close to

0.1 μm at room temperature for GaAlAs-GaAs heterojunctions or in Si.

  - a one-dimensional quantum wire is analogous to a wave guide connected to electron reservoirs. When a voltage is applied between these reservoirs, electrons are injected in the wave guide. The number of one-dimensional channels for an electron depends on the number of energy levels below the Fermi energy. This number N of discrete levels due to the confinement perpendicular to the wire is fixed by the width of the quantum wire. Within these conditions the wire conductance is quantized and equal to $2Ne^2/h$.

  - discrete energy levels in different wells can interact through a tunnel effect. When a polarization is applied between the outer reservoirs, the conductance is small except when the quantum wells energy levels are aligned. Then the current is maximum and decreases for a further increase of the applied voltage. This gives rise to a negative differential resistance (see Fig-
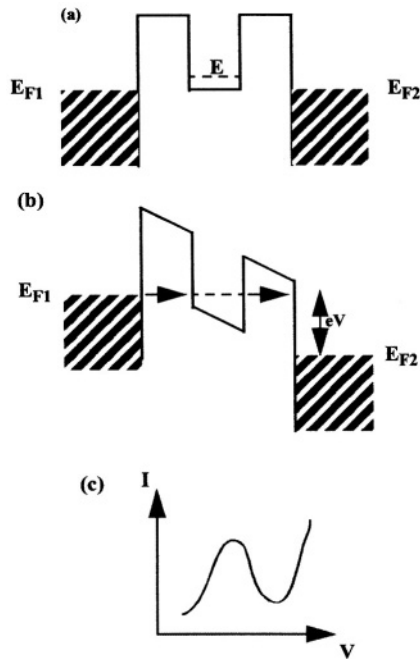
Figure 2: Resonant tunneling effect (a) without and (b) with an applied voltage. (c) Current as a function of the voltage.

ure 2).

These effects which limit the feasibility to reduce the device size below a certain value can also be used to invent new architecture. One electron devices are certainly the most surprising and promising effect. The simplest one is the tunneling junction shown on Figure 3 [6]. It is a metal-insulator-metal junction between two electron reservoirs. When the barrier width or height is large, the probability for an electron to cross the barrier when a polarization is applied is small and the tunneling is quantized: the electrons cross the barriers one by one. Then the system is equivalent to a capacitor C and an electron leak due to tunneling across the insulating layer (Figure 3b). When a voltage V is applied, the tunneling of an electron is possible if the energy difference

$$\Delta E = \frac{Q^2}{2C} - \frac{(Q-e)^2}{2C} \tag{1}$$

for the capacitor with a charge equal to Q (=CV) and to Q-e becomes
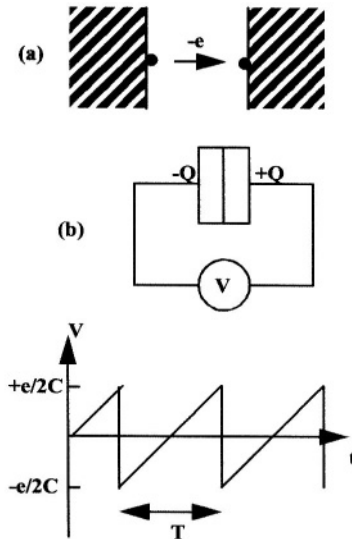
Figure 3: a) Metal - Insulator - Metal tunneling junction; b) Its equivalent diagram and c) the potential for a constant current I (=e/T) as a function of time.

positive. When $\Delta E < 0$, (i.e. $|V| < \dfrac{e}{2C}$) no electron can cross the barrier and we have a "Coulomb blockade". To maintain a constant current I, one must applied a saw tooth potential with a frequency I/e. It is difficult to realize such a system and the following electron box is much easier to make.

Let us take a metallic quantum box separated from two electron reservoirs on one side by an ideal capacitor C_s and on the other one by a tunnel junction with a capacitance C (Figure 4). Electrons can tunnel into the quantum box one by one until a charge $-Ne$, N depending on the applied voltage V. The simplest way to calculate $N(V)$ is to define the ionization level $\varepsilon_i(N, N+1)$. For the box, $\varepsilon_i(N, N+1)$ is equal to the total energy differ-
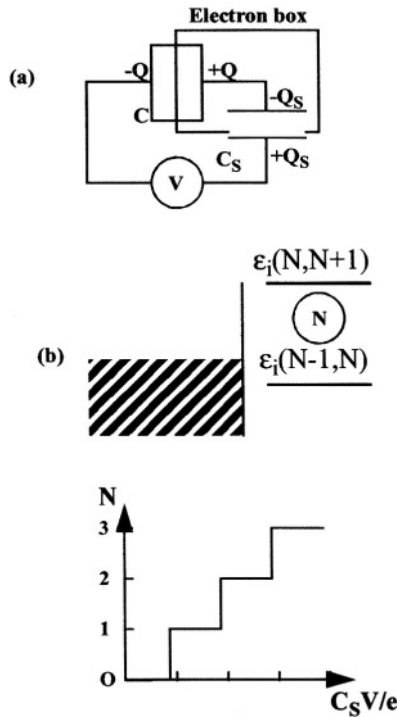
Figure 4: a) Electron box (a) and its energy levels (b). Cs is a tunneling junction. The electron number N stored on the island varies as a staircase as a function of the applied voltage (c).

ence $E_{TOT}(N+1) - E_{TOT}(N)$ which is roughly equal to $\dfrac{dE_{TOT}}{dN}$. Applying the Koopmans theorem, this quantity is equal to the lowest one-electron energy level which can accommodate an extra electron when the box is already charged with N electrons. A classical electrostatic calculation gives the potential of the charged box one must add to the HOMO energy level of the isolated box $\varepsilon_{i,\,metal}$ to get the ionization potential:

$$\varepsilon_i(N, N+1) \;=\; \varepsilon_{i,\,metal} + \frac{e^2}{2(C+C_s)}\left(N + \frac{1}{2} - C_s\frac{V}{e}\right) \tag{2}$$

As shown on Figure 4b, a stable -Ne box charge occurs when the metal Fermi level is located between $\varepsilon_i(N, N+1)$ and $\varepsilon_i(N-1, N)$. A step in $N(V)$ occurs each time the metal Fermi level is aligned with an ionization potential and we can easily control the box charge.

The next step is to realize a one-electron transistor [6] shown on Figure 5 with two tunneling junctions and an ideal capacitor. The gate potential V_G controls the charge of the dot and the current. More complicated devices allow to control the electrons one by one like the electron pump [7] and the single electron turnstile [8]. Experimental results and a good introduction can be found in Ref [9-11].

To observe a Coulomb blockade, the energy difference between two ionizations levels $\dfrac{e^2}{2(C+C_s)}$ as calculated from Equation (2) must be larger
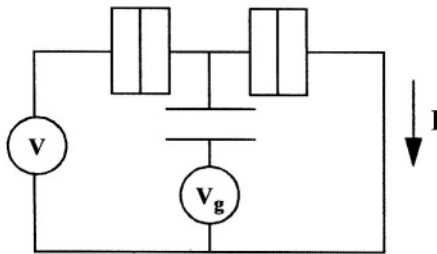
Figure 5: One-electron transistor. The current I and the charge of the island is controlled by the gate potential V_g.

than *kT*. The first experiments were done at low temperature but one must reduce the size to work at room temperature. Single electron electronics has been proposed by Tucker in 1992 [12]. This would allow a further reduction of size and electrical power, both conditions being necessary to increase the speed of a device. Some components have already been realized [13-19] but remain difficulties due notably to non-reproducibility.

3. MOLECULAR ELECTRONICS

If the reduction in size of electronic devices continues at its present exponential pace, the size of entire devices will approach that of molecules within few decades. However, major limitations will occur well before this happens, as discussed previously. For example, whereas in current devices electrons behave classically, at the scale of molecules, they behave as quantum mechanical objects. Also, due to the increasing cost of microelectronic factories, there is an important need for much less expensive manufacturing process. Thus, an important area of research in nanotechnology and nanoscience is molecular electronics, in which molecules with electronics functionality are designed, synthesized and then assembled into circuits through the processes of self-organization and self-alignment. This could lead to new electronics with a very high density of integration and with a lower cost than present technologies. In this section, we review recent progress in molecular electronics and we describe the main concepts at the origin of its development. We show that the latter is strongly connected to the invention of new tools to identify, to characterize, to manipulate and to design materials at the molecular scale. We also stress the importance of the basic knowledge which has still to be obtained in the way towards the integration of molecules into working architectures.

3.1 Concepts and origins of molecular electronics

Quite surprisingly, the first ideas of using specific molecules as electronic devices and of assembling molecules into circuits were proposed more than 30 years ago. At this time, the electronic processors were only in their infancy, and adequate tools to perform experiments on single molecules were not available. However, the concept of molecular electronics is appealing, and two components were proposed, the molecular diode and the molecular wire,

which can be seen as elementary bricks to build more complex devices or circuits. In spite of these early proposals, practical realizations came only recently due to limitations in chemistry, physics and technology. In the following, we briefly describe the basic principles of the two components.

3.1.1 Molecular diode

In 1974, Aviram and Ratner [20] proposed to make an electrical rectifier based on D-σ-A molecules between two metallic electrodes, where D and A are, respectively, an electron donor and an electron acceptor, and σ is a covalent bridge. Figure 6 describes the physical mechanism for the rectification. The electronic states are supposed to be totally localized either on the D side or on the A side. The HOMO(D) and LUMO(D) are high in energy, compared to, respectively, the HOMO(A) and LUMO(A). Therefore, a current can be established at relatively small positive bias, such that the Fermi level at the A side is higher than LUMO(A), and the Fermi level at the D side is lower than HOMO(D), provided that the electrons can tunnel inelastically through the σ bridge. Thus an asymmetric current-voltage $I(V)$ curve is expected like in a conventional electronic diode. In the prototype proposed by Aviram and Ratner, the donor group is made by a tetrathiofulvalene molecule (TTF), the acceptor group by a tetracyanoquinodimethane molecule (TCNQ), and the σ bridge by three metylene bonds. These molecules are seen as the analogs of n and p-type semiconductors separated by a space-charge region. Twenty years have been necessary before the first experimental demonstration of rectifying effects in diodes based on molecular layers [21], and studies have been amplified in this direction recently [22-24]. Nevertheless, the origin of the rectification is still matter of debate [25]. In addition, the Aviram-Ratner principle at the level of a single molecule has not been demonstrated yet.
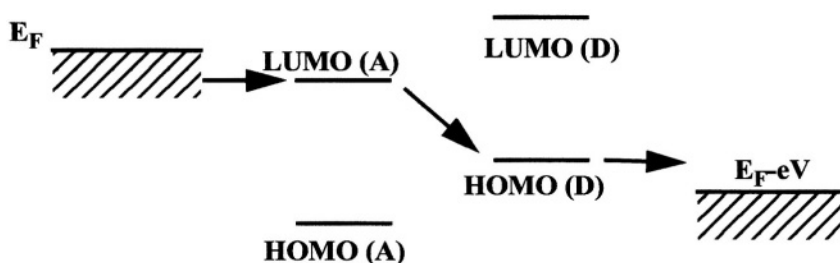
Figure 6: The Aviram-Ratner mechanism for molecular rectification.

3.1.2 Molecular wires

The discovery of the first conductive polymers based on acetylene [26-27] suggested that molecules could have interesting properties to make electrical wires at the molecular scale. These wires are necessary to connect molecular devices into circuits. In 1982, Carter [28] suggested to address the acceptor and donor groups of an Aviram-Ratner diode with polyacetylene chains, and even to control several diodes in the same time. Using this technique, the expected density of components on a chip could be of the order of 10^{14} cm^{-2}, which is far beyond the possibilities of present technologies. One difficulty raised by Carter is that the transport in the molecular chains takes place in the form of solitons whose motion is slow. But this disadvantage would be largely compensated by the higher density.

3.1.3 Molecular circuits

Conventional microelectronic technologies presently follow a top-down approach, processing bulk semiconductor materials to make devices with smaller and smaller sizes. In molecular electronics, the basic components like molecular diodes and wires are used to build more complex devices and circuits. This is the bottom-up approach which starts from the molecular level to build a complete chip. For example, it has been recently proposed to create AND and XOR logical functions using assemblies of molecular films, molecular diodes and nanotubes (wires) [29]. These functions could be used to design additioners and other operations which are currently done in CMOS technologies. However, the assembling of the elementary units will not necessarily lead to the expected device as the interaction between individual molecules may perturb their own function [30]. Thus, other proposals suggest to consider the system as an ensemble and to use directly the chemistry to synthesize molecules with the required functions (e.g. additioners) [31].

3.2 Transport experiments on ensembles of molecules

A great challenge of molecular electronics is to be able to transfer information at the molecular scale in a controlled manner. In the devices described above, it consists of a charged carrier (electron or hole) which is transmitted through a single molecule. During several decades, the impossibility to work at the level of a single molecule has been a major difficulty. However, the characterization of molecular ensembles has been undertaken

by different means which we describe now.

3.2.1 Molecules in a solvent

The first approach consists to study the molecules in a solvent, and to probe the electronic transfer using a combination of chemical and physical methods. It is possible to characterize the electronic transport in solution through the measurement of the oxido-reduction by voltametry and of the electronic excitation by optical absorption. If the chemical reaction takes place inside a molecule, then reaction and intra-molecular transfer become equivalent.

Experiments have been made on donor-ligand-acceptor molecules, like mixed valence compounds recently synthesized [32]. These organo-metallic complexes contain two metallic atoms with different oxidation degrees. The experiments allow the measurement of the electronic transfer between the two sites. For example, Taube has synthesized a stable molecule containing two ruthenium complexes which act as donor and acceptor groups [33]. When the molecule is partially oxidized, a charge transfer is observed between the two ions. Other molecules have been made with a large distance of 24 Å between the two ions, which is obtained by the intercalation of five phenyl groups [34]. An electronic transfer is also observed in this system in spite of the long inter-site distance. This effect is attributed to the electronic coupling induced by the phenyl groups which play here the role of a molecular wire between the two ruthenium ions [35].

Interesting results have been also obtained on biological molecules. In the case of proteins [36], an increase of 20 Å in the distance between the acceptor and donor sites leads to a decrease by a factor 10^{12} of the transfer rate. Thus, in this process, proteins can be seen as a uniform barrier which limits the electronic tunneling. The importance of tunneling effects in biological molecules is presently a well studied topic.

3.2.2 Molecular layers

The second approach is the study of molecules which are self-organized in two-dimensional monolayers on the surface of a conductive substrate. Self-assembled monolayers (SAMs) are obtained by the Langmuir-Blodgett (LB) technique or by chemical grafting on a surface. The SAMs have to be well organized to avoid artifacts due to disorder. Electrical measurements require a second electrode which is made by evaporation of a metal on top of the SAM. This is usually the most difficult task because the metal must not diffuse into the SAM where it could make short circuits [37]. In the

same time, the contact resistance must be small which requires a good control of the metal/SAM interface.

The first results based on this technique have been published by Mann and Kuhn on LB films of alkane chains [38]. Studies of the tunneling through the molecular films show that the molecules are good insulators. Similar results have been obtained on SAMs of n-alkyltrichlorosilane chemically grafted on a Si substrate [39]. These chains realize a barrier of the order of 4.5 eV for the tunneling of electrons or holes [40] and lead to a better insulating layer than SiO_2 at the nanometer scale.

Other works on SAMs concern molecular diodes in the sense of Aviram-Ratner: they are described in previous sections and in ref. [21-25]. Also, nice results have been obtained by Fischer et al [41] on organic heterostructures made with palladium phtalocyanines and compounds based on perylene. Using gold electrodes at 4.2 K, they obtain $I(V)$ curves with clear steps (Figure 7) which are attributed to the resonant tunneling through the molecular levels. The $I(V)$ characteristics is symmetric when the heterostructure is symmetric, but it becomes rectifying when perylene layers are inserted on one side of the structure.
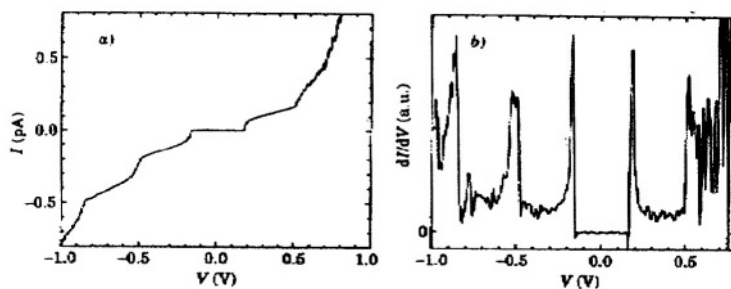
Figure 7: $I(V)$ characteristics of a symmetric Au/Polymer/PcPd/Polymer/Au heterojunction measured at 4.2 K (a) and the corresponding derivative (b)); PcPd is an octasubstituted metal-lophtalocyanine (from ref. [41]).

3.3 STM measurements on single molecules

The invention of the Scanning Tunneling Microscope (STM) [42,43] is a main step for the development of molecular electronics. The STM is based on a sharp tip (curvature radius in the nanometer range) which is placed at a small distance from a conductive surface in a way that electrons can tunnel from one electrode to the other. Using piezoelectric tubes, the position of the STM tip is fixed with an accuracy better than 1 Å, horizontally and vertically. The STM is an efficient tool to study single molecules adsorbed on metallic or semiconductor surfaces [44,45]. It can be used to image, to displace and to characterize single molecules.

3.3.1 STM imaging of single molecules

A natural application of the STM is the imaging of molecules adsorbed on a surface. In this mode, a constant bias is applied between the tip and the substrate. When the tip is displaced laterally, one measures the height of the tip which is adjusted in order to keep a constant tunneling current. The map of the height versus the lateral position is roughly representative of the topography of the surface, and thus gives information on the adsorbates. The adsorption of small molecules like CO and benzene on Rh(111) has been studied in detail [46,47], showing in some cases that self-organization can take place at the surface. Larger molecules like naphtalene or phtalocyanines have been also imaged [48,49]. The STM allows to study the adsorption sites. Nevertheless, the interpretation of the image is not straightforward, as it does not give information on the atomic positions but on the electronic structure.

Most of the work on STM imaging of adsorbed molecules concerns metallic surfaces, and only few semiconductor surfaces. However, as microelectronics technology is based on silicon substrates, there is an increasing need to study organic molecules linked to a silicon surface [50,51]. For example, Figure 8 shows high resolution STM images of a Si(l00) surface after deposition of thienylenevinylene tetramers, which belong to a new class of **π-conjugated** oligomers of particular interest as molecular wires [52]. The silicon dimers, typical of a Si(l00) (2x1) surface, are visible, forming rows of grey bean shaped. On the top of these rows, bright features can be seen, with different shapes corresponding to different adsorption configurations [51]. These results show that the molecules are quite conductive. Detailed studies allow a better understanding of the nature of the bonds between the molecules and the surface. Spectroscopic measurements are also possible, as detailed in the next sections.
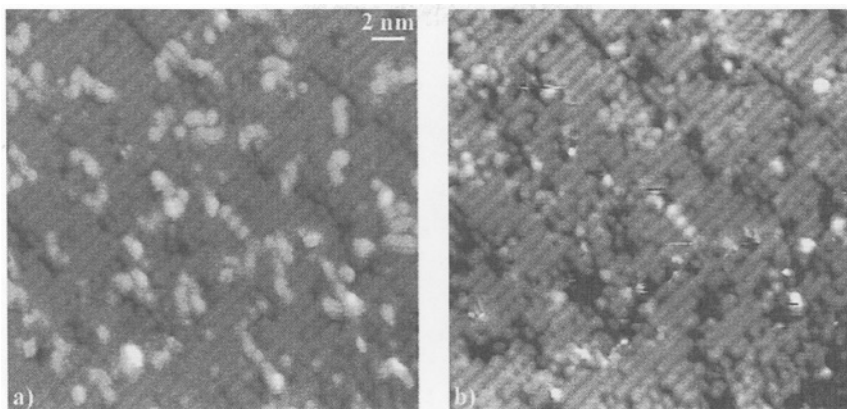
Figure 8: Voltage dependent STM images of the Si(100) surface after deposition of 4TVH oligomers. The sample bias was in (a) -2.1 V and in (b) -1.3 V (from ref. [51]).

3.3.2 STM as a tool to manipulate and to fabricate molecular objects

The STM tip is also a very interesting tool to manipulate the matter at the atomic scale. The forces (Van der Waals, electrostatic, chemical) between the atoms at the tip apex and the imaged object are used to displace atoms or molecules on a surface [53]. The first controlled atomic manipulation was presented by Eigler et al [54]. Xenon atoms were displaced on a nickel surface, by moving the tip which was kept close to the atoms. Artificial structures containing a small number of atoms were made using this technique. Xenon atoms were also transferred vertically from the surface to the tip in a reversible process [55,56].

The manipulation of molecules only came recently. Stipe et al have shown that it is possible to induce the rotation of acetylene molecules by excitation of C-H vibration modes with the STM [57]. This work shows the importance of inelastic processes in the tunneling. This effect can be exploited to perform vibrational spectroscopy on individual molecules [58] and is therefore a powerful technique to identify adsorbates, their chemical bonding and their local chemical environment. Due to the high spatial resolution of the STM, correlations between the electronic structure and vibrational excitation of adsorbed molecules can be determined. Moreover by using inelastic tunneling, molecules can be dissociated, desorbed or even synthesized, which is of essential importance in studies of molecular manipulation. Hla et al have shown that the assembling of two molecules is possible using a STM

[59]. Starting from two C_6H_5I molecules, they first removed the iodine atoms. Then they approached the two phenyl groups and they observed the formation of a biphenyl molecule. This reaction, entirely realized using the STM, was made at 20 K whereas the conventional synthesis is impossible below 180 K. Recently, larger molecules have been manipulated, showing that their adsorption on a surface may induce important atomic reconstructions [60]. The manipulation of specific parts of molecules may also lead to important changes in their $I(V)$ curve [61,62].

3.3.3 STM spectroscopy of molecules

In some conditions, the STM allows to study the electronic structure of molecules in connection with their interactions with the surface. In the spectroscopic mode of the STM, the tip is placed above an adsorbed molecule, and the current is measured as a function of the applied voltage. Thus, using this approach, a direct measurement of the transport properties of a single molecule is possible.

Several studies have been applied to C_{60} molecules because they are quite stable and easy to manipulate due to their size. Joachim et al [63] have measured the current through molecules on a gold substrate, at room temperature and with a small applied bias (50 mV). As the tip-molecule distance is reduced, the current increases at a very high rate which is interpreted by a distortion of the electronic levels due to the pressure induced by the tip. Other measurements at 4.2 K have been recently presented by Porath et al [64,65]. C_{60} molecules are adsorbed on gold substrate covered by a thin amorphous carbon film. The $I(V)$ curves present clear steps which are interpreted by Coulomb blockade effects and resonant tunneling through the discrete states of the molecule. States close to the HOMO-LUMO gap are completely resolved in spectroscopy. The degeneracy of the HOMO and LUMO levels is broken, probably due to the tip-induced electric field or due to a Jahn-Teller effect.

Another way to probe the conductivity of a single molecule is to use slightly defective SAMs. A particular system has been mainly studied, with molecules terminated by a thiol end group. Self-assembly is routinely obtained on gold surfaces (and others) using chemical grafting based on sulfur-gold bonds [66]. In a well-known experiment [67], dodecanethiol SAMs have been made with a small number of defects consisting of conjugated wires which are slightly longer than the dodecanethiol molecules. The dodecanethiol SAM forms a quite insulating layer [38]. STM images of the surface show a smooth surface with only few bright spots at the position of the molecular wires. This result demonstrates that the molecular wires have a

higher conductivity than the surrounding molecules. Other works have been performed in this direction [68].

The spectroscopy of single molecules may be also evidenced by imaging the surface at different tip-sample bias. In the example presented in a preceding section where thienylenevinylene tetramers are adsorbed on Si(l00), the images of the molecules are highly voltage dependent (Figure 8). At sufficiently high negative sample voltages, the molecules are visible, whereas at lower voltages, most of the molecules disappear. The interpretation is the following: at high voltages, electrons can tunnel through the HOMO of the molecule, whereas at lower voltages, only states close to the Fermi level of the semiconductor and associated with the Si dimers can contribute to the tunneling current.

Thus, interesting developments with a STM are taking place in various areas. It remains that the experiments which have been done up to now are at the state-of-the-art level, and their transfer to create new technologies is not straightforward. If the STM is a very good tool to study the transport through a single molecule, it is clear that other approaches have to be developed to make molecular electronic devices.

3.4 Molecules connected to nanoelectrodes

Here we describe other approaches to determine the $I(V)$ characteristics of a single molecule using nanoelectrodes. Compared to STM, these methods lead to stable, permanent and symmetric junctions. Applications of these techniques are already foreseen in the field of chemical and biological sensors.

3.4.1 Co-planar electrodes

This approach is based on lithographic methods to make metallic electrodes separated by a small gap, of the order of 5-10 nm for the smallest ones. This system is used to characterize long molecules which are placed in such manner that they are connected to the two electrodes (Figure 9). The conductivity of carbon nanotubes has been studied using this approach [69,70]. It has been verified that the nanotubes are metallic or semiconducting depending on their geometry. Carbon nanotubes are presently considered as the best candidates to make molecular wires, as the current can flow efficiently in long nanotubes (~ 1-0.1 μm). Co-planar electrodes are also used to measure the conductivity of DNA [71], and even to explore superconductivity effects in
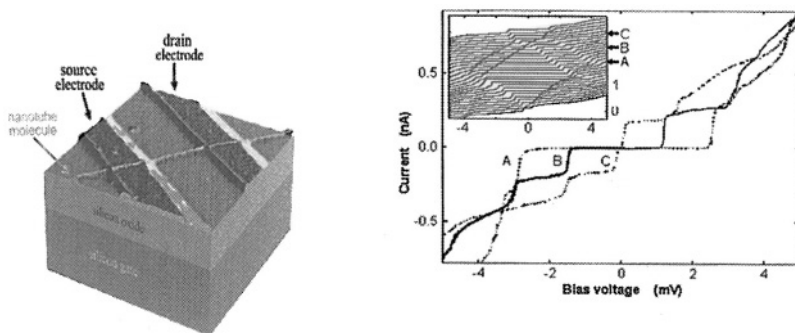
Figure 9: Nanotubes on co-planar electrodes and corresponding $I(V)$ characteristics at different gate voltages (courtesy: C. Dekker).

these systems [72,73].

3.4.2 Nanopores

In this approach, small holes are made in a thin silicon nitride film deposited on a metallic electrode. The pores are filled with the molecules. A second metallic electrode is evaporated on the top of the system to realize an electrical contact. Compared to techniques involving molecular films, a smaller number of molecules are probed in this approach (~1000). The number of junctions which are short circuited is also reduced [74]. Measurements have been realized on 1-4 phenylene diisocyanide [75] and [**1**: 2'-amino-4,4'-di(ethynylphenyl)-5'-nitro-l-benzenedithiol] [76,77]. In the case of the first molecule, a symmetric $I(V)$ curve is obtained. In the case of the second one, it exhibits negative differential resistance with a high peak-to-valley ratio at low temperature (Figure 10). The origin of this effect could be related to the electronic structure of the molecule [78]. In this case, the molecule could be used to realize oscillators.

3.4.3 Breaking junctions

In this third approach, a metallic wire (usually gold) is made by lithography on a flexible substrate. Then the wire is broken using a small mechanical perturbation. At the place where the wire is broken, there is a small gap of nanometer size where molecules can be deposited from a solution. Using piezoelectric tubes, the distance between the two electrodes is adjusted in
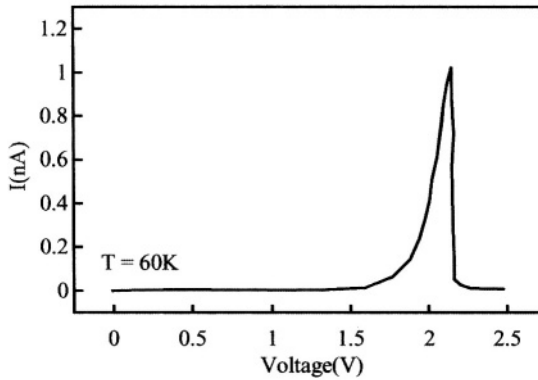
Figure 10: *I(V)* characteristics of a Au-(**1**)-Au device at 60 K (from ref. [77])

such a way that some molecules make a bridge between the electrodes. One difficulty with this technique is that the number of molecules which are connected is unknown. Reed et al have studied the conductance of benzene-1,4-dithiol grafted on gold electrodes [79]. Steps in the *I(V)* curve are obtained, maybe due to Coulomb blockade effects. Other molecules have been studied [80,81], confirming for example that dodecanethiol is good insulator at small bias. Park et al have inserted a C_{60} molecule in a breaking junction [82]. Using a gate voltage applied to the substrate, this system works as a transistor at the molecular level. In addition, a new effect is observed as the electronic transport is coupled to the motion of the C_{60} molecule. The results are explained by the oscillation of the molecule in the electrostatic field between two electrodes. Coupling to internal modes of vibration of the molecule is also suggested.

3.5 Molecular circuits

The fabrication of circuits based on molecules is obviously one main objective of molecular electronics. Even if much work is needed to develop the corresponding technologies, recent progress has been made in this direction. Collier et al [83] have presented a molecular circuit based on the Teramac architecture [84]. This computer architecture is defect-tolerant, meaning that it continues to work up to three percent of defected components. This kind of approach is ideal for molecular electronics since it will necessarily

contain defective components and connections. Logic gates are fabricated from an array of configurable molecular switches, each consisting of a monolayer of electrochemically active rotaxane molecules sandwiched between metal electrodes. AND and OR functions have been realized. The circuit is quite equivalent to Programmable Read Only Memory (PROM). Its fabrication would be much cheaper than in CMOS technologies.

This work illustrates an important orientation of molecular electronics. It could be used to make logic devices at a relatively low cost. It is foreseen that expensive fabrication procedures in the electronic industry could be progressively replaced by techniques derived from molecular electronics to reduce fabrication costs. Thus, the main aim is no longer to realize nanometer scale devices to follow the first Moore's law, but to reduce costs which are presently continuously increasing (second Moore's law).

REFERENCES

1.   D. Kahng and M. Atalla, US patents 3206670 and 3102230 (1960).
2.   T. Sakurai, Jap. Soc. Appl. Phys. 3, 15 (2001).
3.   The International Technology Roadmap for Semiuconductors, Semiconductor Industry Association (Sematech Inc., Austin, Texas 2000); see also http://www.sematech.org for the most recent updates.
4.   M. Schulz, Nature 399, 729 (1999).
5.   G. D. Wilk, R. M. Wallace, and J. M. Anthony, J. Appl. Phys. 89, 5243 (2001).
6.   H. Grabert and M.H. Devoret "Single charge tunneling : Coulomb blockade phenomena in nanostructures" (Plenum Press, New York, 1992)
7.   L. J. Geerligs, V. F. Anderegg, P. A. M. Holweg, J. E. Mooij, H. Pothier, D. esteve, C. Urbina, and M. H. Devoret, Phys. Rev. Lett. 64, 2691 (1990).
8.   H. Pothier, P. Lafarge, P. F. Orfila, C. Urbina, D. Esteve, and M. H. Devoret, Physica B 169, 573 (1991); H. Pothier, P. Lafarge, C. Urbina, D. Esteve, and M. H. Devoret, Europhysics Lett. 17, 249 (1992).
9.   Special Issue on Single Charge Tunneling, Z. Phys. B 85,317 (1991).
10.   D. V. Averin and K. K. Likharev in Mesoscopic Phenomena in Solids, B. L. Al'tshuler, P. A. Lee and R. A. Wenn eds (Elsevier, Amsterdam, 1991).
11.   D. K. Ferry and S. M. Goodnick in Transport in nanostructures (Cambridge University Press, 1997).
12.   J. R. Tucker, J. Appl. Phys. 72, 4399 (1992).
13.   K. Yano, I. Tomoyuki, T. Hashimoto, T. Kobayashi, F. Murai, and S. Moichi, IEDM Tech. Dig. 1993, p. 541.; K. Yano, T. Ishii, T. Hashimoto, T. Kobayashi, F. Murai, and K. Seki, IEEE Trans. Electron Devices 41, 1628 (1994).41
14.   L. Guo, E. Leobandung, and S. Chou, Science 275, 649 (1997); Appl. Phys. Lett. 70, 850 (1997).
15.   A. Nakajima, T. Futatsugi, K. Kosemura, T. Fukano, and N. Yokoyama, Appl. Phys. Lett. 70, 1742 (1997); Appl. Phys. Lett. 71, 353 (1997).
16.   Y. Takahashi, M. Nagase, H. Namatsu, K. Kurihara, K. Iwadate, Y. Nakajima, S. Horiguchi, K. Murase, and M. Tabe, IEDM Tech. Dig. 1994, p. 938; Electron. Lett. 31, 136 (1995); Y. Yakahashi, H. Namatsu, K. Iwadate, M. Nagase, and K. Murase, IEEE Trans. Electron. Devices 43, 1213 (1996).
17.   H. Ishikuro, T. Fujii, T. Saraya, G. Hashiguchi, T. Hiramoto, and T. Ikoma, Appl. Phys. Lett. 68, 3585 (1996).
18.   H. Ishikuro and T. Hiramoto, Appl. Phys. Lett. 71, 3691 (1997); Appl. Phys. Lett. 74, 1126 (1999).
19.   L. Zhuang, L. Guo, and S. Y. Chou, Appl. Phys. Lett. 72, 1205 (1998); E. leobandung, L. Guo, and S.Y. Chou, Appl. Phys. Lett. 67, 2338 (1995).
20.   A. Aviram and M. A. Ratner, Chem. Phys. Letters 29, 277 (1974).
21.   G.J. Ashwell, J.R. Sambles, A.S. Martin, W.G. Parker, and M. Szablewski, J. Chem. Soc., Chem. Commun. 1374 (1990); A.S. Martin, J.R. Sambles, G.J. Ashwell, Phys. Rev. Lett. 70, 218 (1993).
22.   R.M. Metzger, B. Chen, U. Höpfner, M.V. Lakshmikantham, D. Vuillaume, T. Kawai, X. Wu, H. Tachibana, T.V. Hughes, H. Sakurai, J.W. Baldwin, C. Hosh, M.P. Cava, L. Brehmer, and C.J. Ashwell, J. Am. Chem. Soc. 119, 10455 (1997).
23.   D. Vuillaume, B. Chen and R.M. Metzger, Langmuir 15, 4011 (1999). B. Chen and

R.M. Metzger, J. Phys. Chem. B 103, 4447 (1999).

24. R.M. Metzger, J. Mater. Chem. 9, 2027 (1999); ibid 10, 55 (2000).
25. C. Krzeminski, C. Delerue, G. Allan, D. Vuillaume and R. Metzger, Phys. Rev. B, to be published.
26. A. G. MacDiarmid and A. J. Heeger, Synthetic Metals 1, 101. (1980).
27. W. P. Su, J. R. Schrieffer, and A. J. Heeger, J. Chem. Phys, 73, 946 (1980).
28. F. L. Carter, Molecular electronic devices, Dekker, 51 (1982).
29. J. C. Ellenbogen and J. C. Love, Proceeedings of the IEEE 70, 386 (2000).
30. P. Ball, Nature 406, 118 (2000).
31. C. Joachim, J. K. Gimzewski and A.Aviram, Nature 408, 541 (2000).
32. H. Taube, Science 226, 1036 (1984).
33. C. Creutz and H. Taube, J. Am. Chem. Soc. 91, 3988 (1969).
34. C. Patoux, J-P. Launay, M. Beley, S. Chodorowski-Kimmes, J-P. Collin, S. James and J-P Sauvage, J. Am. Chem. Soc. 120, 3717 (1998).
35. S. Larsson, Chemical Physics Letters 90, 136 (1982).
36. C. C. Moser, J. M. Keske, K.Warncke, R. S.Farid and P. L. Dutton, Nature, 355, 796 (1992).
37. R. M. Metzger and C. A. Panetta, New. J. Chem., 15, 209 (1991).
38. B. Mann and H. Kuhn, J. Appl. Phys. 42, 4398 (1971).
39. C. Boulas, J. V. Davidovits, F. Rondelez, and D. Vuillaume, Phys. Rev. Lett. 76, 4797 (1996).
40. D. Vuillaume, C. Boulas, J. Collet, G. Allan and C. Delerue, Phys. Rev. B **58**, 16491 (1998).
41. C. M. Fischer, M. Burghard, S. Roth and K. V. Klitzing, Europhys. Lett. 28, 129 (1994).
42. G. Binning, H. Rohrer, Ch. Gerber and E. Weibel, Phys. Rev. Lett. 49, 57 (1982).
43. G. Binning and H. Rohrer, Rev. Mod. Phys. 59, 57 (1987).
44. J. Gimzewski, Physics World, 29 (1998).
45. J. Gimzewski and C. Joachim, Science 283, 1683 (1999).
46. H.Ohtani, R. J. Wilson, S. Chiang and C. M. Mate, Phys. Rev. Lett 60, 2398 (1988).
47. P. S. Weiss and D. M. Eigler, Phys. Rev. Lett 71, 3139 (1993).
48. V. M. Hallmark, S. Chiang, J. K. Brown and Ch. Woll, Phys. Rev. Lett. 66, 48 (1991).
49. J. Gimzewski and R. Moller, Phys. Rev. B, 36, 1284 (1987).
50. J.S. Hovis, H. Liu, R.J. Hamers, Surf. Sci. 402, 1 (1998).
51. B. Grandidier, J.P. Nys, D. Stiévenard, C. Krzeminski, C. Delerue, P. Frère, P. Blanchard, J. Roncali, Surf. Sci. 473, 1 (2001).
52. C. Krzeminski, C. Delerue, G. Allan, V. Haghet, D. Stiévenard, E. Levillain, and J. Roncali, J. Chem. Phys. **111,** 6643 (1999).
53. S. Gauthier, Applied Surface Science 164, 84 (2000).
54. D. M. Eigler and E. K. Schweizer, Nature 344, 524 (1990).
55. D. M. Eigler, C. P. Lutz and W. E Rudge, Nature 352, 600 (1991).
56. M. F. Crommie, C. P. Lutz and D. M. Eigler, Science 262, 219 (1993).
57. B. C. Stipe, M. A. Rezaei, and W. Ho, Phys. Rev. Lett 81, 1263 (1998).
58. B. C. Stipe, M. A. Rezaei, and W. Ho, Science 280, 1732 (1998).
59. S-W. Hla, L. Bartels, G. Meyer and K-H. Rieder, Phys. Rev. Lett 85, 277 (2000).
60. M. Schunack, L. Petersen, A. Kuhnle, E. Laegsgaard, I. Stensgaard, I. Johannsen and F. Besenbacher, Phys. Rev. Lett 86, 456 (2001).

61. F. Moresco, G. Meyer, K-H. Rieder, H. Tang, A. Gourdon, and C. Joachim, Appl. Phys. Lett. 78, 307 (2001).

62. F. Moresco, G. Meyer, K-H. Rieder, H. Tang, A. Gourdon, and C. Joachim, Phys. Rev. Lett 86, 672 (2001).

63. C. Joachim, J. K. Gimzewski, R. R. Schlittler, C. Chavy, Phys. Rev. Lett. 74, 2102 (1995).

64. D. Porath and O. Millo, J. Apply. Phys. Lett. 81, 2241 (1997).

65. D. Porath, Y. Levi, M. Tarabiah, and O.Millo, Phys. Rev. B 112, 558 (1990).

66. R. G. Nuzzo, L. H. Dubois and D. L. Allara, J. Am. Chem. Soc. 56, 9829 (1997).

67. L. A. Bumm, J. J. Arnold, M. T. Cygan, T. D. Dunbar, T. P Burgin, L. Jones, D. L. Allara, J. M. Tour, P. S. Weiss, Science 271, 1705 (1996).

68. L. A. Bumm, J. J. Arnold, T. D. Dunbar, D. L. Allara, and P. S. Weiss, J. Phys. Chem. B 103, 8122 (1999).

69. S. J. Tans, M. H. Devoret, H. Dal, A. Thess, R. E. Smalley, L. J. Geerligs and C. Dekker, Nature 386, 475 (1997).

70. C. Dekker, Physics Today, 22 (May 1999).

71. D. Porath, A. Bezryadin, S. de Vries and C. Dekker, Nature 403, 635 (2000).

72. M. Kociak, A. Yu. Kasumov, S. Guéron, B. Reulet, I. I. Khodos, Yu. B. Gorbatov, V. T. Volkov, L. Vaccarini, and H. Bouchiat, Phys. Rev. Lett. 86, 2416 (2001).

73. A. Yu. Kasumov, M. Kociak, S. Guéron, B. Reulet, V. T. Volkov, D.V. Klinov and H. Bouchiat, Science 291, 280 (2001).

74. C. Zhou, M. R. Deshpande, M. A. Reed, L. Jones and J. M. Tour, Appl. Phys. Lett. 71, 611 (1997).

75. J. Chen, L. C. Calvet, M. A. Reed, D. W. Carr, D. S. Grubisha, D. W. Bennett, Chem. Phys. Lett. 313, 741 (1999).

76. J. Chen, M. A. Reed, A. M. Rawlett, J. M. Tour, Science 286, 1550 (1999).

77. J. Chen, W. Wang, M. A. Reed, A. M. Rawlett, D.W. Price, and J. M. Tour, Appl. Phys. Lett. 77, 1224 (2000).

78. J. M. Seminario, A. G. Zacarias and J. M. Tour, J. Am. Chem. Soc. 122, 3015 (2000).

79. M. A. Reed, C. Zhou, C. J. Muller, T. P. Burgin, and J. M. Tour, Science 278, 252 (1997).

80. C. Kergueris, thesis from Orsay university (1998).

81. C. Kergueris, J.-P. Bourgoin, S. Palacin, D. Esteve, C. Urbina, M. Magoga and C. Joachim, Phys. Rev. B, 59, 12505 (1999).

82. H. Park, J. Park, A. K. L. Lim, E. H. Anderson, A. P. Alivisatos, and P. L. McEuen, Nature, 407, 57 (2000).

83. C. P. Collier, E. W. Wong, M. Belohradsky, F. M. Raymo, J. F. Stoddart, P. J.Kuekes, R. S. Williams, J. R. Heath, Science 285, 391 (1999).

84. J. R. Heath, P. J. Kuekes, G. S. Snider, R. S. Williams, Science 280, 1716 (1998).

INDEX